

Doctoral Thesis No. 28305

Sparse Synthesis for Hyperdimensional Ptychographic Tomography

Zirui Gao

Doctoral Thesis



Doctoral Thesis No. 28305
ETH Zurich

Zirui Gao

DISS. ETH NO. 28305

Sparse Synthesis for Hyperdimensional Ptychographic Tomography

A thesis submitted to attain the degree of
DOCTOR OF SCIENCES of ETH ZURICH
(Dr. sc. ETH Zurich)

presented by
ZIRUI GAO

M.Sc., ETH Zurich

born on 05.04.1996

accepted on the recommendation of

Prof. Dr. Marco F. M. Stampanoni
Dr. Manuel Guizar-Sicairos
Prof. Dr. Chris Jacobsen
Prof. Dr. Yukio Takahashi

2022

Acknowledgements

The work of this thesis as well as my four years of PhD study could only have been done with the help of a large number of people, and to whom I want to express my sincere gratitude.

First, I want to thank my supervisor Manuel Guizar-Sicairos for providing me the opportunity to start this PhD, and for his endless support throughout the project. I have learned so much from your supervision and our regular discussions, thanks to your extensive expertise in the research field. Moreover, I am grateful for the time and effort you spent to make sure that I can align the project with my personal skills and interests. They have been extremely helpful to my career.

Further, I express my thanks to my PhD supervisor Marco Stampanoni, for offering the opportunity of this doctoral position in ETH Zurich, for keeping track of the progression of the project, and for providing valuable feedbacks and insights on its developments.

I want to thank Johannes Ihli for co-proposing the research projects in this thesis, and for co-supervising the spectroscopy studies. Your proficient experience in materials science and imaging, as well as in scientific writing, has helped greatly the accomplishment of these projects and publications. Similarly, my thanks goes to Mirko Holler, for co-proposing the dynamic imaging projects, for developing the instruments for these experiments, and for his amazing support on the operation of ptycho tomo imaging at the cSAXS beamline.

Moreover, I want to express my gratitude to all current and former members of the CXS group. To Ana Diaz for her overall support on every aspect of beamline operation, office tasks, and daily life. To Andreas Menzel for his guidance as line manager and for the bilateral meetings that generated countless new ideas and insights. To Xavier Donath for his great technical support to all the experiments. To Michal Odstrčil and Klaus Wakonig for their genuine support for my understanding of software packages and reconstruction algorithms. To Mariana Verezhak and Dmitry Karpov for the inspiring discussions and enjoyable off-work gatherings. To Christian Appel and Nicholas Phillips for providing extensive help to the beamtime experiments, and very importantly for their much appreciated aid to my thesis writing. To Tomas Aidukas for helping with code developments. To Irene Rodriguez Fernandez for sharing the ideas and thoughts as fellow PhD students. My four years of work and life were so much more enjoyable because of all of you.

I express special thanks to my collaborators on the battery project from University of Oxford, Ziyang (George) Ning and Bingkun Hu. We have pushed together this highly challenging project for over two years, and persisted after discouraging outcomes until

getting it to work and produce nice results. Your excellent skills on cell fabrication and experimental designs are absolute key to this accomplishment.

In addition, I want to thank my other colleagues and friends in PSI, Jinayuan Zhou, Jörg Raabe, Dario Ferreira Sanchez, and Elisabeth Müller. Your help and advice in different aspects are also crucial to my works in this project.

I acknowledge the financial support by the Swiss National Science Foundation (SNSF), grant number 200021_178788.

Lastly, I express my deepest gratitude to my parents, for always supporting me and giving me strength throughout my life. I also want to thank all my friends in China and all around the world, for your companionship in the four years of my PhD study. And my special thanks goes to Doki, for providing the most generous moral support within her purview.

Abstract

Since the first demonstration of X-ray computed tomography in 1971, it has become an essential diagnostic tool in modern medicine and a key investigative method in material research. The high penetration and non-destructive imaging capability of X-rays allows computed tomography techniques to probe the interior structure of materials in three-dimensions with a previously unfathomable level of detail. Moreover, continuous developments in X-ray computed tomography have led to various improvements and modifications that increase its speed, quality, or widen its application to diverse research fields. On the other hand, technological advancements also bring higher demands on imaging techniques. In order to better understand the fundamental links between structure, composition, and function of complex systems and materials, from living organisms to industrial catalysts, there is often a need for a further level of information beyond static 3D images. This need can be fulfilled by extending computed tomography to higher than three dimensions to resolve properties such as dynamic processes or chemical compositions. As demonstrated in this thesis, these properties are critical to the durability and efficiency of functional materials in various applications, including catalysis, energy conversion, and energy storage. Advancing our understanding of these materials is key to further developments of the related technologies.

Presented in this thesis are works on some of the most representative cases of hyperdimensional tomography: tomographic spectroscopy and dynamic tomography. In particular, these works include novel methodologies that are focused on solving the most critical limitation for hyperdimensional imaging, which is the long acquisition time when aiming for higher spatial, spectral, and temporal resolution. Over three studies, this thesis showcases how a combination of tomographic acquisition and reconstruction processes utilizing sparse synthesis can significantly alleviate this limitation. By leveraging the correlations and continuities in hyper-dimensional imaging, which arise from sample properties and experimental conditions, novel sparse acquisition strategies are developed and demonstrated. These approaches reduce the measurement time by more than one order of magnitude compared to conventional methods, while specialized reconstruction methods are further introduced to avoid any loss of spatial resolution. The presented methods were demonstrated on samples of industrial catalysts, fuel cell membranes, and *operando* lithium battery cells. These methods were able to obtain chemical-state information of the catalysts with 8 times faster imaging speed, and time-resolved structural details of the dynamic systems with up to 40 times higher temporal resolution, compared to conventional approaches. The results provide highly valuable information for understanding the properties or mechanisms of the investigated materials, as well as insights towards improving their design and performance.

Chapters 1 and 2 of this thesis include a brief introduction on (i) X-ray imaging techniques, especially X-ray ptychography, which is the imaging technique used in all included works, (ii) X-ray computed tomography and (iii) hyperdimensional tomography. Following in Chapter 3, X-ray linear polarization-dependent spectroscopic ptychography is demonstrated for crystal grain characterization of polycrystalline materials. The approach serves as an essential step towards ptychographic vector tomography, which also constitutes a type of hyperdimensional tomography. In Chapters 4 to 6, the methodological concepts and experimental realization of sparse hyperdimensional tomography are presented for three case studies. These include (i) hyperspectral nanotomography for chemical state speciation of pristine and industrially used vanadium phosphorous oxide (VPO) catalysts in Chapter 4, (ii) dynamic nanotomography to resolve the controlled hydration process of hydrogen fuel-cell catalyst in Chapter 5, and (iii) *operando* nanoscale laminography imaging of structural changes of cathode particles in solid-state lithium battery cells in Chapter 6. Altogether, these works provide a basis for hyperdimensional imaging utilizing sparsity and demonstrate its potential in a wide variety of applications of material characterization studies.

Zusammenfassung

Röntgen-Computertomografie gehört zum unverzichtbaren Repertoire der medizinischen Diagnosetools und zu einer wichtigen Untersuchungsmethode der Materialforschung. Die hohe Eindringtiefe von Röntgenstrahlen ermöglicht es Computertomografiertechniken, die innere Struktur von Materialien in drei Dimensionen abzubilden. Seit seiner Demonstration im Jahr 1971 hat sich diese Technik stets weiterentwickelt, insbesondere im Hinblick auf Bildqualität, und Aufnahmegeschwindigkeit, woraufhin sich Relevanz und Anwendungsgebiet stets ausgeweitet haben. Auf der anderen Seite stellt der technologische Fortschritt moderne bildgebende Verfahren auch vor neue Herausforderungen. Um die grundlegenden Zusammenhänge zwischen Struktur, Zusammensetzung und Funktion komplexer Systeme und Materialien, von lebenden Organismen bis hin zu industriellen Katalysatoren besser zu verstehen, ist häufig eine weitere Informationsebene erforderlich, die die statische 3-D-Bildgebung der regulären Tomografie komplementiert. Dies ist nötig, um zum Beispiel zeitaufgelöst dynamische Prozesse oder die lokale chemische Zusammensetzung der untersuchten Materialien zu verstehen. Wie später gezeigt wird, sind diese Prozesse entscheidend für die Haltbarkeit und Effizienz von Materialien aus diversen Anwendungsbereichen, einschließlich der Katalyse, Energieumwandlung und Energiespeicherung. Die Verbesserung unseres Verständnisses dieser Materialien ist der Schlüssel zur Weiterentwicklung der verwandten Technologien.

In dieser Dissertation werden multiple Arbeiten und neu entwickelte Methoden der hyperdimensionalen Tomografie vorgestellt. Speziell bezüglich der spektroskopischen und dynamischen Tomografie. Diese erweitern die Röntgen-Computertomografie um eine chemische oder zeitliche informationsebene bzw Dimension. Im Fokus stehen hier neue Konzepte, die sich auf die Lösung der kritischsten Einschränkung der hyperdimensionalen Tomografie konzentrieren, die langen Aufnahmezeiten, insbesondere wenn eine hohe räumliche wie auch zeitliche bzw. spektrale Auflösung angestrebt wird. Anhand drei verschiedener Systeme wird gezeigt wie eine Kombination von tomographischen Aufnahme- und Rekonstruktionsverfahren unter Verwendung eines sparsity Ansatzes diese Einschränkung deutlich reduzieren kann. Unter Ausnutzung der Korrelationen und Kontinuitäten in der hyperdimensionalen Bildgebung, die sich aus den Eigenschaften der Probe und den experimentellen Bedingungen ergeben, werden neuartige Messstrategien entwickelt und demonstriert. Diese Ansätze reduzieren die Messzeit um mehr als eine Größenordnung im Vergleich zu konventionellen Methoden, beruhen gleichzeitig aber auf speziellen Rekonstruktionsansätzen, welche sicherstellen dass die räumliche Auflösung erhalten bleibt. Die vorgestellten Methoden wurden an Proben von industriellen Katalysatoren, Brennstoffzellen-Membranen und Lithiumbatterien demonstriert. Die mit dem Ansatz erzielten Ergebnisse liefern Informationen über die chemische Zusammensetzung der Katalysatoren, wobei die Bildgebungsgeschwindigkeit 8x schneller ist als mit

konventionellen Methoden. Für die Messungen der dynamischen Systeme zeigt sich, dass die Ergebnisse der Strukturcharakterisierung eine bis zu 40x höhere zeitliche Auflösung haben im Vergleich zu herkömmlichen Ansätzen, wobei die hohe räumliche Auflösung für alle Zeitschritte erhalten bleibt. Die Ergebnisse liefern wertvolle Informationen um das Verständnis über Funktionalität und dynamische Prozesse in allen 3 Systemen zu vertiefen, welches in Zukunft zur Verbesserung ihres Designs und ihrer Leistung führen könnte.

Die Kapitel 1 und 2 dieser Dissertation enthalten eine kurze Einführung in (i) bildgebende Röntgenverfahren, insbesondere der Röntgen-Ptychographie, die in allen Arbeiten als bildgebendes Verfahren verwendet wird, (ii) Röntgen-Computertomographie und (iii) hyperdimensionale Tomographie. In Kapitel 3 wird ein Ansatz zur linear polarisations-abhängigen Röntgen-Ptychographie vorgestellt. Der Ansatz ist ein wesentlicher Schritt in Richtung der ptychografischen linearen dichroitischen Vektortomografie, einer dritten Art hyperdimensionaler Tomografie, die eine mikrostrukturelle Charakterisierung von kristallinen Materialien ermöglicht. In den Kapiteln 4 bis 6 werden methodische Konzepte zur experimentellen Umsetzung der hyperdimensionalen Tomographie mit dem sparsity Konzept anhand von drei Fallstudien vorgestellt. Kapitel 4 stellt anhand der Untersuchung von industriellen Vanadium-Phosphor-Oxid (VPO)-Katalysatoren quantitative hyperspektrale Nanotomografie vor. Kapitel 5 realisiert eine Form der dynamischen Nanotomografie zur Auflösung des Hydratationsprozesses eines Wasserstoff-Brennstoffzellen-Katalysators. Kapitel 6 verwirklicht Operando-Laminographie um die strukturelle Entwicklung von Kathodenpartikeln in zwei Festkörper-Lithiumbatterien zu untersuchen. Insgesamt bieten diese Arbeiten eine Grundlage von multidimensionaler Computertomografie unter Verwendung von sparsity Konzepten. Ihr Potenzial wird anhand von verschiedenen Anwendungsbeispielen zur Materialcharakterisierung demonstriert.

Contents

Acknowledgements	iv
Abstract	vi
Zusammenfassung	viii
1 Introduction	1
1.1 Outline	3
1.2 Contributions	4
2 X-ray Imaging and Tomography	7
2.1 Basics of X-ray Imaging	7
2.1.1 Helmholtz Equation and Projection Approximation	7
2.1.2 Coherent X-ray Imaging Techniques	9
2.1.3 X-ray Ptychography	10
2.2 Computed Tomography	12
2.2.1 Fundamental Concepts of Tomography Imaging	13
2.2.2 Fourier Slice Theorem	14
2.2.3 Tomography Reconstruction Methods	15
2.3 Hyperdimensional Tomography	22
2.3.1 Dynamic Tomography	23
2.3.2 Hyperspectral Tomography	23
2.3.3 Tensor Tomography	24
2.4 Sparse Synthesis in Tomography	25
3 Nanoscale Crystal Grain Characterization via Linear Polarization X-ray Ptychography	27
3.1 Abstract	27
3.2 Main Text	27
	ix

3.3	Supplementary Information	35
3.3.1	Materials	35
3.3.2	Sample Mounting for PIC-PXCT	35
3.3.3	Optical and Electron Microscopy	35
3.3.4	PIC-Ptychography	35
4	Sparse X-ray Transmission Spectrotomography for Nanoscopic Compositional Analysis	41
4.1	Abstract	41
4.2	Introduction	42
4.3	Results	44
4.3.1	X-ray Transmission Near-Edge Spectro Tomography	44
4.3.2	XTNES Tomograms of Pristine and Deactivated VPO Catalysts	46
4.4	Discussion	48
4.5	Materials and Methods	53
4.6	Acknowledgements	58
4.7	Supplementary Materials	59
4.7.1	Extended Materials and Methods	59
4.7.2	Selective Oxidation of <i>n</i> -butane to Maleic Anhydride (MA), its Industrial Realization and Relevance	62
4.7.3	Suggested Active Sites in VPO Catalysts	63
4.7.4	Ptychographic Computed X-ray Tomography and Sensitivity to Variations in Incident Energy	63
4.7.5	Local Structure Optimization	65
4.7.6	Supplementary Movies	65
4.7.7	Supplementary Figures	68
5	Dynamic Sparse X-ray Nanotomography Reveals Hydration Mechanism in PEFC Catalyst	79
5.1	Abstract	79
5.2	Introduction	80
5.3	Sparse Dynamic Nanotomography	82
5.4	Iterative Temporal Reconstruction Technique	83
5.5	Vapor Condensation and Water Uptake in a PEFC Catalyst Layer	84

5.6	Reconstruction and Analysis	86
5.7	Discussion	91
5.8	Methods	92
5.8.1	Sample Preparation	92
5.8.2	Measurement and Data Pre-processing	92
5.8.3	Nonrigid Computed Tomography	94
5.8.4	Sparse Dynamic Tomography Reconstruction	96
5.8.5	Spatial Resolution Estimate	99
5.8.6	Numerical Simulations	101
5.9	Acknowledgements	106
5.10	Author Contributions	106
6	Nanoscale <i>operando</i> Laminography of Solid-state Lithium Battery	107
6.1	Introduction	107
6.2	Methods	109
6.2.1	All-solid-state Battery Cell	109
6.2.2	X-ray Ptychographic Laminography	109
6.2.3	Sparse <i>operando</i> Laminography	111
6.2.4	Reconstruction	112
6.3	Results	115
6.4	Conclusion and Outlook	121
7	Summary and Outlook	123
A	Curriculum Vitae	127
	Bibliography	129

Introduction

For most materials and systems in the three-dimensional world, from spaceship frames to human organs, their functionalities are defined by their internal structure which is not readily visible from the outside. Therefore, the importance of computed tomography techniques to modern industry and medicine can hardly be overstated. Computed tomography (CT) provides a non-destructive means to probe the interior of different objects, which is achieved by measuring the transmission of the object at different angles to produce three-dimensional cross-sectional images [1]. While medical CTs are nowadays available in hospitals and clinics, and are well known to the public, other means of computed tomography techniques also found essential uses in biology [2, 3], materials science [4, 5], geology [6] or even archaeology [7].

Over the past five decades since the first demonstration of CT [8], there has been countless innovations towards improved hardware and software designs. While all these developments contribute toward higher efficiency and better performance, there has also been growing interest, especially in the last twenty years, for more demanding applications of CT, including high-speed measurements [9], large sample volumes, nanometric resolution [10], or, as covered in this thesis, extension to hyperdimensional applications.

The word ‘hyperdimensional’ refers to ‘of or relating to space of more than three dimensions’. The idea of hyperdimensional CT comes as a natural extension of the method, with its most common case being dynamic or temporal tomography. If the studied substance is not a static object but changing over time, such as live organs in human body, there is demand to acquire images of its interior not at a single time point, but at several time frames during its functional process. Furthermore, by inducing changes to the imaged object and acquiring its CT image sequentially, it is also possible to study its response to varying thermal, chemical or electrical conditions, which is of interest for most functional materials and systems.

This seemingly simple idea, however, comes with difficulties that would challenge researchers ever since it was first raised [11]. Such that even for the most common dynamic process like the heartbeat, there is not yet a fully established method of temporal CT imaging, and the development of which remains a topic of interest [12–14].

The most important challenge to dynamic CT imaging originates from the assump-

tions of tomography. Because a tomographic reconstruction requires multiple images of the object to be measured from different angles, the acquisition of these images needs certain period of time either for hardware movement, detector readout, or signal processing. As the images are measured sequentially in virtually all existing CT techniques, the total tomography acquisition time is given by the sum of all the measurements. The tomography acquisition time is a major limitation to the achievable speed of CT techniques to resolve dynamic processes. For example, in the case of cardiac imaging, even the fastest modern medical CT machines take several seconds to image a human chest. In this time period the heart would expand and contract multiple times, making it impossible to precisely resolve the heartbeat process with conventional CT without modifications in the measurement strategy, such as using periodicity of movement as a constraint [12, 14].

Similar limitations apply to any hyperdimensional tomography technique, due to the fact that tomography acquisition cannot be arbitrarily fast. As described in Chapter 2, there exists a theoretical criterion that defines the number of images, *i.e.* projections, that need to be taken for tomography in order to measure a given sample volume at a certain resolution, namely the *Crowther criterion* [15]. To measure hyperdimensional tomography means to multiply this given number by the number of frames in the extra dimension, which further increases the required acquisition time considerably. This long acquisition time is then either hindered by experimental constraints, such as available measurement time or radiation damage to the sample, or deemed ineffective by the relatively fast changes that require much faster speed to resolve.

In this thesis, a methodological approach is presented to alleviate these limitations. The approach utilizes sparse sampling in the measurement and novel reconstruction algorithms to largely reduce the required acquisition time. Specifically, reductions of more than one order of magnitude are achieved here without significant loss in the reconstruction quality or resolution. This marked improvement in acquisition speed allows measurements of higher resolution and larger sample volume, it also enables imaging of fast processes that would be previously prohibitive.

The sparse hyperdimensional imaging approach is demonstrated for three studies: hyperspectral tomography on Vanadium Phosphorous Oxide catalyst samples; dynamic tomography on polymer electrolyte membrane fuel-cell catalyst sample; and *operando* laminography on cathode particles in solid-state lithium battery cells. Ptychographic X-ray Computed Tomography (PXCT) was selected as the imaging modality for all three studies [10]. X-ray ptychography is an emerging technique which is getting increased usage in synchrotrons worldwide in the past 10 years [16]. As a coherent lensless imaging technique, it provides a practical way to overcome limitations of lens manufacturing, especially for X-rays, and possesses the ability to achieve nanoscale resolution and quantitative contrast [17]. For these studies, PXCT is combined with sparse acquisition strategies and novel reconstruction methods based on the sparsity approach, in order to reach nanoscale spatial resolution at a measurement speed up to 40 times faster than conventional tomography methods. In all three cases, the outcomes of hyperdimensional imaging with nanoscale resolution provide crucial information regarding the properties

or mechanisms of the studied samples that were previously unknown or only theorized, such as chemical states, hydration mechanisms, or structural changes.

1.1 Outline

Chapter 2 of this thesis includes a brief introduction to the basics of X-ray imaging, coherent imaging techniques, and computed tomography. It also includes an introduction to hyperdimensional tomography, including some of the most commonly used techniques, and to the concept of sparse synthesis in tomography.

Chapter 3 presents a novel nanoscale crystal grain characterization method for vanadium pentoxide samples. The method is based on polarization imaging contrast of X-ray spectroscopic ptychography, which works without the need for a polarization analyzer. The method is demonstrated in 2D as a first step towards X-ray polarization vector tomography. The chapter also covers basics for chemical analysis using X-ray spectroscopic ptychography, applied to vanadium-oxide-based materials.

Chapter 4 presents the introduction and demonstration of *ab initio* sparse X-ray transmission spectrotomography, applied for 3D nanoscopic chemical analysis of industrial Vanadium Phosphorous Oxide (VPO) catalysts. These VPO catalysts are used in the production of precursors of household and industrial plastics worldwide. With sparsity implementation, hyperspectral imaging of these catalysts is obtained without loss of resolution, with only 11% of the projections dictated by the *Crowther criterion*. The method allows a combined structural, compositional, and chemically quantitative characterization of pristine and industrially-used VPO catalyst samples, with 26.5 nm half-period resolution for representative sample volumes. The results present a general description of the restructuring process of the catalyst during industrial use, and provide insights towards improved design for increasing the lifetime of these catalysts.

Chapter 5 presents a novel dynamic sparse X-ray nanotomography method applied to resolve ionomer hydration mechanisms in a polymer electrolyte membrane fuel-cell catalyst. Applying sparsity to temporal nanotomography opens the opportunity for studying various dynamic processes at a temporal resolution more than one order of magnitude higher than the conventional sampling approaches. In the presented work, the controlled hydration process of a hydrogen fuel cell catalyst sample is imaged with 28 nm half-period resolution and a temporal resolution of 12 minutes, compared to the 8 hours measurement time which would be required by the conventional approach for each tomogram. The results provide detailed information on the water condensation and structural changes in the water uptake process of these catalysts, which is essential for their working mechanisms.

Chapter 6 presents the dynamic sparse X-ray laminography method for imaging of *operando* cathode particles in solid-state battery cells. The method is a generalization of the dynamic nanotomography method presented in Chapter 5. It was extended to the laminography geometry, which allows measurement of extended flat samples and is

very well suited for *operando* measurements. Furthermore, ptychographic laminography is demonstrated in an interior configuration, where the imaged volume is completely contained within the sample in all directions, which enables measurement of particles of 10 μm diameter inside solid-state battery cells of 0.2 cm^2 area and 350 μm thickness. This capability to perform interior laminography allows characterization of dynamic features at nanoscopic level inside micrometer-scaled samples, and enables a whole host of new opportunities for *operando* measurements. Finally, the dynamic model was generalized to include more complex dynamics and allow reconstruction of processes which include repeated charge / discharge cycles. Preliminary analysis of the results reveals the structural changes and lithiation / delithiation process inside the *operando* cathode particles with nanoscale resolution. The outcomes of this work further demonstrates the power of the sparse hyperdimensional imaging method for generalized applications of high-resolution and high-speed imaging of *operando* samples.

A summary and outlook of this work are given in Chapter 7, including possible further extensions for the methods presented here.

1.2 Contributions

The work presented in this thesis was performed as part of a research team, and in collaboration with other research groups. For clarity, an overview of the contributions of the PhD student, Zirui Gao, are described explicitly below for each chapter, along with collaborations with other people.

Chapter 3

- Performed the experiments in collaboration with Mirko Holler, Manuel Guizar-Sicairos and Johannes Ihli.
- Analyzed the datasets in collaboration with Johannes Ihli and Manuel Guizar-Sicairos.
- Wrote the manuscript with contributions from all authors.

Chapter 4

- Performed the experiments in collaboration with Mirko Holler, Michal Odstreil, Manuel Guizar-Sicairos and Johannes Ihli.
- Developed the reconstruction algorithm and reconstructed the XTNES datasets.
- Analyzed the XTNES datasets in collaboration with Manuel Guizar-Sicairos and Johannes Ihli.

- Performed the μ XRF and μ XRD experiments in collaboration with Johannes Ihli and Dario Ferreira Sanchez.
- Wrote the manuscript with contributions from all authors.

Chapter 5

- Proposed the study and designed the experiments in collaboration with Manuel Guizar-Sicairos, Mirko Holler, Christian Appel and Johannes Ihli.
- Performed the experiments in collaboration with Christian Appel, Manuel Guizar-Sicairos, Mirko Holler and Johannes Ihli.
- Developed the reconstruction algorithm and reconstructed the datasets.
- Interpreted the results in collaboration with Christian Appel and Manuel Guizar-Sicairos.
- Wrote the manuscript with contributions from all authors.

Chapter 6

- Proposed the study in collaboration with Ziyang Ning, Johannes Ihli and Manuel Guizar-Sicairos.
- Designed the battery cells in collaboration with Ziyang Ning, Bingkun Hu and Johannes Ihli.
- Performed the experiments in collaboration with Bingkun Hu, Ziyang Ning, Nicholas Phillips, Mirko Holler, Manuel Guizar Sicairos and Johannes Ihli.
- Developed the reconstruction algorithm and reconstructed the datasets.
- Interpreted the results in collaboration with Bingkun Hu, Ziyang Ning and Manuel Guizar-Sicairos.

Apart from the contents covered in this thesis, the PhD project of Zirui Gao also includes contributions towards new functionalities or improved performance of research software for the cSAXS beamline (X12SA), Swiss Light Source. These contributions are described below. The data processing and analysis codes are publicly available on the cSAXS software website <https://www.psi.ch/en/sls/csaxs/software>.

- Developed new scan control scripts and optimized data processing pipelines for scanning small-angle X-ray scattering (SAXS) and small-angle scattering tensor tomography (SASTT) experiments.
- Improved performance and reliability of tomography and laminography alignment codes.
- Optimized laminography scan and reconstruction pipelines.

X-ray Imaging and Tomography

2.1 Basics of X-ray Imaging

The history of X-ray imaging traces back to the year 1895, when Wilhelm Conrad Röntgen presented the first X-ray image of the hand of his wife Anna Bertha Ludwig, immediately stunning the whole world with its amazing potential, and ultimately sparked the development of a whole new research area [18].

X-rays are defined as electromagnetic waves of high energy and short wavelength, typically in the range of 10 picometers to 10 nanometers. X-rays are very similar to visible light due to the fact that they are both electromagnetic waves. Yet the higher photon energy of X-rays, especially hard X-rays, which are loosely defined to be of photon energies higher than 1 keV, allows them to penetrate a wide range of common materials opaque to visible light, thus granting great versatility for clinical and scientific usage. X-ray imaging techniques have therefore their own category under the field of optical imaging.

The very fundamental concept behind X-ray imaging lies in how X-rays interact with matter. For various imaging approaches, there are several simplified models to describe the main types of interactions such as absorption, refraction, scattering, or diffraction. In this chapter, the concept of X-ray imaging will be explained starting from the scalar Helmholtz equation and its pertinent approximations.

2.1.1 Helmholtz Equation and Projection Approximation

The equation that models electromagnetic waves' interaction with matter is the inhomogeneous Helmholtz equation:

$$[\nabla^2 + k_0^2 n_\omega^2(x, y, z)] \psi_\omega(x, y, z) = 0, \quad (2.1)$$

where ψ_ω denotes the complex-valued wave field of a monochromatic component of the wave, $k^2 = \omega^2/c^2$ denotes the wave number, n_ω is the refractive index of the material, ∇^2 is the Laplace operator, and (x, y, z) denotes the Cartesian coordinates. Equation (2.1) is the mathematical basis for most X-ray imaging techniques, however depending on the

complexity of the actual scenario, finding an analytical solution for it is often very difficult or impossible. For practical applications, it is useful to look for simplified solutions with certain approximations.

For a wave-field propagating mainly along the z -axis, which can be used to describe many cases of X-ray imaging, it is useful to introduce the following approximation of the wave function

$$\psi_\omega(x, y, z) = \tilde{\psi}_\omega(x, y, z) \exp(ikz), \quad (2.2)$$

where we introduce explicitly a fast oscillatory term in z , in the form of $\exp(ikz)$, and $\tilde{\psi}_\omega$ denotes a slowly varying envelope function. Inserting it into Eq. (2.1) yields

$$\left\{ 2ik \frac{\partial}{\partial z} + \nabla^2 + k^2 [n_\omega^2(x, y, z) - 1] \right\} \tilde{\psi}_\omega(x, y, z) = 0. \quad (2.3)$$

For the next approximation, due to the weak interaction of X-rays with matter, the perturbation of the wave caused by a single contributing scatterer on the beam path can be assumed to be sufficiently weak. Thus, we can approximate the wavefront after passing the object in terms of an integral of all contributions of the object along the beam path. This assumption is known as the projection approximation [19]. We here also apply the paraxial approximation, thus assuming only a small contribution of the second order derivative along z . With these approximations the second order derivative in Eq. (2.3) can be neglected

$$\left\{ \frac{\partial}{\partial z} - \frac{k[1 - n_\omega^2(x, y, z)]}{2i} \right\} \tilde{\psi}_\omega(x, y, z) = 0. \quad (2.4)$$

Using the projection approximation, the wavefront after passing the object is expressed in terms of the integral of contributions along the z axis. Thus assuming the wave field propagates through the object from z_0 to z_1 , the solution of Eq. (2.4) is:

$$\tilde{\psi}(x, y, z = z_1) \approx \tilde{\psi}(x, y, z = z_0) \exp \left\{ \int_{z_0}^{z_1} \frac{k[1 - n_\omega^2(x, y, z)]}{2i} dz \right\} \quad (2.5)$$

In the X-ray regime, refractive indices of most common materials are close to 1, thus they are commonly rewritten as:

$$n_\omega(x, y, z) = 1 - \delta_\omega(x, y, z) + i\beta_\omega(x, y, z), \quad (2.6)$$

where δ_ω and β_ω are the real and imaginary components of the refractive index, which describe the phase and absorption properties of the material in the interaction with X-rays, respectively. These coefficients are often much smaller than 1, so that their higher order contributions in n_ω^2 can be neglected, and Eq. (2.5) can be then rewritten

$$\tilde{\psi}(x, y, z = z_1) \approx \tilde{\psi}(x, y, z = z_0) \exp \left\{ \int_{z_0}^{z_1} -ik[\delta_\omega(x, y, z) - i\beta_\omega(x, y, z)] dz \right\}. \quad (2.7)$$

Equation (2.7) shows the most commonly used model for X-ray imaging. For the classic case of X-ray absorption imaging, according to Eq. (2.7), the intensity of the transmitted X-rays is given by

$$\begin{aligned} I(x, y, z = z_1) &= \left| \tilde{\psi}(x, y, z = z_0) \exp \left\{ \int_{z_0}^{z_1} -k\beta_\omega(x, y, z) dz \right\} \right|^2 \\ &= I_0(x, y, z = z_0) \exp \left\{ \int_{z_0}^{z_1} -2k\beta_\omega(x, y, z) dz \right\}, \end{aligned} \quad (2.8)$$

where I_0 is the intensity of the incident X-ray beam. Therefore, X-ray absorption imaging measures the integrated absorption coefficient along the beam path, and does not include any contribution from the phase contrast coefficient.

2.1.2 Coherent X-ray Imaging Techniques

As shown in Eq. (2.8), X-ray absorption imaging only measures the absorption coefficient, β_ω , and the phase coefficient, δ_ω , does not show in the measurable intensity after the object. Yet for hard X-rays, typically with energy above 1 keV, the δ_ω coefficient is usually several orders of magnitude larger than β_ω . Therefore, getting access to the phase component provides much higher contrast, and enables higher speed and signal-to-noise ratio for hard X-ray imaging [20].

Measurement of the phase, however, cannot be achieved as easily as measuring the absorption. While absorption images can be obtained by measuring the intensity of the transmitted X-ray wave field, the phase of the exit wave field cannot be measured directly by any existing X-ray detector. Therefore, the phase information of the transmitted wave field has to be recovered from intensity measurements. This is commonly known as the *phase problem*, which also occurs in other fields of imaging [21]. Luckily, the interference properties of X-rays allow a variety of phase-contrast imaging methods to be developed [22]. These include X-ray interferometry [23, 24], X-ray holography [25, 26] and propagation-based phase-contrast methods [27, 28].

In the X-ray regime, propagation-based phase contrast methods have a specific advantage, because optical devices such as lenses or reflectors for X-rays are more difficult to make and have much lower efficiency compared to the visible light regime. Moreover, the development of modern X-ray sources, especially synchrotron light sources, allows access to high-brilliance coherent X-rays, which greatly enhances the performance of propagation-based methods. The combination of all these factors resulted in the introduction of coherent X-ray diffractive imaging (CDI), which is a form of lenseless approach using diffraction and far-field propagation for imaging of nanoscale structures [29, 30].

In CDI, complex-valued images of the object are reconstructed from the measured far-field intensities, *i.e.* diffraction patterns, with iterative phase retrieval algorithms [31, 32]. The main advantage of CDI is that the lenseless approach circumvents the need for

lenses and thereby any limitations posed by their limited numerical aperture or optical aberrations, while its resolution is theoretically only limited by diffraction [33].

2.1.3 X-ray Ptychography

X-ray ptychography is a type of coherent diffractive imaging technique, which incorporates scanning the sample relative to the X-ray illumination and measuring a diffraction pattern for each scanning position. It provides high resolution and quantitative images of the complex-valued transmissivity of the sample [16, 17, 34–37], with state-of-the-art applications reaching sub-20 nm resolution in 3D [38–40]. This section will cover the basics of X-ray ptychography, as it is the main imaging method used in the thesis.

In X-ray ptychography, the sample is typically scanned across a focused X-ray beam. The interaction of the X-ray beam with the sample is described in Eq. (2.7) in Section 2.1. For simplified representation, it can be rewritten as

$$\Psi(x, y) \approx \hat{P}(x, y) \hat{O}(x, y), \quad (2.9)$$

where $\Psi(x, y)$, $\hat{P}(x, y)$, and $\hat{O}(x, y)$ represent the wave field after the sample, the wave field of the incident beam, and the complex-valued transmissivity of the sample, namely

$$\begin{aligned} \Psi(x, y) &= \tilde{\psi}(x, y, z = z_1), \\ \hat{P}(x, y) &= \tilde{\psi}(x, y, z = z_0), \\ \hat{O}(x, y) &= \exp \left\{ \int_{z_0}^{z_1} -ik [\delta_\omega(x, y, z) - i\beta_\omega(x, y, z)] dz \right\}. \end{aligned} \quad (2.10)$$

In conventional ptychography, also known as far-field ptychography, the propagation distance of the beam after the object until it reaches the detector plane is large enough that the wave propagation can be described by the Fraunhofer far-field approximation [41]

$$\Psi'(x', y') = \frac{ke^{ikz} e^{\frac{ik}{2z}(x'^2 + y'^2)}}{2i\pi z} \iint_{-\infty}^{+\infty} \exp \left\{ -\frac{ik}{z}(xx' + yy') \right\} \Psi(x, y) dx dy, \quad (2.11)$$

where $\Psi'(x', y')$ denotes the wave field on the detector plane, and z denotes the distance from sample to detector. Equation (2.11) can be expressed in terms of a Fourier transform (FT)

$$\Psi'(\xi, \eta) \propto \mathcal{F}\{\Psi(x, y)\}|_{\substack{f_x=\xi \\ f_y=\eta}} = \mathcal{F}\{\hat{P}(x, y) \hat{O}(x, y)\}, \quad (2.12)$$

where $\xi = kx'/(2\pi z)$, $\eta = ky'/(2\pi z)$ denotes coordinates in Fourier space. Note that apart from constant terms and terms that depend on z , in Eq. (2.12) we have additionally neglected a parabolic phase term outside the integral. This term can be safely ignored, as it will cancel out with its complex conjugate term in the back-propagation process, which allows us to use the simple form of Fourier transform and its inverse when phasing the

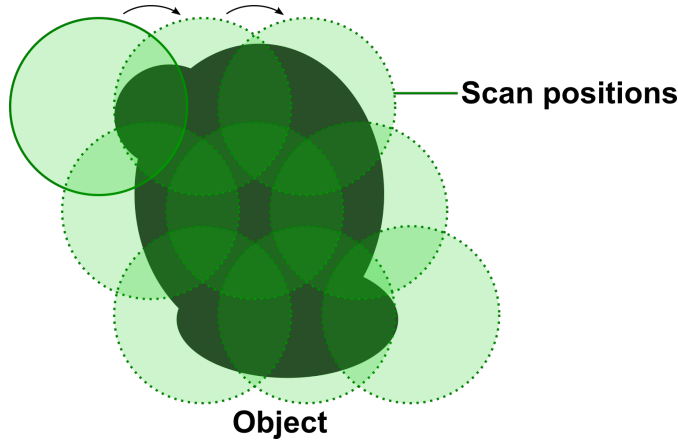


Figure 2.1. Schematic of ptychography scan. For ptychography the sample is scanned relative to the incident illumination, shown as green circles in the reference frame of the sample, while ensuring that there is a substantial amount of overlap between neighboring illuminated regions. These overlaps are subsequently used as constraints during the image reconstruction.

diffraction patterns [41]. When measured with a detector, the intensity of the diffracted beam is obtained

$$I(\xi, \eta) = |\Psi'(\xi, \eta)|^2 = |\mathcal{F}\{\hat{P}(x, y) \hat{O}(x, y)\}|^2, \quad (2.13)$$

In ptychography, a series of diffraction patterns are obtained by moving the sample to different positions relative to the incident beam, and measuring a diffraction pattern for each position, such that we have

$$I_j(\xi, \eta) = |\mathcal{F}\{\hat{P}(x - x_j, y - y_j) \hat{O}(x, y)\}|^2, \quad (2.14)$$

where (x_j, y_j) are the positions of the beam relative to the object in the sample plane, and I_j are the measured diffraction patterns. These positions are arranged so that the incident illumination patterns overlap, see Fig. 2.1, these overlapped regions serve as important constraints for the ptychography image reconstruction.

All measured diffraction patterns are then used to reconstruct the illumination $\hat{P}(x, y)$ and the sample transmissivity $\hat{O}(x, y)$. Multiple algorithms for iterative phase retrieval have been proposed for the reconstruction problem. Whilst the initial approach relied on prior knowledge of the illumination [34], a very important development was the possibility to simultaneously reconstruct the probe $\hat{P}(x, y)$, because X-ray probes are often not well characterized. This was then incorporated in ptychography reconstructions [35, 42], and utilized in reconstruction algorithms such as the extended ptychographic iterative engine (ePIE) [43] and the difference map (DM) [44]. Later approaches showed the importance to incorporate noise statistics, which results in the development of maximum likelihood refinement (ML) [45, 46] and least-squares maximum-likelihood (LSQ-ML) method [47].

Various code packages are also available for ptychography data processing and reconstruction [48–50]. In practice, these reconstruction methods can also be applied in sequence for better convergence of the results, for example by using DM to explore solution space effectively and converge to the vicinity of the solution, and ending with iterations of LSQ-ML to recover the solution that best fits the noise statistics.

Compared to X-ray absorption microscopy, the main advantage of X-ray ptychography is its high sensitivity and quantitateness for both absorption and phase contrast of the sample, making it a powerful tool for imaging nanoscale samples at high spatial resolution.

2.2 Computed Tomography

As described in Eq. (2.7), X-ray imaging of projections measures the integral of all contributions from the sample along the beam path of the X-ray. Since the high penetration of X-rays allows projections through the interior of thick samples, the question arises of how a three-dimensional model of the interior structures can be obtained from the measurements. Although mathematical studies of this reconstruction problem began in the early 20th century, realization of this technique was only after the 1960s, facilitated by the increased power and availability of computers. And this technique is named computed tomography, or CT.

The first CT scan in history was commissioned on 1 October 1971 by radiologist James Ambrose on a patient’s brain in Atkinson Morley Hospital in the UK [51], using the first functional CT scanner invented by Sir Godfrey Hounsfield [8]. The scanner combined an X-ray generator and a detector, which rotated around the human body to acquire X-ray images at different rotation angles. These images were then fed into a computer program to reconstruct cross-sections of the brain.

Ever since its invention, the fundamental concept of CT has stayed mostly the same: by combining a set of X-ray transmission measurements taken from different orientation angles with respect to the object to produce three-dimensional cross-section images of its interior. Nevertheless, CT methods have grown far more sophisticated and versatile from its first initial clinical use, and have extended its applications far beyond medical imaging [52]. At the smallest length scale, they have been applied to tiny specimens such as fruit flies [53], cellular structures [54] or computer chips with resolution better than 20 nm [10]. At the other extreme, for large specimens, researchers have built a two-story-tall system to scan aerospace components of several meters in size for imperfections.

In the rest of this section, basic concepts for tomography imaging and reconstruction techniques will be presented, and an introduction to the hyperdimensional extensions of CT methods is included.

2.2.1 Fundamental Concepts of Tomography Imaging

The basic concept of X-ray CT, also called X-ray tomography in short, originates from X-ray projection principles described in Eq. (2.7). From Eq. (2.7) the contribution of the object is given by

$$\begin{aligned}\hat{O}(x, y) &= \exp \left\{ \int_{z_0}^{z_1} -ik [\delta_\omega(x, y, z) - i\beta_\omega(x, y, z)] dz \right\} \\ &= \frac{\tilde{\psi}(x, y, z = z_1)}{\tilde{\psi}(x, y, z = z_0)}.\end{aligned}\quad (2.15)$$

Equation (2.15) shows that the integrated transmissivity of the object can be obtained from the incident and exit X-ray wave fields. In the case of absorption imaging, the integrated absorption coefficient β_ω of the object can be obtained by measuring the beam intensities with and without the object, as shown in Eq. (2.8). And in phase contrast and some coherent imaging techniques, the integrated phase coefficient δ_ω is obtained similarly by characterizing the incident and exit wave field. Note that for ptychography, the integrated complex-valued transmissivity of the object is reconstructed simultaneously with the X-ray probe, such that a separate measurement of the incident wave field is not needed, as discussed in Section 2.1.3.

Computed tomography is based on the concept of reconstruction from integrated transmissivity, or projection. For a simple model, we can assume that the integrated property f from the object transmissivity is measured, and consider a three-dimensional object inside empty space. In each measurement, we measure the projection p , which is a two-dimensional image given by

$$p(x, y) = \int_{-\infty}^{\infty} f(x, y, z) dz, \quad (2.16)$$

where (x, y, z) denotes Cartesian coordinates of the three-dimensional space. This process is defined as ‘projection’ or ‘forward projection’.

In X-ray tomography measurements, multiple projections are measured at different orientation angles of the sample with respect to the X-ray beam direction of propagation. If we assume the rotation axis to be the y axis, and the beam is rotated counter-clockwise with respect to the sample by angle θ , the measured projections are given by

$$p_\theta(x', y) = \int_{-\infty}^{+\infty} f(x' \cos \theta - z' \sin \theta, y, x' \sin \theta + z' \cos \theta) dz', \quad (2.17)$$

where (x', y, z') denotes a rotated set of Cartesian coordinates, with z' going along the direction of the beam propagation after rotation. Schematics of the rotated projection lines are shown in Fig. 2.2. As the y coordinate in Eq. (2.17) is not affected by the rotation, at any fixed value $y = y_0$, the projection equation can be reduced to two-dimension

$$p_\theta(x') = \int_{-\infty}^{+\infty} f(x' \cos \theta - z' \sin \theta, x' \sin \theta + z' \cos \theta) dz'. \quad (2.18)$$

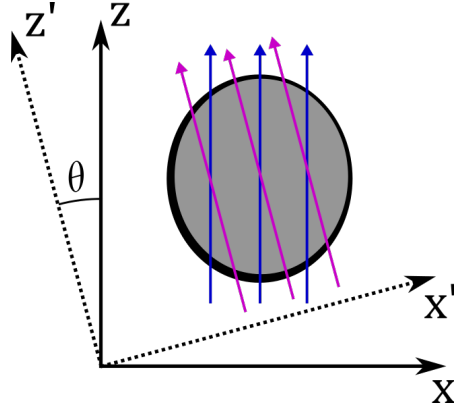


Figure 2.2. Schematics of tomographic projection lines. Blue arrows show the projection lines, or beam paths, for line integrals along the z axis. Purple arrows show projection lines with the beam rotated around the y axis by an angle θ .

Equation (2.18) is also known as the *Radon transform* [55], it represents the projection of a two-dimensional slice of the object taken perpendicular to the rotation axis. Thus, the tomography reconstruction problem of retrieving $f(x, y, z)$ can be separated into reconstruction of consecutive slices of $f(x, z)$ along the y axis, which is done by processing the one-dimensional projections $\{p_\theta(x')\}$ of each slice.

To better explain the tomography reconstruction methods, we will start from the Fourier slice theorem, which serves as the core mathematical concept for tomography.

2.2.2 Fourier Slice Theorem

The Fourier slice theorem, also known as central slice theorem or projection-slice theorem, states the relation between tomographic projections of an object and its Fourier transform. To start, the 1D Fourier transform of any projection function $p(x)$ is given by:

$$\mathcal{F}\{p_\theta(x)\} = \int_{-\infty}^{+\infty} p_\theta(x) \exp(-2\pi i x f_x) dx, \quad (2.19)$$

where f_x denotes coordinate in Fourier space. Similarly, the 2D Fourier transform of the object slice $f(x, z)$ is given by:

$$F(f_x, f_z) = \mathcal{F}\{f(x, z)\} = \iint_{-\infty}^{+\infty} f(x, z) \exp[-2\pi i(x f_x + z f_z)] dx dz, \quad (2.20)$$

where (f_x, f_z) denotes Cartesian coordinates in 2D Fourier space. If we take a one-dimensional slice from the Fourier transform $F(f_x, f_z)$ through its origin, for example

along the line $f_z = 0$:

$$\begin{aligned}
 S(f_x) &= F(f_x, 0) = \iint_{-\infty}^{+\infty} f(x, z) \exp(-2\pi i x f_x) dx dz \\
 &= \int_{-\infty}^{+\infty} \left[\int_{-\infty}^{+\infty} f(x, z) dz \right] \exp(-2\pi i x f_x) dx \\
 &= \int_{-\infty}^{+\infty} p_{\theta=0}(x) \exp(-2\pi i x f_x) dx.
 \end{aligned} \tag{2.21}$$

Thus the central slice of the FT equals the 1D Fourier transform of the projection given in Eq. (2.19) when $\theta = 0$, namely:

$$F(f_x, 0) = \mathcal{F} \{p_{\theta}(x)|_{\theta=0}\}. \tag{2.22}$$

Moreover, for any slice through the origin taken from $F(f_x, f_z)$, which can be obtained by rotating the f_x axis by angle θ to the new direction ($f_x = f_x' \cos \theta, f_z = -f_x' \sin \theta$), it can be proven that

$$S_{\theta}(f_x') = F(f_x' \cos \theta, -f_x' \sin \theta) = \mathcal{F} \{p_{\theta}(x')\}, \tag{2.23}$$

where $p_{\theta}(x')$ is the projection with the beam rotated in the plane by the same angle θ , as given by Eq. (2.18). Equation (2.23) is known as the general form of the Fourier slice theorem in two dimensions, and it can be easily generalized to higher dimensions.

The Fourier slice theorem states that the Fourier transform of a projection of the object is the same as a slice from the higher-dimensional Fourier transform of the object. It indicates the correlation between the object and its projections through Fourier space, and provides theoretical basis and insights for tomography reconstruction methods.

2.2.3 Tomography Reconstruction Methods

Because CT reconstructions are carried out in computers which use numerical arrays as data structure, tomography measurements and data processing are usually based on discrete arrays for sampling the projections and object. Therefore, the discrete form of projection function, Eq. (2.17), becomes

$$\mathbf{p}_{\theta} = \mathbf{A}_{\theta} \mathbf{f}, \tag{2.24}$$

where \mathbf{p}_{θ} is the array of pixels in the projection image at a rotation angle θ , \mathbf{f} is an array of voxels in the volume of the object, and \mathbf{A}_{θ} is the matrix that represents the forward projection process given by Eq. (2.17). Assuming the projection consists of m pixels in total, and the object is modeled by n voxels, \mathbf{p}_{θ} and \mathbf{f} consist of 1D arrays of size m and n respectively, in which case \mathbf{A}_{θ} is given by a sparse matrix of size $m \times n$.

The tomography reconstruction problem then becomes finding the solution of the object \mathbf{f} that best fit the measured projections \mathbf{p}_{θ} . In this section, we will cover two

types of reconstruction methods commonly used in tomography: filtered back-projection and iterative reconstruction techniques.

Filtered back-projection

According to the Fourier slice theorem, taking a projection is equivalent to sampling one slice of the Fourier transform of the higher-dimensional object. This property is used as the basis for back-projection based methods to reconstruct the object through Fourier-space synthesis.

As an example, shown in Fig. 2.3a is a Shepp-Logan phantom within an array of 200×200 pixels used as a model object. This phantom resembles the model of a human head and is commonly used to showcase and test tomography reconstruction methods [56]. The 2D Fourier transform of the object, shown in Fig. 2.3b, is visualized by plotting the logarithm of its amplitude. The projection of the model object at $\theta = 0^\circ$, as given by Eq. (2.17), is shown in Fig. 2.3c.

To recover the slice, embedded in 2D Fourier space, related to this projection, we can take the transpose of the projection matrix \mathbf{A}_θ in Eq. (2.23) and multiply it with the projection array, such that

$$\hat{\mathbf{f}}_\theta = \mathbf{A}_\theta^\top \mathbf{p}_\theta. \quad (2.25)$$

This operation is known as a back-projection. For the model object, the back-projection of the 0° projection is shown in Fig. 2.3e, and its Fourier transform is shown in Fig. 2.3f, similarly by plotting its logarithm amplitude. As expected, the Fourier transform of the back-projection contains only one slice along the 0° direction. According to the Fourier slice theorem, this slice is equivalent to the 0° slice in the Fourier transform of the original object. This also applies to projections taken at any rotation angles, and through this relation we can sample the entire Fourier space of the model object by measuring projections at various angles.

Therefore, if multiple projections of the object are measured at different orientations, we can sum together the back-projected images from each projection to combine the sampled slices in Fourier space, namely

$$\hat{\mathbf{f}}_{\text{BP}} = \sum_{\theta} \mathbf{A}_\theta^\top \mathbf{p}_\theta. \quad (2.26)$$

Equation (2.26) provides an estimate for the model object to within a constant normalization factor. As an example, 90 projections are taken from the model object with θ in the range of 0° to 178° with a step size of 2° . These projections are shown in Fig. 2.3g, which contains one projection in each row sorted by angle θ . This assembled image of all projections is commonly referred to as a *sinogram*. The sum of all back-projections is shown in Fig. 2.3h, with its Fourier transform shown in Fig. 2.3i.

While this process of back-projection is conceptually straightforward, its result, as shown in Fig. 2.3h, is severely blurred and does not provide an accurate reconstruction of the model object. The reason for this blurring can be understood from the Fourier

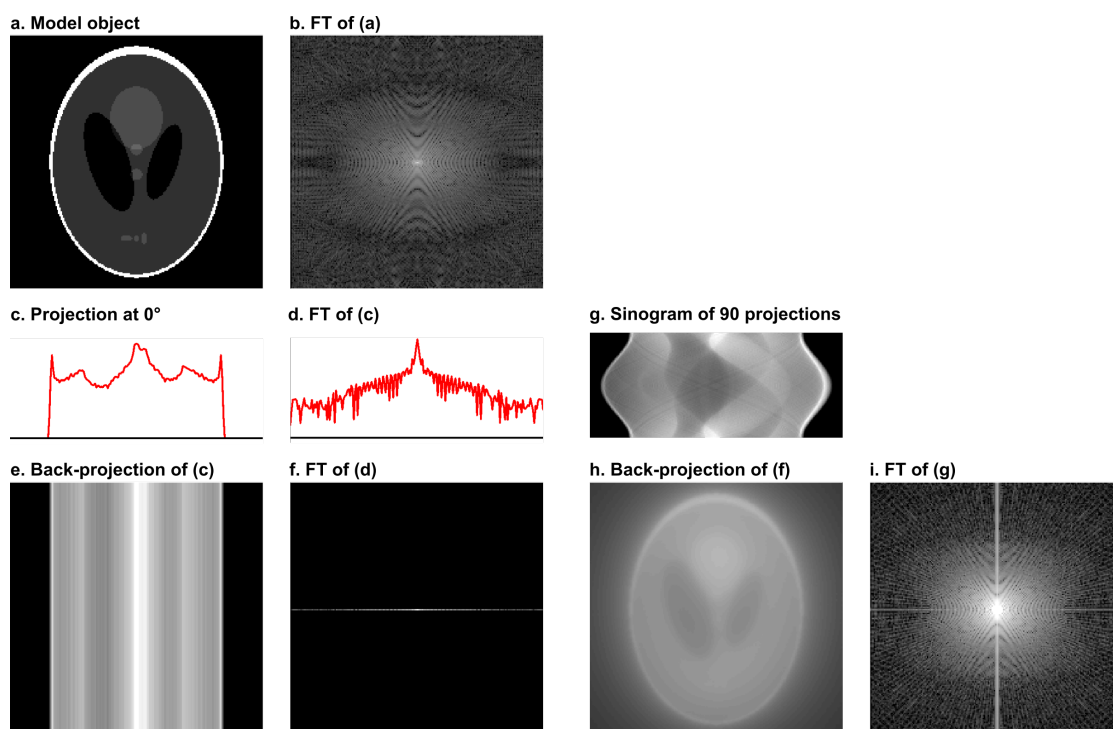


Figure 2.3. Demonstration of back-projection. a) The Shepp-Logan phantom used as model object. b) Fourier transform (FT) of (a), visualized by showing its logarithm amplitude. c) 1D projection of the object at $\theta = 0^\circ$. d) 1D FT of (c). e) Back-projection of the single projection in (c). f) Visualization of FT of (d). g) Sinogram that consists of 90 projections, with θ from 0° to 178° . h) Back-projection of all the projections in sinogram (g). i) FT of the reconstruction in (h).

space image shown in Fig. 2.3i: the slices of different directions in Fourier space are simply added together in the back-projection, thus for regions near the origin, where they intersect, this sum results in a heavy over counting of the amplitude. Because this effect gets stronger the closer it is to the origin, it causes the low-frequency components to be heavily over weighted, and results in blurring in the real-space image.

To solve this issue, we can apply a frequency-domain filter to the projections to weight down the low frequency components. The typical approach is to apply a multiplicative filter to the Fourier transform of the projections, namely

$$\mathbf{p}_{\theta h} = \text{DFT}^{-1} \{ \mathbf{h} \text{DFT} \{ \mathbf{p}_\theta \} \}, \quad (2.27)$$

where DFT and DFT^{-1} denotes discrete 1D Fourier transform and inverse transform, \mathbf{h} is the frequency filter in Fourier space, and $\mathbf{p}_{\theta h}$ denotes the filtered projection. Considering the overlapping of slices in the 2D Fourier space, as shown in Fig. 2.3i, we can set this

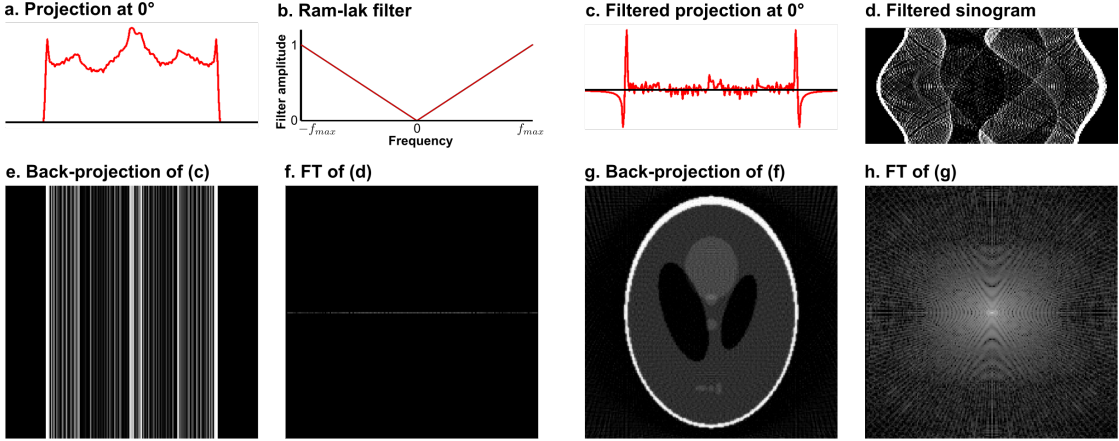


Figure 2.4. Demonstration of filtered back-projection. a) 1D projection of the object at $\theta = 0^\circ$ b) Ram-lak frequency filter. c) 1D projection in (a) after applying the Ram-lak filter. d) Filtered sinogram consisting of 90 projections. e) Back-projection of the filtered projection in (c). f) FT of (d). g) Back-projection of all the filtered projections in (f). h) FT of the reconstruction in (g).

filter proportional to the frequency:

$$\mathbf{h} = \frac{|f|}{f_{max}}, \quad (2.28)$$

where f_{max} is the highest frequency of the 1D Fourier transform. This filter, as shown in Fig. 2.4b, is commonly known as the *Ram-Lak* filter. The filtered projection at 0° and its back-projection is shown in Fig. 2.4c and 2.4e, respectively. The Fourier transform of the filtered back-projection in Fig. 2.4e is shown in Fig. 2.4f. In Fourier space, we can see that the amplitude at low frequencies, *i.e.* close to the center, are reduced heavily by the filter, compared to Fig. 2.3f.

This frequency filter is applied to all projections, resulting in a filtered sinogram that consists of all 90 filtered projections, as shown in Fig. 2.4d. Afterwards, these filtered projections can be back-projected using the same approach in Eq. (2.26), with a normalization coefficient

$$\hat{\mathbf{f}}_{\text{FBP}} = \frac{\pi}{2n_p} \sum_{\theta} \mathbf{A}_{\theta}^T \mathbf{P}_{\theta} \mathbf{f}, \quad (2.29)$$

where n_p denotes total number of projections. Equation (2.29) shows the *filtered back-projection (FBP)* method for tomography reconstruction. The FBP reconstructed object is shown in Fig. 2.4g, with its Fourier transform shown in Fig. 2.4h. The features of the reconstructed object match well with the model object, however noisy patterns can be seen at a small length scale. In the Fourier transform of the reconstructed image, shown in Fig. 2.4h, the low-frequency region around the center appears identical to the Fourier transform of the model object shown in Fig. 2.3b. Yet in the high frequency

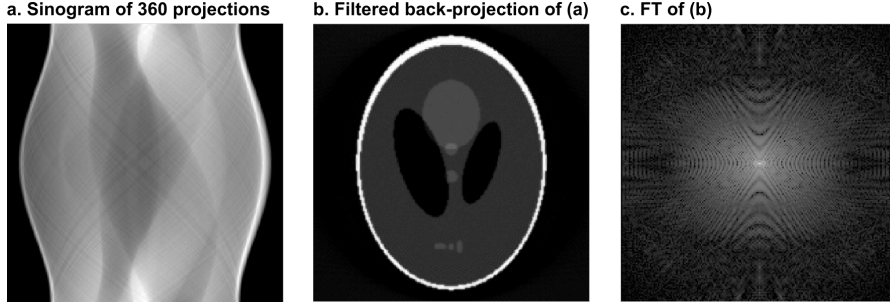


Figure 2.5. Demonstration of filtered back-projection with sufficient number of projections. a) Sinogram containing 360 projections of the object, with θ from 0° to 179.5° . d) Filtered back-projection of all projections in (a). c) Visualization of FT of the reconstruction in (b).

region around the edges, it differs from the model object due to gaps between the slices, these give rise to the high frequency noises in the reconstructed object.

This issue can be solved by increasing the number of measured projections, in the given example 90 projections are insufficient for reconstructing the model object with diameter of 184 pixels to the highest resolution. The number of projections needed to completely fill the Fourier domain is given by the *Crowther criterion* [15]

$$n_p = \frac{\pi D}{2d}, \quad (2.30)$$

where n_p denotes the required number of projections, D is the diameter of the object, and d is the sought half-period resolution. In our example, for an object diameter of 184 pixels and resolution of 1 pixel half-period, the number of projections required by the *Crowther criterion* is 289. Therefore, when 360 projections are taken from the model object, as shown in the sinogram in Fig. 2.5a, the FBP reconstruction, shown in Fig. 2.5b, matches well with the model object even at the smallest length scale.

The filtered back-projection method is widely used in various applications of CT for image reconstruction. The main advantage of the FBP method is its high accuracy and high processing speed, which makes it especially suitable for on-site reconstructions.

Iterative reconstruction techniques

Apart from FBP, an alternative type of methods commonly utilized in tomography reconstructions are iterative techniques, in which the reconstructed object goes through iterative refinements until converging to the final result. Various approaches have been proposed for the refinement formula. Here we will introduce the iterative refinement method based on gradient descent.

First, if a reconstruction of the object is denoted as $\hat{\mathbf{f}}$, using Eq. (2.24) we can calculate the projections of the reconstructed object

$$\hat{\mathbf{p}}_\theta = \mathbf{A}_\theta \hat{\mathbf{f}}, \quad (2.31)$$

where \mathbf{A}_θ is the forward projection matrix of the measurement process, and the simulated projection $\hat{\mathbf{p}}_\theta$ has the same size as the measured projection \mathbf{p}_θ . For reconstruction, we want to minimize the difference between the simulated projections and the measurements, thus we define the error metric to be

$$\epsilon = \sum_{\theta} \|\mathbf{p}_\theta - \hat{\mathbf{p}}_\theta\|^2, \quad (2.32)$$

where $\|\cdot\|$ denotes the Euclidean norm of the array. The simulated projections $\hat{\mathbf{p}}_\theta$ can be further substituted using Eq. (2.31)

$$\epsilon = \sum_{\theta} \left\| \mathbf{p}_\theta - \mathbf{A}_\theta \hat{\mathbf{f}} \right\|^2. \quad (2.33)$$

The goal of the reconstruction is then to find the object $\hat{\mathbf{f}}$ that minimizes the error ϵ . A commonly used method for such minimization is the iterative gradient descent approach. In our case, if we denote the reconstructed object in each iteration as $\hat{\mathbf{f}}^{(\mathbf{k})}$, the update based on the gradient descent direction of error ϵ is given by:

$$\hat{\mathbf{f}}^{(\mathbf{k}+1)} = \hat{\mathbf{f}}^{(\mathbf{k})} - \gamma \frac{\partial \epsilon}{\partial \hat{\mathbf{f}}^{(\mathbf{k})}}, \quad (2.34)$$

where $\gamma > 0$ is the learning rate, and $\partial \epsilon / \partial \hat{\mathbf{f}}^{(\mathbf{k})}$ is the gradient of the error evaluated with respect to $\hat{\mathbf{f}}$. To calculate this gradient, we take the Eq. (2.31) and explicitly write the matrix multiplication with indices

$$\hat{p}_{\theta i} = \sum_j A_{\theta i j} \hat{f}_j, \quad (2.35)$$

the error ϵ given by Eq. (2.33) can then be expressed as:

$$\epsilon = \sum_{\theta} \sum_i \left(p_{\theta i} - \sum_j A_{\theta i j} \hat{f}_j \right)^2. \quad (2.36)$$

We then can obtain its derivative with respect to each component of $\hat{\mathbf{f}}$

$$\begin{aligned} \frac{\partial \epsilon}{\partial \hat{f}_j} &= \sum_{\theta} \sum_i \frac{\partial}{\partial \hat{f}_j} \left(p_{\theta i} - \sum_{j'} A_{\theta i j'} \hat{f}_{j'} \right)^2 \\ &= \sum_{\theta} \sum_i \left[2 \left(p_{\theta i} - \sum_{j'} A_{\theta i j'} \hat{f}_{j'} \right) \left(-\frac{\partial}{\partial \hat{f}_j} \sum_{j'} A_{\theta i j'} \hat{f}_{j'} \right) \right] \\ &= \sum_{\theta} \sum_i \left[2 \left(p_{\theta i} - \sum_{j'} A_{\theta i j'} \hat{f}_{j'} \right) \left(-\sum_{j'} A_{\theta i j'} \delta_{j j'} \right) \right] \\ &= \sum_{\theta} \sum_i \left[-2 A_{\theta i j} \left(p_{\theta i} - \sum_{j'} A_{\theta i j'} \hat{f}_{j'} \right) \right], \end{aligned} \quad (2.37)$$

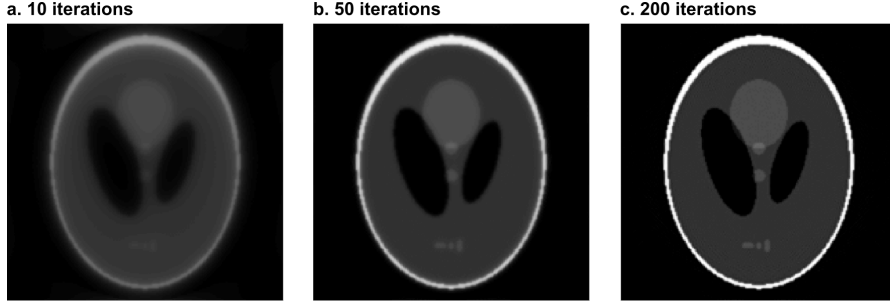


Figure 2.6. Demonstration of iterative reconstruction technique based on gradient descent. Shown are the reconstructions using the 360 projections shown in Fig. 2.5a after (a) 10, (b) 50 and (c) 200 iterations.

and thus we can write the gradient $\partial\epsilon/\partial\hat{\mathbf{f}}^{(k)}$ in a compact form as:

$$\frac{\partial\epsilon}{\partial\hat{\mathbf{f}}^{(k)}} = -2 \sum_{\theta} \left[\mathbf{A}_{\theta}^{\top} \left(\mathbf{p}_{\theta} - \mathbf{A}_{\theta} \hat{\mathbf{f}}^{(k)} \right) \right]. \quad (2.38)$$

By inserting Eq. (2.38) into Eq. (2.34), we can get the final formula for the iterative gradient descent

$$\hat{\mathbf{f}}^{(k+1)} = \hat{\mathbf{f}}^{(k)} + 2\gamma \sum_{\theta} \left[\mathbf{A}_{\theta}^{\top} \left(\mathbf{p}_{\theta} - \mathbf{A}_{\theta} \hat{\mathbf{f}}^{(k)} \right) \right]. \quad (2.39)$$

As shown in Eq. (2.38), the gradient update term is the back-projection of the differences between measured projections \mathbf{p}_{θ} and simulated projections $\hat{\mathbf{p}}_{\theta}$, which has similar form to Eq. (2.26).

Equation (2.39) provides a straightforward and effective method for iterative tomographic reconstruction. Here it is demonstrated on the same model object, shown in Fig. 2.3a, using the 360 projections shown in Fig. 2.5a. The starting guess $\hat{\mathbf{f}}^{(0)}$ is set to all-zero and the learning rate γ is set to 10^{-5} . The results of the iterative reconstruction after 10, 50, and 200 iterations are shown in Fig. 2.6a, 2.6b, and 2.6c, respectively. The reconstructed object shows convergence after 200 iterations, and the converged result matches well the model object.

Similar formulas to Eq. (2.39) can also be found in many other iterative reconstruction methods. For example, in the Simultaneous Iterative Reconstruction Technique (SIRT) [57], the iterative update is given by:

$$\hat{f}_j^{(k+1)} = \hat{f}_j^{(k)} + \frac{\omega_k}{\sum_{\theta} \sum_{i'} A_{\theta i' j}} \sum_{\theta} \sum_{i'} A_{\theta i' j} \frac{p_{\theta i} - \sum_{j'} A_{\theta i' j'} \hat{f}_{j'}^{(k)}}{\sum_{j'} A_{\theta i' j'}}, \quad (2.40)$$

where ω_k is the relaxation coefficient at iteration k . In practical applications of these iterative methods, the starting guess $\hat{\mathbf{f}}^{(0)}$ is often the FBP reconstruction of the projections, or a low-resolution image obtained from prior knowledge of the object. The relaxation

coefficients are tuned based on multiple parameters, including sample size, resolution and imaging contrast, to get a desired speed of convergence.

The convergence of iterative reconstruction techniques, including the gradient descent and the SIRT method, can be mathematically proven for general cases, if the relaxation parameters are in a certain range [58–60]. Therefore, these reconstruction methods are applicable in all types of tomography experiments. Compared to the FBP method, iterative reconstruction techniques requires considerably longer computation time, as they need one forward-projection and back-projection process for each iteration. However, iterative reconstruction techniques are often more robust against measurement noise and angular undersampling, and work better when certain constraints or prior knowledge of the sample are applied to the reconstruction. Therefore, they are commonly used in addition to FBP for refinement of the results, or in cases where certain constraints or higher-dimension reconstruction methods need to be applied.

2.3 Hyperdimensional Tomography

In its 50 years of development, computed tomography has benefited from a wide variety of technical advances, including brighter X-ray sources, solid-state detectors, precision machining, and semiconductor integration, all of which allow for improved designs of CT devices for higher speed and better image quality. Tomography reconstruction methods have also become orders of magnitude faster, thanks to the rapid growth of computing power and more efficient computation algorithms. All of these advancements opened the possibility to image more sophisticated structures at different length scales, and also allowed extensions of CT to higher dimensions.

The term ‘hyperdimensional’ means ‘of or relating to space of more than three dimensions’. It is used here to represent a class of imaging techniques that not only acquire static three-dimensional images of the samples, but also introduce extra factors that cause changes in the sample between different frames of tomography acquisition. These factors can be any physical or experimental quantity, such as time, temperature, X-ray energy, or coordinates in reciprocal space, and are often considered as extra dimensions in the reconstruction and analysis.

Hyperdimensional tomography provides the opportunity to measure a wider range of material properties. For example, adding a spectral dimension to tomography measurements allows characterization of chemical properties, or the extension to tensor tomography provides information about the macroscopic arrangement and orientation of the nanostructures. This section will cover the concepts of some of the most commonly used hyperdimensional tomography techniques, which are utilized for the works presented in the thesis.

2.3.1 Dynamic Tomography

Dynamic tomography, also referred to as four-dimensional computed tomography (4DCT), is probably the most intuitive concept for hyperdimensional tomography. Ever since the time of the first clinical CT scan, it was realized that the specimens imaged by tomography, such as live human organs, can be constantly changing over time. Initially, these dynamic changes were considered to be sources of errors in tomography, as conventional CT assumes the sample to be static during the imaging process. However, as technologies advance, tomography methods kept getting faster and more stable, ultimately allowing them to deal with or even characterize the dynamic changes.

In a typical dynamic tomography experiment, a series of tomography measurements are consecutively conducted on the evolving sample, and the imaged volume of the sample is reconstructed for each measurement. If the speed of the tomographic measurement is fast enough, dynamic changes in the sample can be analyzed from comparing the reconstructions for different time points. This general idea can also be applied to changes of the sample that are introduced in a controlled fashion, such as by adjusting over time the temperature or humidity of the surrounding environment, or by applying pressure or radiation to the sample. In some cases, it is even possible to image samples of functional materials in their designed working environment, which is defined as *operando* imaging. This ability of dynamic tomography methods to resolve spontaneous or induced changes in the samples provides a great amount of information towards understanding their characteristics or working mechanisms, and can find its applications in an extremely wide range of studies, from living organisms [61–63] to energy conversion [64] or battery materials [5, 65].

2.3.2 Hyperspectral Tomography

In Section 2.1, it was shown that X-ray interaction with matter is defined by the refractive index of the material, as described by Eq. (2.1). A material’s refractive index depends on both its composition and the X-ray photon energy. When measuring the refractive index of a material at different X-ray energies, an important phenomenon that occurs is that the refractive index of the material, both its real and imaginary components, will change abruptly when the beam energy reaches certain values, causing a sharp increase in the absorption and a dip in the phase. These energy values are called ‘absorption edges’, and the physical theory behind this phenomenon is related to the energy levels of electrons in different atoms, which produces a resonant effect when the X-ray photon energy is close to the binding energy of an inner-orbit electron. Therefore, we can use this fact to determine the atomic compositions of different samples by measuring their refractive indices at different X-ray energies and characterizing the energies of the absorption edges. In absorption measurements, the X-ray absorption profile versus incident X-ray photon energies is called the ‘absorption spectrum’, and the associated characterization technique is known as ‘X-ray absorption spectroscopy’ or XAS.

Further, by using fine energy sampling, the refractive index spectrum of the material in a close range of the absorption edges contains more information about its chemical composition and crystal structure. When applied in the near-edge absorption regime, this technique is called ‘X-ray absorption near-edge spectroscopy’ or XANES, and has been widely used for chemical analysis of various types of materials [66–68].

X-ray spectroscopy can be combined with CT in order to obtain a XAS or XANES spectrum for each voxel. In this case, a series of tomography measurements are conducted at different X-ray energies. As tomography reconstructions provide the absorption and/or phase contrast information for each voxel in the sample volume, the absorption or phase spectrum of each voxel can be obtained by combining reconstructions at different energies. These voxel-wise spectrums allows local compositional or chemical analysis, which can then reveal elemental distributions or chemical phases in the sample volume. These features are often considered as key properties of various heterogeneous materials, for example the charging mechanisms of battery cathodes [69, 70], or catalytic active sites in industrial catalysts [71–77].

2.3.3 Tensor Tomography

In conventional X-ray CT, one of the fundamental assumptions is that the sample’s interaction with the X-ray beam is isotropic. This means that any voxel inside the sample will contribute to the absorption or phase contrast of the X-ray beam the same way in all the projections, regardless of the incident direction of the beam with respect to the sample. This assumption works well in most cases of tomography applications, in which the materials are either isotropic, or the anisotropic interactions are sufficiently weak at the imaged length scale. However, there exists a wide range of anisotropic materials or structures in various research fields, such as monocrystals, magnetic systems, or organic fibers. For these materials, conventional tomography is often insufficient for characterizing their underlying 3D structures, which in turn determine the material functionality. Therefore, there is a demand to obtain information about the anisotropy within each voxel, including the underlying structure orientation and degree of anisotropy.

To this end, different types of tensor tomography techniques have been proposed. Instead of conventional CT, which reconstructs one scalar value per voxel, these techniques reconstructs for each voxel a multi-component tensor that contains information about local anisotropy. There is a wide scope of tensor tomography techniques that use different contrast mechanism and experimental configurations to image tensors of different properties. These techniques include tensor tomography based on dark-field imaging [78], magnetization vector tomography [79] and small-angle X-ray scattering tensor tomography (SASTT) [80, 81]. These techniques provide information about local orientations of magnetization, nanoscopic structures, or even obtain a six-dimensional model of the reciprocal space. Further details about these methods are beyond the scope of this thesis and will not be covered here, we refer interested readers to the original publications.

The work of this PhD project also includes algorithm developments toward recon-

struction methods of SASTT, which are covered in the publication *Z. Gao, et al. "High-speed tensor tomography: iterative reconstruction tensor tomography (IRTT) algorithm." Acta Crystallographica Section A: Foundations and Advances 75.2 (2019): 223-238* [82], as well as their application to biomineralization [83] and nervous tissue in brains [84]. These publications are not included in this thesis, as most of its work was done prior to the PhD program. However, they include work on hyperdimensional tensor tomography that is conceptually related to the polarization imaging contrast method, which is covered in Chapter 3 of this thesis, especially its possible extension to vector tomography.

2.4 Sparse Synthesis in Tomography

In all applications of computed tomography, a key factor that gets recurring attention is the imaging speed. A CT scan requires a certain amount of projections to be measured based on the size and resolution of the imaged 3D volume, as given by the *Crowther criterion* in Eq. (2.30). As this factor can go beyond the order of thousands in high-resolution imaging, it causes a ‘gap’ between the speed of CT scans and 2-dimensional measurements of the same imaging modality, with the former being significantly slower and unable to capture fast-changing processes that can be resolved by 2D imaging techniques. This has been considered as a major limitation of CT, and it poses an even increased challenge for hyperdimensional applications of CT.

In hyperdimensional CT, tomography measurements are repeated at different sampling points of the extra dimension, such as time, temperature, or X-ray energy. This further increases the acquisition time, to a level that practical applications of hyperdimensional imaging often need to use smaller sample volume or lower resolution, compared to static tomography measurements with the same system, in order to reduce the total measurement time to an acceptable range, or to be fast enough to capture the changes in the sample [76, 85, 86].

To address these challenges, sparse synthesis has been implemented in tomography to largely alleviate the problem of lengthy acquisition time. The concept of sparsity is simply to acquire fewer data than what would be normally required, to speed up the measurement by a factor. It was initially demonstrated for conventional CT that reconstruction from fewer measurements is possible by applying prior knowledge of the sample in the reconstruction procedure [87, 88]. In hyperdimensional tomography, sample images from consecutive tomography measurements are not fully independent and usually only change slightly between neighboring frames. These tomography measurements therefore show a strong correlation of information, which can be leveraged to retrieve hyperdimensional tomograms with much fewer measurements. This concept has been demonstrated on 4DCT applications, showing that dynamic processes can be reconstructed from reduced number of projections by applying prior information or iterative refinement [89, 90].

The main focus of this thesis is the development of novel methodologies utilizing sparsity in hyperdimensional imaging, which aims to largely alleviate the speed limitations.

These techniques combine sparse sampling acquisition strategy, high-dimensional reconstruction models, and iterative refinement algorithms to create a general and versatile approach for hyperdimensional imaging. Moreover, in the works of this thesis, the sparse synthesis is implemented in a manner that is particularly well-suited for tomographic imaging with nanoscale resolution. Nanoscale X-ray 3D imaging is highly useful for material characterization, but also has the highest demand for improved measurement speed due to its long acquisition time compared to other techniques such as microtomography.

In Chapter 4 and Chapter 5 of this thesis, sparse implementations in hyperspectral tomography and dynamic tomography are demonstrated in case studies of chemical speciation of catalysts, and hydration mechanisms of ionomer materials. The developed methods enhance the speed of hyperdimensional measurements by a ratio of 8 times and 40 times, respectively, without drastic reduction of sample volume or imaging resolution. In Chapter 6, the dynamic imaging method is generalized and applied to laminographic imaging of *operando* cathode particles in battery cells, to resolve their structural changes during charge cycles. Altogether in this thesis we introduce methods to leverage sparsity for hyperdimensional nanotomography which are applicable for diverse imaging techniques and a wide breadth of applications.

Nanoscale Crystal Grain Characterization via Linear Polarization X-ray Ptychography

*The content of this chapter is covered in the publication: Z. Gao, M. Holler, M. Odstrcil, A. Menzel, M. Guizar-Sicairos, and J. Ihli. "Nanoscale crystal grain characterization via linear polarization x-ray ptychography." *Chemical Communications* 56, no. 87 (2020): 13373-13376. [91]*

3.1 Abstract

X-ray linear dichroism and X-ray birefringence microscopy are yet to be fully utilized as instruments in the microstructural characterization of crystalline materials. Here, we demonstrate analyser-free X-ray linear dichroism microscopy using spectroscopic hard X-ray ptychography. First experiments enabled a spectroscopic and microstructural characterisation of polycrystalline vanadium pentoxide on the nanoscale, outside of diffraction-contrast based methods.

3.2 Main Text

X-ray linear dichroism- [92–96] and X-ray birefringence microscopy [97–99] measure local changes of a material's refractive index as a function of incident beam polarization and energy. These measurements are commonly conducted in the vicinity of or across an X-ray absorption edge or resonant energy, associated with a chemical element of the material [99]. Probing the spectral response of this element at multiple polarization states of the illumination allows the extraction of local orientational properties, *e.g.* bond anisotropies [95,99]. This is possible as near-edge spectra, frequently the pre-peak region, are sensitive to the coordination geometry of the chemical element relative to the electric field vector

of the illumination [92]. Or in other words the sample-relative linear polarisation state of the illumination.

This polarization dependency, similar to the optical polarization microscope [100], allows in the case of materials with a net-orientation or anisotropy, *e.g.* most non-cubic and some cubic crystalline materials, the characterisation of crystal grains (CGs) within polycrystalline, composite or hierarchically structured materials [95–98]. Characterisation here refers to shape and size determination of grains, as well as unique orientation determination [95, 97] when extended to vector tomography [79]. Yet, such microstructural characterisation is hardly ever performed using X-ray microscopy modalities based on a linear polarization imaging contrast (PIC). Such limited use compared to diffraction-contrast-based methods is largely a result of three factors. One being the commonly weak signal emergent from linear polarization mechanisms, leading to strict signal-to-noise ratio requirements for measurements. Two, existing high-resolution implementations require intricate sample preparation, *e.g.* approaches based on photoemission electron microscopy operate at low X-ray energies and require thin, flat, and surface conductive samples [94–96]. Three, other implementations require either a polarizer-analyser setup or extensive prior knowledge of the specimen [98, 101].

Here, we demonstrate the utilisation of a linear polarization imaging contrast in an analyser-free spectroscopic X-ray ptychography framework and show how it can lessen the restraints posed by existing PIC microscopy methods. X-ray ptychography is an imaging technique that combines scanning transmission X-ray microscopy with lensless computational imaging [16, 35]. Ptychography allows the retrieval of the complex-valued transmission function of the imaged sample, *i.e.* images of both absorption and phase contrast are obtained. The spatial resolution of these images is in theory limited only by the detectable angular extent of the specimen-scattered intensity [16, 35]. Currently attainable are images below 10 nm spatial resolution [102] with an apparently improved signal-to-noise ratio compared to conventional X-ray microscopy methods.

In these first experiments we characterized the spectral response of vanadium pentoxide (α -V₂O₅) grains to mutually orthogonal polarization states, $\varphi = 0^\circ$ and $\varphi = 90^\circ$. Two ptychographic image series, one per polarization state, were acquired across the vanadium *K*-edge, 5460-5520 eV, with a maximum step size of 1 eV. Figure 3.1a displays the corresponding analyser-free “PIC-Ptychography” acquisition scheme. Using Fourier ring correlation, the full-period spatial-resolution of individual ptychographic image reconstructions was estimated to be 110.4 nm for the phase component and 183 nm for the absorption component. The spatial resolution of the complex-valued image is 119.2 nm. For further details, regarding acquisition, image reconstruction and resolution evaluation please see the Supplementary Methods as well as Supplementary Figure 3.4 and 3.5. For an animation of the spectral image series at both polarisation states, please see Supplementary Movie 3.1.

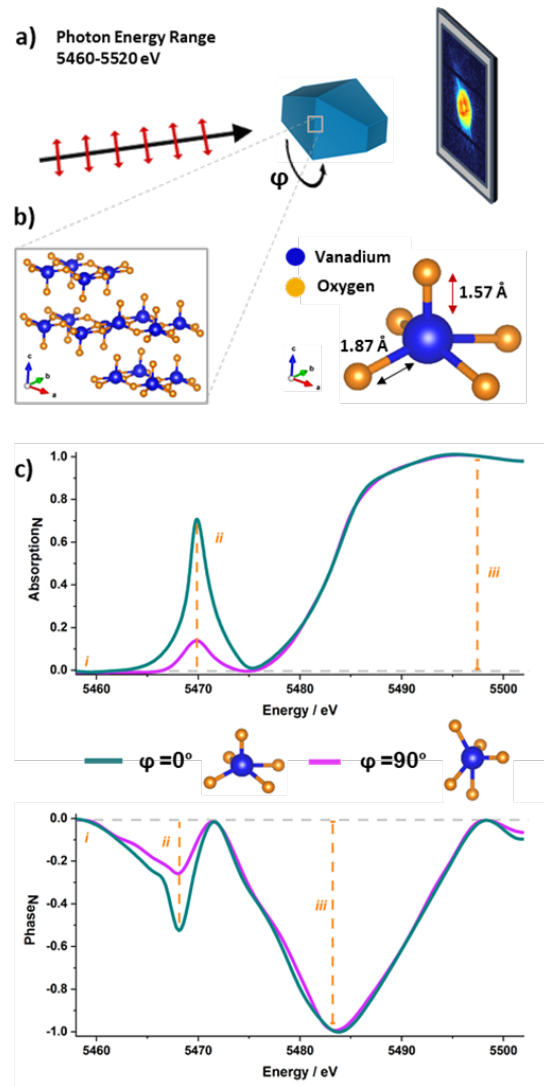


Figure 3.1. Linear Polarization Dependent X-ray Ptychography of a Vanadium Pentoxide Crystal. (a) Schematic representation of PIC-Ptychography data acquisition. Using monochromatic, coherent X-rays of fixed linear polarisation, two hyperspectral ptychographic image series were acquired across the V K -edge (5460 to 5520 eV). Following the acquisition of the first series the sample holder was azimuthally rotated from, $\varphi = 0^\circ$ (green line) to $\varphi = 90^\circ$ (purple line) around the axis of beam propagation, to create the required relative change in incident polarisation state. Shown in turquoise is a 3D Wulff construction of a vanadium pentoxide (V_2O_5) single crystal with the provided coordinate system denoting the main crystallographic axis. (b) Graphical depiction of V_2O_5 layered orthorhombic crystal structure (in rectangle), composed of distorted $[VO_5]$ square pyramids. To note is the shorter apical bond of these pyramids (red up-down arrow), aligned parallel to the crystallographic c -axis of the crystal (vertical direction), causing an anisotropic electron density distribution and giving rise to the here utilized X-ray linear dichroism [103]. (c) Example vanadium K -edge spectra collected of an apparent single crystal at 0° and 90° sample rotation, stressing the intensity variation in the pre-edge as well as the location of study-relevant features (vertical dashed line). Features include (i) the projected refractive index retrieved from measurements below the vanadium K -edge. (ii) Pre-peak intensity variations reflective of the apical bond orientation at (5468 & 5070 eV). (iii) Edge jump magnitude in absorption and negative peak height in phase to extract local vanadium concentrations. Figure reproduced from [91] / CC BY-NC.

Vanadium pentoxide was selected for these initial experiments due to its potential use as cathode material [104, 105] and heterogeneous catalyst [106]. For both applications, functionality is dependent on grain size, crystallinity, orientation, and morphology of the material. Moreover, the intensity of the pre-peak is known to be sensitive towards the relative incident beam polarisation [107]. This sensitivity, as described in [107], is a result of the layered crystal structure of vanadium pentoxide [107]. Vanadium pentoxide is composed of alternating and distorted $[\text{VO}_5]$ square pyramids. By distorted we refer to the fact that each pyramid possesses a shorter apical V-O bond compared to the bonds that make up the base of the pyramid [107]. Such a vanadium coordination geometry results in a stronger oxide - X-ray interaction, or pre-peak intensity, when the electric field vector of the illumination is more aligned with the apical bond of the pyramids. See Figure 3.1b for a graphical representation.

Figure 3.1c shows the absorption and phase spectra of a V_2O_5 crystal at orthogonal polarization states. These spectra demonstrate the pre-peak sensitivity towards changes in polarisation, a sensitivity that is visible in both the absorption and the phase spectra. Further, highlighted in Figure 3.1c are study-relevant material properties that can be extracted from either of these spectra. The former being (i) the projected refractive index retrieved from image reconstructions acquired below the vanadium K -edge, here at 5460 eV. (ii) The local vanadium coordination geometry or apical bond orientation extracted from pre-peak intensity variations. In the phase spectra, the pre-peak centre is located at 5468 eV. In the absorption spectra, we find the centre at 5470 eV. (iii) Local projected vanadium concentrations retrieved from either the edge jump magnitude in absorption or negative peak height in phase after baseline correction.

Provided in Figure 3.2 are property corresponding distribution maps of two polycrystalline V_2O_5 particles, at orthogonal linear polarization states. Due to the single-component nature of the sample, (i) projected refractive index and (iii) vanadium-concentration maps are proportional to each other, *i.e.* both are reflective of local integrated thickness variations, and thusly appear similar to each other. Furthermore, based on the measured changes in the complex-valued transmission function and the known sample composition, these properties were converted to (i) local thickness and (iii) projected vanadium concentrations. This is shown in Figure 3.2a on the example of phase-based image reconstructions. Moreover, it is evident in Figure 3.2a that the extracted thickness and concentration maps are hardly affected, as expected, by a relative polarisation change of the incident illumination.

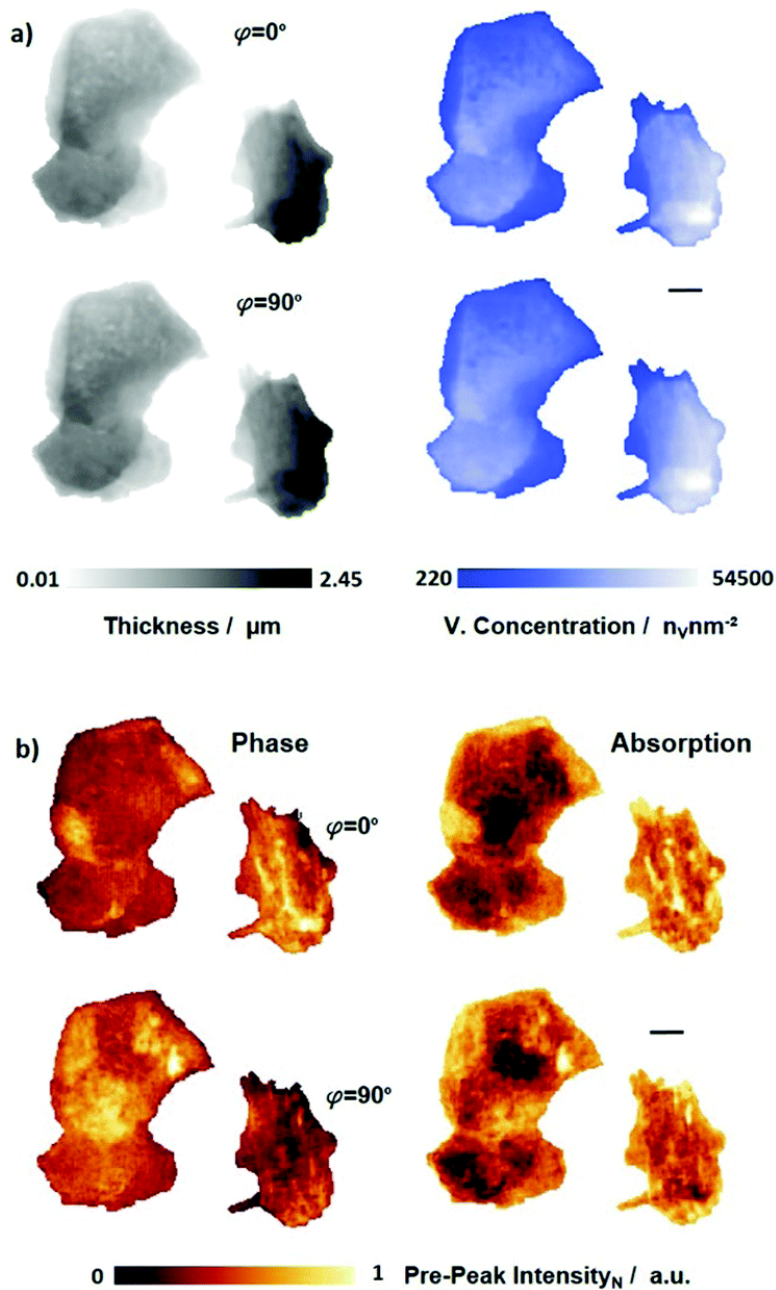


Figure 3.2. Ptychographic image reconstructions of polycrystalline V_2O_5 particles at mutually orthogonal polarizations. (a) Thickness and vanadium concentration maps of two polycrystalline V_2O_5 particles at orthogonal linear polarization states ($\varphi = 0^\circ$ and $\varphi = 90^\circ$). Maps were extracted from the phase component of ptychographic vanadium K -edge image series. The thickness map follows a colour map running from white to black, with black indicating the thickest part of the sample, the vanadium concentration colour map runs from blue to white, with white areas indicating areas of highest vanadium concentration. (b) Pre-peak intensity maps at $\varphi = 0^\circ$ (top) to $\varphi = 90^\circ$ (bottom) extracted from the same image series. Shown are the phase (left) and the absorption (right) pre-peak intensity response to changes in linear polarisation. Pre-peak intensities are normalized to the vanadium concentration. Pixel size is 48.8 nm. Scale bars are 1 μm . Figure reproduced from [91] / CC BY-NC.

Figure 3.2b shows pre-peak intensity maps of both phase and absorption contrast after normalization by the integrated vanadium concentration. These maps show a substantial change in the pre-peak intensity distribution as the sample-relative polarisation state of the illumination is changed from $\varphi = 0^\circ$ to 90° . Given the polycrystalline nature of the sample, this polarisation sensitivity is even visible in a single polarisation-state map, in which we already see the emergence of spatial domains of near-equal pre-peak intensity. Considering the vanadium-concentration normalization, the existence of these domains can be related to a common orientation of the apical bond and as such to the crystallographic c -axis of a particular or a set of V_2O_5 grains. A comparison of local pre-peak intensities across the mutually orthogonal polarization states confirms that the observed differences indeed arise from CGs of different orientation. Note the expected gain or reduction in pre-peak intensity in selected domains when the linear polarisation is changed. Other domains, conversely, only show minimal intensity variation, this is expected for several scenarios: one, the case where the orientation of the crystallographic c -axis is perpendicular to the imaging plane or at 45 degrees to both tested polarisation states, two, the potential presence of amorphous domains, and three, if multiple randomly oriented grains are in the path of the X-ray beam. Due to their random orientation and number, such an ensemble average will exhibit a lower intensity variation when the sample-relative linear polarisation state is changed. For example, the pre-peak intensity loss of one grain might fully or partially be offset by the intensity gain of another or multiple equally illuminated grain(s) of a different orientation. Importantly, these pre-peak intensity maps are not only in morphological agreement with scanning electron micrographs (SEM), Figure 3.6, but also partially match the visible grains therein. The partial match in grain identification is due to the SEM being surface-sensitive and thereby only probing the outermost or surface-running grains, while PIC-Ptychography is acquired in transmission geometry and as such probes the entire sample thickness, *i.e.* surface-buried grain boundaries are only visible in the latter.

As shown in Figure 3.3a, the acquired pre-peak intensity maps of both polarisations can be combined to obtain a map of the dominant CGs in the two-polycrystalline particles. It should be noted that with two polarizations quantitative orientation maps of the c -axis cannot be obtained. In the smaller V_2O_5 particle several surface-running grains are visible in both phase and absorption contrast. These grains, roughly 200 nm in diameter, share a common orientation among each other and are most likely a result of a secondary nucleation process. The larger particle consists of multiple nearly micron-sized domains. While pairs of these domains appear to share a common orientation, indicative of a preferred crystallographic orientation, the variation in orientation between these pairs appears moderately large, which suggests this arrangement to have originated from particle aggregation during the synthesis or the annealing process. This grain map is corroborated so far possible by micrographs acquired with an optical polarizing microscope, which are shown in Figure 3.7.

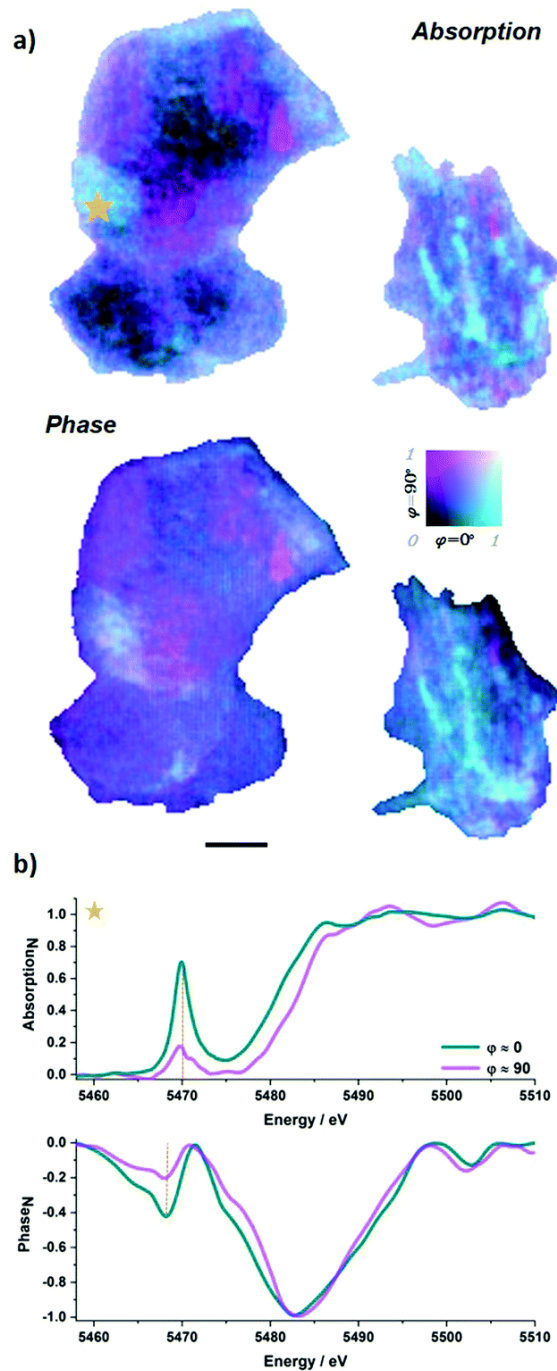


Figure 3.3. Grain map and local spectral response of polycrystalline vanadium pentoxide particles. (a) Absorption and phase based grain maps. Maps were constructed by merging V K -edge pre-peak intensity image reconstructions acquired at orthogonal polarization states. A bivariate colour map is used to highlight the alignment of the different V_2O_5 grains, *i.e.* the orientation of the apical bond of the $[VO_5]$ unit, with the incident polarisations. Note that quantitative angular orientations of the crystallographic c -axis cannot be obtained with only two polarizations. Scale bar is 1 μm . (b) Pixel-level X-ray near-edge absorption and phase spectra acquired from a polycrystalline vanadium pentoxide particle at mutually orthogonal polarization states. A star in (a) highlights the location of the pixel. Spectra are post-edge normalized and smoothed by 3-point adjacent-averaging. Figure reproduced from [91] / CC BY-NC.

In contrast to the measured difference in spatial resolution, grain maps extracted from the phase, shown in Figure 3.3a, do not appear to be significantly improved compared to the absorption. The basis behind this observation can be seen in Figure 3.3b, which shows pixel-level spectra at orthogonal polarisation states. Evident in these spectra is that the difference between the maximum pre-peak intensity in the absorption spectra across polarisations is nearly twice that of the phase. This suggests the phase is less sensitive to changes in polarization, similar to the observation made within the context of X-ray magnetic circular dichroism (XMCD) [79]. A second explanation emerges from a closer look at the phase spectra. The pre-peak in the phase spectra possesses a larger spread in energy. This spread of the signal among different energies reduces the maximum contrast in the current and previous means of evaluation. Such spread may in the future encourage fitting of the pre-peak to attain a better result or possibly allow the extraction of secondary information from the phase pre-peak, *e.g.* a more detailed view into the probed coordination geometry.

In summary, we have introduced a technique for linear-polarization-dependent nano-imaging. The method uses X-ray linear dichroism ptychographic spectroscopy and is analyser-free. The current demonstration with two polarization states provides contrast between grains at different crystalline orientations, but with two polarizations is limited to qualitative grain orientation maps. Quantitative characterisation and associated unique mapping of c-axis orientations [95], becomes possible with additional relative orientations of the sample, and possibly the incorporation of a vectorial ptychography formalism [100, 108, 109]. The presented 2D approach will find application, for example, within an in-situ characterisation context of intercalation materials or energy storage materials [110, 111]. However, to fully exploit the penetration depth of hard X-rays, future efforts are placed in the combination of PIC-ptychography and computed tomography, specifically vector tomography [79, 112]. The associated acquisition of additional tomographic orientations of the sample allows a sensitivity to the out-of-plane component in 3D. This combination would open a new investigative space, in particular for ptychographic X-ray computed tomography (PXCT) studies for which large parts of the scientific interest not only stem from composition and structural variation of the sample, as commonly retrieved in PXCT measurements, but also, and additionally, from grain characteristics and their orientational distribution. Such capabilities would find ubiquitous applications in biomineral [96], energy storage [113, 114], heterogeneous catalysis [115], and additive manufacturing research [116].

The raw data can be obtained under DOI: [10.5281/zenodo.4059817](https://doi.org/10.5281/zenodo.4059817).

We acknowledge the support of the Swiss National Science Foundation, grant numbers PZ00P2_179886 and 200021_178788.

3.3 Supplementary Information

3.3.1 Materials

Analytical grade vanadium Pentoxide (V_2O_5), was purchased from US Research Nanomaterials Inc. Laboratory grade Ethanol was purchased from Sigma-Aldrich. The UV curable epoxy resin was type NOA-81, Norland Products.

3.3.2 Sample Mounting for PIC-PXCT

To ensure a homogenous dispersion of crystalline material for PIC image acquisition, 1 mg of the purchased V_2O_5 powder was dispersed in 10 ml of EtOH and sonicated 2 times for 15 minutes each. Following, 5 μ l of this slurry was deposited on a silicon nitride membrane, 1.5 mm in diameter -1000 nm thick, and left to dry in air. The silicon nitride membrane was as densely populated by apparently individual V_2O_5 crystals and polycrystalline aggregates ranging from 200 nm to 20 μ m in diameter. The membrane was then mounted on a 2-pin sample holder, constructed of OMNY pins [117]. See Figure 3.4 for details.

3.3.3 Optical and Electron Microscopy

Scanning electron microscopy (SEM) of the samples was carried out using an FEI Nova NanoSEM 650. Optical Micrographs were acquired using a Leica DM2500M. See Figures 3.6 and 3.7.

3.3.4 PIC-Ptychography

X-ray ptychography is a lensless imaging technique in which the phase problem is solved by means of iterative phase retrieval algorithms and as such provides the complex-valued refractive index of the specimen imaged, *i.e.* images of both absorption and phase contrast are obtained [16, 35].

Data Acquisition, Ptychographic Reconstruction and Spatial Resolution Estimation at a Single Energy: PIC-PXCT experiments were carried out at the cSAXS beamline of the Swiss light source (SLS). The photon energy was selected using a double-crystal Si(111) monochromator. Measurements were carried out around the vanadium *K*-edge, 5.460 to 5.520 keV. A Fresnel zone plate with 120 μ m diameter, outermost zone width of 60 nm, and locally displaced zones to provide perturbations of the illumination wavefront, was used to define the illumination onto the sample [118]. As the focal length of the zone plate changes with beam energy, the sample to zone plate distance was adjusted so that the focused beam had a diameter of \sim 5 μ m at the sample plane for all energies. Based on this illumination diameter we then set a constant scanning

step size for all projections of 0.6 μm using a Fermat spiral scanning grid [119] therewith ensuring sufficient overlap at all energies. Coherent diffraction patterns were acquired with an in-vacuum 1.5k Eiger detector with a 75 μm pixel size approximately 7.2433 m downstream of the sample [120, 121]. An evacuated flight tube was positioned between the sample and detector to reduce air scattering and absorption. Measurements were carried out using the positioning instrumentation described in Holler *et al.* [122, 123] at room temperature.

Ptychographic scans consisting of 624 diffraction patterns at maximum were acquired each with an exposure time of 0.1 seconds. From each diffraction pattern a region of 440 x 440 pixels was used in the ptychographic reconstructions. Reconstructions were obtained with 1000 iterations of the difference-map algorithm [35] followed by 500 iterations of maximum likelihood refinement [42, 45] using the PtychoShelves package [50].

The spatial resolution of a ptychographic image reconstruction was estimated by Fourier ring correlation (FRC) [124]. Two independently acquired ptychographic images of the same area, taken at a photon energy below the V K -edge were used for this purpose. The estimation is based on the intersection of FRC curves with a one-bit threshold curve [124]. The full-period spatial resolution for the phase is estimated to be 110.4 nm, for the absorption 183 nm, and for the complex image reconstruction to be around 119.2 nm. Please see Figure 3.5 for the corresponding correlation curves.

Although the complex-valued transmissivity is reconstructed with both phase and amplitude / absorption components simultaneously, phase image reconstructions, in the studied X-ray energy range and for the given sample, possess a higher spatial resolution compared to the absorption reconstructions. This is because the real part of the refractive index decrement is on average 10 times larger than the imaginary part across the studied X-ray energy range, as such phase contrast provides a better signal-to-noise ratio and in turn image reconstructions of higher spatial resolution. This situation is further evident in the spatial resolution of the complex-valued image reconstruction tending strongly towards the phase estimate.

The X-ray dose imparted to the sample per ptychographic scan was estimated to be $\sim 10^6$ Gy. The dose was estimated based on the accumulated area flux density during a scan and the mass density of the specimen [125].

Acquisition and Reconstruction of PIC-Ptychography Datasets: The image acquisition and reconstruction procedure outlined above was carried out 2 times, at 0 and 90 degrees of sample rotation normal to the fixed linear beam polarisation and repeated at ~ 60 energies across the vanadium K -edge where the relevant pre-edge and edge region was scanned in 0.5 eV steps. Since the pixel size depends on the photon energy the reconstructed projections were resized to the largest pixel size. A region of the field of view without particle was used to estimate and remove the constant and linear phase components, perform phase unwrapping, and to normalize the transmission / absorption [126]. Lastly projections were aligned with subpixel accuracy [127] resulting in a complex-valued X-ray transmission near-edge spectrum (XTNES) image stack per

polarisation state, *i.e.* stacks of phase and absorption as a function of energy.

In total, we collected a PIC-Ptychography dataset for each of three different sets of polycrystalline particles located on the same silicon nitride membrane, one of which is shown and discussed in the main text. All datasets show similar results.

Micro-spectroscopy Analysis: Following reconstruction, the two hyperspectral and complex-valued image stacks, measured with orthogonal linear polarization, were first rotated to a common orientation and then spatially registered by means of a normalized mutual information metric [128]. Pixel-level absorption and phase spectra were next normalized to account for variations in sample thickness, *i.e.* to retrieve numerically comparable pre-edge intensities across both polarisation states. Considering that the sample is entirely consistent of V_2O_5 , said normalisation was performed based on the magnitude of the absorption edge jump, or magnitude of the phase drop, respectively, as these quantities are proportional to the total vanadium concentration and thereby proportional to the local sample thickness. The pixel-level X-ray absorption near edge spectra (XANES) and X-ray phase near edge spectra (XPNES) were further normalized through linear regression of pre- and post-edge regions. Rudimentary crystal grain visualisation, Figure 3.3, was achieved by mapping to cyan and magenta the pre-edge intensities from 0 and 90 degrees polarisation angle, respectively.

Supplementary Movie 3.1. Ptychographic Phase and Absorption Image Reconstructions across the Vanadium K -edge. Shown is an excerpt of the acquired the spectral-image series used in the main text, highlighted is the transition from pre-edge to white line. To note is the feature / contrast delay from phase to absorption in accordance with the spectra presented in Figure 3.1.

Supplementary movie can be downloaded from <https://doi.org/10.1039/D0CC06101H>.



Figure 3.4. Optical Micrograph of the 2-Pin Sample Holder. To facilitate the acquisition of images at two sample-relative polarization states, we constructed a simple 2-pin sample holder, as shown above. The holder was created by fixing two OMNY sample holder pins (Membrane Type) at ~ 90 degrees to each other. The silicon nitride membrane, carrying the sample, was then glued onto this holder. Scale bar is 5 mm. Measurements were carried out with a fixed horizontal beam polarisation, following the acquisition of the first spectral image series the sample holder was azimuthally rotated to create the second polarization state with respect to the sample. Figure reproduced from [91] / CC BY-NC.

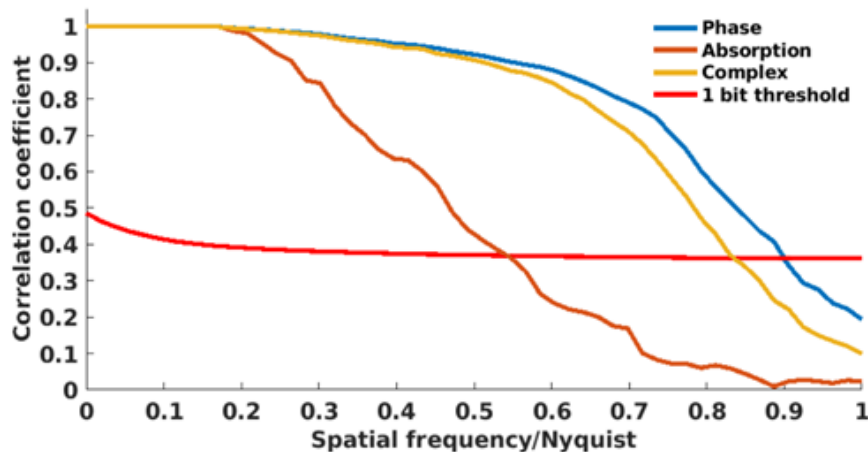


Figure 3.5. Spatial Resolution of Ptychographic Image Reconstructions. Fourier ring correlation (FRC) curves were calculated from ptychographic images acquired below the V K -edge at a single polarisation state. The resolution estimate is based on the one-bit threshold criterion. Pixel size is 48.82 nm. Figure reproduced from [91] / CC BY-NC.

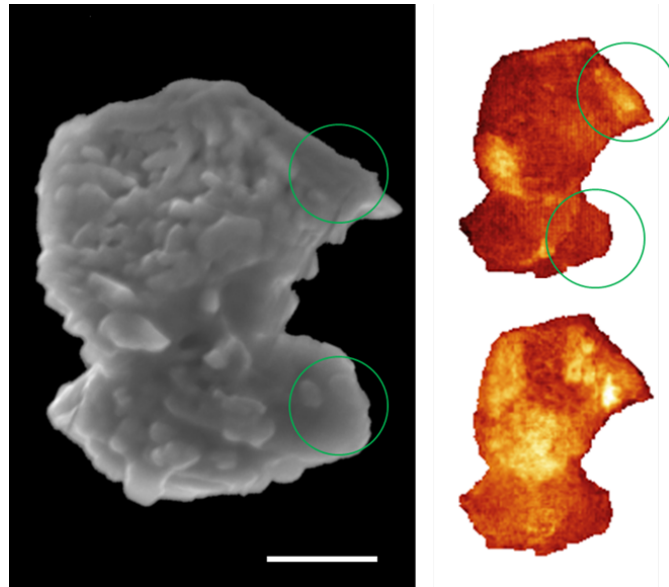


Figure 3.6. Comparison of Scanning Electron Micrograph and PIC-Ptychography Pre-Peak Intensity Maps of one of the Investigated Vanadium Pentoxide Particles. Left, scanning electron micrograph. Scale bar 2 μm . Right, phase-based pre-peak intensity maps at orthogonal linear polarisation states as shown in Figure 3.2. $\varphi = 0^\circ$ (top) to $\varphi = 90^\circ$ (bottom). Green circles indicate two dominant crystal grains (CGs) visible in both the surface sensitive electron microscopy and the transmission based PIC-Ptychography. Figure reproduced from [91] / CC BY-NC.

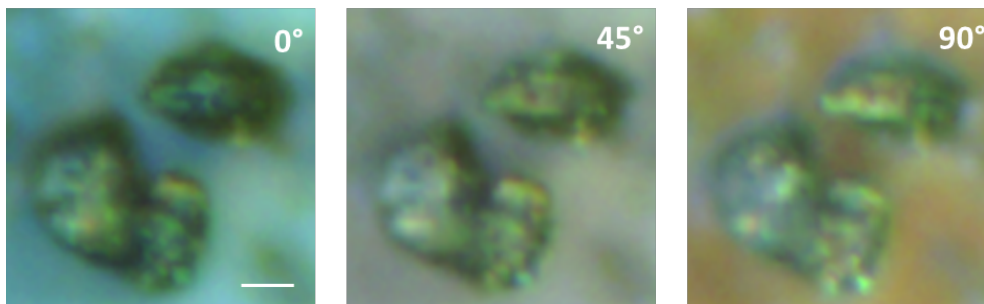


Figure 3.7. Vanadium Pentoxide Crystals under a Polarizing Optical Microscope. Optical micrographs of the vanadium pentoxide particles shown in the main text acquired at increasingly crossed polarizers, *i.e.* 0, 45 and 90 degrees. Scale bar is 2 μm . Figure reproduced from [91] / CC BY-NC.

Sparse X-ray Transmission Spectrotomography for Nanoscopic Compositional Analysis

*The content of this chapter is covered in the publication: Z. Gao, M. Odstrcil, S. Böcklein, D. Palagin, M. Holler, D.F. Sanchez, F. Krumeich, A. Menzel, M. Stampanoni, G. Mestl, J.A. van Bokhoven, M. Guizar-Sicairos and J. Ihli. “Sparse ab initio x-ray transmission spectrotomography for nanoscopic compositional analysis of functional materials.” *Science Advances* 7.24 (2021): eabf6971. [129]*

4.1 Abstract

The performance of functional materials is either driven or limited by nanoscopic heterogeneities distributed throughout the material’s volume. To better our understanding of these materials, we need characterization tools that allow us to determine the nature and distribution of these heterogeneities in their native geometry in 3D. Here we introduce a new method based on X-ray near-edge spectroscopy, ptychographic X-ray computed nanotomography, and sparsity techniques. The method allows the acquisition of quantitative multimodal tomograms of representative sample volumes at sub-30 nm half-period spatial resolution within practical acquisition times, which enables local structure refinements in complex geometries. To demonstrate the method’s capabilities, we investigated the transformation of vanadium phosphorus oxide catalysts with industrial use. We observe changes from the micron to the atomic level, and the formation of a location-specific defect so far only theorized. These results led to a re-evaluation of these catalysts utilized in the production of plastics.

4.2 Introduction

Composition and structure define a material’s functionality [130]. While we can determine and sometimes predict the relationship between structure and emergent functionality for simple single-component materials with some effort, we frequently face difficulties when dealing with structurally and compositionally more complex materials such as heterogeneous catalysts, energy storage materials or biominerals [5, 131, 132]. Here, functionality is often defined by local heterogeneities in structure and or composition such as interfaces between two components or selected crystallographic defects, distributed in a larger volume [133, 134]. The distribution of these heterogeneities within frequently hierarchically structured assemblies, spanning multiple length scales, and their interaction with the local environment, further guides the material’s functionality or device performance. As such we face the challenge to provide characterization tools that allow us to determine the nature and distribution of these heterogeneities in their native geometry in 3D. This is to better our understanding of current and aid the design of next-generation materials.

X-ray absorption near-edge spectroscopy (XANES), the measurement of X-ray excitation characteristics of a chemical element in response to variation in incident energy, has become the dominant method for chemical speciation and component identification in various research fields [135, 136]. While initially limited to bulk analysis, the increasing importance of advanced composite materials [5, 132, 134, 137–139] has led to the development of XANES imaging, and eventually to XANES tomography [71–77], adding a structural characterization element and aiming to identify and localize local heterogeneities in a system-representative sample volume, *i.e.* providing the desired characterization tool. These techniques are especially of interest when aiming for nanoscale resolution to reveal features at the scale in which different chemical phases intertwine in these materials [5, 132, 134, 137–139]. However, current XANES tomography implementations [71–77] suffer from two particular difficulties when in pursuit of nanoscopic features in representative sample volumes: access to local quantitative density or elemental concentrations requires effort in calibration and normalization that is often overlooked, and lengthy acquisition times [22]. Until now, spectral tomogram synthesis involved the acquisition of one tomogram per energy to generate the hyperspectral dataset. The required number of projections per tomogram scales with the sought spatial resolution and the diameter of the sample following the Crowther criterion [15]. Iterative reconstruction methods, such as the simultaneous algebraic reconstruction technique (SART) [140], were following introduced to relax the number of projections while preserving the quality of the tomographic reconstruction.

Here, we introduce a novel acquisition scheme and iterative reconstruction technique that leverages the sparsity of information in a hyper-spectral tomogram to relax the required number of projections further, thereby significantly reducing XANES tomogram acquisition times [22]. Specifically, using the introduced reconstruction technique, we were able to reduce the number of projections to 11% of the Crowther criterion at no

significant cost of spectral or spatial resolution. Such a reduction is possible, as signal variation across the spectra is heavily correlated and can be reduced to spatially-localized and consistent grey-level changes, our reconstruction leverages this correlation to significantly relax the required measurements.

Even though the developed reconstruction technique is applicable to a wide range of tomography techniques, we here selected ptychographic X-ray computed tomography (PXCT) [141] as the vehicle of choice in order to provide an easier or more direct access to quantitative values [22]. PXCT readily provides quantitative tomograms of the complex-valued refractive index distribution, *i.e.* phase and absorption. As a lensless imaging technique, its spatial resolution is not limited by aberrations or technical limitations in the fabrication of optics, which is a significant challenge for X-ray wavelengths, this makes PXCT prolific in terms of signal to noise ratio (SNR) and with outstanding resolving power. The combination of PXCT’s high resolution and quantitateness with our sparse reconstruction method for spectral tomography, following termed sparse X-ray transmission near-edge spectro (XTNES) tomography, enables the acquisition of a 3D picture of representative volumes with nanometer resolution, which reconstructs into quantitative values of electron density, absorption, elemental concentration, and oxidation state. This ultimately allows a local, quantitative characterization of structure, chemical composition and coordination geometry.

In this first application, we examined a pristine and an industrial used vanadium phosphorus oxide (VPO) catalyst. These oxides are used to catalyze the selective oxidation of *n*-butane (C_4H_{10}) to maleic anhydride (MA) ($C_4H_2O_3$). MA is a precursor in the production of plastics, with a steadily increasing production quantity of currently 2 million tons per year [142, 143]. In consideration of the reaction by-products, carbon monoxide and carbon dioxide, a financial and environmental incentive is present to increase the productivity of these catalysts. State-of-the-art catalysts are a composite of hierarchical porosity, and one of the factors that hinders catalyst improvement is that the composition and spatial distribution of its vanadium phosphate phases (Table 4.1) are not precisely known. Another factor is that during reactor operation, the catalyst undergoes a series of structural and compositional changes that culminate in a gradual loss of catalyst productivity. Due to the compositional uncertainty, the aforementioned changes are yet to be fully understood, leading to an active discussion regarding the best catalyst design, the most desirable active phase, and the nature of active sites in general [144–148]. Historically, V=O bonds or V^{5+}/V^{4+} redox pairs on the catalyst’s surface are considered to be the active sites in the initial hydrogen transfer reaction to activate *n*-butane on the catalyst surface. The former, *i.e.* the cleaving of alkane C-H bonds, is suggested to be the rate-limiting step [143, 145, 147–150]. More recently, P=O bonds were theoretically suggested to play an equally important role [151, 152]. Naturally, materials of increased structural disorder, exhibiting more of these bonds at their surfaces, find employment in industrial VPO catalysts [153, 154], for example, defect-rich nanoparticles and amorphous phases. Please see the Supplementary Materials and Figure 4.4 for further details regarding VPO and their industrial use.

The XTNES tomography measurements presented here provide answers to some of these uncertainties, explicitly those surrounding catalyst structure, composition, active sites, and productivity. The multimodal hyperspectral tomograms revealed a structural and chemical transformation following four years of industrial reactor utilization. That is from a mesoporous catalyst of high surface area composed of a series of amorphous and nanocrystalline vanadium phosphate phases, to a macroporous catalyst composed of micron-sized and defect-rich vanadyl pyrophosphate crystals. When evaluated against catalytic performance, this transformation directly implies the used catalyst to be more productive on a surface area-specific basis than the pristine and equilibrated catalyst. By utilizing the quantitiveness of XTNES to perform local structure optimizations on vanadyl pyrophosphate crystals that were in contact with the reactive medium, we were able to correlate this increased productivity of the used catalyst to vanadyl defects, which create unsaturated P=O bonds that are accessible from {200} terminated facets. Hence, catalysts of highest activity might not be derivable from amorphous surface deposits enriched in V^{5+} or the interaction of nanometer-sized V^{5+} and V^{4+} components as previously targeted but rather through defect engineering of highly crystalline vanadyl pyrophosphate crystals [149, 150]. These observations currently aid the design of improved VPO catalysts and hopefully highlight the prowess of XTNES tomography including local defect and potential active site characterization.

4.3 Results

4.3.1 X-ray Transmission Near-Edge Spectro Tomography

Clariant AG provided the pristine and the used VPO catalyst bodies, *i.e.* pellets [155]. The latter were sourced from an industrial fixed-bed reactor after four years of known operation history. The reactor coolant temperature was gradually increased from 400°C to ~420°C following the first year of operation to ensure steady reactor performance. From performance profiles, Figure 4.5, we can estimate that a catalyst equilibrium state and structure was reached after ~1.5 years of operation. Bulk examination revealed the used catalyst to exhibit a 70% decrease in specific-surface-area and a ~10% reduction in productivity after four years of operation, Table 4.2. As shown in Figure 4.1A, samples intended for tomographic examination were extracted from the central region of randomly selected catalyst pellets and shaped into cylinders roughly 12 μm in diameter.

High-resolution tomographic projections (Figure 4.6) were acquired at 60 X-ray photon energies across the vanadium *K*-edge, between 5.443 and 5.530 keV. For a target spatial resolution of 25 nm, a conventional spectrotomography measurement using analytical reconstruction technique, *i.e.* satisfying the Crowther sampling criteria, would require the acquisition of 628 projections at each energy. Following our sparse sampling approach, we measured at each energy, only 68 projections resulting in a reduction in acquisition time per XTNES tomogram from more than one week to less than 20 hours. To retain information from a high diversity of incident angles, which aids the sparse

synthesis, we further introduced a unique offset to the first projection angle of each single-energy-tomogram [156]. Figure 4.1B and 4.1C illustrate the acquisition strategy. Similar angle interleaved acquisition strategies found previous application within the field of time resolved X-ray tomography [156, 157].

At these photon energies, the phase of the complex-valued projections provides a better signal-to-noise ratio and spatial resolution compared to the amplitude. Therefore, high-resolution processing was conducted using the phase, while the amplitude, or absorption signal was used as low-resolution reference.

The reconstruction of the sparse XTNES tomograms was carried out using a novel iterative algorithm based on principal component analysis (PCA) [158] and SART [140]. The reconstruction process involves a non-centered PCA decomposition of a downsized hyperspectral tomogram to extract a set of spectral modes with their corresponding component tomograms to be used as initial guess. The initial guess is then iteratively refined using all the high-resolution projections at all energies. This process results in a set of spectral modes and their corresponding tomograms at the highest resolution, from which we can calculate the XTNES tomogram. The half-period spatial resolution of the obtained XTNES tomograms was determined using 4D Fourier shell correlation (FSC) and found to be limited by the voxel size, here 26.50 nm. The corresponding full-period resolution is 53.0 nm. Please see the Methods Section for a detailed explanation of the reconstruction procedure and Figure 4.7 for details regarding resolution estimates. Further, the reader is referred to Figure 4.8 which provides a comparison of different analytical and iterative tomogram reconstruction methods to showcase the benefit of the introduced sparse spectral tomogram reconstruction method.

The phase and absorption spectra of two voxels extracted from the pristine catalyst are shown in Figure 4.2A. The provided absorption spectra were obtained using a Kramers-Kronig transformation (KKT) of the phase spectra [159]. Given that this is the method's first application, we transformed the phase signal to absorption via a KKT to allow an easier analysis and validation of the reconstructed spectra, owed to the established analysis routines for XANES spectroscopy and the availability of reference spectra [160]. For example, a comparison of one of the provided voxel-level absorption spectra with spectra from the literature, shown in Figure 4.9, confirms that the voxel consists mainly of vanadyl pyrophosphate. The typical approach for the analysis of XANES spectra, as well as XANES tomography, is to compare the measured spectra to those of a list of reference components. A particular match with one, or a linear combination of multiple reference spectra, allows the identification of a single or fractional quantification of multiple components [71, 135, 161]. The quantitiveness of ptychography-based XTNES tomography affords us with a different analysis approach to reach the same goal. This approach is based on the extraction of a set of key quantities directly from the acquired phase or absorption spectra of each voxel. The quantities extracted in the present case include: (i) Local electron densities obtained from the phase signal away from the resonant edge. (ii) Local vanadium concentrations retrieved from the edge jump magnitude. (iii) Local vanadium oxidation states determined by the position of the ab-

sorption edge. (iv) The local vanadium coordination geometry inferred from pre-edge peak intensity variations. Please see Figure 4.2A for a graphical illustration and the method section for further details about how these quantities are obtained. Instead of a comparison of spectra, we compare the extracted set of quantities with those of a list of possible, or considered, reference components, shown in Table 4.1. If a match of the measured set with those of a single reference component is not possible, a linear combination of multiple reference components can be explored to best describe the measured set of quantities. While the typical spectrum comparison-based analysis is reliant on the availability of reference spectra or reference materials from which spectra can be collected, the quantity-based analysis is largely free of this constraint. In this study, a selected number of reference spectra of components with known oxidation state are used to convert measured edge-energies to oxidation state. However, the quantities used in this manuscript for component identification are also readily available in the literature for a vast amount of materials. This makes the presented approach well suited for the examination of materials where reference spectra are hard to come by, as is often the case for industrial materials. For cases in which reference spectra are available, this approach could of course leverage this extra information to add additional constraints for a refined material characterization.

4.3.2 XTNES Tomograms of Pristine and Deactivated VPO Catalysts

Figure 4.2B-D shows compound volume renderings of the tomogram extracted quantities (i), (ii) and (iii) for both the pristine and used VPO catalyst, together with orthoslices of the individual quantities. Please refer to Movie 4.1&4.2 for an animated representation. Associated histograms and correlations of these quantities are shown in Figure 4.10.

It is evident from a structural comparison of the electron density tomograms, *i.e.* the outcome of a conventional PXCT measurement, that the catalyst undergoes a structural reorganization during reactor operation. The catalyst’s nanoporosity and fine structure are lost, leaving behind a mesoporous structure composed of micron-sized domains. Accordingly, a decrease in surface area and widening of the pore network is registered, as shown in Figure 4.11 and Table 4.2. An increase in average electron density ($\pm\sigma$) from $0.66 (\pm 0.007)$ to $0.86 (\pm 0.006)$ $n_e \text{ \AA}^{-3}$ further suggests that the observed changes in structure are a product of phase transformation processes. Lastly, based on the electron density distribution, shown in Figure 4.2C&D and Figure 4.10, there appears to be little compositional variance within the pristine and used catalyst. While this may appear to conflict with the reported ill-defined nature of VPO catalysts [144–148], in reality, we find numerous industrial VPO catalyst components to possess comparable electron densities. The situation is similar for vanadium concentration and vanadium oxidation state, Table 4.1. This renders schemes based on a single value for component identification insufficient. For example, an electron density of $0.86 n_e \text{ \AA}^{-3}$ as dominantly observed in the used catalyst could equally be interpreted, among others, as $(\text{VO})_2\text{P}_2\text{O}_7$, $\text{V}(\text{PO}_3)_3$, and $\text{VO}(\text{HPO}_4) \cdot 0.5\text{H}_2\text{O}$, all known to be possible catalyst components [145, 147, 153, 154].

An identification of components becomes possible, when electron density, vanadium concentration, and vanadium oxidation state are considered together, as demonstrated in Fig 4.10. Based on this correlative identification approach, we identified three distinct components in the pristine catalyst. Identification was limited to materials reported in the literature to be present in VPO catalysts, shown in Table 4.1 [145,147,153,154]. These being amorphous vanadium-rich metaphosphate, nanocrystalline vanadyl pyrophosphate ($(\text{VO})_2\text{P}_2\text{O}_7$) and vanadium hydrogenphosphate ($\sim(\text{VO})\text{PO}_4 \cdot 2\text{H}_2\text{O}$). While the latter is present in the form of isolated, micron-sized objects, the former two, which account for the majority of the sample volume, are found in nano-sized domains. Notably, domains of these two components are spatially intertwined, with the minor metaphosphate phase preferentially facing the pore space or reaction environment, thereby increasing the vanadium concentration and oxidation state at the catalyst surface. The catalysts composition changes with reactor operation. In the used catalyst we identified only two components, namely small islands of VOPO_4 (<10 vol.%) and a dominantly defect-rich vanadyl pyrophosphate. The latter appears throughout the entire catalyst in micron-sized domains that exhibit a variance in vanadium concentration and oxidation state, which are known to occur in solid-state transformation processes.

Intensity variations of the vanadium pre-edge peak (iv) are discussed separately and shown in Figure 4.3A&B. These variations provide a first glance at the microstructure of the catalysts, *e.g.* allowing the detection of crystalline and amorphous domains [97]. This is made possible by the combination of using a linearly polarized illumination and the net-anisotropy of most crystalline materials [91, 162]. Notably, it is the spatial extent of regions with increased pre-peak intensities that reaffirm the loss of amorphous domains and the catalyst's nanocrystalline structure during reactor use. In the used catalyst, we find vanadyl pyrophosphate crystals with a coherent domain size of multiple microns, which suggests the presence of chemically more defined surfaces than were available in the pristine catalyst. Based on the Bragg peak intensity ratio of the vanadyl pyrophosphate reflections, these surfaces, which are available for selective oxidation, are present in the form of {200}- and with progressing use increasingly {024}-terminated facets.

To obtain a better understanding of the defect-rich crystal structure of these surfaces, which drive the catalytic conversion process, we calculated the average electron density, vanadium concentration, and vanadium oxidation state of vanadyl pyrophosphate in direct contact with the reactive medium, shown in Figure 4.3C. These values were combined with ratiometric V/P measurements, to locally specify the vanadyl pyrophosphate crystal structure by means of ground-state total energy calculations. See Supplementary Materials for details. Figure 4.3D presents a comparison of the ideal vanadyl pyrophosphate crystal structure and the calculated structure of the outermost 80 nm of the used catalyst. Visible is the loss of a single vanadyl group per unit cell following reactor use. The resulting vacancy is selectively accessible in the {200} direction. Thereby creating unsaturated P=O bonds on the surface of these facets and increasing the oxidation state in neighboring vanadium atoms. Unsaturated P=O bonds on the {200} surfaces of vanadyl pyrophosphate have so far only been theorized to exist

and were recently suggested to be active sites in the conversion of *n*-butane to maleic anhydride [151, 152].

4.4 Discussion

As losses in specific-surface-area (70%) stand in no relation to the reduction in catalyst productivity ($\sim 10\%$), it is hard to argue that the catalyst performs worse after reactor use. Far from it, assuming an equal density of active sites in the pristine and the used catalyst, the used catalyst performs astonishingly well on a surface-area-specific scale even after four years of reactor operation, Figure 4.5. This poses the question as to why and how to leverage this information to design improved VPO catalysts or increase the lifetime of existing catalysts.

Spectral nanotomography measurements provide a first answer to this question. The detected loss of amorphous vanadium-rich metaphosphate and increasing absence of secondary vanadium phosphate phases with progressing reactor operation, suggest both to be of minor importance regarding catalyst productivity, which is surprising given their previous consideration as active site carriers [149, 150]. Rather, catalyst productivity in the used catalyst appears to derive from a significantly increased density and availability of active sites per unit area on the surface of vanadyl-deficient and crystalline vanadyl pyrophosphate grains. In addition to the previously suggested V-O bond on {200} terminated facets, the here identified unsaturated P=O bonds [151] appear to contribute to the catalyst's productivity. The latter possesses more uncompensated negative charge and, therefore, a higher affinity to extract the hydrogen atom (H) from the *n*-butane C-H bond [152], see Supplementary Material. Based on these results, rather than focusing on the purposeful introduction and maintenance of amorphous vanadium-rich metaphosphate and as such V^{5+} rich phases on the catalyst surface through phosphate dosing [142], current catalyst design studies, of industrial collaborators for improving MA yield and selectivity, are targeting the production of catalysts with narrower pore space and composed of vanadyl-deficient vanadyl pyrophosphate. Structural and compositional observations and resulting conclusions were only possible through the examination of catalysts extracted from an industrial reactor operated under low phosphate dosing conditions (< 1 ppmv) and following long-term use, which allows us to probe an evolved catalyst structure that emerges only after years of use in an industrial setting [149].

In summary, we developed a novel acquisition and reconstruction procedure for angularly sparsely sampled spectro-tomograms that can be utilized by a wide variety of imaging techniques. Application within the framework of PXCT allowed for a structural, compositional and chemically quantitative characterization of a functional material at a representative sample volume with a half-period spatial resolution of sub-30 nm, or full-period resolution of sub-60nm, providing sufficient constrains to perform ab initio structure refinements in complex geometries on the voxel level. Furthermore, the method allows for quantitative spectro-nanotomography with a much-reduced acquisi-

tion time and dose. A combination that satisfies an existing demand of the research community [163] and lessens a number of difficulties in spectral -tomography, such as spatial resolution limitations imposed by imaging optics. Further, this combination provides a more direct access to quantitative information, *e.g.* electron density and elemental concentration, and reduces the acquisition time of near-edge spectral tomograms. This method effectively puts in-situ studies targeting fundamental electrochemical and catalytic processes within reach.

Moreover, the increased brightness and coherent flux of emerging 4th generation synchrotrons could lead to even further increased spatial-resolution and faster acquisition. These developments alongside the presented method will open the door for nanoscale extended X-ray absorption fine structure (EXAFS) [136,164] and dedicated X-ray polarisation [97] tomography studies.

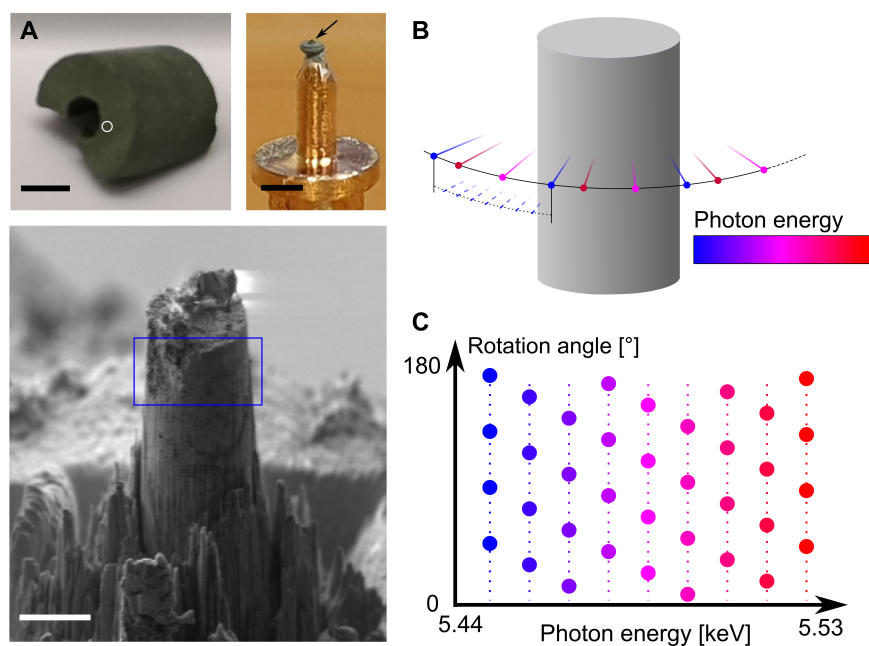


Figure 4.1. Illustration of sparse XTNES acquisition. (A) Examined VPO catalyst pellet as retrieved from the reactor (top left). Preshaped sample mounted on a tomography pin (top right, black arrow) and focused ion beam milled sample cylinder (bottom). Scale bars are 5 mm, 1 mm and 10 μm . The white circle indicates the region from which the sample cylinder was extracted. The blue rectangle indicates roughly the field of view during XTNES tomogram acquisition. Photo credit: Zirui Gao, PSI, ETHZ. (B) Spectral tomograms were assembled by acquiring a series of angularly sparse ptychographic tomograms across the vanadium K -edge. (C) Graphical illustration of the acquisition scheme of tomography angular orientations versus x-ray photon energy. For each energy, the Crowther criterion is indicated by small dots, while larger dots indicate angularly sparse measured projections. At each energy, an offset to the angle based on a golden ratio is added to each projection to maximize the available information diversity. Figure reproduced from [129] / CC BY.

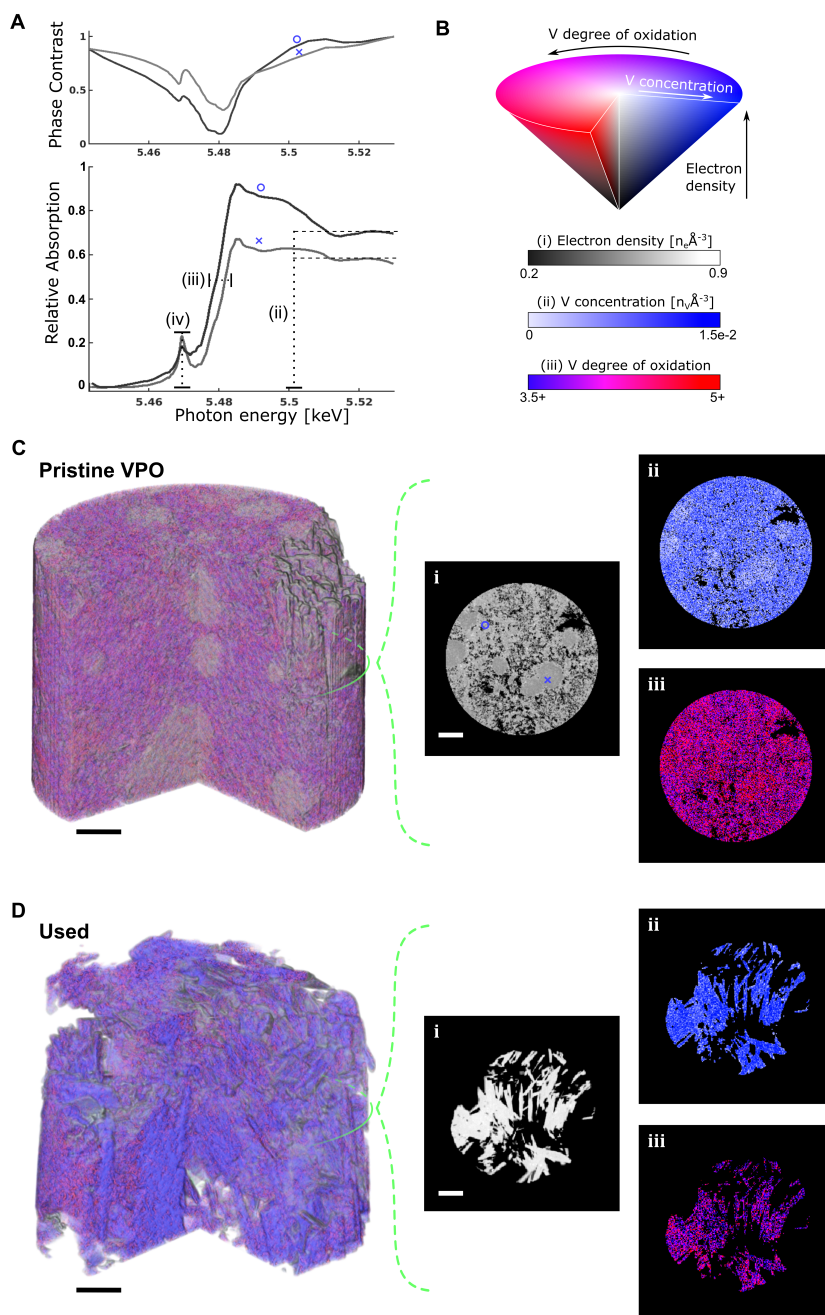


Figure 4.2. Local vanadium K -edge spectra and XTNES tomograms of industrial VPO catalysts. (A) Example of two voxel-level phase and KKT-obtained absorption spectra. From these spectra, we obtain quantitative values for (i) the electron density, (ii) vanadium concentration, (iii) vanadium oxidation state, and (iv) pre-peak intensity. (B) Hue saturation value 3D color map used for the combined visualization of electron density, vanadium concentration, and vanadium oxidation state. (C) 3D volume rendering of the pristine catalyst based on the color map presented in (B) and axial virtual slices taken from the middle of the catalyst sample highlighting the individual quantities. (D) 3D volume rendering and virtual slices of the used catalyst based on the color map in (B). Scale bars, 2 μm . The positions of the voxels discussed in (A) are marked in (C) using a cross and a circle, respectively. Figure reproduced from [129] / CC BY.

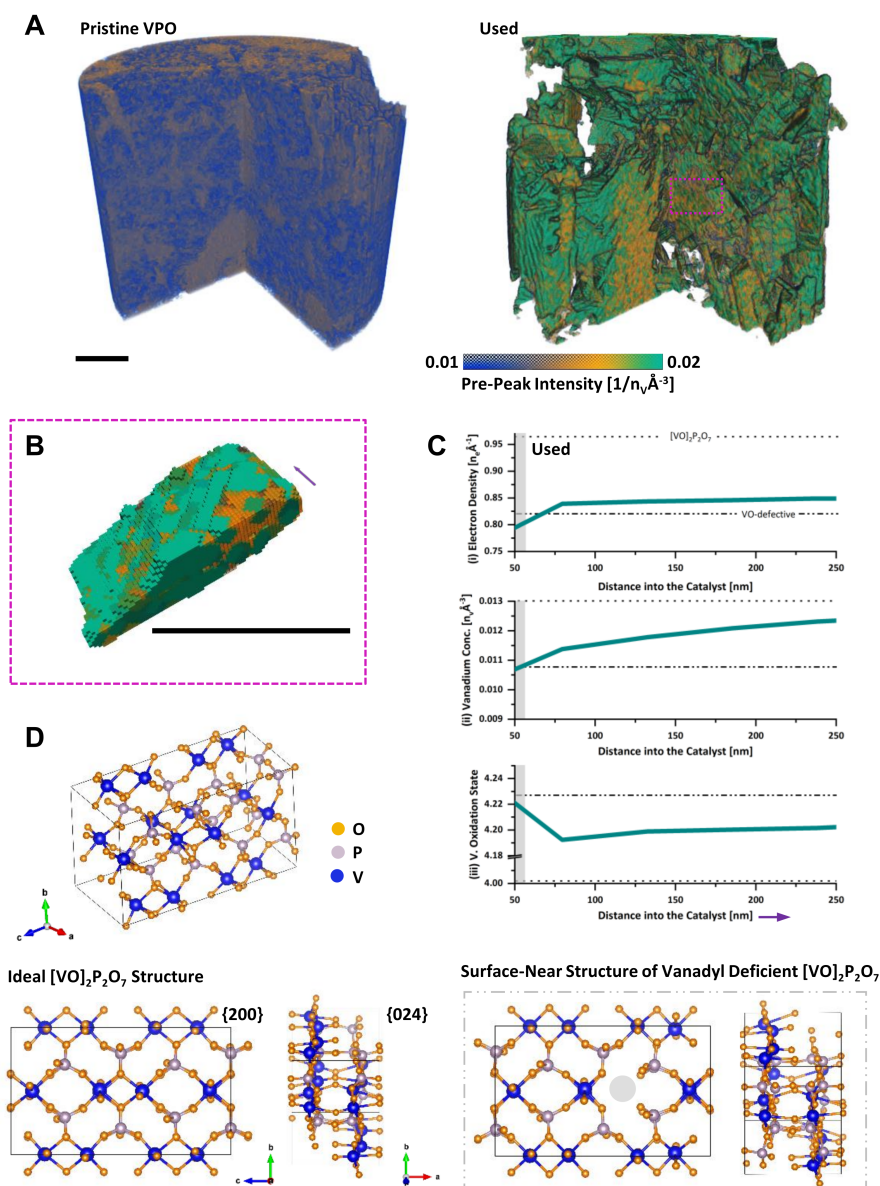


Figure 4.3. Microstructural analysis, local structure optimization, and defect Identification in vanadium phosphorus oxide catalysts. (A) Pre-peak intensity volume renderings, shown as (iv) in Fig. 4.2A, of the pristine and used VPO catalyst. (B) Volume rendering of the pre-peak intensity of a single vanadyl pyrophosphate $[(\text{VO})_2\text{P}_2\text{O}_7]$ grain found in the used VPO catalyst. Changes in pre-peak intensity are displayed in the form of a gradient color map ranging from blue to green. Scale bars, 2 μm . (C) 3D distance maps of XTNES extracted quantities—(i), (ii), and (iii)—from the pore space into the used VPO catalyst. Magnitudes encountered within the first 80 nm of the material are shown in gray, which were used as boundary conditions for ground-state total energy calculations of the crystal structure of vanadyl pyrophosphate in contact with the reactive medium, thereby found to be vanadyl deficient (VO). The gray dotted lines show reference values of both the ideal and defective structure. (D) Ideal crystal structure of vanadyl pyrophosphate including 200 and 024 surface projections as well as vanadyl defective projections of the calculated catalyst structure in contact with the reactive medium (gray box). Figure reproduced from [129] / CC BY.

4.5 Materials and Methods

Materials: Pristine and used industrial VPO catalyst pellets, roughly 5 mm in diameter, manufactured under identical conditions were provided by Clariant AG. The used catalyst pellets were sourced from an industrial fixed-bed reactor after four years of operation, *i.e.* after an overall time on steam of 38,000 hours. Specifically, they were extracted from a catalyst bed, operated in upward gas flow configuration and at near constant salt bath or reactor temperature. The catalyst bed housing reactor tubes had a dimension of 21 by 3700 mm ($w \times h$). The hydrocarbon inlet concentration was ~ 1.8 mol. %, water was added to the feed steam at a concentration of ~ 2 mol. % throughout, phosphates were added at a concentration of ~ 0.01 pmmv. The salt bath temperature was held at $\sim 400^\circ\text{C}$ until 16,000 hours of operation before gradually increasing the temperature to 420°C to ensure a steady conversion rate in face of catalyst deactivation, see Figure 4.5. Observable was a gradual and delayed loss in MA yield and catalyst selectively up $\sim 19,000$ hours of catalyst use or two years of operation, reflective of a still evolving catalyst structure up to this time point. One randomly selected pellet from each the pristine and used catalyst population was subjected to spectro-tomographic examination. Samples were stored in environment-isolated containers as much as possible prior to examination. The industrial VPO catalysts themselves are porous bulk type vanadium phosphate catalysts and as such they are predominantly composed of vanadyl pyrophosphate, $(\text{VO})_2\text{P}_2\text{O}_7$, and to a lesser extent of various vanadium phosphate phases, $\text{VO}_x\text{PO}_4(\text{H}_2\text{O})_n$ [142]. Furthermore, catalysts are sparsely decorated with bismuth oxide nanoparticles, which are added to increase catalytic activity and selectivity towards maleic anhydride. Chemical composition and selected properties of both sample populations are listed in Table 4.2.

Sample Preparation: A pristine and a used VPO catalyst pellet were first mechanically fractured, after which a central piece from each pellet was mounted on a tomography pin. The mounted samples were then pre-shaped using a micro-lathe [165] to a diameter of 100 μm before being reduced to a final diameter between 10-12 μm using focused ion-beam (FIB) milling.

Data acquisition: XTNES-tomography experiments were carried out at the cSAXS beamline of the Swiss Light Source, Paul Scherrer Institut, Switzerland. The photon energy was selected using a double-crystal Si(111) monochromator. The horizontal aperture of slits, located 22 m upstream of the sample was set to 20 μm in width, to create a horizontal virtual source point that coherently illuminated a Fresnel zone-plate 220 μm in diameter and with an outermost zone width of 60 nm [166]. The Fresnel zone-plate was designed with locally displaced zones to improve imaging quality and phase accuracy [118]. Coherent diffraction patterns were acquired using an in-vacuum Eiger 1.5M area detector, with a 75 μm pixel size, placed 5.23 m downstream of the sample inside a flight tube under vacuum. For the PXCT measurements we employed the nanotomography instrument described in Holler *et al.* [10]. This instrument incorporates interferometrically controlled 3D stages for precise nanopositioning with an accuracy reaching 10 nm, aiming to minimize motion- or geometry-induced errors which have a negative impact

on the achievable spatial resolution. Each ptychographic scan, or projection, covered a field-of-view of $\sim 16 \times 10 \mu\text{m}^2$ (horizontal \times vertical) and consisted of ~ 160 scanning positions with an average step size of $1 \mu\text{m}$. Positions followed a Fermat-spiral scanning pattern [119]. The exposure time per point was 0.1 seconds.

Sparse-XTNES tomograms were collected by acquiring a series of sparse-tomograms at different photon energies across the vanadium K -edge. Each sparse tomogram covered the full tomographic angular range of 180° . Measurements were collected with an energy step of 0.5 eV across the vanadium K -edge (5.465-5.487keV), and a coarser step of 5 eV in the pre-edge (5.443-5.465 keV) and post-edge (5.487-5.540 keV) regions. In total, 60 sparse-tomograms were acquired, each with 11% of the Crowther criterion angular sampling [15]. To maximize the information content for the reconstruction of a sparse-XTNES-tomogram, each sparse tomogram had a different starting angle given by the golden ratio sequence [167], but only computed in the range between zero and one angular step size. Angle interleaved acquisition strategies have found previous application within the field of time resolved tomography [156, 157].

Ptychographic Image Reconstructions: For each ptychographic image reconstruction, *i.e.* each tomographic projection, a region of 600×600 pixels of the detector was used, resulting, in an image pixel size of 26.10 to 26.52 nm, depending on the illumination energy. Reconstructions were obtained with 200 iterations of the difference map (DM) algorithm [35] followed by 300 iterations of maximum likelihood (ML) refinement [45], using the PtychoShelves package [50]. The reconstruction pixel size can be in theory adjusted by changing the region of the detector depending on the incident X-ray energy, however in our case this was not possible due to the small energy step size of 0.5 eV.

Processing of Ptychographic Projections: Due to the superior spatial-resolution and improved signal-to-noise ratio of the phase signal in the hard X-ray regime, compared to absorption, high-resolution XTNES-tomograms were reconstructed from the acquired phase signal, while the absorption was used only as low-resolution reference [168]. Changes in the real part of the scattering factor, which are associated with the phase, across the vanadium K -edge are nearly twice as large when compared to changes in the imaginary part of the scattering factor, which is associated with the absorption.

As the pixel size of projections depends on the X-ray photon energy, we resized all complex-valued ptychographic projections to a common pixel size of 26.52 nm using an interpolation based on fast fractional Fourier transform [169, 170]. Next, the phase of the reconstructed 2D projections was extracted by post-processing alignment and removal of constant and linear phase components, and the projections aligned using a tomographic consistency approach [170].

XTNES-tomogram Reconstruction: In order to reconstruct a XTNES tomogram from an angularly sparse, *i.e.* angularly under-sampled, set of projections, a new iterative algorithm, based on a combination of PCA [158] and SART [140], was developed. The aim is to reconstruct a set of spectral modes $w_k(E)$, where $k = 1, 2, 3, \dots$ is the mode number, and their corresponding component tomograms $X_k(\mathbf{r})$. The hyperspectral real

part of refractive index δ , which is associated with phase contrast, is then given by

$$\delta(\mathbf{r}, E) = \sum_k X_k(\mathbf{r}) * w_k(E). \quad (4.1)$$

First, to obtain a starting guess for reconstruction of $X_1(\mathbf{r})$, the measured projections at each energy and rotation angle, namely $\{P_{\theta,E}(\mathbf{r}_{2D})\}$, are spatially down-sampled by a factor 16, and low-resolution tomographic reconstructions are obtained for each energy. At this resolution the Crowther criterion is satisfied, so a conventional tomographic reconstruction per energy can be performed. We then perform a non-centered PCA on the reconstructed hyperspectral tomograms and we take the first principal coefficient, namely $w_1(E)$, and the corresponding 3D spatially-resolved component tomogram. The tomogram was then interpolated to the original voxel size with Fourier transform based interpolation, using this as the starting guess of $X_1(\mathbf{r})$ accelerates the convergence, while using zeros as a starting guess is also possible.

The refinement is carried out with an iterative algorithm, similar to SART, using the high-resolution projections. For each iteration the components are updated by

$$\Delta X_1(\mathbf{r}) = \tau * \text{FBP} \left\{ \sum_E \left[\left(P_{\theta,E}(\mathbf{r}_{2D}) - \hat{P}_{\theta,E}(\mathbf{r}_{2D}) \right) * w_1(E) \right] \right\}, \quad (4.2)$$

where τ denotes the update ratio, $P_{\theta,E}$ denotes the measured projection at rotation angle θ and energy E , and $\hat{P}_{\theta,E}$ denotes the projection computed from the current estimate, and $\text{FBP}\{\}$ denotes filtered back-projection over all rotation angles and energies [171]. The ratio τ is calculated as

$$\tau = \alpha * \frac{N_E}{\sum_E [w_1(E)]^2}, \quad (4.3)$$

where $\alpha = 0.2$ is the relaxation constant, and N_E denotes number of energies. $\hat{P}_{\theta,E}$ are computed by

$$\hat{P}_{\theta,E} = \mathcal{P}_\theta \{ X_1(\mathbf{r}) * w_1(E) \}, \quad (4.4)$$

where \mathcal{P}_θ denotes a tomographic projection at rotation angle θ . Note that SART uses normally a back-projection, but here we use FBP because it showed faster convergence. This update is applied until convergence, which we defined as less than 0.1% improvement in the error criteria, which is defined as

$$\epsilon = \text{RMS} \left\{ \left(P_{\theta,E}(\mathbf{r}_{2D}) - \hat{P}_{\theta,E}(\mathbf{r}_{2D}) \right) * w_1(E) \right\}, \quad (4.5)$$

where RMS denotes root mean square calculation. Notice that by reducing the error with respect to the high-resolution projections, the update step refines the resolution of

the initial low-resolution guess. Once convergence is reached for $X_1(\mathbf{r})$, we proceed with refinement of the next modes. First, we remove all contributions of the first component from the projections by

$$P'_{\theta,E}(\mathbf{r}_{2D}) = P_{\theta,E}(\mathbf{r}_{2D}) - \mathcal{P}_{\theta}\{X_1(\mathbf{r}) * w_1(E)\}. \quad (4.6)$$

Now, taking $\{P'_{\theta,E}(\mathbf{r}_{2D})\}$ as the new data, we down-sample again and compute a low-resolution spectral tomogram from them. The whole procedure above is then repeated to get $w_2(E)$ and $X_2(\mathbf{r})$. Due to orthogonality of coefficients in PCA decomposition, the reconstruction of the latter does not interfere with previous modes. We then repeat the procedure until the fourth component tomogram $X_4(\mathbf{r})$ is reconstructed, which was in these cases the last component to show signal above the noise. Note that the total number of acquired projections for the pristine catalyst is 4677, which is approximately 8 times those required for a single tomogram sampled following the Crowther criteria, and similar for the used catalyst. From an information-content view our measurement justifies recovery of four components.

After this process, we obtain a set of spectral modes and the corresponding component tomograms at the finest resolution. Finally, the hyperspectral tomograms can be calculated using Eq. (4.1). This reconstruction approach leverages sparsity on the data ab initio by only allowing a finite number of orthogonal spectral modes in the reconstruction, following the logic that only a finite number of chemical variations of the resonant element(s) are in occurrence. This is unlike methods that use spatial regularization or total variation, *i.e.* our approach relies neither on favoring smooth nor spatially sparse or piece-wise continuous solutions.

To note, when inspecting reconstructions we observed that the second spectral mode was picking up small and reversible sample motions / deformations that correlated with the degree of X-ray absorption by the probed chemical element. While this observation is interesting in its own right and the topic of a future manuscript, for purposes of chemical analysis we here discarded the use of that mode.

Extraction of Chemical Information from the XTNES-tomogram: Following the determination of pore volume and catalyst-associated volume by means of threshold segmentation, several spectral features were calculated for each catalyst-associated voxel, see Figure 4.2A. To allow the calculation of these features, which are at times extracted from relatively small changes in the spectrum and as such susceptible to noise, we first applied a $2 \times 2 \times 2$ binning to the reconstruction to a voxel size of 53 nm. Voxel-level phase spectrums were next converted to absorption spectra using a Kramers-Kronig transformation (KKT) [160]. See the ‘‘Kramers-Kronig transformation (KKT)’’ section in the Supplementary Materials for details. The resulting voxel-level X-ray absorption near-edge spectra were then corrected by removing the native energy dependence of the attenuation coefficient through linear regression of the pre- and post-edge region, *i.e.* 5.443-5.465 keV and 5.495-5.540 keV, respectively [75]. This correction is needed to obtain quantitative vanadium concentrations and pre-edge intensities as well as to

determine the V K -edge position following the method of Koningsberger and Prins [66]. The vanadium concentration values were refined using corresponding features in the phase signal. Voxels possessing a vanadium concentration of less than $10^{-3} \text{ n}_V \text{ \AA}^{-3}$ were removed from further analysis. Vanadium K -edge positions, *i.e.* resonant-edge energies, were determined using the method of Koningsberger [66] and then converted to vanadium oxidation state. This conversion was achieved through linear interpolation using the known edge energies of $\text{V}(\text{PO}_3)_3$ and $(\text{VO})\text{PO}_4$ as lower and upper bound. $\text{V}(\text{PO}_3)_3$ and $(\text{VO})\text{PO}_4$ were selected as reference components due to their known Vanadium oxidation state V^{3+} and V^{5+} and because they are known possible components present within VPO catalysts, see Table 4.1. This conversion from edge energy to oxidation state resulted in a couple of voxels with an apparent oxidation state of greater than V^{5+} as can be seen in the corresponding histograms, Figure 4.10. These unrealistic values are a result of reference point selection and edge position measurement uncertainty in selected voxels, *i.e.* those where spectrum normalization was difficult or failed. The general reliability of the applied phase-to-absorption KKT was validated by comparing the resulting XANES spectrum with the XANES spectrum extracted from the absorption component of ptychography images and with a XANES spectrum of the same VPO catalyst acquired using a dedicated x-ray absorption spectromicroscopy setup (Fig. 4.13).

XTNES error estimation: The single-voxel electron density and vanadium concentration uncertainties, at 52-nm voxel size, were estimated on the basis of their standard deviations (SDs) (σ). Measurement uncertainty of electron density was calculated on a region of air surrounding the imaged catalyst pillars and found to be $0.007 \text{ n}_e \text{ \AA}^{-3}$ for the pristine sample and $0.006 \text{ n}_e \text{ \AA}^{-3}$ for the used catalyst sample. The measurement uncertainty of the vanadium concentration was calculated similarly and found to be $0.0042 \text{ n}_V \text{ \AA}^{-3}$ for the pristine catalyst and $0.0034 \text{ n}_V \text{ \AA}^{-3}$ for the used catalyst. Oxidation state and pre-peak intensity are undefined in the air region, so a similar approach cannot be used. To estimate those errors, we selected an isolated micrometer-sized grain from the used sample, which shows a single chemical composition, $(\text{VO})_2\text{P}_2\text{O}_7$, and calculated the SD of edge center energy and pre-peak intensity in that grain. This way, we determined the measurement uncertainty of edge center energy to be 1.1 eV, or 0.22 eV in oxidation state. The uncertainty of pre-peak intensity was found to be 0.02 ($1/\text{n}_e \text{ \AA}^{-3}$). These uncertainty values are used as estimate for both samples because of the highly heterogeneous structure of the pristine catalyst.

When calculating the mean value of a region of interest, such as the surface distance maps shown in Fig. 4.3C, the error is calculated using the standard error of the mean (SEM), which equals the SD of the voxels included in the SD calculation divided by square root of the number of voxels. The error values were too small to be visible as error bars in Fig. 4.3C.

4.6 Acknowledgements

Ptychographic XTNES tomography experiments were performed at the coherent small-angle X-ray scattering (cSAXS) beamline; XRD/XRF and XANES experiments were performed at the micro X-ray absorption spectroscopy (MicroXAS) beamline, both located at the Swiss Light Source of the Paul Scherrer Institut in Villigen, Switzerland. Ptychographic tomography instrumentation was supported by the Swiss National Science Foundation (SNF) (R'EQUIP, 145056, OMNY) and the Competence Centre for Materials Science and Technology (CCMX) of the ETH-Board, Switzerland. Clariant AG is acknowledged for the provision of samples and material characterization expertise. Electron microscopy work was performed at the Scientific Center for Optical and Electron Microscopy (ScopeM) ETH Zürich. We thank X. Donath and M. Birri for technical support at the cSAXS and MicroXAS beamlines, respectively. We also thank E. A. Mueller Gubler for assistance with sample preparation and G. Sun for help with monitoring the scan and acknowledge the use of computational resources provided by the Swiss National Supercomputing Centre (CSCS).

Funding: The work of Z.G. and J.I. was supported by funding from the SNF, project numbers 200021_178788 and PZ00P2_179886, respectively.

Author contributions: M.G.-S. and J.I. conceived the study. Z.G., M.H., J.I., M.O., and M.G.-S. performed XTNES experiments. Z.G. developed the reconstruction algorithm and applied it to XTNES datasets. Z.G., M.G.-S., and J.I. analyzed XTNES datasets. Z.G., J.I., and D.F.S. performed μ XRF and μ XRD experiments. J.I. and D.F.S. analyzed the μ XRF and μ XRD data. F.K. and J.I. acquired and analyzed electron microscopy data. D.P. and J.I. performed structure refinements. S.B. and G.M. provided samples, performed bulk characterization experiments, and contributed to writing of the manuscript. J.A.v.B., M.O., A.M., and M.S. contributed to discussions. J.I., Z.G., and M.G.-S. wrote the manuscript. All authors read and approved the manuscript.

Competing interests: The authors declare that they have no competing interests.

Data and materials availability: All data needed to evaluate the conclusions in the paper are present in the paper and/or the Supplementary Materials. Additional data that support the findings of this study are available under DOI ([10.5281/zenodo.4505125](https://doi.org/10.5281/zenodo.4505125)). VPO catalyst samples, equivalent to the ones examined in this study, can be provided by Clariant AG pending scientific review and after an agreement is reached between the interested party and Clariant AG. Requests for such materials should be submitted to G.M. (Gerhard.Mestl@clariant.com).

4.7 Supplementary Materials

4.7.1 Extended Materials and Methods

Spatial Resolution of XTNES Tomograms: The spatial resolution of the sparse-XTNES tomograms was estimated using Fourier shell correlation (FSC) [124]. To do so we divided the full hyperspectral dataset in half and two independent spectro-tomograms were reconstructed. To estimate the spatial resolution of the entire hyperspectral tomogram we then calculated the correlation between these two tomograms in Fourier domain and estimated the resolution based on the intersection with a half-bit threshold. For both samples, we estimate a half-period spatial resolution of ~ 26 nm, Figure 4.7a, for the 4D hyperspectral tomogram. The full-period resolution is accordingly twice this value.

However, one must consider that the chemical information resides in changes of the spectra. These changes consequently have different signal-to-noise ratio than the whole signal, and therefore also different resolution. To estimate the spatial resolution of such changes in spectra we take from the two independently reconstructed hyperspectral tomograms, the coefficients $X_k(\mathbf{r})$, $k = 1, 2, 3, 4$ as defined in Eq. (4.1) in the main text and calculate the 3D FSC for each one of them. The half-period resolution results are shown in Figure 4.7b and 4.7c for the pristine and used catalyst, respectively, which provide upper and lower bounds for the spatial resolution of the different spectral modes. It should be noted that this does not directly correspond to the resolution of the different components (i)-(iv).

Kramers-Kronig transformation (KKT): KKT of voxel-level phase spectra were calculated based on a piecewise Laurent polynomial method, as described in Watts (2014) [159]. Phase spectra, which were obtained from tomography reconstructions, were linearly interpolated between energies in the measured range, and extrapolated to the energy range from 0 to 500 keV using values at both edges of the spectra. Then for each energy point within the measured range, an absorption value of the transformed spectrum is calculated using analytical formulas derived from integration of the input phase spectrum over the whole energy range, these formulas are given in Eq. (10) and Table 1 in Watts (2014) [159].

Dose Estimation: The X-ray dose imparted to the specimens in a XTNES tomogram was estimated to be on the order of $\sim 10^8$ Gy. The estimated dose is based on the average area flux density of each ptychographic scan and the mass density of the specimen [125]. For this calculation the sample was assumed to consist entirely of vanadyl pyrophosphate.

Tomogram Analysis: Analysis, segmentation, and 3D rendering was carried out either using in-house developed Matlab routines or using Avizo. Prior to the analysis of the pristine XTNES tomogram we masked out the outermost 200 nm of the imaged cylinder, Figure 4.14. The masked region contained sample preparation artefacts in the form of FIB-milling implanted gallium and redeposited material.

Porosity Analysis: The catalyst pore-network was isolated by means of threshold

segmentation of the structural / electron density tomogram, followed by morphological operations to refine the segmentation. Pore size distributions (PSD), Figure 4.11, were calculated based on 3D thickness maps [172]. In consideration of the spatial-resolution estimates, apparent pores with a diameter smaller than 52 nm were excluded from size distributions. The connected pore volume was calculated based on neighborhood-based component labelling.

Interfacial Changes To map the average change in density and chemical composition from the pore space across the interface into the bulk catalyst interior we calculated a series of 3D Euclidian maps up to 250 nm into the catalyst with an average step size of 25 nm. Maps were calculated using the binary mask defined in the pore analysis step.

Component Identification: Component identification was carried out via multivariate comparison. Compared were the voxel-level measured electron density, vanadium concentration and oxidation-state values with those of a table of reference components or materials. Material identification possibilities were as such limited to the considered components, provided in Table 4.1 are electron density, vanadium concentration and oxidation state values of potential materials previously reported to be found within or as part of VPO catalysts [145, 147, 153, 154]. Identification was based on the closest match between experimental and tabulated values. Provided in Figure 4.10 are 1D and 2D correlation histograms of the measured / extracted values of the two catalyst samples. Added to these plots are markers of the identified components. In the presented case we largely refrained from a partial volume effect based analysis, *i.e.* the occupation of a single voxel by two or multiple materials, leading to voxel-level average electron density, vanadium concentration values and oxidation state weighted in accordance to the volumetric fractional occupancy of a voxel by the present materials. A combination of materials was only considered to account for the detection of V^{3+} in the pristine sample, explainable by a partial occupancy of $V(PO_3)_3$ and amorphous or nanocrystalline $(VO)_2P_2O_7$ (50/50). See also Figure 4.10.

General Material Characterization Methods

Catalyst Composition: The population average chemical composition of the industrial VPO catalysts was determined by inductively coupled plasma atomic emission spectrometry (ICP-AES). The catalyst was dissolved in aqueous H_2SO_4 prior to the measurement.

Bulk Vanadium Oxidation State: Following dissolution in aqueous H_2SO_4 , the catalyst's average oxidation state was determined using redox titration. $KMnO_4$ and $FeSO_4$ were used as titration reagents to determine the amounts of V^{4+} and V^{5+} in the respective catalyst samples. The reported vanadium oxidation state in Table 4.2 represents the concentration average of both species.

Catalytic Properties and Performance: The performance of industrial VPO catalyst samples was evaluated over the whole catalyst lifetime using a 3-channel IR sensor (butane, CO, CO_2) after scrubbing all organic acids (maleic anhydride, acetic acid, acrylic

acid) and drying of the reaction gas.

Porosity: Average pore size and total porosity of the pristine and used VPO catalyst, were determined on a bulk level by nitrogen physisorption and Mercury intrusion porosimetry. Prior to each measurement, the sample was degassed for 10 h. The pore diameters were calculated using the Washburn equation with a contact angle of 140° . The bulk- average results are given in Table 4.2.

Scanning X-ray Fluorescence and X-ray Diffraction Tomography: Scanning microbeam diffraction (μ XRD) and microbeam fluorescence (μ XRF) tomography experiments of the pristine VPO catalyst examined in the main text were carried out at the microXAS beamline of the Swiss Light Source (SLS), Paul Scherrer Institut (PSI), Switzerland. For μ XRD & μ XRF experiments an 11.3 keV incident beam was focused with a Kirkpatrick–Baez (KB) mirror system to a size of $\sim 1 \times 1$ ($H \times V$) μm^2 . For microbeam X-ray fluorescence, XRF spectra were collected using two Si drift diode detectors (KETEK), which were placed at opposite sides of the sample perpendicular to the direction of X-ray propagation. Using two detectors on opposite sides of the sample helps alleviate self-absorption effects on the tomography reconstruction. Diffraction patterns collected from LaB_6 powder were used to calibrate the sample-to-detector distance. The detector, an Eiger 4M, was positioned about 8.3 cm from the sample. After aligning the tomography pin with the sample stage’s center of rotation, we simultaneously recorded XRD patterns and XRF signals.

Several tomographic slices across the sample height of the pristine catalyst, with a vertical step size of 1 μm , were reconstructed from a series of horizontal line scans, during which the sample was scanned through the X-ray beam with a step size of 0.5 μm . 61 angular projections were acquired per tomographic slice. In case of the acquired XRF, spectra was integrated in the energy range of the V K - α signal in order to obtain a single sinogram per axial slice. A simultaneous iterative reconstruction technique (SIRT) [57] algorithm was then applied to obtain the tomographically reconstructed volume. The diffraction tomograms were obtained similarly, for those the measured diffraction patterns at each scanning point were first azimuthally integrated using the Bubble interface of PyFAI [173]. The one-dimensional diffraction patterns were next analyzed as a function of position and rotation to construct one sinogram per 2θ value, generating a total of about ~ 4000 sinograms covering a total range of 1.5 – 56° in 2θ with a step size of $\sim 0.01^\circ$. Smaller 2θ angles, and the transmitted intensity, were recorded by a SiC diode, which was integrated to the 2 mm diameter beamstop. Following tomographic reconstruction, this procedure allowed the acquisition of the full powder-XRD pattern per voxel of the tomographically reconstructed volume [174]. Voxel-level diffraction patterns were fitted using XRDU for phase identification [175]. We refrained from any voxel-level refinement operations due to insufficient data quality. Please see Figure 4.12, for visualizations of both the μ XRF and μ XRD tomograms.

Micro X-ray Absorption Near-Edge Spectroscopy (μ -XANES): μ -XANES measurements of the pristine VPO catalyst pillar were similarly acquired at the MicroXAS beamline of the SLS, PSI. A beam focused with a Kirkpatrick–Baez (KB) mirror system

to a size of $\sim 0.7 \times 0.7$ ($H \times V$) μm^2 was used. A photon energy range of 5400-5600 eV or across the V K -edge was used for the XANES measurements. Data were acquired in 0.3 eV steps using the aforementioned beamstop-integrated SiC diode placed behind the sample. For each incident photon energy we collected one line scan across the pillar width, for which the sample was scanned in lateral direction in steps of 0.5 μm . The acquired spectra were next averaged and the resulting V K -edge XANES were processed using Athena [161]. Resonant-edge energy determination followed IFEFFIT's algorithm, used to find the first peak of the first derivative of $\mu(E)$ [161]. Please see Figure 4.13 for the obtained spectra.

4.7.2 Selective Oxidation of n -butane to Maleic Anhydride (MA), its Industrial Realization and Relevance

The selective oxidation of n -butane to maleic anhydride ($\text{C}_4\text{H}_2\text{O}_3$) and its chemical derivatives maleic acid and fumaric acid over vanadium phosphorus oxides (VPO) was industrially first realized by Monsanto in 1974. These chemical intermediates find use in nearly all areas of chemistry, most prominently in the production of unsaturated polyester resins, *i.e.* the production of household and industrial plastics. Given the continuing demand in the former, the annual production of maleic anhydride is continuously increasing, exceeding 2 million tons by 2020 [142, 143]. This important catalytic conversion process operates under kinetic control. The exothermic conversion of n -butane to maleic anhydride over vanadium phosphorus oxides in presence of oxygen possesses two main reaction by-products in the form of carbon monoxide and carbon dioxide. Both of which are thermodynamically more favorable, Figure 4.4. This leads to strict requirements on the catalyst concerning thermal and chemical stability and the reactor with regards to heat transfer capacities to provide a constant reaction environment, *e.g.* temperature and feed composition. The current generation of heterogeneous catalysts and reactors exhibit maleic anhydride yields of $\sim 60\%$ [145].

Industrial conversion is frequently carried out in fixed-bed reactors, operating at roughly 400°C . These reactors consist of a series of actively cooled reactor tubes ($>10,000$ tubes; with an inner diameter of ~ 20 mm), filled with porous VPO catalyst bodies or pellets. Pressurized, preheated mixtures of air, n -butane (< 2 vol.%), and water (< 3 vol.%) are continuously fed through the reactor tubes from the bottom. Reaction products are syphoned off from the top and further cycled for refinement purposes in selected cases [145]. Due to known catalyst deactivation mechanisms, commonly registered in the form of decreasing yield and selectivity as well as a decreasing phosphorus to vanadium ratio in the catalyst bodies, additionally added to the feed-stream is a trialkyl phosphate ester at concentrations up to 10 ppmv. The industrial VPO catalysts utilized in these fixed-bed reactors are generally of the porous bulk type, *i.e.* predominantly composed of vanadium phosphate phases such as vanadyl pyrophosphate and prepared from precursors such as vanadyl hydrogenphosphate hydrates ($\text{VO}(\text{HPO}_4)(\text{H}_2\text{O})_n$) by thermal pre-treatment at $\sim 500^\circ\text{C}$ in an inert atmosphere. While catalysts based on vanadyl

pyrophosphate possess a nominal ratio of phosphate to vanadium of 1, catalysts are generally prepared with an over-stoichiometric amount of phosphate by means of phosphate dosing during synthesis, as catalytic peak performance is observable at bulk P/V ratios of roughly 1.1. The additional phosphate is, among other opinions, believed to be present in form of vanadium-rich amorphous metaphosphate. The latter is poorly bound to crystalline vanadyl pyrophosphate stabilizing exposed V^{4+} [142]. Notably, pristine catalysts may contain up to 30% of amorphous material which may explain the frequent observation of higher-than-expected sample-averaged vanadium oxidation state, *i.e.* vanadyl (VO_2) groups in the catalyst may exist as V^{5+} defects [142,145–148].

4.7.3 Suggested Active Sites in VPO Catalysts

Modeling studies have suggested that the P=O bond is the active site for initiating the VPO chemistry, by extracting the H from the *n*-butane C–H bond. [152] The ability of P=O to cleave alkane C–H bonds arises from a mechanism that decouples the proton transfer and electron transfer components of this H atom transfer reaction. The study’s authors demonstrated that placement of a highly reducible V^{5+} next to the P=O enhances the activity of the P=O bond to extract the proton from an alkane, while simultaneously transferring the electron to the V to form V^{4+} . As such, introducing a VO vacancy thus makes the P=O bonds have more uncompensated negative charge, and, therefore, have higher affinity to the H in butane. It is fair to assume, then, that the defected structure shown in the main text will show high activity in the conversion process of *n*-butane to maleic anhydride.

4.7.4 Ptychographic Computed X-ray Tomography and Sensitivity to Variations in Incident Energy

Ptychographic X-ray computed tomography (PXCT) [141] is a combination X-ray ptychography and computed tomography. Ptychography is a lensless imaging technique in which the phase problem is solved by means of iterative phase retrieval algorithms [32]. During a ptychographic scan, or the acquisition of a tomographic projection, the sample is scanned at positions where the incident illumination overlaps. At each scanning point a far-field diffraction pattern measured. By reconstructing these diffraction patterns together and leveraging the illumination overlap the solution of the phase problem becomes well constrained. By applying ptychography at different projection angles, *i.e.* sample orientations, PXCT is able to retrieve the complex-valued refractive index distribution, n , of the imaged sample. This provides tomograms of both phase and amplitude contrast whose spatial resolution is not limited anymore by the imaging optics but the angular extent to which the specimen-scattered intensity can be detected [141]. Solution of the phase problem in conjunction with the removal of resolution-limiting optics allows PXCT to provide us with quantitative phase and absorption tomograms of high spatial-resolution and signal to noise ratio when compared to other state of the art X-ray

microscopy techniques.

PXCT measurements are commonly conducted far from any sample-relevant absorption edges, *i.e.* resonant energies, to allow the conversion of the phase tomogram, *i.e.* the real part of the refractive index decrement, δ , to electron density, n_e , as well as the conversion of the amplitude tomogram, *i.e.* the imaginary part β of the refractive index to absorbance, μ [168]. However, it is worth to remember that δ and β can be expressed as the real and imaginary parts of the atomic scattering factor, *i.e.* $f_0 = f_1 + if_2$ which are known to be energy dependent. As such it comes to no surprise that the refractive index distributions retrieved by PXCT are equally sensitive to changes in the respective scattering factor, Δf_E , at or near sample-relevant absorption edges, Figure 4.13 [168].

$$n = 1 - \delta + j\beta = 1 - \frac{r_e}{2\pi} \lambda^2 \sum_k n_{at}^k \left(f_1^k + if_2^k \right) \quad (4.7)$$

This energy dependence is commonly used in techniques such as X-ray absorption near-edge spectro- (XANES) tomography, [71, 136] in which a series of tomograms are measured across a selected absorption edge to localize and characterize the chemical nature of the edge-specific element in the specimen. Such applications using PXCT are still rare, despite the advantages PXCT offers as base tomography technique, *i.e.* dose efficiency, high spatial-resolution, easier access to the quantitative hyperspectral information. Despite these advantages PXCT is not used for transmission spectroscopy due to multiple interlinked factors, being predominantly: the extensive acquisition time of a single high-resolution PXCT dataset which can be more than 8 hours for a 15 μm diameter sample at 20 nm spatial resolution, the limited amount of available beamtime at PXCT-capable synchrotron beamlines, radiation damage, and physical stability of the experimental setup and the sample during tomogram acquisitions. Factors, which made these measurements previously practically impossible, henceforth forcing prior demonstrations examples to compromise either on the field of view, the energy range and/or the energy sampling [76, 168, 176], *i.e.* the total number of energies at which tomographic projections are collected across an absorption edge. The here shown introduction of sparse angular sampling reduces the acquisition time by an order of magnitude while retaining nm spatial resolution and sufficient spectral resolution, which establishes sparse X-ray transmission near-edge spectro (XTNES) tomography as a viable tool for quantitative chemical speciation on the nanoscale in 3D. The basis of this sparsity implementation in the context of X-ray spectro-tomography acquisition is rooted in the nature of spectral signal changes being inherently correlated. From a signal perspective, it is then clear that the information content in a hyperspectral volume does not require Crowther sampling for each energy if appropriate reconstruction methods are applied as in the presented case.

4.7.5 Local Structure Optimization

All ground-state total energy calculations in this work have been performed with the all-electron full-potential DFT code FHI-aims [177, 178]. Electronic exchange and correlation was treated with the PBE functional [179]. Geometry optimization was done with the “tier2” atom-centered basis set using “tight” settings for numerical integrations. Local structure optimization is done using the Broyden-Fletcher-Goldfarb-Shanno method relaxing all force components to smaller than 10^{-2} eV/Å. DFT calculations presented in the current manuscript relied on the automatic optimization of the spin states as implemented in the FHI-aims package. All structures presented correspond to the singlet spin state.

In the case of the “ideal” vanadyl pyrophosphate crystal, the experimental unit cell parameters ($a = 7.738$ Å, $b = 9.587$ Å, $c = 16.589$ Å) were used. In the case of the defected structure, with one $[(VO)_2]$ element missing, the full reoptimization of the unit cell parameters has been conducted. The resulting unit cells parameters were: $a = 8.310$ Å, $b = 9.683$ Å, $c = 16.041$ Å.

We have a relatively large size of the unit cell, this is because the periodic model of the vanadyl pyrophosphate crystal has a stoichiometry of $[(VO)_2]_8[P_2O_7]_8$, comprising 104 atoms, and the fact that all electrons are accounted for explicitly, 1184 electrons in total in the case of an “ideal” crystal. Therefore Brillouin zone integration was performed with a reciprocal space mesh consisting of only the gamma point. The size and the location of the $[(VO)_2]$ vacancy was chosen based on the experimental data on vanadium to phosphorus ratio, vanadium concentration, vanadium oxidation state, and the total electron density in the unit cell.

4.7.6 Supplementary Movies

Supplementary Movies 4.1 and 4.2: Volume Rendering of and Orthoslices Through XTNES Tomograms. Shown are volume rendering and cut slice animations of the hue-saturation-value renderings presented in Figure 4.2 of the main text.

Supplementary movies can be downloaded from <https://doi.org/10.1126/sciadv.abf6971>.

4. Sparse X-ray Transmission Spectrotomography for Nanoscopic Compositional Analysis

Compound	Electron Density $n_e \text{ \AA}^{-3}$	[V] $n_v \text{ \AA}^{-3}$	V K-Edge eV	Pre-Edge* r.I.	[P]/[V] /	Oxidation State	Geometry [†]
V_{metal}	1.58	0.068	5465			0	
Bi_{metal}	2.35						
Bi_2O_5	1.71						
$BiPO_4$	1.63						
H_3PO_4	0.58						
$V_2O_3(29)$	1.37	0.039	5475.7	Very Weak	-	3	O
VO_2	1.29	0.033	5478.1	Moderate	-	4	O
$V_2O_5(29)$	0.96	0.022	5480.9	Strong	-	5	P
$(VO)_2P_2O_7$ crystalline(26)	0.96	0.013	5478.7		1	4	O
$(VO)_2P_2O_7$ V5+ defect-rich(26)	~0.88	~0.012	~5478.7		1	4 & 5	
$(VO)_2P_2O_7$ amorphous(26)	~0.66	~0.009	~5478.7		1	4 & 5	
$V(PO_3)_3$	0.83	0.007	5474.4	Very Weak	3	3	O
$VO(PO_3)_2$ - α (75)	0.89	0.016	5475.6	Very Weak	2	4	O _d
$VO(PO_3)_2$ - β (76)	0.85	0.015	5475.9	Very Weak	2	4	O _d
$V_2O(PO_4)$	1.09	0.021	5476.1	Weak	1	4	O
$VO(HPO_4) \cdot 4H_2O$	0.68	0.0057			1	4	O _d
$VO(HPO_4) \cdot 2H_2O$ - α	0.75	0.007			1	4	O _d
$VO(HPO_4) \cdot 2H_2O$ - β	0.69	0.007	5476.9	Moderate	1	4	O _d
$VO(HPO_4) \cdot 0.5H_2O$ (77)	0.89	0.009			1	4	O _d
$VO(HPO_4)$ (78)	0.90	0.001			1	4	O _d
$(VO)PO_4 \cdot 2H_2O$ (79)	0.68	0.007	5482.8	Strong	1	5	O _d
$(VO)PO_4$ - α	0.96	0.012	5482.5	Strong	1	5	O _d
$(VO)PO_4$ - β	0.94	0.012	5482.5	Strong	1	5	O _d

Table 4.1. Structural and Chemical Makeup of Reference Compounds. The electron density and vanadium concentration of reference compounds were calculated using tabulated molecular weight and mass density values. Oxidation state and coordination geometry information were extracted from listed references in the first column [148] *Relative pre-peak intensities are compared to listed vanadium oxides of distinct oxidation states. †O-octahedral, T-tetrahedral, P-square pyramidal, d-distorted.

Sample	Pristine	Used
Bulk Analysis		
Composition		
Bismuth Bi [wt.%]	2.0	1.30
P/V	1.075	1.038
Total Surface Area [m ² g ⁻¹]	~20	~6
Total Porosity [%]	43	52
Average Pore Diameter [nm]	33	187
Mean Vanadium Oxidation State	4.08	4.02
Ptychographic X-ray Transmission Near-Edge Spectro Tomography[#]		
Total Porosity [%]	~40	~57
Average Pore Diameter [nm]	~85	~185
Mean Vanadium Oxidation State	4.086	4.036

Table 4.2. Properties and Composition of Pristine and Used Industrial VPO Catalysts.

Bulk Analysis: Data were provided by Clariant AG.

Ptychographic X-ray Transmission Near-Edge Spectro Tomography: [#] Provided estimates are subject to finite image resolution and image-segmentation limitations. The resolution of the sparse XTNES tomograms allows for imaging > 80% and > 90% of the total catalyst pore volume for the used and pristine samples, respectively. For average pore diameter calculations, a pore diameter of 52 nm was the considered lower limit.

4.7.7 Supplementary Figures

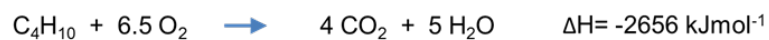
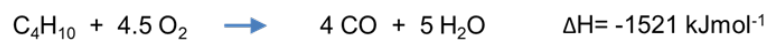
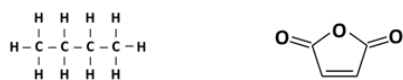
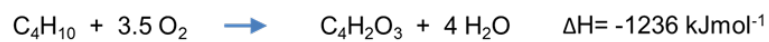


Figure 4.4. Oxidation of *n*-butane to Maleic Anhydride and The Thermodynamically More Favorable By-Products. [145] Figure reproduced from [129] / CC BY.

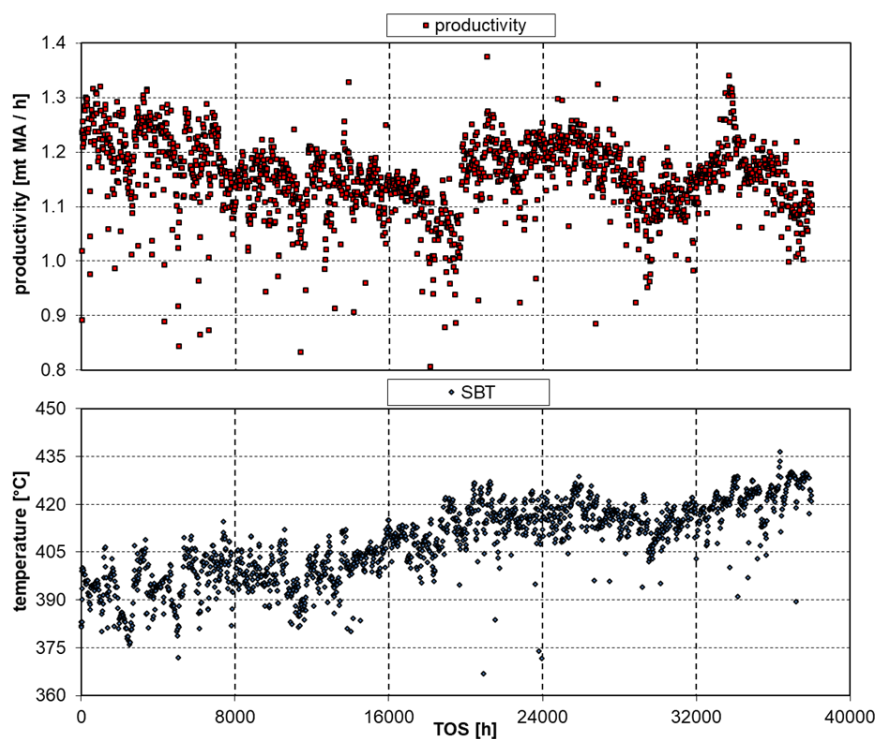


Figure 4.5. VPO Catalyst Performance over Catalyst Lifetime in an Industrial Fixed-Bed Reactor. Shown in (a) are industrial catalyst productivity data in metric tons of MA per hour (red squares), of the studied catalyst in the main text. Provided in (b) is the reactor's salt bath temperature (SBT -blue rhombs) or temperature over the catalyst lifetime or time on steam (TOS). Using XTNES tomography we examined a VPO catalyst at the first and last time point. Figure reproduced from [129] / CC BY.

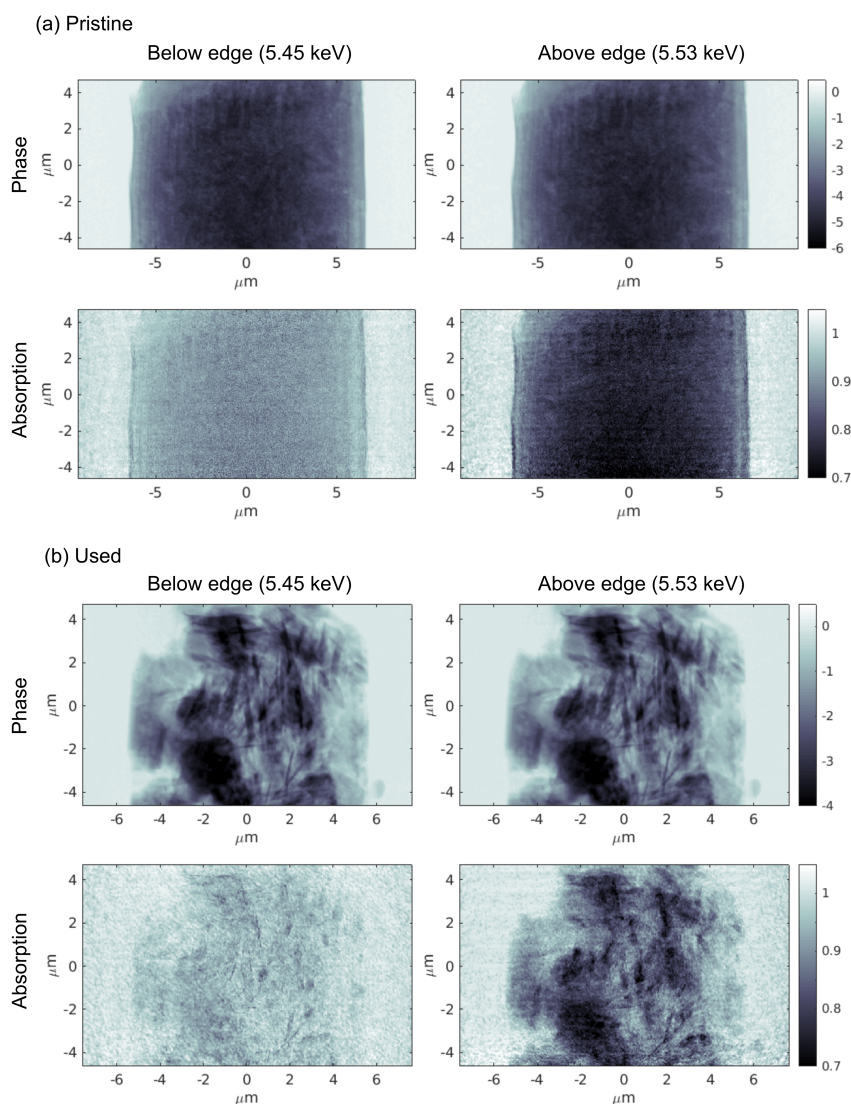


Figure 4.6. Example of Reconstructed High-Resolution Ptychography Images Utilized in the Tomographic Reconstruction Process. Shown are typical reconstructed ptychography images (tomographic projections) acquired for both samples. (a) Images of the pristine catalyst sample and (b) the used catalyst sample are acquired below the V K -edge at 5.45 keV and above the edge at 5.53 keV. Shown are both the phase (top rows) and amplitude component (bottom rows). All complex-valued tomographic projections used in this study can be downloaded from DOI [10.5281/zenodo.4505125]. Figure reproduced from [129] / CC BY.

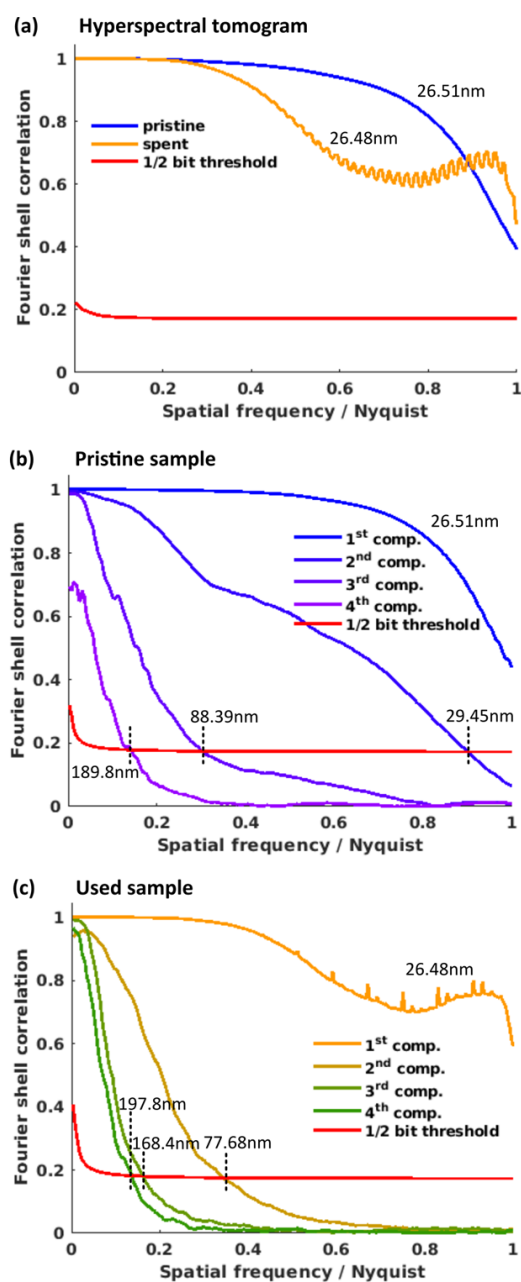


Figure 4.7. Fourier Shell Correlation (FSC) of XTNES Tomograms. Provided are FSC curves of the 4D hyperspectral tomograms, according to Eq. (4.1) in the main text, for the pristine and used catalyst. (a) FSC curves for the entire hyperspectral tomograms alongside resolution estimates. Both the pristine and the used catalyst tomogram reached a voxel-size-limited half-pitch spatial resolution. The tomogram voxel sizes are 26.51 nm for the pristine and 26.48 nm for the used catalyst. FSC curves of the first 4 component tomograms, $X_k(\mathbf{r})$, and the corresponding half-period resolution estimates are shown in (b) for the pristine and (c) for the used catalyst sample. Figure reproduced from [129] / CC BY.

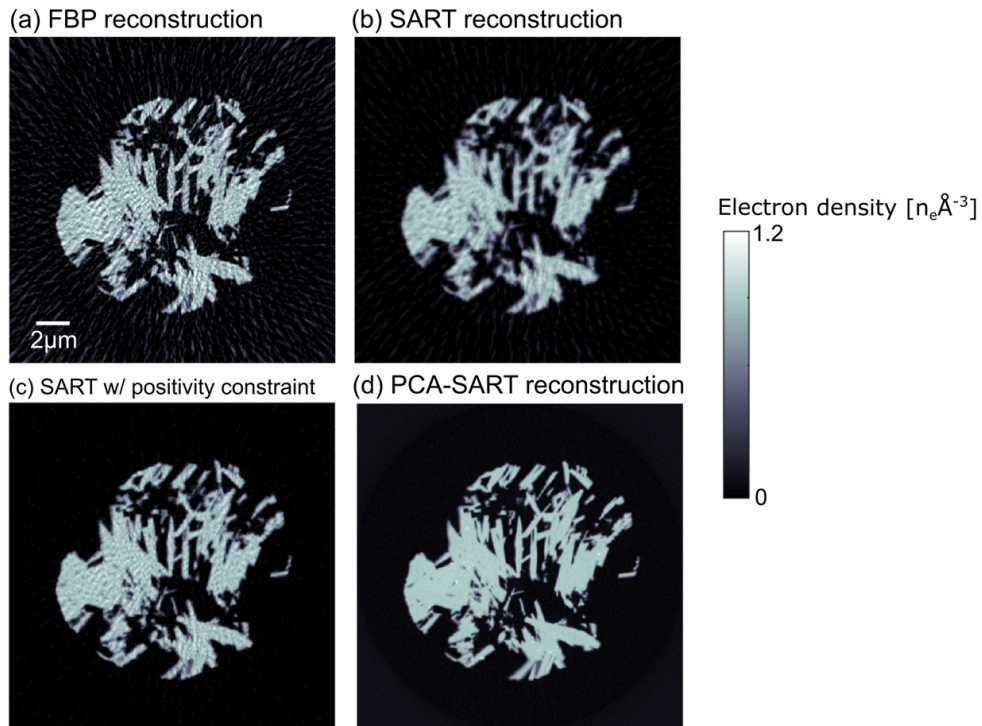


Figure 4.8. Comparison of Analytical and Iterative Tomogram Reconstruction Methods. Shown is a comparison of common analytical and iterative tomogram reconstruction methods and the here introduced method, which leverages the sparsity of information in a hyper-spectral tomogram. Specifically compared are axial orthoslices of electron density tomogram reconstructions of the used VPO catalyst, at 5.451 keV, using different reconstruction methods: (a) the conventional filtered back-projection (FBP) method was used as an example of analytical reconstruction methods, (b) iterative SART method without constraints and (c) SART method with positivity constraint. Tomogram reconstructions shown in (a) to (c) were obtained using all 68 equal angular sampled projections of identical illumination energy. Shown in (d) is the XTNES reconstruction of the electron density at the same energy utilizing the entire sparse spectral-tomogram dataset. Figure reproduced from [129] / CC BY.

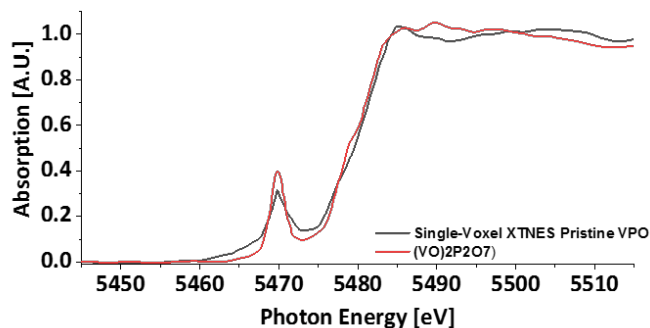


Figure 4.9. Comparison of a Voxel-level Vanadium *K*-edge Absorption Spectra Extracted from the Pristine VPO XTNES Tomogram with a Literature Reported Vanadium *K*-edge Absorption Spectra a VPO Catalyst Component. The voxel-level absorption spectra were obtained from the high-resolution phase spectra following a Kramers Kronig transformation. The voxel-level spectra is best described by a spectra of vanadyl pyrophosphate as reported in Ruitenbeck [145]. See Figure 4.2C(x) for the approximate location of the voxel in the XTNES tomogram. Figure reproduced from [129] / CC BY.

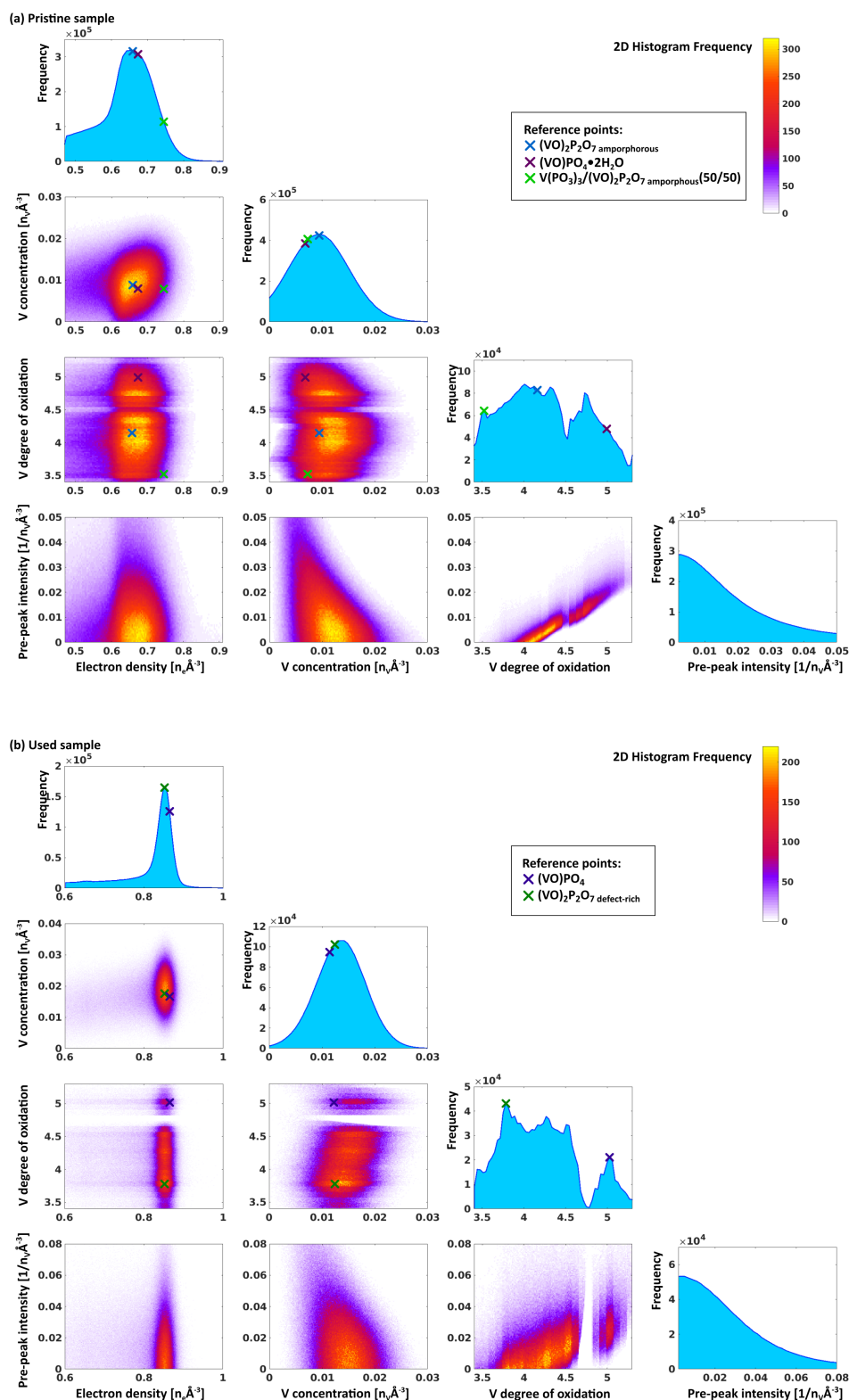


Figure 4.10. Histogram and Correlative Bivariate Histograms of Electron Density and Chemical Information Extracted from the XTNES Tomogram. (a) Pristine and (b) used catalyst. See Method section in Supplementary Materials for details on chemical speciation. Compositional reference values of identified catalyst components, such as $(\text{VO})\text{PO}_4$, $(\text{VO})\text{PO}_4 \cdot 2\text{H}_2\text{O}$, $\text{V}(\text{PO}_3)_3$, $(\text{VO})_2\text{P}_2\text{O}_7$ defect-rich, $(\text{VO})_2\text{P}_2\text{O}_7$ amorphous are marked in the histograms or listed explicitly in Table 4.2. Figure reproduced from [129] / CC BY.

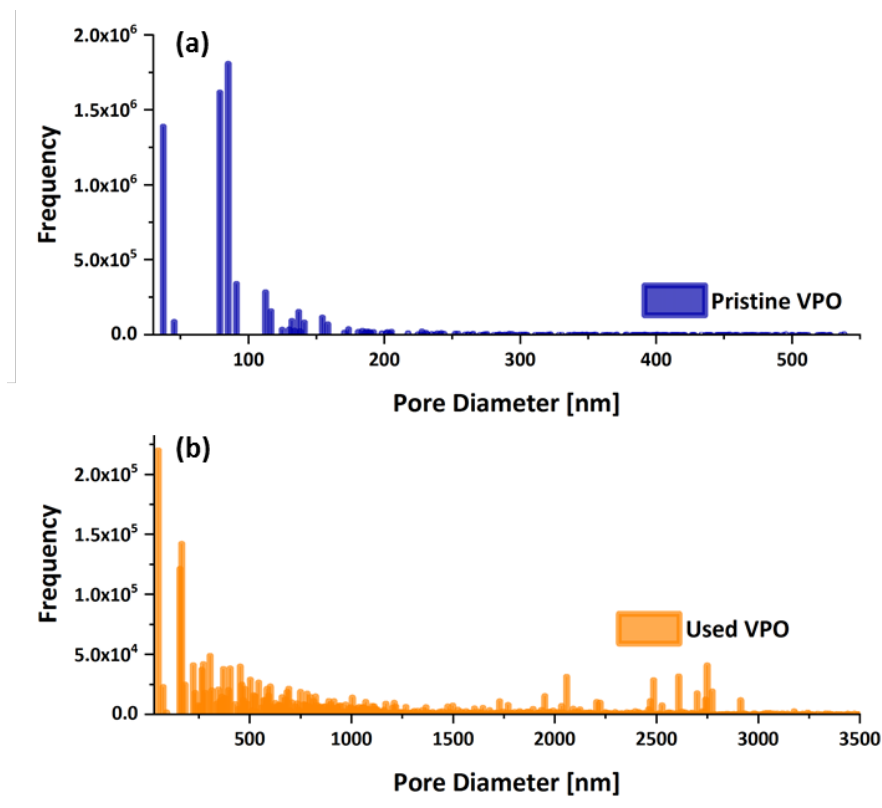


Figure 4.11. Pore Size Distributions and Pore Network Connectivity. Pore size distributions (PSD) of (a) the pristine and (b) the used VPO catalyst, extracted from the electron density tomogram by means of 3D thickness-map calculations. (c) Zoom of the 100-500 nm pore range for both samples. The zoom corresponds to the grey shaded area in (a) and (b). The smallest pores considered were 52 nm in diameter, which corresponds to two half-period resolution elements. For the case of the pristine catalyst the 5 biggest pore networks comprise roughly ~ 60 vol.% of the total pore volume. Figure reproduced from [129] / CC BY.

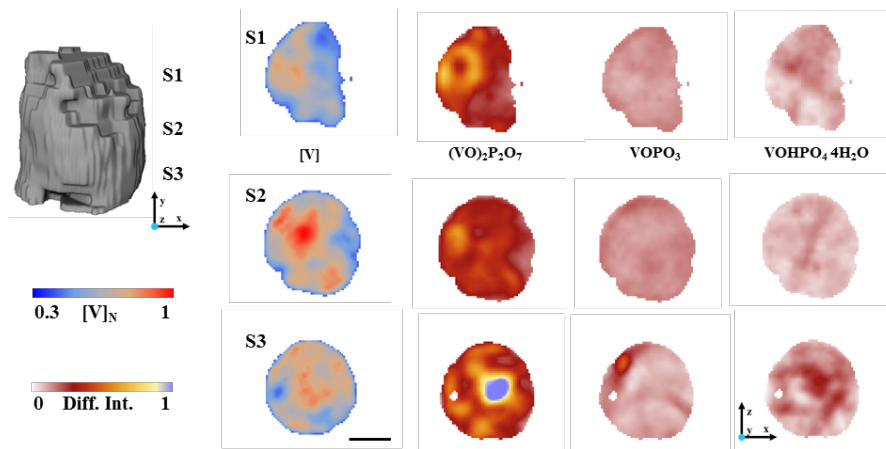


Figure 4.12. Micro X-ray Fluorescence and Diffraction Tomography of a Pristine Industrial VPO Catalyst. Shown is a volume rendering of the imaged pristine catalyst and axial orthoslices of both the acquired vanadium distribution obtained by means of XRF tomography and main crystalline catalyst components obtained through XRD tomography. Provided orthoslices, S1-S3, were taken at different heights across the catalyst to highlight variations in vanadium concentration and composition. Scale bar is 5 μm . Figure reproduced from [129] / CC BY.

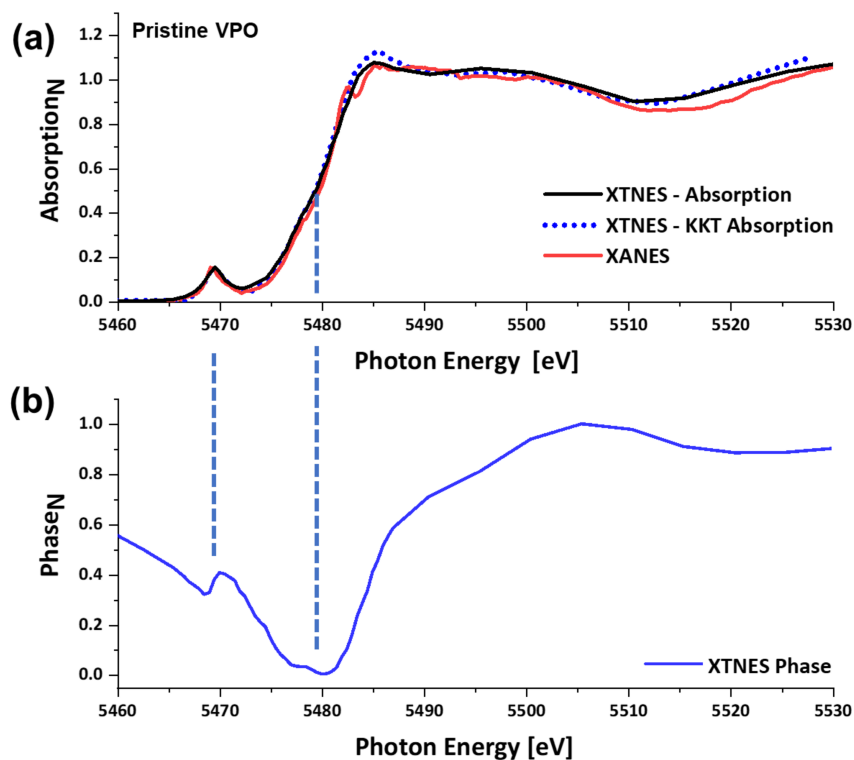


Figure 4.13. Sample-Averaged Normalized Vanadium *K*-edge Absorption and Phase Spectra of the Pristine VPO Sample. (a) Comparison between sample-averaged absorption spectrum from the ptychography XTNES absorption component (black); the absorption spectrum resulting from a Kramers-Kronig transformation of the XTNES phase component (blue, dashed); and XANES spectrum measured at the MicroXAS beamline of the SLS using a dedicated X-ray absorption spectro-microscopy setup (red). (b) Average phase spectrum from XTNES tomography. All spectra were normalized (N) to a post-edge value of 1 for comparison purposes. While minor differences across the absorption spectra are visible, absorption edge and pre-peak position as well as pre-peak intensity are well matched across the techniques and/or following a KKT of the phase spectra. Figure reproduced from [129] / CC BY.

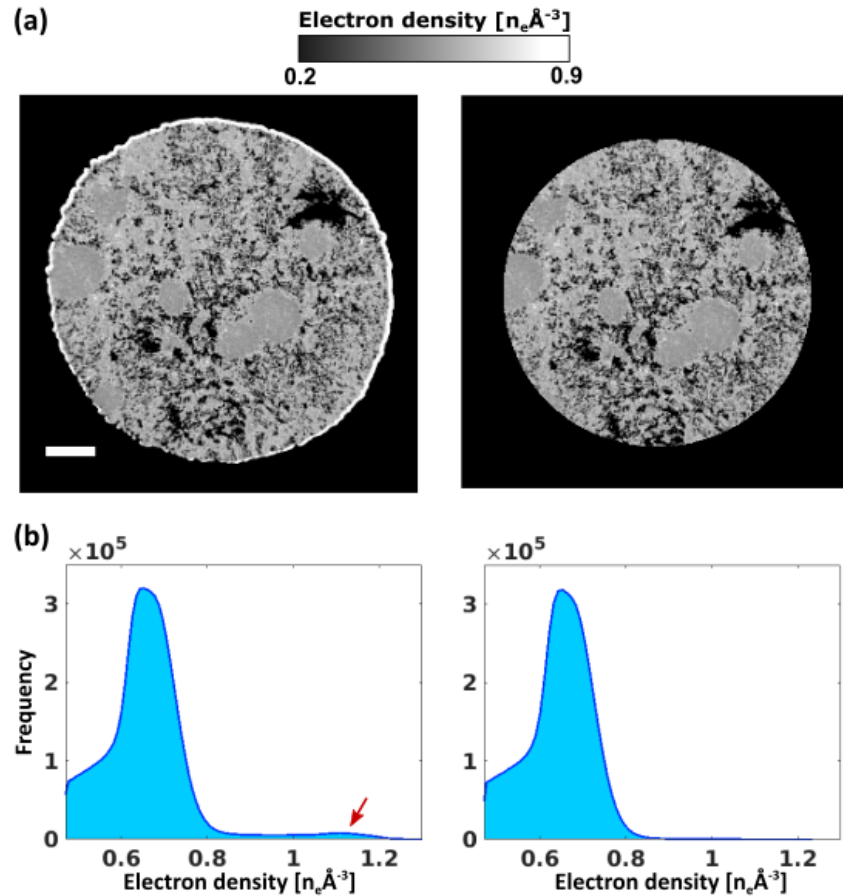


Figure 4.14. Cylindrical Mask Applied to the Pristine VPO XTNES Tomogram. (a) Axial slice of the electron density of the pristine VPO XTNES tomogram before (left) and after (right) masking. (b) Electron density histograms of the whole sample volume before and after masking. The red arrow highlights the higher electron density bump removed by masking out the outermost 200 nm. Figure reproduced from [129] / CC BY.

Dynamic Sparse X-ray Nanotomography Reveals Hydration Mechanism in PEFC Catalyst

The content of this chapter is covered in the manuscript: Z. Gao, C. Appel, M. Holler, K. Jeschonek, K. Brunnengraber, B. J. M. Etzold, M. Kronenberg, M. Stampanoni, J. Ihli and M. Guizar-Sicairos. “Dynamic sparse X-ray nanotomography reveals ionomer hydration mechanism in polymer electrolyte fuel-cell catalyst.” In preparation.

5.1 Abstract

Tomographic imaging of time-evolving samples is a challenging yet important task for various fields such as biomechanics, catalysis, and energy materials. In the nanoscale, current approaches face limitations of measurement speed or resolution due to lengthy acquisitions and sample movement or deformation during the measurement. Here we introduce and demonstrate a dynamic nanotomography measurement and reconstruction technique based on a combination of sparse synthesis and non-rigid tomography. We demonstrate an increase in temporal resolution of 40 times compared to conventional methods, while retaining high spatial resolution and possessing high stability against sample deformation. Using ptychographic X-ray computed tomography as imaging modality, we are able to resolve the controlled hydration process of a polymer electrolyte fuel cell (PEFC) catalyst sample with 28 nm half-period spatial resolution and a temporal resolution of 12 minutes. We demonstrate that our method provides quantitative density information about the water intake process of these catalysts, therewith paving the way for wider application of dynamic tomography at the nanoscale.

5.2 Introduction

Studying dynamic systems with computed tomography (CT) has been of great interest ever since the first introduction of the technique, as its penetrative and non-destructive properties provide a unique ability to image the interior of operando systems. Thus, the extension of computed tomography techniques for imaging of dynamic processes has been an important topic over the past few decades and has motivated the development of dynamic tomography techniques across a wide range of length- and timescales in various research fields such as biology, chemical industry or energy materials [9, 11, 62, 180, 181]. These techniques have been utilized in different imaging modalities for a diverse spectrum of applications, ranging from CT imaging of cardiac and respiratory motions [11, 13, 182], X-ray microtomography of wingbeats of insects [53], or electron nanotomography of molecular interactions [183].

The performance of dynamic tomography techniques is often defined by their achievable spatial and temporal resolution. While these specifications vary greatly in different length scales and scenarios, a common constraint experienced by almost all these techniques is the limitation on measurement speed. This includes limitations on both the highest achievable temporal resolution, and the total acquisition time required in case of periodic processes. For the fastest applications of X-ray microtomography, state-of-the-art methods can achieve a speed of 1000 Hz [9]. For nanotomography the imaging rates are considerably slower, with a time scale normally on the order of hours [184, 185].

This limitation is chiefly driven by the underlying assumptions of conventional tomography, which assumes the sample is static during acquisition. In order to measure a 3D volume at a desired resolution, a certain number of tomographic projections need to be taken at different relative orientation angles between the object and the incident illumination. The number of projections is determined by the Crowther sampling criteria and, for a fixed volume, it grows inversely proportional to the sought resolution [15]. When aiming for higher resolution, the increased number of projections increases concomitantly the acquisition time. Another limiting factor is the mechanical overhead needed to rotate the sample relative to the imaging device, which can become a bottleneck in high-speed applications [186].

Furthermore, for a given photon flux the total acquisition time for a 3D volume scales inversely proportional to the fourth power of the sought resolution [125], resulting in substantially longer acquisition times when aiming to resolve nanoscale features. So while nanoscale dynamics are of paramount importance for many applications, the acquisition times put strong limits on either the achievable temporal resolution, or the measurable sample volume for dynamic tomography.

To address these challenges, several 4D computed tomography methods have been proposed based on various methodological approaches. Some of these methods focus on improved hardware design and acquisition protocol to increase acquisition speed [9, 186]. Others try to reduce the required number of projections so that the same dynamic process can be imaged with less measurements, which are often referred to as sparse tomography

[14, 129, 187–189].

For sparse tomography the projections are reduced to only a subset of measurements compared to the Crowther criteria, namely with reduced angular sampling [14, 189]. Applying sparsity in the measurement largely enhances measurement speed, yet inevitably impairs imaging quality compared to the conventional approach due to angular under-sampling. However, these effects can often be mitigated with specially designed reconstruction methods, based on models for the properties of the sample and its dynamics. Existing techniques achieve such goal by utilizing different strategies such as using prior information about the sample [89] or numerical constraints in the modelling of dynamics [90].

We here propose a measurement approach and reconstruction algorithm designed specifically for the challenges of the nanoscale regime. Our method combines sparse sampling, non-rigid tomography, and an iterative reconstruction technique to reach the highest resolution. We demonstrate an increase of 40-fold in temporal resolution compared to conventional nanotomography, together with high stability against sample deformation. To note, for sparse-tomography to work it is necessary to iteratively reconstruct the time-dependent dataset with a 4D model. In this approach, we model sample deformations using the non-rigid computed tomography (NCT) method [190], which is then combined with a step-function-based sparse dynamic reconstruction method to fully retrieve the dynamic process.

As a first demonstration, we imaged the controlled hydration process of a hydrogen polymer electrolyte fuel cell (PEFC) catalyst sample. PEFCs hold great potential as environmentally friendly alternatives to combustion based engines for the transportation sector, since they use H_2 and O_2 to generate water and electric energy. Besides significant progress in research on the material, PEFCs are not yet used commercially on a regular basis [191]. Chemically modified and new designs for catalytic sites with improved activity are setting new standards for the catalyst’s performance potential, however, when these materials are tested under realistic conditions, *i.e.* in catalyst layers within fuel cell stacks, it becomes apparent that other factors limit the PEFC performance [192]. Insufficient water management is a particular example, where liquid water saturates the complex structure of the catalyst layer and hinders the transport of gaseous components, namely H_2 and O_2 , to the catalytically active sites. While characterization of water content in operating fuel cells is already accessible via neutron imaging [193] and full field X-ray tomography on the micrometer scale [194], quantitative measures at the nanoscale are still missing. Since the electrochemical reaction takes place on the nanoscale, it is crucial to obtain the catalyst layer’s structure on this length scale and as close as possible to realistic working conditions. Of particular interest at the nanoscale is the ionomer in the catalyst which is only able to fulfil its proton-conducting role after it absorbs water molecules. We here demonstrate an unprecedented combination of 28 nm half-period spatial resolution in 3D with a temporal resolution of 12 minutes, applied to investigate the humidity-induced changes in a catalyst layer sample with a 20 μm diameter and 10 μm height.

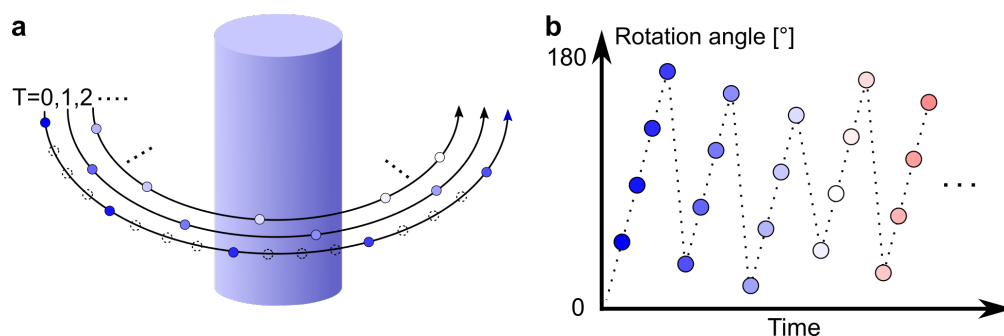


Figure 5.1. a) Measurement strategy of sparse dynamic tomography, each dot represents one projection measured at a given sample orientation. Dashed-line dots represent projections that would be needed by the Crowther criteria but that are skipped by sparse sampling. b) Schematic plot of rotation angles versus time. At the start of each sparse tomogram, *i.e.* time frame, an angular offset is added based on golden ratio.

5.3 Sparse Dynamic Nanotomography

The core concept of our sparse dynamic nanotomography method consists of two parts: measurement and reconstruction. The measurement technique, as illustrated in Fig. 5.1, includes a set of sparse sequential tomography measurements, *i.e.* time frames, covering the time lapse of the whole dynamic process. Similar to conventional tomography, for these tomography measurements, projections of the sample are measured at different sample orientation angles from 0 to 180 degrees. Sparsity is applied to each tomography acquisition by taking only a small proportion of total number of rotation angles required by the Crowther criteria. An angular offset, calculated with golden ratio, was added to the starting angle of each tomogram to maximize diversity of information content for more efficient spatial sampling, as shown in Fig. 5.1b [129, 187, 188].

In our reconstruction approach, we model the dynamic processes combining two methods, as shown in Fig. 5.2. First, we consider deformations of the sample that cause relative movement, expansion, or contraction of the whole or any part of the sample. This is defined as any change of the sample that can be mapped on the original state by a time-dependent deformation-vector field [190]. Second, we represent the local changes in electron density by a voxel-wise temporal step function, as described in Fig. 5.3a.

The combination of these two models, shown in Fig. 5.2, can accurately account for various dynamic processes. For example phase transitions such as solid melting or liquid condensation or evaporation which include concomitant deformation of the sample structure [195, 196]; chemical reactions such as oxidation or lithiation in energy materials; quantifying the dynamics and water content for cement hydration [197]; and mechanical deformation including crack formation.

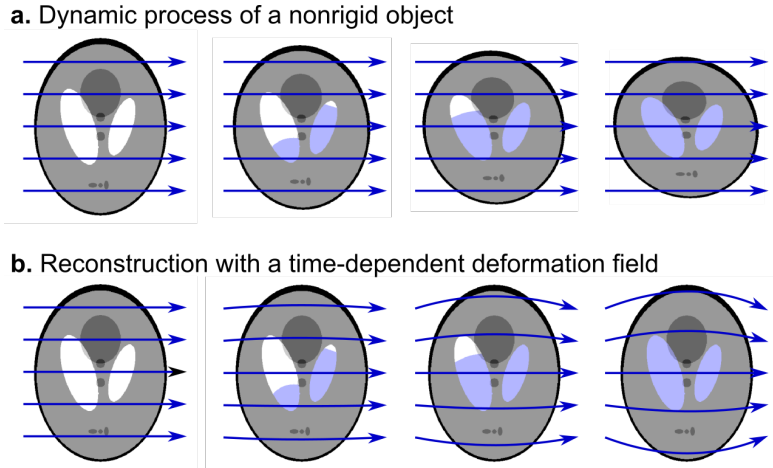


Figure 5.2. Schematic of a dynamic liquid-filling process and the reconstruction technique. a) Tomography measurements of the dynamic process with the object deforming during the process. b) Reconstructed localized dynamics with deformation correction, which accounts for the deformation of the sample using a time-dependent deformation field and allows localized dynamics to be retrieved on a stable sample structure. Blue arrows in a) represent normal projection lines and curved-lines in b) represent curved integration path for projections using the non-rigid computed tomography (NCT) approach.

5.4 Iterative Temporal Reconstruction Technique

For the reconstruction, all measured projections are first aligned with the tomography projection alignment method described in [170]. Then we apply the NCT method to reconstruct deformations of the sample during the whole measurement process. As previously described in [190], this method extracts a vector-based time-dependent deformation field, which is then used on the tomographic projections and back-projections. The NCT method can effectively model and correct the deformations of the sample during measurement, and allows us to use a simplified model for the local change of density in individual voxels. Using the non-rigid correction, we can assume that the changes are ‘localized’, such that local electron density changes in the sample can be represented at their starting position throughout the whole process. This simplifies the local dynamics significantly, as it allows us to exclude any intertwining effects between neighbouring voxels caused by deformation or movement, and to use a much simpler model to encode the remainder dynamics as changes are constrained within each individual voxel. A more detailed description and results of the NCT method can be found in the methods section.

In our approach, we assume that the imaged quantity of each voxel changes like a step function in time, as shown in Fig. 5.3, which shows a transition from the start value N_0 to the end value N_1 at a certain time point T . This assumes that the local changes

at each voxel occur within one of the tomographic time frames, we further discuss the performance of the reconstruction algorithm when this assumption is not satisfied in the Methods subsection “Numerical simulations”.

Dynamics that consist of a step function for each voxel can be uniquely defined by the three variables N_0 , N_1 and T , shown in Fig. 5.3a. These three quantities can be interpreted as the initial state, the final state, and the transition time of each voxel, and can be used to reconstruct a full 3D volume for each time interval. This is illustrated in Fig. 5.3b for a simulated dataset of a liquid-filling process.

The reconstruction problem is then reduced to reconstructing the N_0 , N_1 and T , variables for each voxel of the 3D volume. We developed a method based on iterative refinement where we use adapted projections and back-projections according to the reconstructed deformation field. Refinements are applied simultaneously to the N_0 , N_1 and T variables at each voxel based on differences between the projections generated by the current iteration of the variables and the measured projections. As a result, the method is able to reconstruct the start and end states of the sample at full spatial resolution, and retrieve the transition time values with a temporal resolution equal to the length of a time frame, *i.e.* the measurement time of one sparsely-sampled tomogram. A more detailed description of the reconstruction algorithm can be found in methods section. Note that the transition-time T can be used to directly extract contours or isosurfaces of phase transition or water filling. Already these reduced volumetric parameters can be considered one step ahead in the analysis of the 4D dataset.

During the reconstruction we do not apply any spatial constraint nor any restriction on the values of N_0 , N_1 nor on the difference between them. Instead, we only assume a transition between two states for each voxel and the local values can either increase, decrease or stay unchanged. This also means that apart from capturing water condensation in empty pore space, *i.e.* an increase in electron density, the method also allows reconstruction of other structural changes, such as crack formation or a decrease in density accompanied by a volume expansion or swelling process, as it is demonstrated in the experimental results.

5.5 Vapor Condensation and Water Uptake in a PEFC Catalyst Layer

We demonstrate our approach by imaging vapor condensation and the structural response upon water uptake in a standard platinum / carbon (Pt/C) catalyst. Layers of these catalysts are used in fuel cells as the cathode electrode of a membrane electrode assembly for a PEFC stack. A schematic representation of a PEFC stack is shown in Fig. 5.4a, in which the two gases H_2 and O_2 undergo an electrochemical reaction to generate electricity and water in an environment with complex surface chemistry. Within the catalyst layer, the electrochemical reactions are driven by catalytic active sites of small hydrophilic Pt nanoparticles with an average diameter of 3 nm. The nanoparticles are distributed on

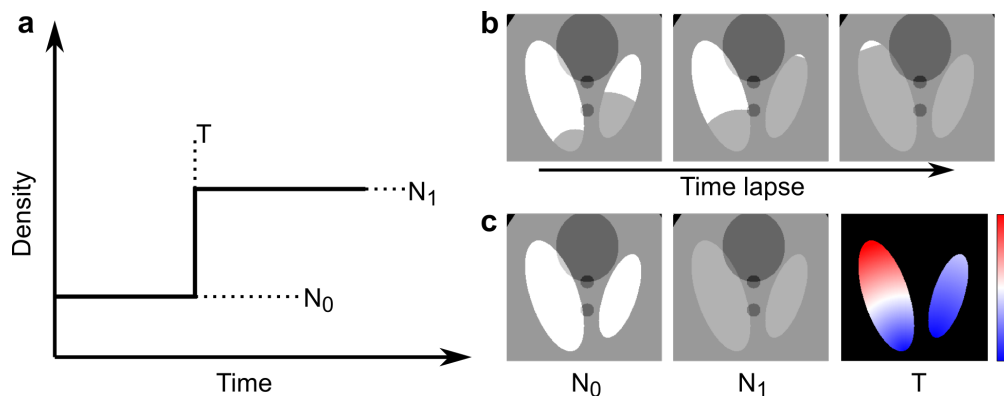


Figure 5.3. a) Step function model of dynamic process in a voxel. The step function is uniquely defined by values N_0 , N_1 and T . b) Time frames of the dynamic liquid filling process, and c) the variables N_0 , N_1 and T that model the process. The colormap for T , represents transition time, ranging from the start to the end of the process, with colors from blue to red.

the surface of a hydrophobic carbon support, Vulcan XC72R, and partially covered by a binder, *i.e.* the ionomer, which is the hydrophilic polymer NafionTM. Understanding water condensation in this environment is greatly desired. Liquid water saturation, either from vapor condensation or as the product of the electrochemical reaction, hinders the transport of gaseous components, *i.e.* H_2 and O_2 , to the Pt nanoparticles. Moreover, since these nanoparticles and the relevant porous network are only a few nm in size, it is important to understand vapor condensation within the catalyst on the nanoscale.

The uptake of water molecules plays another important role within the catalyst layers. The ionomer acts as a binder, but also as the proton conducting element between anode and cathode catalyst layer. It can only fulfil this role in its hydrated state, which also explains why PEFCs are usually operated at high relative humidity (RH) of 80-100% because this humid atmosphere is beneficial for their performance. However, upon water uptake the nanoscale structure of the ionomer is expected to change with a decrease in density and an expansion into unoccupied space [198]. These structural changes may additionally hinder the transport of the gaseous components within the catalyst layers together with liquid water condensation. Therefore, understanding the role of water in this complex environment is desired for further improving the performance of PEFC materials.

We prepared a 20 μm -diameter pillar extracted from a catalyst coated membrane for a membrane electrode assembly of a PEFC. A scanning electron microscope (SEM) image of the sample is shown in Fig. 5.4b. Experiments were performed at room temperature while the atmospheric conditions surrounding the sample were controlled by an airflow system, the latter providing humidified nitrogen with a RH ranging between 80-93%. As shown in Fig 5.4c, the RH was slowly increased from 81% to 92% in steps of 0.1% over a time span of 34 h. The sample is then kept at a RH reading of 92%, which was found to

saturate the humidity sensor. The sample continues to absorb water after the saturated humidity reading is reached, as shown in the water intake in Fig 5.4c, which is calculated from the integrated electron density of the sample, calculated from the 2D projections.

For each time interval, indicated in Fig. 5.4c, a tomography measurement is made with sparsely sampled angular orientations. Each of these sparse tomograms contain 25 sample angular orientations in the range from 0 to 180 degrees, which corresponds to a sparsity ratio of 2.2% compared to the 1,122 projections required by the Crowther criterion for a 28 nm half-period resolution. As mentioned above, the starting angles at each time frame were adjusted using a golden ratio approach [129,167,187] for more efficient spatial sampling. Each sparse tomography measurement took 12 minutes, including overhead, while the relative humidity was increased by 0.1% after each sparse acquisition.

5.6 Reconstruction and Analysis

Using the NCT method, we obtained a deformation vector field that characterizes the expansion of the sample, as shown in Fig. 5.5c. After the non-rigid correction, we reconstruct the N_0 , N_1 and T variables that define the dynamic process, shown in Figs. 5.5a, 5.5b, and 5.5d, respectively. A comparison of the improvement obtained by using the NCT method, and more details on the reconstruction procedure, can be found in the methods section.

During the controlled hydration process, we observe water condensation in the outer layer of the sample pillar. This is shown in Fig. 5.5a and 5.5b which depict axial tomography slices from the reconstructed tomograms of the start and the end states of the sample. We can clearly see the difference in electron density between these states at low and high relative humidity, especially the filling of pores in the outer layer. The transition time T shown in Fig. 5.5d can further be correlated with the readout of environment relative humidity during the dynamic measurement.

With these variables, N_0 , N_1 and T , we can reconstruct the tomograms at each time frame during the whole dynamic hydration process. To identify the actual changes in electron density as well as to illustrate the high resolution of our method, we zoom in to examine two $1.7 \times 1.7 \mu\text{m}^2$ regions inside the sample, as shown in Fig. 5.6. In the first region, Fig. 5.6a-5.6d, we can clearly observe the process of water condensation into the porous catalyst structure over the timescale of a few hours. Initial changes in the electron density (ED) become visible after the RH approaches 91%. Focusing on the two highlighted regions (red & blue boxes), we observe that these changes take place within about 5 hours. In this time-interval, the average ED in the highlighted region in Fig. 5.6a increases by approximately $0.34 \text{ e}/\text{\AA}^3$, as shown in Fig 6b, a value that matches the tabulated ED of water of $0.333 \text{ e}/\text{\AA}^3$. We further note that our method is able to capture multiple stages of the condensation process, since a total of 25 time frames are reconstructed for this time-span of 5 h, some of the representative frames are shown in Fig. 5.6a.

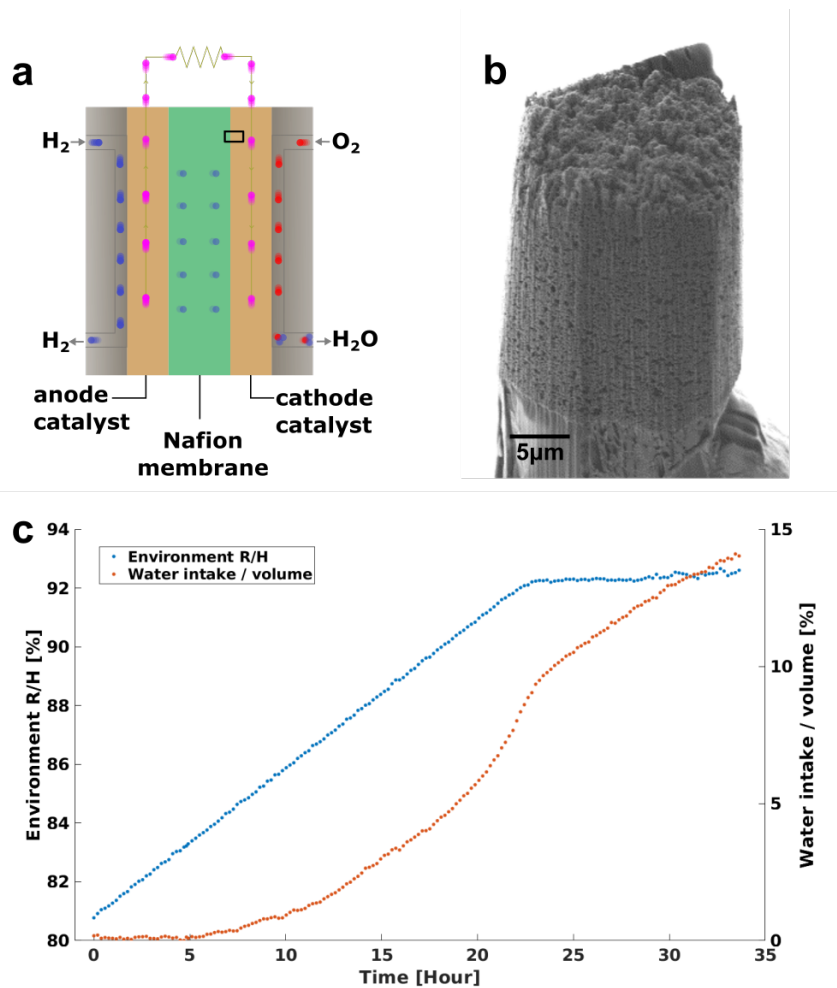


Figure 5.4. a) Schematic of the structure of a polymer electrolyte fuel cell, black square indicates the interface from which the sample was taken. b) SEM image of the sample pillar. c) Blue dots show the environment relative humidity versus time, each dot represents the starting time of one sparsely sampled tomographic measurement. Red dots show the amount of water intake, which is estimated from the integrated electron density obtained from 2D projections.

The ED difference between final and initial state is shown in Fig. 5.6c. The difference clearly shows that the porous regions of the catalyst become filled with water. Looking at the transition time T in Fig. 5.6d, it seems that the water condensation in the larger pores occurs in 2 steps. Initially, some condensation is visible already early on at the edge of the larger pores followed by a rather quick filling of the full volume. This agrees with the expected behaviour of the catalyst material. Water will initially not adsorb on the hydrophobic carbon surface, but on the small hydrophilic Pt nanoparticles as well as get absorbed in the ionomer of the catalyst. Once condensation starts, it continues to draw water from the humid atmosphere and starts to fill up the pores rapidly.

The second region, Fig. 5.6e to 5.6h, exhibits an entirely different behaviour. During the increase of humidity, the electron density in the central part of the ionomer decreases (blue box) from $0.64 \text{ e}/\text{\AA}^3$ to $0.55 \text{ e}/\text{\AA}^3$ and increases in the adjacent pore volume (red box) from 0.26 to $0.47 \text{ e}/\text{\AA}^3$. The quantitative change in electron density, in particular the decrease in the ionomer, cannot be explained by water condensation but is instead related to structural changes within the ionomer. The ionomer is expected to change its nanoscale structure upon water uptake. A significant decrease in density of up to 25% has been observed in literature [198], which is accompanied by swelling on a molecular level, which is below the resolution limits for our measurements. The fully wetted ionomer is expected to have an electron density of $0.434 \text{ e}/\text{\AA}^3$ compared to $0.593 \text{ e}/\text{\AA}^3$ in its dry state. With a half-period resolution of 28 nm, we cannot resolve the high-density Pt nanoparticles, which are of approximately 3 nm in diameter and have an ED $\sim 5.167 \text{ e}/\text{\AA}^3$, due to partial volume effects the ED measured in each voxel is potentially higher due to the presence of these unresolved particles. In addition, each voxel may also contain the carbon support, with an ED of $0.59\text{-}0.61 \text{ e}/\text{\AA}^3$ that does not change with hydration. Nevertheless, we still observe a clear decrease in ED for multiple voxels within the second region, as highlighted in Fig. 5.6g, from which we can deduce which voxels are mostly occupied by the ionomer. Our method is also able to resolve the ionomer swelling into the surrounding pore-space and its decrease in ED in 3D and with a half-period resolution of 28 nm which is, to the best of our knowledge, not yet reported in the literature before.

The significant changes of the ionomer's nanostructure demonstrate that water saturation and absorption in the PEFC catalyst layer plays not only a role in empty pores but can also induce significant changes in the nanostructure of the ionomer. Optimizing the ionomer content is an important parameter that correlates with PEFC performance [199,200]. Its swelling may further hinder the diffusion of gaseous components to the catalytic active sites, in particular when taking into account that in operando conditions additional water is generated as a product of the electrochemical reaction. The capability to directly image the ionomer swelling in-situ will play an important role to study its structural response upon water uptake from nanometre to micrometre length scales, and our method is ideally suited to capture these changes.

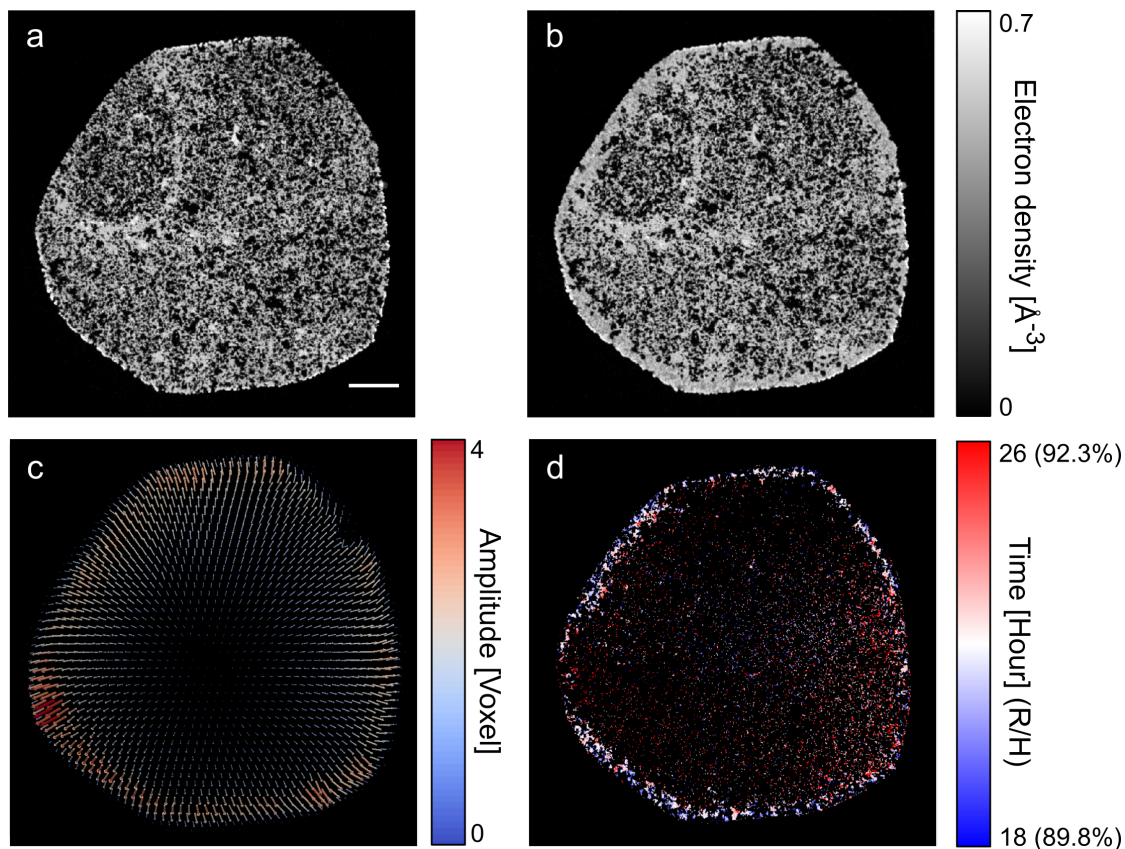


Figure 5.5. Dynamic tomography reconstruction of the catalyst sample. a) Axial tomographic slice of the reconstructed electron density tomogram at start state. Scale bar is 3 μm . b) The same slice of electron density tomogram at end state, where filling of the pores can be observed. c) Reconstructed deformation vector field of the sample between the low and high humidity state. Arrows indicating the vector field are upscaled 15 times to improve visibility. d) Map of the transition time T (or corresponding environment relative humidity) of the same slice. This map shows with color coding the time point when localized changes occur in each voxel.

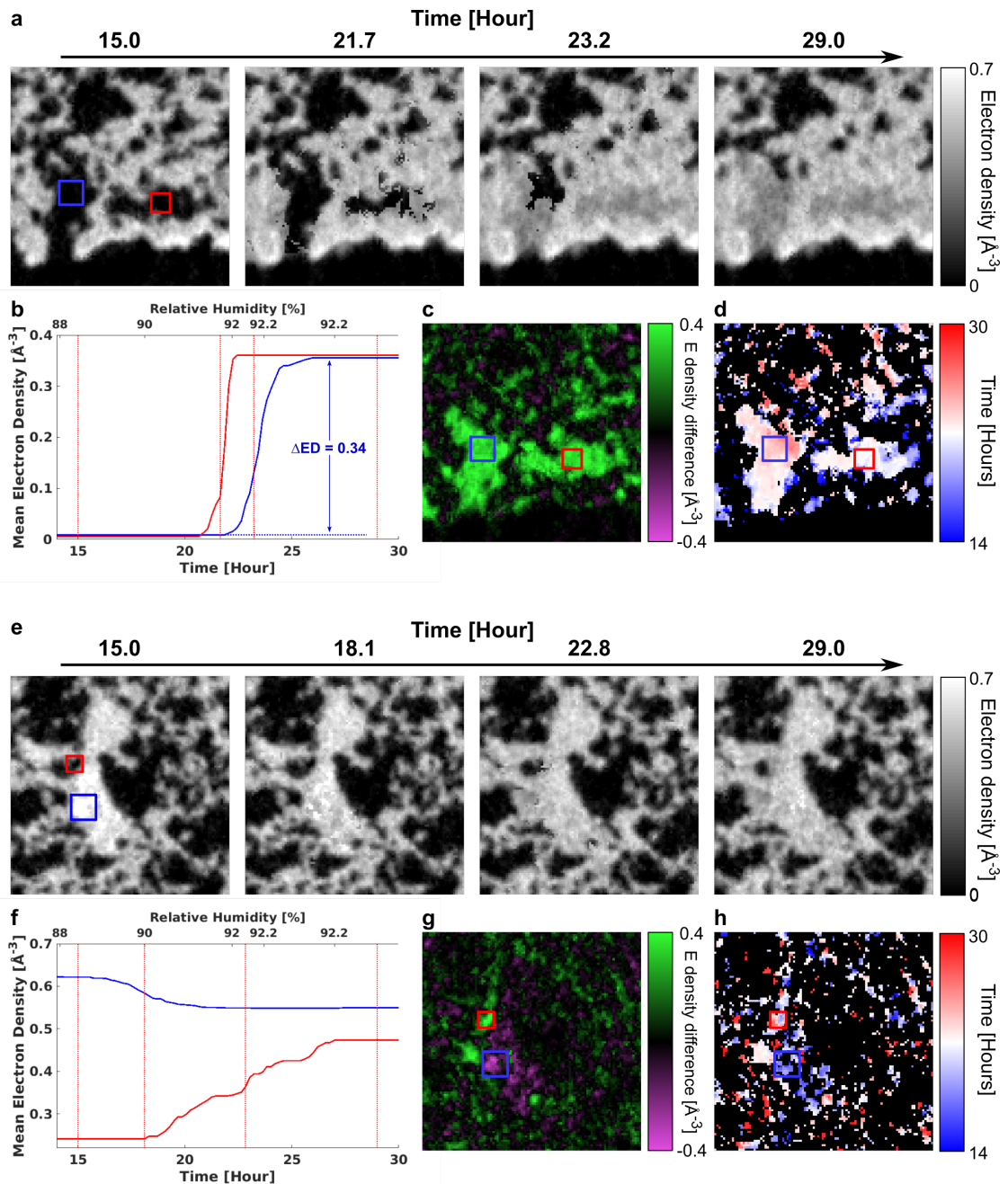


Figure 5.6. Reconstruction inset of $1.7 \times 1.7 \mu\text{m}^2$ areas of an axial tomography slice. a) Reconstructed time-lapse electron-density tomograms showing pore condensation. b) Evolution over time of the average electron density of the rectangle regions in a marked by blue and red. Vertical lines represent time frames of the tomogram insets shown in a. The increase in electron density matches that of water, $0.333 \text{ e}/\text{\AA}^3$. c) Electron density difference between the start and end states. d) Transition-time map of the region. e) to h) show the same but for a second region that contains water absorption and swelling of the ionomer.

5.7 Discussion

We have introduced a novel experimental and reconstruction method for dynamic sparse X-ray nanotomography and demonstrated it by imaging the controlled hydration process of a polymer electrolyte fuel cell catalyst. During the hydration process, this sample experienced a combination of representative changes including deformation, water condensation, and pore filling. For the first time we have observed in the nanoscale the wetting, including local expansion and decrease in ED, of one of its central components: the hydrophilic ionomer. We have shown that 3D dynamics are reconstructed with quantitative electron density values, as demonstrated by the recovered water ED upon pore condensation.

The reconstructions, with a 3D half-period spatial resolution of 28 nm, were obtained from a dataset that was measured with 1/40 of the conventionally required number of projections. This corresponds to one 3D temporal frame every 12 min, which is a marked improvement over the conventionally needed 8 hours. Measurement time is a severe bottleneck for 3D imaging nanoscale dynamics in representative volumes, our demonstration here reaches a rate of almost 362,000 resolution elements per second, which improves nanoscale scanning rates at this resolution by almost 2 orders of magnitude. Given that synchrotron experimental time is scarce and valuable, our development opens the door to a whole new regime of possible dynamical studies.

Further, the implementation of NCT correction allows our method to have excellent stability against sample movement or deformation, which enables identification and quantification of dynamic events with higher precision. The step-function model also allows the transition time to be directly reconstructed instead of being obtained from post-processing of tomograms, this greatly eases the analysis steps in many dynamic studies where the key information is given by the time of transition.

Thanks to the versatility and robustness of our method, it can be applied at various length-scales and illumination probes with minimal changes to the hardware and measurement protocols. As examples, these include X-ray microtomography, transmission electron tomography, and optical tomography. The technique can be readily generalized, for example by modelling dynamics using a sequence of step transitions, as opposed to just one. In this manner the method could be applied to more complex or periodic systems, such as operando imaging of the charge-discharge cycle of batteries. With the emerging upgrade to 4th generation synchrotrons, and concomitant improvement of optics and instrumentation, an increase of two orders of magnitude in the available coherent flux is expected. With this increase the speed of the method can be brought down to seconds for nanoscale characterization, granting great potential for elucidating mechanisms of biological or chemical systems.

5.8 Methods

5.8.1 Sample Preparation

The catalyst sample was taken from a membrane electrode assembly for a polymer-electrolyte fuel cell. The membrane was produced by spray coating a commercial NafionTM (NR-211, Ionpower) with a catalyst ink using a custom-built coating system. The catalyst ink was prepared by dispersing 20 mg of catalyst powder (HiSPEC 3000, Johnson Matthey) in a mixture of 138 μl of deionised water with less than 1.1 S cm⁻¹ and 4841 μl 2-propanol (99.9 % VLS grade, Roth[®]) with a vial tweeter. 20 wt% NafionTM resin solution (EW 1100, Sigma Aldrich) was added to the mixture to achieve an ionomer/carbon weight ratio of 0.54. The custom-built setup comprises a computerized numerical control system equipped with an ultra-sonic spraying nozzle, for which argon is used as the carrier gas. The catalyst-coated membrane was prepared by spraying 160 cycles at a flow of 60 $\mu\text{l}/\text{min}$ over an area of $2.5 \times 2.5 \text{ mm}^2$ of the NafionTM membrane, which is placed on a heated plate beneath an infrared lamp to accelerate the drying process.

The imaged μ -pillar was milled down to a diameter of 20 μm from the catalyst coated membrane using a focused ion beam-scanning electron microscope (FIB-SEM). It was then transferred to a copper sample holder [117] using a micro manipulator. The final sample pillar is shown in the SEM image in Fig. 5.4b.

5.8.2 Measurement and Data Pre-processing

The sparse dynamic nanotomography measurements were performed at the cSAXS beamline, Swiss Light Source, Paul Scherrer Institut, Switzerland. An X-ray energy of 6.2 keV was selected using a double-crystal Si(111) monochromator. A set of slits were located 22 m upstream of the sample and the horizontal aperture was set to 20 μm opening, which creates a secondary source that coherently illuminates a Fresnel zone plate downstream with 200 μm diameter and 60 nm outermost zone width. The Fresnel zone plate was designed with locally displaced zones to improve imaging quality and phase accuracy [118]. The sample was placed 1.48 mm downstream the focal point of the zone plate to get an illumination of 5 μm diameter. Coherent diffraction patterns were acquired using an in-vacuum Eiger 1.5M area detector placed 5.23 m downstream of the sample inside a flight tube under vacuum [121]. Ptychography scans of the sample were measured using the flexible tomography nano imaging end-station fIOMNI [122], a dedicated instrument for X-ray scanning microscopy which achieves positioning accuracy better than 10 nm by using laser interferometry feedback [123]. The 2D projection field of view was $27 \times 10 \text{ }\mu\text{m}^2$. 2D ptychograms were measured following a Fermat spiral trajectory [119] with an average step size of 1 μm and a 0.05 second exposure time per point, each 2D scan took 23 seconds. For this experiment, we have modified the setup to be able to measure under controlled relative humidity via an air flow system that mixes dry and humidified nitrogen gas, combined with a humidity sensor that monitors and controls

the relative humidity of the air surrounding the sample.

Prior to the dynamic tomography measurement, several groups of 2D scans were measured at different relative humidities to locate the ionomer rich regions in the catalyst and to estimate the amount of water intake. Before ramping up the RH we waited 10 hours for the sample to stabilize at 81% RH, as shown in Fig. 5.7a. We define the stabilized time point, at which the dynamic tomography measurements were started, as $t_0 = 0$, as shown in Fig. 5.7a. All measurements before that time were excluded from the present analysis.

As described in the main text and in Fig. 5.4, sparsely sampled tomograms were measured repeatedly while the relative humidity was gradually increased from 81% to 92% in 35 hours. The sparse-tomography measurement strategy is shown in Fig. 5.7b. For each sparsely-sampled tomogram, the sample was rotated to 25 different angles from 0 to 180 degrees, and one ptychographic 2D projection was taken at each angle. After each tomogram, the sample was rotated back to 0 degrees, and the process was repeated with an angular offset given by the golden ratio [167]. In total 173 sparsely sampled tomograms were measured, for simplicity we define the starting time of each sparsely sampled tomogram as $t = t_0, t_1, \dots, t_{171}, t_{172}$, and use $Proj(t_i)$ to denote the set of 25 projections measured between t_i and t_{i+1} .

Ptychography scans were reconstructed with an iterative phase retrieval algorithm, with of 300 iterations of difference map [35] followed by 500 iterations of maximum likelihood [45], using the PtychoShelves package [50]. Then from the reconstructed complex-valued images, we extract the phase component, we then use phase unwrapping [201] and we remove constant and linear phase offset terms [126]. We denote the outcome phase projections as $P(t_i) = phase\{Proj(t_i)\}$ for further analysis.

All projections were subsequently pre-aligned with a tomography alignment approach based on multi-resolution projection matching with deep subpixel accuracy [170]. The volume percentage of water intake at each time frame, shown in Fig. 5.7a, is estimated from the 2D projections as

$$W_i = \frac{A}{\rho V_p N_A Z} \eta_{ED} \left(\sum P(t_i) - \sum P(t_0) \right), \quad (5.1)$$

where $A = 18 \text{ g/mol}$ is the molecular mass of water, $\rho = 1 \text{ g/cm}^3$ is the density of water, V_p is the volume of the sample pillar, N_A is the Avogadro constant, and $Z = 10$ is the number of electrons in a water molecule. The coefficient η_{ED} , used for converting phase into electron density [17], is given by

$$\eta_{ED} = \frac{1}{\lambda l r_0}, \quad (5.2)$$

where λ is the X-ray wavelength, l is the side length of pixel in the projection, and r_0 is the classical electron radius.

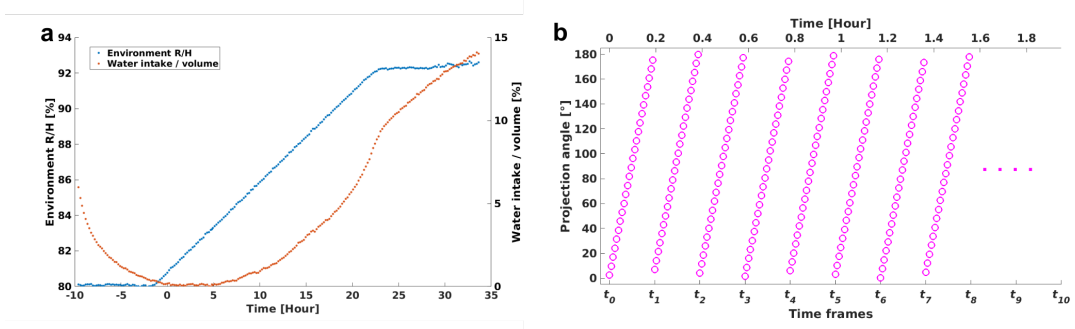


Figure 5.7. Acquisition for the dynamic hydration process. a) The full measurement process, including 10 hours wait time for the sample to stabilize after initial tests of the humidity environmental chamber. Each dot represents the starting time of one sparsely-sampled tomogram, with relative humidity values shown in blue and the amount of water intake shown in red. The latter is estimated using the integrated electron density obtained from 2D projections. b) Measured projection angles in each sparse tomogram.

5.8.3 Nonrigid Computed Tomography

In micro- and nanotomography applications, deformations of the sample often have a significant effect on the measurement of dynamic processes, and in some cases can become the limiting factor of the imaging method [202]. In our case, as deformations of the sample structure can be observed during its water uptake process, we adopted the nonrigid geometry computed tomography (NCT) method [190] to quantitatively reconstruct the deformation field.

A deformation vector field $\Gamma(\vec{r}, t)$ describes the deformation of the sample structure at time t relative to its starting state at t_0 , with the latter used as the reference state. At any time point t_i , projections of the reconstructed model considering the deformation field can be calculated as

$$\hat{P}(t_i) = \mathbf{A}_N(\Gamma(\vec{r}, t_i)) N(\vec{r}, t_i), \quad (5.3)$$

where $N(\vec{r}, t_i)$ is the reconstructed sample at t_i , and $\mathbf{A}_N(\Gamma(\vec{r}, t_i))$ is the projection matrix under curved geometry given by deformation field $\Gamma(\vec{r}, t_i)$, as defined in Eq. (3a) in [190].

In the NCT method [190], the time-evolving deformation vector field $\Gamma(\vec{r}, t)$ is calculated from discretized vector fields $\Gamma(\vec{r}, t_i)$ which describe the deformation of the i^{th} tomogram. However, in our case a large number of tomograms were measured with a very low sparsity ratio, making it unfeasible to reconstruct one discretized vector field for each tomogram. Therefore, we approximate the dynamics of the deformation field as a linear function of the environment relative humidity. This is a reasonable assumption considering that the changes are driven by the RH and since the deformation field is small, namely with an average of 1.5 voxels (26 nm) and a peak value of 5 voxels (87 nm). We

found that a linear approximation proportional to the environmental relative humidity, $RH(t_i)$, was sufficient to describe the time evolution of the deformation field. We then modelled the latter as

$$\Gamma(\vec{r}, t_i) = r_H(t_i) \Gamma(\vec{r}, t_{end}), \quad (5.4)$$

where $r_H(t_i)$ is a linear ratio calculated from the environmental relative humidity

$$r_H(t_i) = \frac{RH(t_{end}) - RH(t_i)}{RH(t_{end}) - RH(t_0)}, \quad (5.5)$$

and where $t_{end} = t_{172}$ is the starting time for the last sparse tomogram.

In this approximation, one 3D volume estimate can be reconstructed from the projections at each time frame:

$$g_i(\vec{r}) = \text{FBP}_{\Gamma(\vec{r}, t_i)} \{P(t_i)\}, \quad (5.6)$$

where $\text{FBP}_{\Gamma(\vec{r}, t)} \{ \}$ denotes filtered back projection with a curved projection geometry given by the deformation field $\Gamma(\vec{r}, t)$, using the adjunct matrix \mathbf{A}_N^T , as given by Eq. (3b) in [190]. Using these reconstructed volumes, the iterative update of the final deformation field $\Gamma(\vec{r}, t_{end})$ can be described as

$$\Gamma^{(k+1)}(\vec{r}, t_{end}) = \Gamma^{(k)}(\vec{r}, t_{end}) + \sum_i \frac{1}{r_H(t_i)} \Delta\Gamma \{g_i(\vec{r}), g_0(\vec{r})\}, \quad (5.7)$$

where $\Delta\Gamma$ is the update term based on the tomography reconstructions of the measured projections, given by Eq. (4) in [190]. $\Gamma^{(k)}(\vec{r}, t_{end})$ denotes the reconstructed deformation field in iteration k . Starting from an all-zero initial guess, five iterations were applied to the deformation field to get the final result, shown in Fig. 5.5c.

The improvement provided by the non-rigid tomography correction can be demonstrated by taking the difference of the tomography reconstructions from the first 20 sparse tomograms, which are measured at 81% RH in the first hour, and the last 20 sparse tomograms, which are measured at 92% RH in the last hour. Such reconstructed tomograms of the start state and the end state are shown in Figs. 5.8a and 5.8b, respectively. Figs. 5.8c and 5.8d show the difference between the two states without and with the non-rigid correction, respectively. In Fig. 5.8c we can see outline layers around the sample and around individual pores, such edge artefacts are expected if the sample is expanding from its starting state during the dynamic process. In such case, the difference between the starting and end state is dominated by the geometrical deformation of the sample, if not corrected, these artefacts are difficult to separate from water uptake effects, because an increase of density at a voxel which starts empty can either be caused by water condensation, or by nearby high-density material expanding into the voxel. This ambiguity affects the precision of further reconstruction of dynamics. For comparison, Fig. 5.8d shows the difference with the NCT correction, which accounts for the geometrical expansion of the sample. The latter shows effects that can be largely attributed to water uptake and absorption, for example showing empty voxels being filled with water.

Similar to Eq. (4) in [190], a spatial convolution with a Gaussian filter, with a standard deviation of 30 voxels, is applied to the calculation of the deformation vector field to regularize the result and avoid local variations. This step avoids abrupt changes of the deformation field at a small length scale, typically smaller than 20 pixels, i.e. 350 nm, which would result from overfitting noise and sparse-sampling artefacts. Deformations at a smaller scale can be captured by the localized dynamics, as shown in Fig. 5.6e-5.6h.

5.8.4 Sparse Dynamic Tomography Reconstruction

Once the time-dependant deformation field is obtained, we proceed to reconstruct the local voxel-wise dynamics. Following the step-function model described in Fig. 5.3, we can define the initial state, final state, and transition time for each voxel in the 3D volume as $N_0(\vec{r})$, $N_1(\vec{r})$, and $T(\vec{r})$, such that for any given time frame t_s , the state of the sample is given by:

$$N(\vec{r}, t_s) = \begin{cases} N_0(\vec{r}) & , t_s \leq T(\vec{r}) \\ N_1(\vec{r}) & , t_s > T(\vec{r}) \end{cases} \quad (5.8)$$

The reconstruction problem is then reduced to retrieve $N_0(\vec{r})$, $N_1(\vec{r})$ and $T(\vec{r})$. For this purpose, we developed an iterative refinement approach. The initial guess for the starting state, $N_0(\vec{r})$, is

$$N_0(\vec{r}) = \langle \text{FBP}_{\Gamma(\vec{r}, t)} \{P(t)\} \rangle_{t_0 \leq t \leq (t_0+20)}, \quad (5.9)$$

where $\langle \rangle$ denotes average over several time frames, in particular here the first 20 time frames are used. Similarly for the initial guess of $N_1(\vec{r})$ we used the average of the last 20 time frames, namely

$$N_1(\vec{r}) = \langle \text{FBP}_{\Gamma(\vec{r}, t)} \{P(t)\} \rangle_{(t_{end}-20) \leq t \leq t_{end}} \quad (5.10)$$

For the transition time $T(\vec{r})$ the initial guess are constant values:

$$T(\vec{r}) = \frac{t_0 + t_{end}}{2}. \quad (5.11)$$

Figure 5.9 shows a schematic of one iteration of the reconstruction process. In each iteration, one time frame t_s between t_0 and t_{end} is randomly selected. The modelled sample state at t_s is then calculated based on the current reconstruction with the step function model given in Eq. (5.8). Applying the conditional process to the whole sample volume then gives us the tomogram $N(\vec{r}, t_s)$. From this modelled tomogram we then apply a forward projection:

$$\hat{P}(t_s) = \text{FP}_{\Gamma(\vec{r}, t_s)} \{N(\vec{r}, t_s), \theta(t_s)\}. \quad (5.12)$$

Here $\text{FP}_{\Gamma(\vec{r}, t_s)} \{ \}$ represents the projection operator under the curved projection geometry given by the deformation field $\Gamma(\vec{r}, t_s)$ and $\theta(t_s)$ denotes the sample orientation angles which were measured in the s-th sparse tomogram.

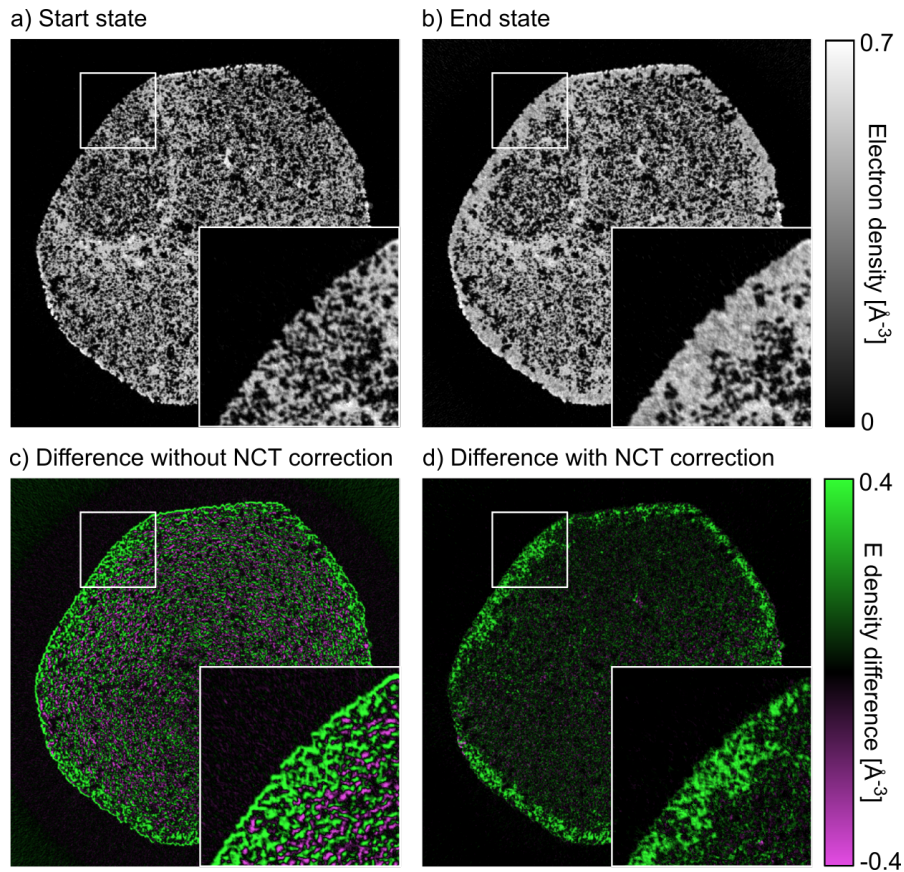


Figure 5.8. a) Axial tomography slice from the starting state of the sample. b) Same tomography slice from the end state of the sample. c) Difference of electron density between the start and end state of the sample without NCT, an outline layers around the pore edges are clearly visible and the difference is heavily dominated by the sample geometrical expansion. d) Difference after correction with NCT method, the outline artefacts are mostly removed, and the difference matches water filling of pores in the sample.

We then compute the difference between the modelled and measured projections, followed by a back-projection of this difference in order to compute a 3D map of corrections, namely

$$N_c(t_s, \vec{r}) = R_1(\vec{r}) * \text{BP}_{\Gamma(\vec{r}, t_s)} \left\{ R_2(t_s) * \left(P(t_s) - \hat{P}(t_s) \right) \right\}, \quad (5.13)$$

where $\text{BP}_{\Gamma(\vec{r}, t_s)} \{ \}$ denotes the back projection with curved projection geometry given by the deformation field $\Gamma(\vec{r}, t_s)$, R_1 and R_2 denote normalization arrays that are used in the simultaneous algebraic reconstruction technique (SART) [59, 140], which can be calculated with unit-valued projections and a unit-valued tomogram, respectively

$$R_1(\vec{r}) = \frac{1}{\text{BP}_{\Gamma(\vec{r}, t_s)} \{ P(t_s) = 1 \}}, R_2(t_s) = \frac{1}{\text{FP}_{\Gamma(\vec{r}, t_s)} \{ N(\vec{r}) = 1 \}}. \quad (5.14)$$

The correction map in Eq. (5.13) adopts a strategy similar to SART to estimate the update corrections to the current reconstruction [140].

In the next step we apply refinement corrections to $N_0(\vec{r})$, $N_1(\vec{r})$, and $T(\vec{r})$ based on values of $N_c(\vec{r}, t_s)$. The correction values are given by:

$$\begin{aligned} N_0(\vec{r}) &= N_0(\vec{r}) + \Delta N_0(\vec{r}), \\ \Delta N_0(\vec{r}) &= \begin{cases} \varepsilon * N_c(\vec{r}, t_s) & (t_s \leq T(\vec{r})) \\ 0 & (t_s > T(\vec{r})) \end{cases}, \end{aligned} \quad (5.15)$$

$$\begin{aligned} N_1(\vec{r}) &= N_1(\vec{r}) + \Delta N_1(\vec{r}), \\ \Delta N_1(\vec{r}) &= \begin{cases} 0 & (t_s \leq T(\vec{r})) \\ \varepsilon * N_c(\vec{r}, t_s) & (t_s > T(\vec{r})) \end{cases}, \end{aligned} \quad (5.16)$$

$$\begin{aligned} T(\vec{r}) &= T(\vec{r}) + \Delta T(\vec{r}), \\ \Delta T(\vec{r}) &= \begin{cases} 0 & , t_s \leq T(\vec{r}) \ \& \ \text{sign}(N_1(\vec{r}) - N_0(\vec{r}))N_c(t_s, \vec{r}) \leq 0 \\ -\varepsilon * \tau * \delta(t_s, \vec{r}) * N_c(\vec{r}, t_s) & , t_s \leq T(\vec{r}) \ \& \ \text{sign}(N_1(\vec{r}) - N_0(\vec{r}))N_c(t_s, \vec{r}) > 0 \\ -\varepsilon * \tau * \delta(t_s, \vec{r}) * N_c(\vec{r}, t_s) & , t_s > T(\vec{r}) \ \& \ \text{sign}(N_1(\vec{r}) - N_0(\vec{r}))N_c(t_s, \vec{r}) < 0 \\ 0 & , t_s > T(\vec{r}) \ \& \ \text{sign}(N_1(\vec{r}) - N_0(\vec{r}))N_c(t_s, \vec{r}) \geq 0 \end{cases}, \end{aligned} \quad (5.17)$$

where ε is an update relaxation factor that is gradually reduced during iterations for convergence, we typically use

$$\varepsilon = 10^{-4} * 0.998^k, \quad k = 1, 2, \dots, \quad (5.18)$$

where k is the iteration number, and τ is a scaling ratio based on the units used for time and tomogram values. It can be estimated using quantitative values of T and N_0 ,

$$\tau = \frac{\langle T(\vec{r}) \rangle}{\langle N_0(\vec{r}) \rangle} \quad (5.19)$$

where $\langle \rangle$ denotes average over the whole sample volume, and $\delta(t_s, \vec{r})$ is the time relaxation ratio given by

$$\delta(t_s, \vec{r}) = \frac{1}{8} \frac{(t_{end} - t_0)}{(t_{end} - t_0) + 8|T(\vec{r}) - t_s|}, \quad (5.20)$$

which reduces the correction if the transition time of the target voxel is far from the current time frame t_s , adding this relaxation ratio is important for dealing with noise in the data.

In this iterative reconstruction method, Eqs. (5.15) and (5.16) are used to calculate the updates applied to the start and end state tomograms, respectively. These updates are similar to the conventional SART method, but with changes constrained to the voxels that apply to each of them at the time frame t_s . For voxels in which $T(\vec{r})$ is smaller than t_s the update is applied to the start state, and conversely to the end state for voxels for which $T(\vec{r})$ is larger than t_s .

As illustrated in Fig. 5.9, the refinement of transition time in Eq. (5.17) is applied times based on the sign and amplitude of the correction, $N_c(t_s, \vec{r})$, and the state of the voxel at time t_s . In the example illustrated in Fig. 5.9 for ΔT , we have $t_s < T(\vec{r})$, $sign(N_1(\vec{r}) - N_0(\vec{r})) > 0$, and $N_c(t_s, \vec{r}) > 0$, for this case the correction ΔT is in the negative direction, since the error would be potentially reduced if the value of T of that particular voxel was reduced. This situation corresponds to the second line of Eq. (5.17). When iterated over all the time frames, the transition time of all voxels will converge at the time frame where the change occurred.

After one iteration of refinement, another time frame t_s is selected randomly and the whole process is iterated until convergence. In our case we applied 2500 iterations for the numerical simulations and 5000 iterations for the experimental data.

5.8.5 Spatial Resolution Estimate

To estimate the spatial resolution of the reconstruction, the measured data was split into two subsets by taking every second time frame, namely the first set containing projections $\{P(t_0), P(t_2), \dots, P(t_{172})\}$ and the second set containing $\{P(t_1), P(t_3), \dots, P(t_{173})\}$. The non-rigid correction and sparse dynamic tomography reconstruction method was then applied to both sets independently, to reconstruct two separate sets of results, namely $\{N_0^{(1)}(\vec{r}), N_1^{(1)}(\vec{r}), T^{(1)}(\vec{r})\}$, and $\{N_0^{(2)}(\vec{r}), N_1^{(2)}(\vec{r}), T^{(2)}(\vec{r})\}$.

With these two sets of reconstructed results, at each time frame t_i , we calculate the reconstructed sample volume as given by equation (5.8), namely $N^{(1)}(\vec{r}, t_i)$ and $N^{(2)}(\vec{r}, t_i)$. Then we compute the Fourier shell correlation (FSC) [124] between the two reconstructed volumes and compare the correlation curve to the 1/2 bit threshold, as shown in Fig. 5.10. The estimate of spatial resolution is given by the coordinate of the first intersection. For all reconstructed time frames in the process, the half-period spatial resolution was estimated to be in the range of 27.8 nm to 28.7 nm. The correlation curves of a few example time frames are shown in Fig. 5.10.

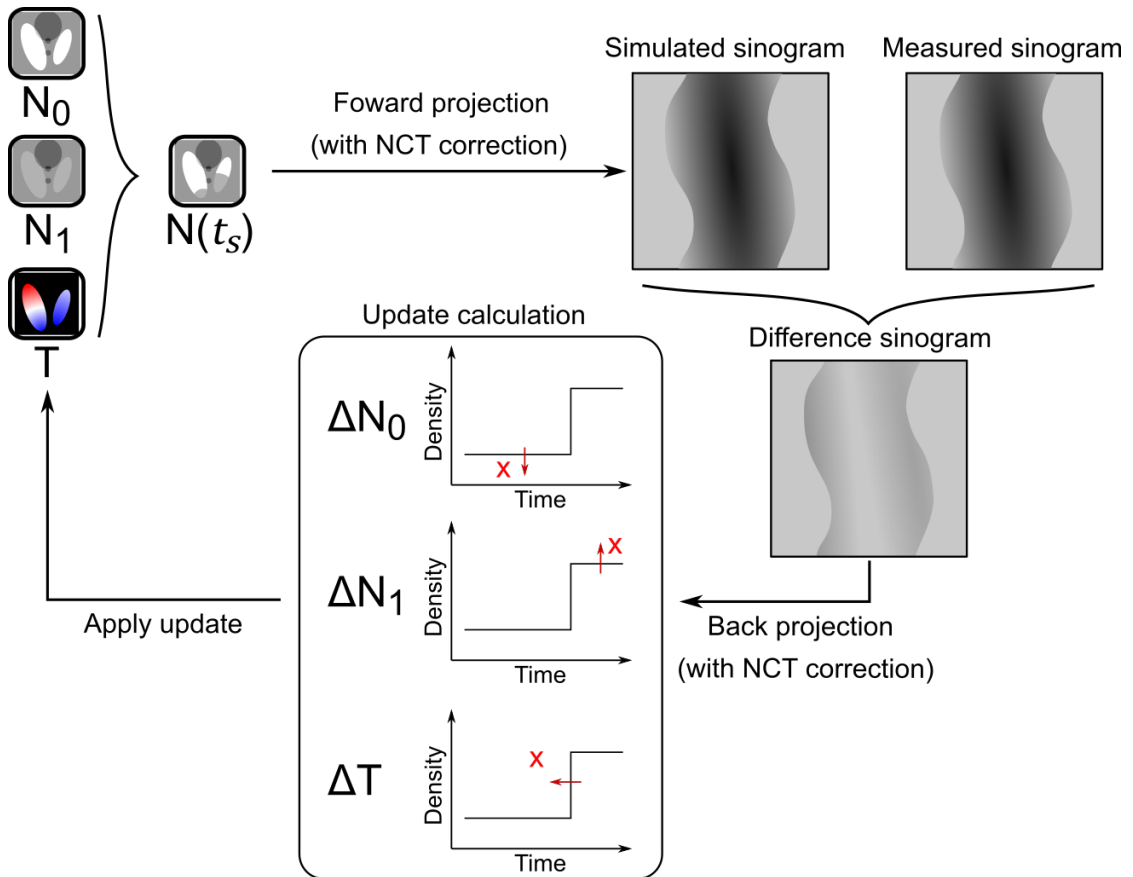


Figure 5.9. Illustration of the sparse dynamic reconstruction technique. Sub-figures within the “update calculation” box illustrate the update strategy, where the step-function represents the current model, the red cross represents an example of a change suggested by the back-projected correction $N_c(t_s, \vec{r})$. For illustration purposes we portray corrections at three different values of t_s . The arrows represent direction of refinement for different variables N_0 , N_1 and T given by Eqs. (5.15)-(5.17).

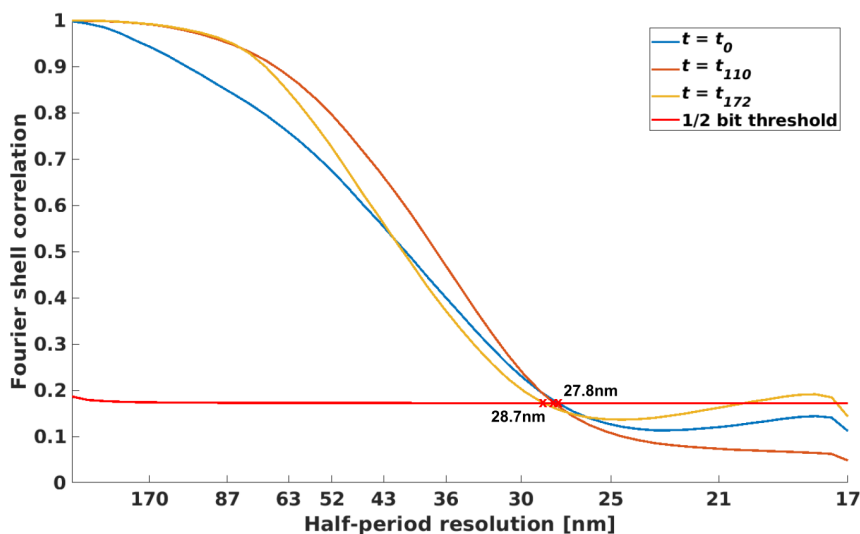


Figure 5.10. Fourier shell correlation (FSC) curves of selected timeframes reconstructions from two independent subsets of the data. Half-period spatial resolution is given by the first intersection with the 1/2 bit threshold curve.

5.8.6 Numerical Simulations

For demonstration and characterization of the sparse dynamic reconstruction method, we carried out numerical simulations and reconstructions. In this manner we could study, for example, the effects of noise and other mismatches between the dynamics and the models used for reconstruction.

For the first scenario, we simulate a liquid filling process in a two-phase porous material. The model is generated with a pillar shape within an array of $200 \times 200 \times 5$ voxels, and the pores are filled with simulated liquid starting from the pore surfaces to the centre, as shown in the top row of Fig. 5.11a. The diameter of the pillar is 160 voxels, which means that the number of projections needed to satisfy the Crowther criteria is 250. Within each time frame, 6 projections were simulated at different sample rotation angles, which corresponds to a sparsity ratio of 2.4%. A total of 80 time frames were simulated, the liquid filling starts at the 20th time frame and finishes at the 50th frame.

The reconstructed dynamic process from these projections is shown in the bottom row of Fig. 5.11a. The results agree quite well with the ground truth, both on the filling time and shape of the liquid-filling front. Quantitative comparison of the total amount of liquid intake, shown in Fig. 5.11c, also shows good agreement between the model and reconstruction. Figure 5.11b shows the values of N_0 , N_1 and T , which uniquely define the dynamic process, top and bottom panels show the model and the reconstruction, respectively. The normalized root-mean-square error (NRMSE) for the transition time T

was 1.38 time frames, which indicates a relatively accurate reconstruction of the dynamic process with 30 time frames duration.

The second simulation is intended to evaluate the robustness of the reconstruction method against noise, in particular to understand the effect of sparse sampling and compare directly to conventional sampling that satisfies the Crowther criteria. The liquid-filling simulation was repeated with different sparsity-sampling ratios ranging from 1% to 50%. Random noise of Gaussian distribution with 2% standard deviation of the average value of the projections was added to the projections to simulate measurement noise. The error on the reconstruction was estimated using the NRMSE, given by

$$e = \sqrt{\frac{\sum_t \sum_{\vec{r}} [N(\vec{r}, t) - N_m(\vec{r}, t)]^2}{n_V n_t}}, \quad (5.21)$$

where $N(\vec{r}, t)$ denotes the reconstructed tomograms at each time frame, $N_m(\vec{r}, t)$ denotes modelled tomograms at each time frame, or ‘ground truth’, and n_V and n_t denote the total number of voxels and time frames, respectively.

The NRMSE versus sparsity ratio is shown in Fig. 5.12. The results were compared with the reference value of conventional filtered back-projection (FBP) reconstructions with the same amount of noise added per projection and with full angular sampling, which corresponds to 250 projections. As expected, the error drops with higher sparsity ratio, and even outperforms the conventional FBP method at >15% ratio. This is due to the iterative refinement, and the fact that we use in our reconstruction a large number of projections, *i.e.* all time frames simultaneously. In the range of 3% to 15% sparsity ratio, the error is relatively constant, and it grows more sharply when the ratio goes below 2%. Notice that two sample states, N_0 and N_1 , are to be reconstructed from 80 sparsely sampled tomograms at different time frames. The latter gives lower-bound ratio of $2/80$ or 2.5% sparsity ratio, in order to have enough total projections to reconstruct the two sample states, which agrees with the observed sharper increase of the error below 2% sparsity ratio.

Another important aspect to consider is the performance of the reconstruction code when the assumption of a single step-function change per voxel is not satisfied. Here we consider the case of a gradual linear transition of material density. Again, a pillar of porous material was generated with 160 voxels diameter within an array of 200x200x5 voxels. In the dynamic process, the density of part of the structure is increased linearly over 40 time frames, within a total period of the simulation of 80 time frames. The same sparsity ratio of 2.4% was applied, with 6 projections simulated at each time frame. The model and reconstructed results are shown in Fig. 5.13a.

The dynamics per voxel are modelled in the reconstruction with step function, which does not allow representation of a gradual change. The reconstruction algorithm resolves this by splitting the temporal transition into several voxels, such that each voxel has a step function but the average of a few voxels undergoes a more gradual transition. In the reconstruction in Fig. 5.13b this can be observed as noise that resembles a salt-and-pepper pattern. In effect, the algorithm creates a compromise of the spatial resolution of

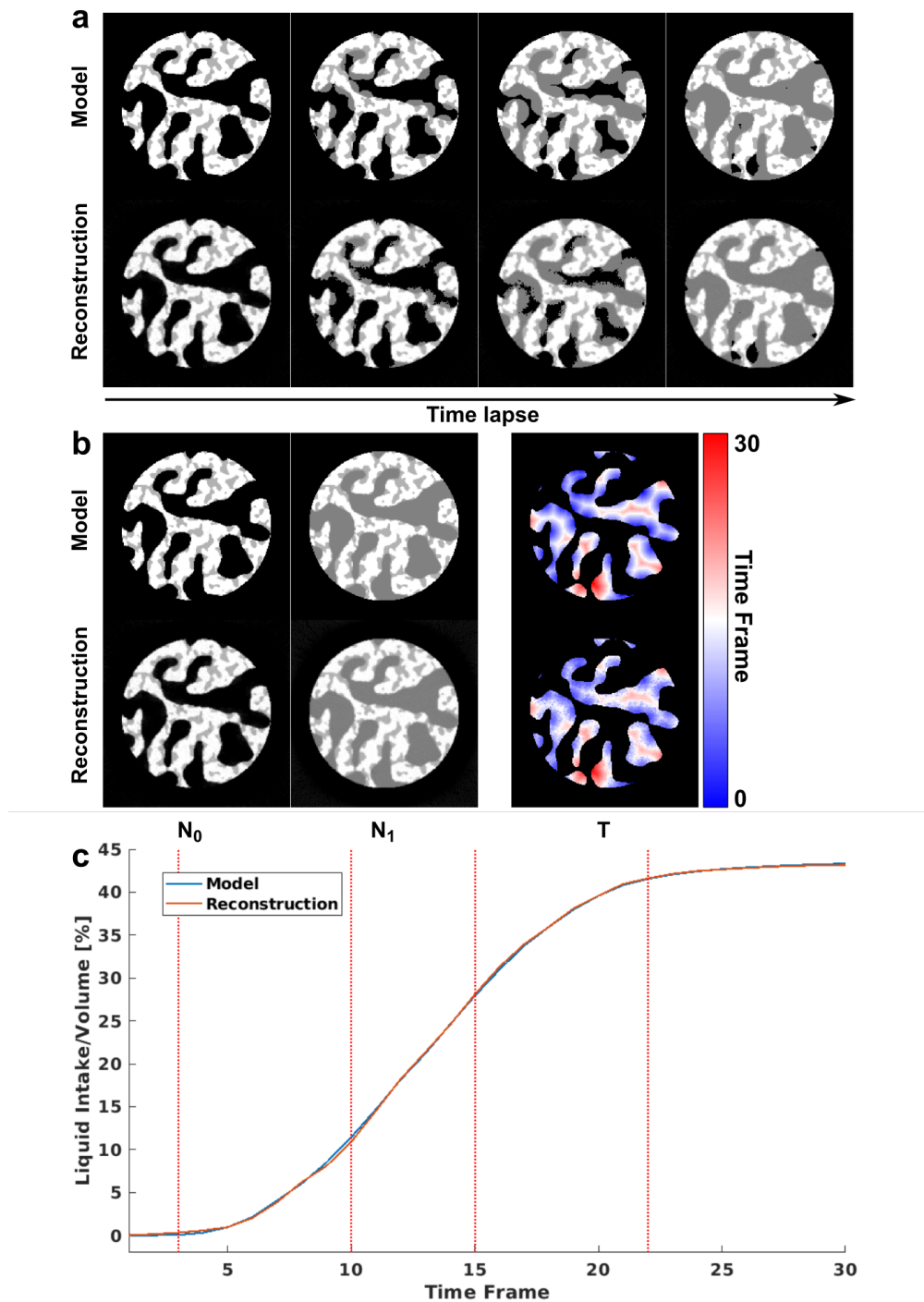


Figure 5.11. Numerical simulation of liquid filling process in a porous sample. a) Model and reconstructed time-lapse tomograms of the dynamic process. b) Model and reconstructed N_0 , N_1 and T . c) Comparison of total amount of liquid intake over time calculated from the model and the reconstruction. Dashed lines refer to the time frames shown in (a).

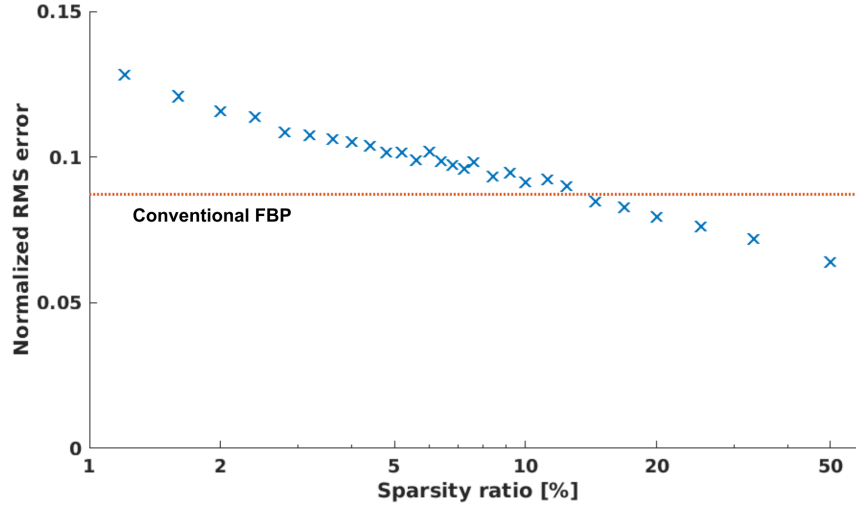


Figure 5.12. Noise level of the reconstructions at different sparsity ratios. The NRMSE were calculated between the reconstruction and the model, or ‘ground truth’. Dashed line represents the noise level of the conventional filtered back-projection (FBP) method, which is applied without sparse sampling, as reference.

the dynamics in order to accommodate a more complex temporal behaviour. In Fig. 5.13a one can also see that the changing voxels were correctly identified, so the spatial locations of the transition are recovered correctly.

The value for the average density of a region of 20×15 voxels, indicated by a red square in Fig. 5.13a, is shown in Fig. 5.13c. The average shows a relatively good match with the model, indicating that the method still provides useful information for these cases. In Fig. 5.13c, small differences of the average values for the start and the end states can be observed. These differences are potentially due to the step-function model not being able to capture the small changes at the very start and very end of the transition, resulting in a slight delay of the reconstructed start time of transition, and conversely, an earlier end time for the end of the dynamics. This mismatch in the reconstruction of the exact start and end of the dynamics also causes a small bias in the reconstructed densities of N_0 and N_1 . While these effects can be removed by introducing a more complex function for the voxel-level response, they can alternatively be alleviated by up-sampling the reconstruction voxels. With the latter strategy a resolution element in the reconstruction contains several voxels, which the algorithm can then leverage to represent more complex dynamics. It should be noted that in our experimental demonstration we apply this spatial oversampling by using a reconstruction voxel size of 17.4 nm, while the resolution is about 28 nm.

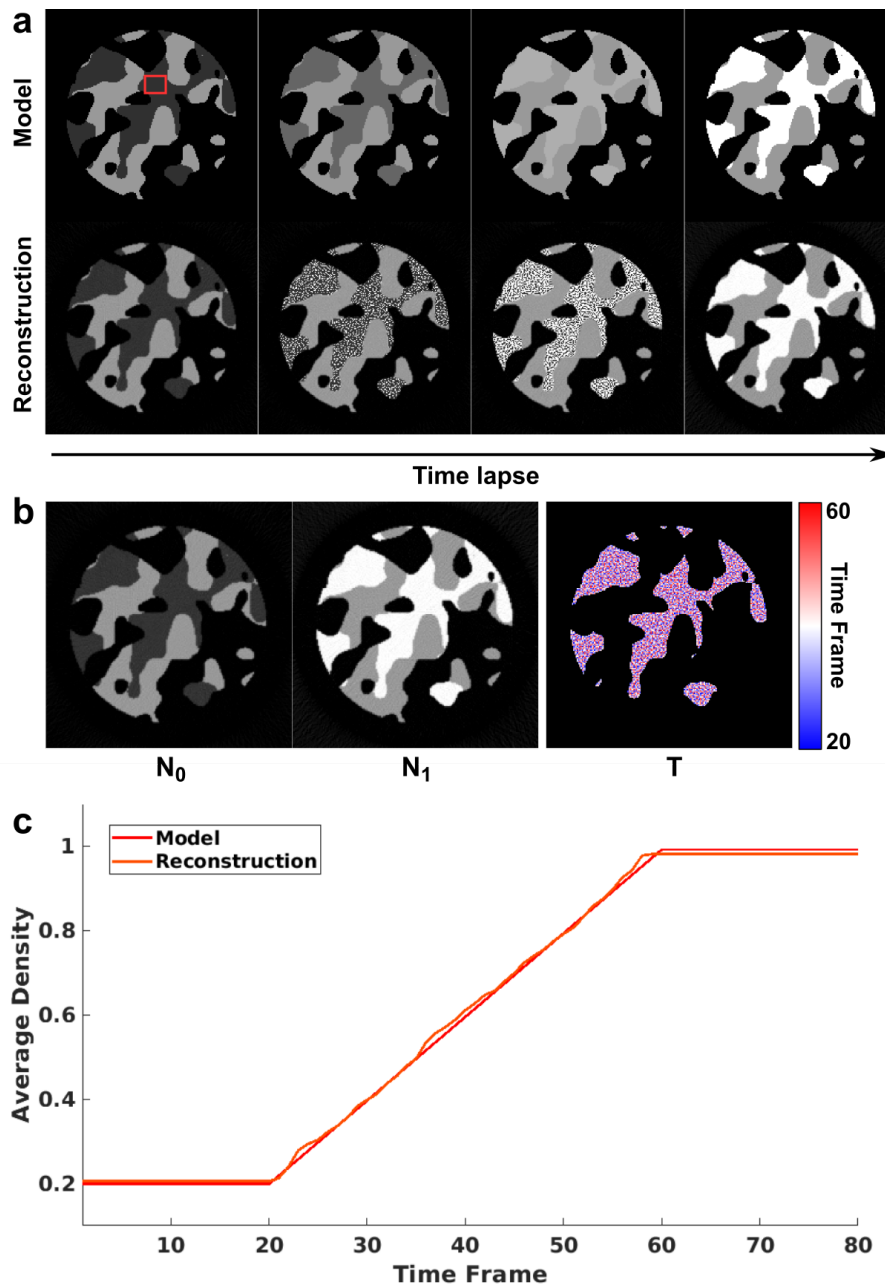


Figure 5.13. Simulation of gradual linear local dynamics. a) Model and reconstructed time lapse tomograms of the dynamic process based on slow linear changes. b) Reconstructed results of N_0 , N_1 and T . c) Comparison between model and reconstructed average density dynamics of a 20×15 -voxel region marked by red rectangle in a).

5.9 Acknowledgements

The authors acknowledge the Paul Scherrer Institute, Villigen PSI, Switzerland, for the provision of synchrotron radiation beamtime at the cSAXS beamline of the Swiss Light Source. The work of Zirui Gao and Johannes Ihli was supported by funding from the Swiss National Science Foundation (SNSF), project numbers 200021_178788 and PZ00P2_179886, respectively. Christian Appel has received funding from the European Union's Horizon 2020 research and innovation program under the Marie Skłodowska-Curie grant agreement No 884104 (PSI-FELLOW-III-3i) and from Chalmers initiative for advancement of neutron and X-ray techniques. We thank E. A. Mueller Gubler for assistance with sample preparation and X. Donath for technical support.

5.10 Author Contributions

M. G.-S., Z. G., M. H, C. A., and J. I. conceived the project. K.B., K.J. and B.J.M.E., provided and prepared the catalyst coated membrane. Z. G., C. A., M. G.-S., M. H., and J. I. performed the PXCT experiments. Z. G. developed the reconstruction algorithm and processed the data. Z. G., C. A., and M. G.-S. analyzed the results. Z. G., M. G.-S., and C. A. wrote the manuscript. J.I., M. K., and M. S. contributed to discussions and provided suggestions to the manuscript. All authors read and approved the manuscript.

Nanoscale *operando* Laminography of Solid-state Lithium Battery

This chapter includes work in collaboration with Bingkun Hu and Ziyang Ning, and is part of their PhD projects in Department of Materials, University of Oxford, UK.

6.1 Introduction

Lithium-based rechargeable batteries have become a cornerstone for modern life, with their applications extending from electronics to transportation. In lithium batteries, the cathode material is the fundamental component which stores and releases electric energy during charge and discharge cycles. Therefore, the electrochemical properties of cathode materials and their structural and compositional changes during charging and discharging processes directly determine the performance of the batteries [203–205].

When studying the dynamic changes of cathode materials during working cycles, the main challenge is that the most interesting changes usually occur at a nanoscopic length scale, and nanoscale imaging resolution is required to characterize them [206, 207]. This is due to the fact that the working mechanism of these materials is based on insertion and removal of Li-ions at the atomic level, and it is the unique electrochemical response to this lithiation / delithiation process that defines the characteristics of different materials [208, 209]. Moreover, this demand for nanoscale resolution makes it extremely challenging to conduct *operando* imaging on cathode materials, because of both the difficulties of designing the imaging hardware and battery setup for such experiment, and the limitations of imaging speed due to the long measurement time required for high-resolution imaging [210].

Due to these difficulties, previous studies on *operando* imaging of cathode materials were mostly conducted in two alternative ways. The first is to image specimens of cathode materials extracted from of cycled batteries at different states of charge [113, 211], which can achieve nanoscale resolution on a micrometer-sized sample volume, but is prone to changes and/or damage to the material during the extraction process, and cannot image

the same specimen twice at different stages of working cycle. Therefore, one cannot be sure that fractures or other defects have occurred because of charge or discharge, or if they were the result of mechanical stress. The second way is to use a low rate for cell cycling, or to pause the cycle during charge or discharge, in order to gain enough time for nanoscale imaging [65, 212]. While this approach can track the same specimen through the whole process at high resolution, the functional properties of cathode materials are often rate-sensitive, and their performance and degradation might be significantly different when working at slow cycling speed compared to normal working speed [213, 214].

We here propose a new imaging approach, which uses all-solid-state lithium batteries, ptychographic X-ray laminography, and sparse dynamic imaging to conduct *operando* imaging on single particle of cathode materials with sub-100 nm spatial resolution and at a cycle rate of 0.1 C, or 10 hours per charge / discharge. The method is employed to investigate batteries with two different types of commonly-used cathode materials, polycrystalline $\text{LiNi}_{0.8}\text{Mn}_{0.1}\text{Co}_{0.1}\text{O}_2$ (NMC811) and LiCoO_2 , and to resolve the dynamic transitions of these materials in the first two charge-discharge cycles.

All-solid-state lithium batteries with ceramic solid electrolytes are considered as next-generation batteries because of their greater stability and safety, as well as higher energy density compared to conventional liquid-state lithium-ion batteries [215, 216]. This new technology also facilitates nanoscale imaging of the cathode materials, because the all-solid-state battery designs provide high resilience and stability against X-ray radiation damage and scanning motion.

Computed X-ray laminography is a three-dimensional microscopy technique where the axis of rotation is not perpendicular to the illumination direction [39, 217]. This tilted measurement geometry allows imaging of large-area planar samples without extraction of pillars, thus is especially suited for *operando* imaging of solid-state battery cells. For this measurement, we are able to focus the imaging field of view on a single cathode particle of 10 μm diameter, buried within the cathode layer of battery cells with 5 mm diameter and 350 μm thickness. This configuration of imaging of a small volume contained in the whole sample, known as interior laminography, greatly enhances measurement speed and allows nanoscale resolution to be reached, while avoiding drastic modifications of size and shape of the battery cells, which might change their electrochemical behaviors significantly.

Lastly, by applying an extended approach of the sparse sampling method for dynamic imaging, as described in Chapter 5, to the laminography geometry and to a model that includes several dynamic changes per voxel, we were able to reach a temporal resolution 27 times higher than that of conventional laminography imaging. This enables dynamic imaging on the cathode particles at a rate of 0.1 C, or 10 hours per each charge / discharge, of the battery cells, with around 10 hours pause between each charge / discharge. This configuration allows *operando* imaging at charge rates closer to the normal working conditions of these batteries, which are also comparable to the rates commonly used for performance benchmarking in labs [218, 219]. The increased-speed of our method gives it higher potential to resolve the degradation mechanisms of these cathode materials under

their designed working conditions.

6.2 Methods

6.2.1 All-solid-state Battery Cell

The design of the battery cells used for the experiment is illustrated in Fig. 6.1. The core of the battery cell is composed of a lithium metal anode, the Arggyrodite ($\text{Li}_6\text{PS}_5\text{Cl}$) solid electrolyte, and the composite cathode in the bottom layer of the electrolyte. For this experiment we used two types of materials as the cathode: $\text{LiNi}_{0.8}\text{Mn}_{0.1}\text{Co}_{0.1}\text{O}_2$ (NMC811) (D50: 9-15 μm) and LiCoO_2 . The composite cathode powders were prepared by mixing NMC811 / LiCoO_2 , $\text{Li}_6\text{PS}_5\text{Cl}$, and carbon nanofiber at a weight ratio of 20:70:10. The loading of cathode active material is reduced to 0.4 mg/cm^2 to make a sparsely distributed layer of cathode particles. To prepare the solid-state batteries, composite cathode powders and 10 mg arggyrodite powders are pressed together into a pellet in a stainless steel die set at a pressure of 400 MPa. A 5 mm Li foil with a thickness of about 50 μm is then pressed onto the pellet as the anode. The size of the battery core is 5 mm in diameter and 350 μm in thickness. Two current collectors made of thin foil of copper and aluminum are attached to anode and cathode sides, respectively. A hole of 3 mm diameter was punched in the center of the copper collector, to allow the X-ray beam to go through without interacting with the copper foil. All components were packed and sealed into a pouch made of plastic and aluminum foil under vacuum without exposure to air.

6.2.2 X-ray Ptychographic Laminography

The experiments were performed at the cSAXS beamline, Swiss Light Source, Paul Scherrer Institut, Switzerland. The laminographic nano-imaging (LamNI) instrument, which is designed for high-resolution 3D scanning X-ray microscopy via hard X-ray ptychographic laminography, is used for the measurements [39, 40].

In the LamNI, the battery cells were mounted onto a tilted plane with respect to the X-ray beam, as shown in Fig. 6.2. The design of the battery allows the X-ray beam to penetrate through the whole cell at this tilted geometry while avoiding the Cu current collector, which is important since the X-ray absorption factor of copper is much higher compared to other components. As the X-ray beam passes through the whole cell, the only non-uniform layer in the beam path is the cathode particles embedded inside the solid electrolyte, which also generates the strongest X-ray diffraction. This configuration enables interior laminography, which focuses on a small thickness range around the particle of interest, instead of the thickness of the whole battery cell, and in turn greatly enhances the speed of laminography imaging.

For ptychography imaging, an X-ray energy of 12.4 keV was selected with a double

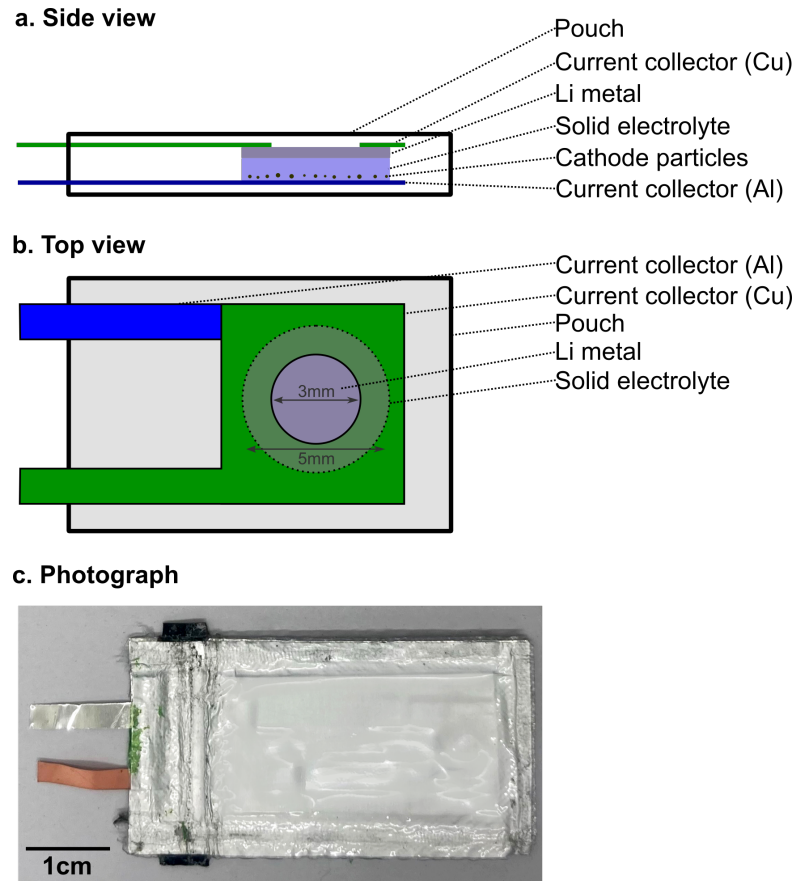


Figure 6.1. Solid-state battery design. a) and b) Side view and top view of the battery cell design. c) Photograph of a real cell.

crystal Si(111) monochromator. This energy is higher than the optimal operation energy of the beamline, which is at 6.2 keV, and it causes less coherent flux to be available and lower efficiency of the Fresnel zone plate lenses, resulting in reduced imaging quality. However, it is needed in this interior laminography configuration to penetrate the entire thickness of the battery cell. The X-ray beam is focused with a Fresnel zone plate of 100 μm diameter with designed wavefront perturbations [118], which is located 56.5 mm upstream of the sample to create an illumination of approximately 6 μm diameter on the plane of the sample particle. The X-ray diffraction patterns were measured with a detector downstream. For 2D projections, a circular field of view of 30 μm diameter on the plane of the sample was used, with scanning step size of 1 μm and exposure time of 0.2 seconds. Each 2D ptychography measurement took 89 seconds. The battery cell was then rotated in its plane around a rotation axis that is tilted to an angle of 61° with respect to the X-ray beam propagation direction, and is perpendicular to the battery plane, as shown in Fig. 6.2. In this laminography geometry, multiple projections are measured at different rotation angles in a range of 0° to 360° , and the three-dimensional image of the sample can be reconstructed from these projections.

The cathode layers in these battery cells were fabricated with a reduced density of particles, such that the sample can be positioned with only one cathode particle in the beam path for the whole rotation. This way we can image a volume of 30 μm diameter that contains only the particle of interest, compared to the total thickness of 350 μm of the entire cell. This adaptation of interior laminography speeds up the measurement significantly and concomitantly improves achievable resolution for a given measurement time.

The battery cell was connected to a potentiostat to control the charge / discharge cycles and monitor the voltage of the cell. For *operando* imaging, the charge and discharge processes were synchronized with image acquisitions using the potentiostat control software.

6.2.3 Sparse *operando* Laminography

For the *operando* measurements, two pristine battery cells were selected with different types of cathode material, namely cell A with NMC811 and cell B with LiCoO₂. Both cells were set to undergo two full cycles of charge-discharge, while acquiring continuously the laminography projections.

The configurations of battery cycles were similar for both cells, as shown in their voltage profiles in Fig. 6.3. The cells were first measured in a static state for 10-15 hours to acquire images at their pristine states, and were then charged to 4.3V for NMC811 and 4.2V for LiCoO₂ under constant current. The charging current is calculated from the total capacity of the cell based on their loaded amount of cathode material, and corresponds to a charge / discharge rate of 0.1 C for these batteries. After the cells were fully charged, the charging current was removed by opening the circuit, and they were kept at charged state for 10 hours for the second set of static measurements. After that,

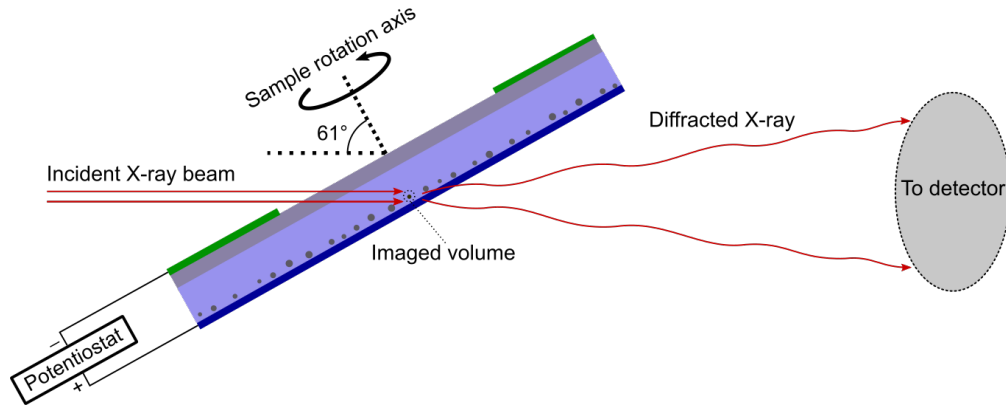


Figure 6.2. X-ray laminography measurement setup. The battery cell was mounted on a tilted plane with respect to the X-ray beam for laminography imaging. Imaging field of view was focused on a single particle in the cathode layer.

the cells were discharged under the same current until 2.7V, followed by another pause for 10 hours. This is followed by the second charge-discharge cycle with the same current settings and slightly shorter pause time for scheduling purposes.

During the first charging process of cell B, a fraction of the data were lost due to unexpected beamloss of the synchrotron. Apart from this glitch, the voltage profiles of both cells match quite well with the standard curves of these cathode materials. This confirms that the sample particles were measured under *operando* conditions that are very similar to their normal working states.

To enable dynamic 3D nanoscale imaging at this speed, we applied a sparse sampling method to the laminography rotation angles. This implementation is very similar to the approach for tomography as described in Section 5.3 of Chapter 5. As shown in Fig. 6.4, 20 projections were measured from 0° to 360° rotation angle in each sparsely sampled laminography dataset, or laminogram, which corresponds to 3.7% of the 544 projections required by the laminography sampling criteria [39] at 100 nm resolution. An angular offset was added to the start of each laminogram for more efficient angular sampling.

6.2.4 Reconstruction

The 2D ptychograms were reconstructed using the PtychoShelves package [50], by applying 300 iterations of difference map [44] followed by 100 iterations of maximum likelihood refinement [45]. After that, all the projections for each sample were aligned with a tomography alignment approach based on multi-resolution projection matching via tomographic consistency [170]. The aligned projections were then used as input for the sparse dynamic reconstruction method for laminography.

This reconstruction method is based on the same concept as the sparse dynamic

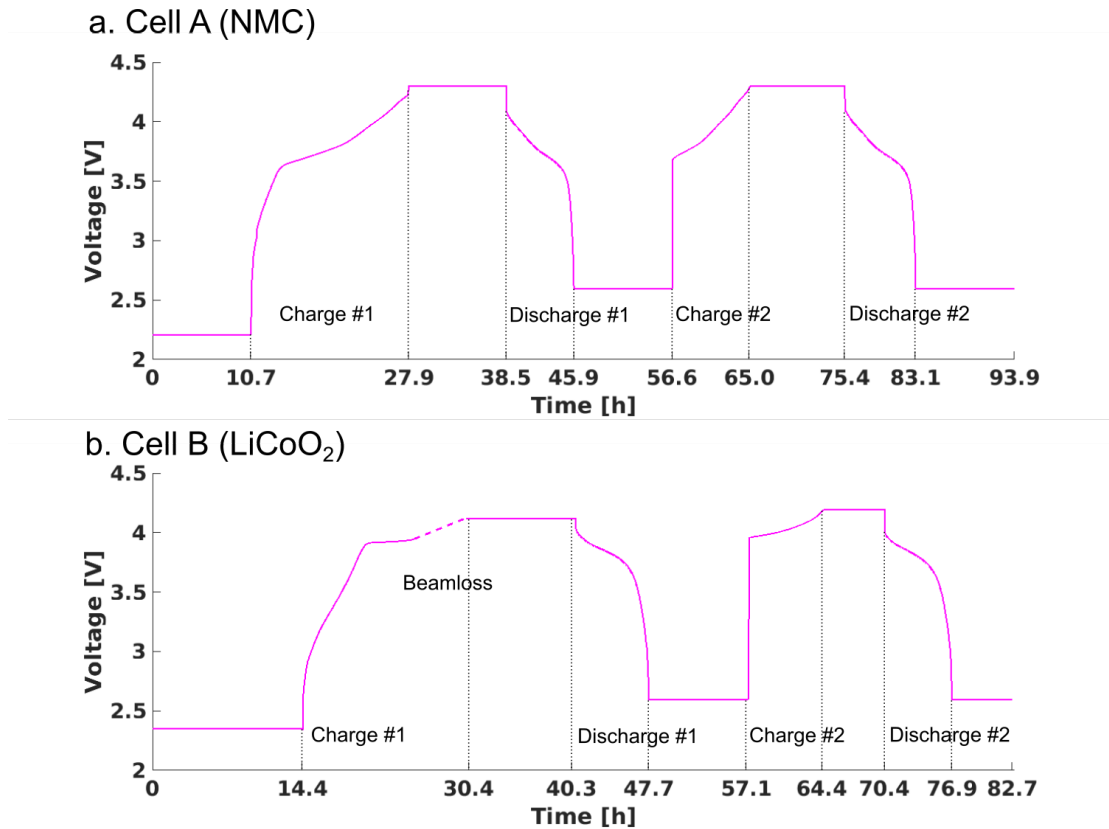


Figure 6.3. Voltage profiles of the battery cells during measurement. Each battery cell went through two charge-discharge cycles, with pauses between each charging and discharging process, for the *operando* measurements. For cell B, an unexpected beamloss caused some data to be missing during the first charge.

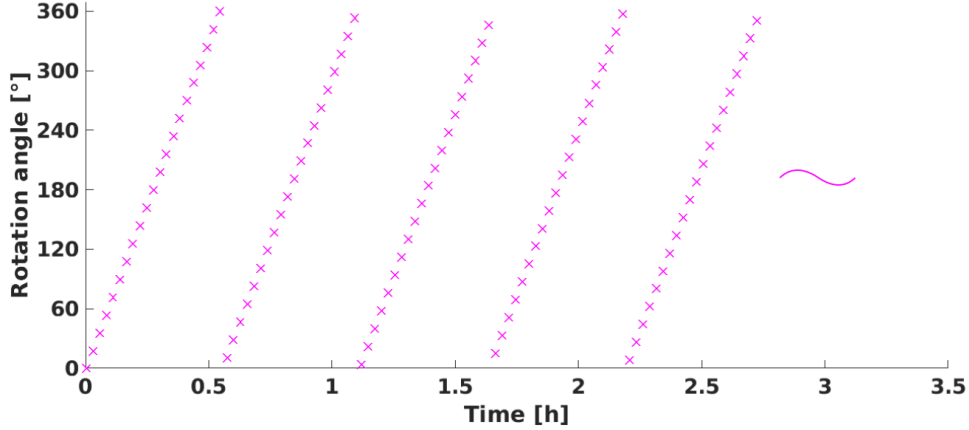


Figure 6.4. Acquisition scheme of laminography rotation angles. In each sparsely sampled laminogram acquisition, 20 projections were measured with rotation angles from 0° to 360° . An angular offset was added between each laminogram measurement for more efficient spatial sampling.

tomography reconstruction method described in Section 5.8.4. In the case of cathode particles, the nonrigid correction method was not applied because the particles were embedded in solid electrolyte and did not show signs of strong deformation during the measurement. The reconstruction of the dynamic process uses the same model as in Section 5.4, which represents the dynamic changes with the starting state N_0 , the end state N_1 and the transition time T . In the case of the battery cells, this modelling is applied sequentially to each charge and discharge process, resulting in a total of 5 sample states for each static period, and 4 transition times for each charge or discharge. For laminography reconstruction, the tomographic forward and back projections used in Eq. (5.12) to (5.14) were replaced with the equivalent forward and back projections under laminography geometry. The iterative update functions were the same as given in Eq. (5.15) to (5.20). The updates were applied sequentially for four randomly selected time points, one in each charge and discharge process, and repeated over for 5000 iterations until convergence.

As demonstrated in Chapter 5, the sparse dynamic reconstruction method allows the dynamic process to be reconstructed at a temporal resolution that is almost two orders of magnitudes higher than conventional methods, without loss in spatial resolution. The sparsity method relies on the changes to be monotonic during the dynamic process, which is a reasonable approximation for each charge or discharge of the battery cathode particles. In this case, the temporal resolution of the reconstruction is given by the measurement time of one sparsely sampled laminogram, which is around 30 minutes, as shown in Fig. 6.4. This temporal resolution allows for 16 to 20 time frames to be reconstructed for each charge or discharge process of the cathode particles, which provides a great amount of information for resolving their dynamic changes.

6.3 Results

To showcase the reconstructed results, we took a horizontal slice at a plane parallel to the flat surface of the battery cell, from the reconstructed 3D volume of the cathode particle. The resolved timeframes of this slice at different stages of the battery cycles are demonstrated. Shown in Fig. 6.5 are the results for the NMC811 sample, which include four time frames at different cell voltages in each charge or discharge process. The diameter of the particle is around 10 μm and the pixel size of the images is 70 nm. The color-coding of the images is based on relative electron density (ED) values of the particle with respect to the surrounding electrolyte, noting that for laminography, only the difference in ED values can be quantitatively resolved [39]. Therefore, reference densities of the substrate material are needed to derive absolute values of ED.

The presented results contain abundant information, with clear indications of different types of changes in the particle. First is the decrease and increase of ED of the whole particle during the charge and discharge, respectively. This is more clearly demonstrated by computing the difference of relative ED before and after each charge and discharge, shown in Fig. 6.6a. These changes in density match the expectation based on delithiation and lithiation of the NMC811 particle, which acts as the fundamental mechanism for the cathode material to store and release energy.

The high temporal resolution of the method allows fine characterization of ED changes in the whole process, for example, the average relative ED of the extracted slice of the NMC811 particle was calculated at each time frame, and the results are shown in Fig. 6.6b. Comparing with the voltage profile of the battery cell in Fig. 6.6c, most of the periodic changes of average ED matches the charge and discharge cycles. However, in some time periods, marked by red arrows in Fig. 6.6b, the density changes appear to be toward the opposite direction of the charge or discharge process they are in. This finding remains to be validated while taking into account possible changes of the density of the electrolyte, which affects quantification of relative density. Nevertheless, this response may suggest a different behavior or non-equilibrium state of the NMC811 particle during normal charging cycles.

Moreover, the nanoscale imaging resolution allows changes at a smaller scale to be detected. For example, the formation of a crack in the center of the particle can be observed in both charging processes, marked by red arrows in Fig. 6.5, and the crack disappears during discharge. This phenomenon has been reported in previous studies, and is believed to be caused by the volume shrinkage and expansion of the NMC811 during charge and discharge [113, 220]. Obtaining *operando* images of the crack formation is an important step forward toward understanding the structural changes of NMC materials in battery cycles.

For the LiCoO_2 sample, results with similar arrangements are shown in Fig. 6.7, with one frame missing in the first charge due to beamloss. Again, the same trends of density changes as result of delithiation and lithiation can be observed in the charging and discharging process, respectively. Differences between the start and end state of each

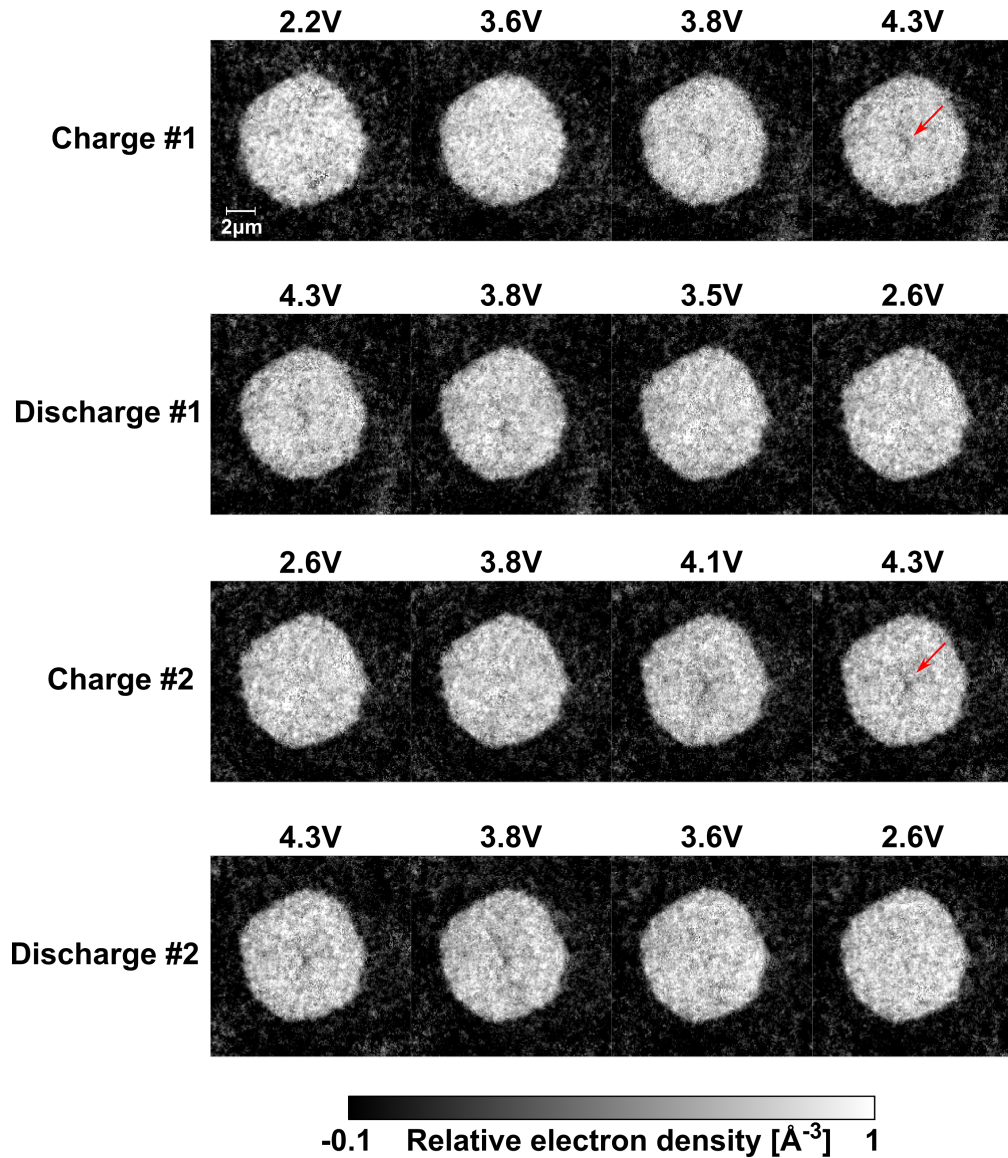


Figure 6.5. Reconstructed images of a horizontal tomographic slice in the NMC811 sample at different time frames. Shown are four time frames at different voltages in each charge and discharge process. Red arrows point to a crack inside the particle that appeared during both charging process.

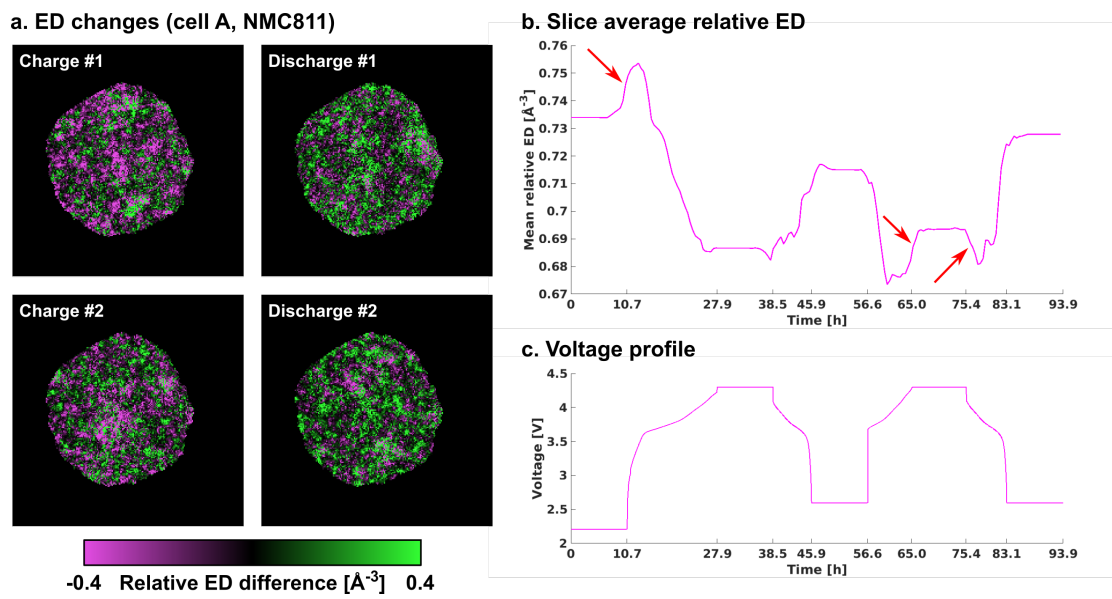


Figure 6.6. Analysis of ED changes in the NMC811 sample. a) Changes of relative ED in each charge / discharge process, *i.e.* differences of relative ED between reconstructed images before and after each process. b) Average relative ED of the demonstrated slice in the whole measurement. Red arrows indicate time periods in which the ED changes are opposite to the normally expected direction. c) Voltage profile of cell A during the whole measurement.

charge and discharge are shown in Fig. 6.8a. However, the volume changes of LiCoO₂ particles are the opposite of NMC811, namely the unit cell volume of LiCoO₂ expands while charging to 4.2 V (Li_{0.5}CoO₂) and shrinks during discharge [221]. This behavior can be observed in the reconstructions, by looking at the gap between smaller particles marked by the red arrow in Fig. 6.7, which appears to be squeezed when charging, and opens again when discharging.

The evolution of the average ED of this tomographic slice is shown in Fig. 6.8b, and the voltage profile of this battery cell is shown in Fig. 6.8c. Apart from the first charge, trends of ED changes in the whole time period match the battery cycles. The increase of relative ED at the start of the first charge, marked by red arrow in Fig. 6.8b, might be caused by the decomposition of argyrodite at high voltage in pristine LiCoO₂ battery, which can result in density changes of the surrounding electrolyte and affects the reconstructed relative ED of the particle.

In this section, we presented the sparse tomography reconstructions and preliminary analysis of the results. Already, these results show the capability of sparse laminography approach to conduct *operando* nanoscale imaging of the cathode particles with high temporal resolution. We believe that further analysis of the results could potentially provide new insights towards understanding the working mechanisms of these promising cathode materials.

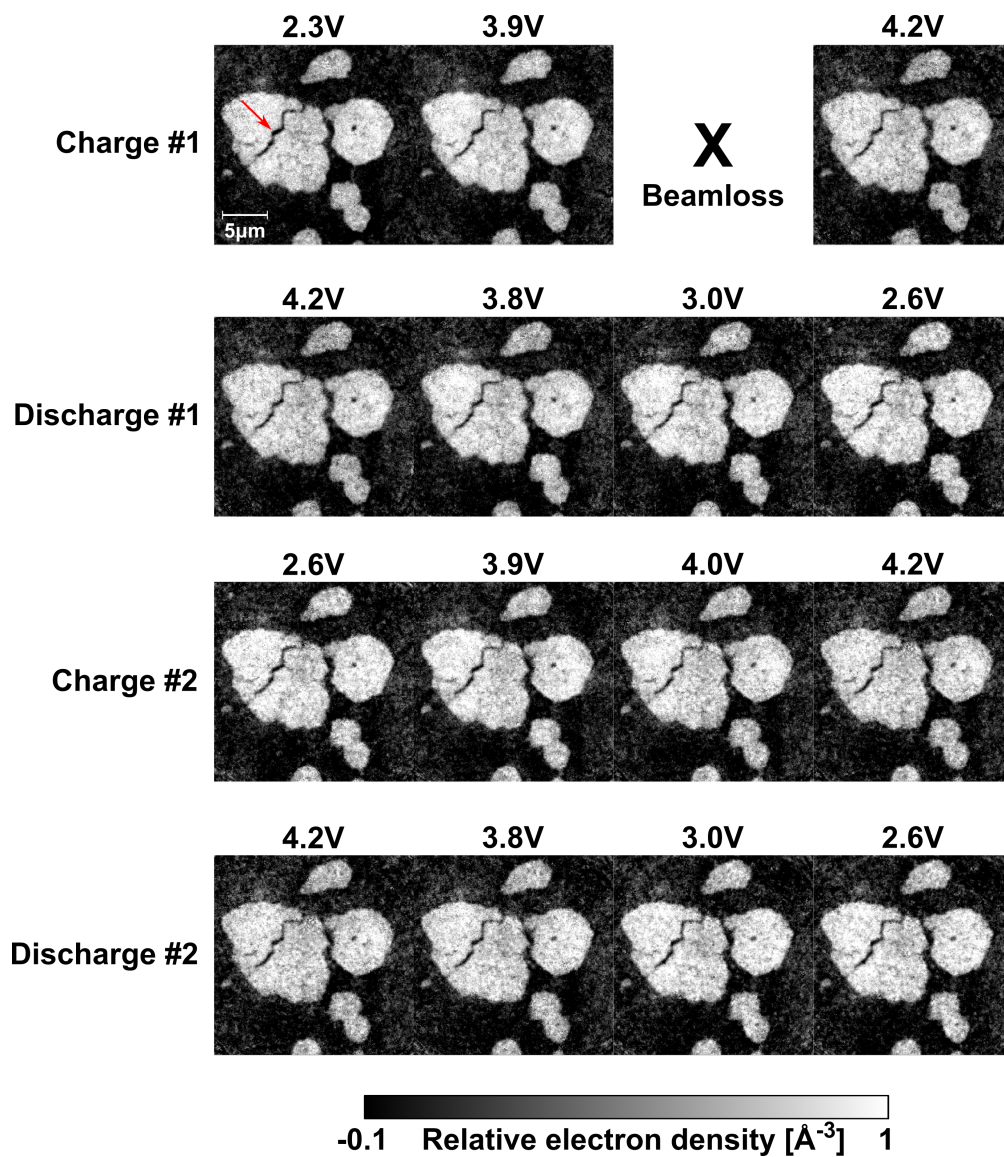


Figure 6.7. Reconstructed images of a horizontal tomographic slice in the LiCoO_2 sample at different time frames. Shown are four time frames at different voltages in each charge and discharge process. The red arrow points to a gap between two particles that closes and opens in each charge and discharge process, respectively.

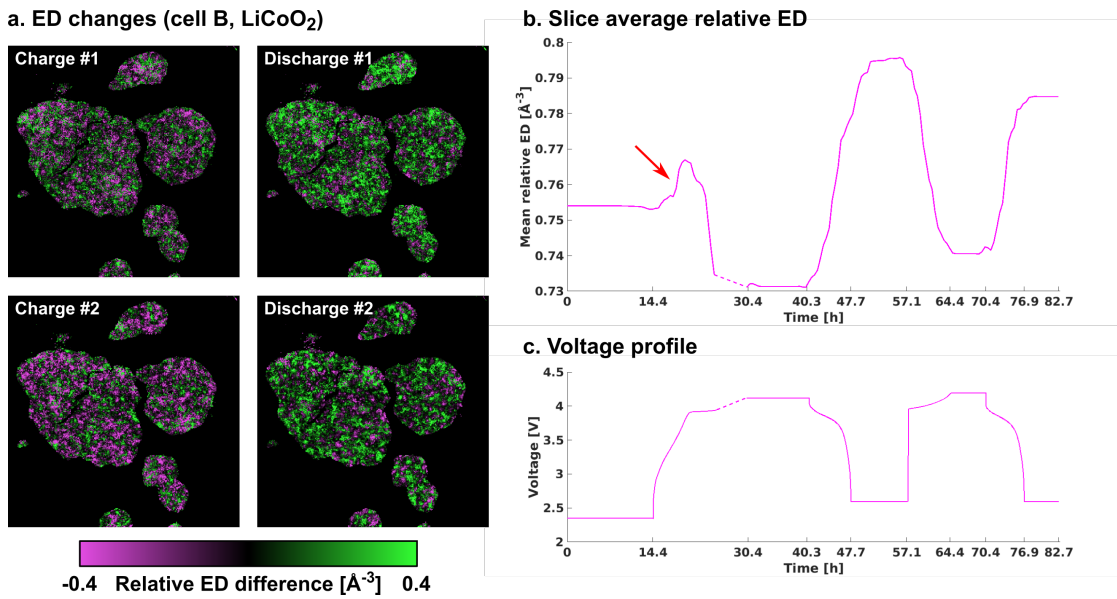


Figure 6.8. Analysis of ED changes in the LiCoO₂ sample. a) Changes of relative ED in each charge / discharge process, *i.e.* differences of relative ED between reconstructed images before and after each process. b) Average relative ED of the demonstrated slice in the whole measurement. The red arrow indicates a time period at the start of the first charge in which the ED change is opposite to the normally expected direction. c) Voltage profile of cell B during the whole measurement.

6.4 Conclusion and Outlook

Presented in this chapter is a generalization of the sparse dynamic 3D imaging method, utilized for *operando* laminography of solid-state batteries. The approach uses the same concepts, including sparse sampling, state-transition model, and iterative reconstruction method, as the dynamic tomography method covered in Chapter 5, but is different from the original method in two aspects. First, it uses the laminography geometry instead of conventional tomography for three-dimensional imaging, and second, it is applied to a series of monotonic processes, namely the charge / discharge cycles of battery cells, that are combined into a full dynamic imaging procedure. Moreover, the approach utilizes interior laminography configuration to significantly speed up the measurements for thick samples. Although the imaging quality and spatial resolution are worse compared to previous chapters, mainly due to the higher X-ray energy, this configuration allows measurement of normal-sized battery cells, instead of miniaturized designs, which provide higher stability as well as more flexibility for future studies.

In the preliminary analysis, dynamic changes of the NMC811 and LiCoO₂ particles show good agreement with known properties of these materials, including the density changes from lithiation or delithiation process, and opposite types of structural changes in these two materials. Moreover, the nanoscale imaging resolution and relatively fast cycle speed, enabled by high temporal resolution of the method, allow *operando* characterization of nanoscopic changes inside these cathode particles under their designed working conditions.

To conclude, our method is able to provide *operando* images of the cathode material particles inside all-solid-state battery cells, with minimal changes to the design and working conditions of these cells. As a result, the voltage profile of these cells matches well with the standard behavior of the electrolyte and cathode materials. With nanoscale imaging resolution, we are able to resolve the lithiation / delithiation process as well as the structural changes of the imaged particle inside a working battery. Our results provide highly valuable information for understanding the working mechanism of these materials at nanoscopic level.

While further analysis is still in progress, the results already demonstrate the capability of our method to resolve 4-dimensional images of *operando* battery cathode particle samples accross multiple charging cycles. Together with the results in Chapter 5 for the hydration of fuel cell catalyst, we have demonstrated the effectiveness and potentials of the sparse dynamic 3D imaging approach for boosting the speed of *operando* imaging with nanoscale resolution, and open the possibility of its applications to various other samples in a wide range of research fields, including biology, chemical industry, and electronics.

Summary and Outlook

Presented in this thesis is a novel approach of sparsity implementation for hyperdimensional imaging. It is demonstrated in three applications: hyperspectral ptychographic tomography in Chapter 4, dynamic ptychographic tomography in Chapter 5, and *operando* ptychographic laminography in Chapter 6. The main goal of this approach is to alleviate the speed limitations of tomographic imaging, and to allow hyperdimensional measurements with larger sample volume, higher spatial resolution, and faster speed. These improvements are especially useful in cases where nanoscale spatial resolution is desired. As in such cases, the measurements are much slower, and the total acquisition time or radiation dose on samples become the limiting factors for hyperdimensional imaging.

In the case of hyperspectral tomography of VPO catalysts, demonstrated in Chapter 4, the sparse synthesis is able to reduce the total measurement time by a factor of 9, or to 11% of the time required by conventional methods. This reduction allowed hyperspectral imaging of specimens with 12 μm diameter size at resolution of sub-30 nm half-period to be conducted within days, instead of weeks, which greatly enhances the time and dose efficiency of the imaging method without loss of spatial resolution. It also enables imaging of more samples or larger sample volume in the scheduled measurement time, which is crucial for studies of functional materials, such as these VPO catalysts, in order to obtain statistics over multiple samples or representative sample volumes.

In the case of dynamic tomography and laminography, demonstrated in Chapter 5 and 6, sparse sampling ratios of 1/40 and 1/27 are applied to the acquisitions for measurements of the dynamic process of controlled hydration of a fuel cell catalyst sample, and cathode particles in *operando* solid-state battery cells, respectively. The sparse synthesis in this scenario improves the temporal resolution of 4D imaging method by up to 40 times compared to conventional approaches, enabling its application to dynamic processes which would otherwise be too fast for nanoscale tomography imaging.

The concept of the reconstruction techniques for sparsely sampled measurements is based on modelling of hyperdimensional changes and reducing the number of independent functions to be reconstructed. In most applications of hyperdimensional imaging, changes of the three-dimensional sample properties are not arbitrary and follow certain patterns or correlations across the spectral, time or other extra dimensions. In other

words, instead of reconstructing one independent volume of the sample at each frame of the extra dimension, reconstruction models are applied to capture the majority of these changes to reproduce a close approximation of the hyperdimensional process. In the case of hyperspectral tomography, this is achieved by using a linear PCA model for the voxel-level spectral responses of the catalyst samples and reconstructing the first four PCA components. In the cases of dynamic tomography / laminography, the reconstruction is based on a step-function model for the density changes, which consists of three parameters: the initial state, the final state, and the transition time. These reconstruction models are specifically designed for the presented applications, yet can be easily generalized, or adapted, for various similar instances of hyperdimensional imaging. Their effectiveness is proved by numerical simulations, and by validation and analysis of the results of real samples.

Apart from the methodological advances, this thesis also covers detailed descriptions of the experimental realization of these studies. These experimental details, including sample size and shape, battery cell design, energy step size, and angular sampling, are key to the efficiency and resolving power of sparse hyperdimensional imaging techniques. They provide valuable guidelines for application of similar methods in future studies.

To note, as discussed in Sections 4.5 and 5.8.6, in both cases the number of independent components reconstructed in the model can be correlated with the total number of tomography measurements multiplied by the sparsity ratio. In other words, the amount of independent parameters that are effectively reconstructed is roughly equal to the total number of projections measured divided by the number of projections required for one static tomography measurement, which is given by the *Crowther criterion*. This correlation can be understood as an upper threshold for the measurement and reconstruction based on sparse sampling synthesis. More specifically, sparse synthesis does not straightforwardly increase the amount of independent information that can be extracted from the data beyond the tomography sampling requirements, and its implementation is highly dependent on the purpose of the hyperdimensional imaging technique, and on the property and response of the samples.

The hyperdimensional imaging methods presented in this thesis can find applications in a wide range of studies. Hyperspectral ptychographic tomography can be used for XANES- or XTNES-based chemical speciation for multiple elements with absorption edges in the hard or soft X-ray energy ranges. For example, similar chemical analysis could be applied to copper in Cu-Zn catalysts, iron in neural cells, or manganese and nickel in battery NMC or LMNO materials. Similarly, the dynamic ptychographic tomography / laminography method is also applicable to various types of dynamic processes, as long as their speed is not too fast for ptychographic imaging, and they can be modelled with a series of monotonic changes. These applications include *operando* imaging of industrial catalysts, studies of pressure or temperature response of structural materials, or even *in-vivo* imaging of organic specimens.

Another future application of hyperdimensional ptychographic tomography is polarization vector tomography. As demonstrated in Chapter 3, 2D ptychography with po-

larization imaging contrast can resolve and differentiate crystal grains inside vanadium pentoxide particles. By applying rotations in the measurement and orientation modelling in 3D, this polarization imaging contrast can be extended to vector tomography for unique orientation determination of crystal grains or nanostructure orientations. Such capability can find applications in a wide variety of fields, from polycrystalline materials to additive manufacturing. This topic, as well as possible implementations of sparsity in vector tomography, are to be investigated in the future.

Furthermore, the implementation of sparse sampling requires little to no modifications to the tomography imaging device or setup. This means that its application is not limited to ptychographic tomography, but to virtually all tomography imaging techniques based on different imaging modalities and at different length scales. The ability of sparse tomographic synthesis to provide high-resolution results with fewer measurements is desirable in most applications, thus its wider implementations can be expected in other hyperdimensional imaging scenarios of various imaging modalities, as enhancement in measurement speed and efficiency is a universal pursuit within all fields of tomographic imaging.

The more general concept of hyperdimensional imaging is not limited to four dimensions. For example, based on the two methods of 4D imaging covered in this thesis, a combined five-dimensional study can be proposed for dynamic chemical speciation of *operando* catalysts or battery cathodes, to reveal changes of their local chemical states and compositions during operation. Such an approach would provide an unprecedented level of information that has the potential to revolutionize current understandings of these materials, however it also poses enormous challenges to the speed and stability of existing imaging techniques, especially when aiming for nanoscale resolution.

These difficulties encountered by more ambitious studies of hyperdimensional imaging will soon get a major advance from the ongoing upgrade to 4th-generation light sources worldwide. The upgrades include extensive improvements to these synchrotron facilities that are designed to provide much higher coherent flux compared to the current generation, and are expected to significantly boost the speed of X-ray imaging, especially for coherent-based imaging techniques such as ptychography. The work presented in this thesis suggests that sparsity implementations will play a key role in future applications of hyperdimensional tomography, in that it exploits the full potentials of new-generation light sources to reach the fastest imaging speed at the highest resolution. Moreover, in X-ray imaging, the amount of information that can be extracted from a sample is fundamentally limited by radiation damage, which can affect both the structure and chemical composition of the sample. This makes it particularly important to develop methods that reduce the number of measurements required, as those presented in this work. In summary, further developments of sparse hyperdimensional tomography will provide a broad range of new opportunities for future studies of advanced imaging and material characterization.

Curriculum Vitae

Name: Zirui Gao
Birth: Apr 5, 1996
Nationality: Chinese

Education

Doctor of Science *Apr 2018 - Mar 2022*
ETH and University of Zurich, Institute for Biomedical Engineering, Switzerland.
Paul Scherrer Institute, Coherent X-ray Scattering Group, Switzerland.

Master of Science in Physics *Sep 2015 - Jan 2018*
ETH Zurich, Department of Physics, Switzerland.
Tokyo Institute of Technology, School of Computing, Japan. (Exchange program)

Bachelor of Science in Applied Physics *Sep 2011 - Jun 2015*
University of Science and Technology of China, School of Physical Sciences, China.

Peer-reviewed Publications

Z. Gao, M. Guizar-Sicairos, V. Lutz-Bueno, A. Schröter, M. Liebi, M. Rudin, and M. Georgiadis, “High-speed tensor tomography: iterative reconstruction tensor tomography (IRTT) algorithm,” *Acta Crystallographica Section A*, vol. 75, no. 2, pp. 223–238, Mar 2019 [82].

Z. Gao, M. Holler, M. Odstrcil, A. Menzel, M. Guizar-Sicairos, and J. Ihli, “Nanoscale crystal grain characterization via linear polarization X-ray ptychography,” *Chem.*

Commun., vol. 56, pp. 13373–13376, 2020 [91].

M. Georgiadis, A. Schroeter, **Z. Gao**, M. Guizar-Sicairos, D. S. Novikov, E. Fieremans, and M. Rudin, “Retrieving neuronal orientations using 3D scanning SAXS and comparison with diffusion MRI,” *NeuroImage*, vol. 204, p. 116214, 2020 [222].

T. A. Grünewald, M. Liebi, N. K. Wittig, A. Johannes, T. Sikjaer, L. Rejnmark, **Z. Gao**, M. Rosenthal, M. Guizar-Sicairos, H. Birkedal, and M. Burghammer, “Mapping the 3D orientation of nanocrystals and nanostructures in human bone: Indications of novel structural features,” *Science Advances*, vol. 6, no. 24, p. eaba4171, 2020 [83].

Z. Gao, M. Odstreil, S. Böcklein, D. Palagin, M. Holler, D. F. Sanchez, F. Krumeich, A. Menzel, M. Stampanoni, G. Mestl, J. A. v. Bokhoven, M. Guizar-Sicairos, and J. Ihli, “Sparse ab initio x-ray transmission spectrotomography for nanoscopic compositional analysis of functional materials,” *Science Advances*, vol. 7, no. 24, p. eabf6971, 2021 [129].

M. Georgiadis, A. Schroeter, **Z. Gao**, M. Guizar-Sicairos, M. Liebi, C. Leuze, J. A. McNab, A. Balolia, J. Veraart, B. Ades-Aron, S. Kim, T. Shepherd, C. H. Lee, P. Walczak, S. Chodankar, P. DiGiacomo, G. David, M. Augath, V. Zerbi, S. Sommer, I. Rajkovic, T. Weiss, O. Bunk, L. Yang, J. Zhang, D. S. Novikov, M. Zeineh, E. Fieremans, and M. Rudin, “Nanostucture-specific X-ray tomography reveals myelin levels, integrity and axon orientations in mouse and human nervous tissue,” *Nature Communications*, vol. 12, no. 1, p. 2941, 2021 [84].

Bibliography

- [1] The Nobel Prize in Physiology or Medicine 1979. NobelPrize.org. Accessed 6 Jan 2022. Available: <https://www.nobelprize.org/prizes/medicine/1979/summary/>
- [2] W. A. Kalender, “X-ray computed tomography,” *Physics in Medicine and Biology*, vol. 51, no. 13, pp. R29–R43, jun 2006. Available: <https://doi.org/10.1088/0031-9155/51/13/r03>
- [3] G. Pontone, S. Scafuri, M. E. Mancini, C. Agalbato, M. Guglielmo, A. Baggiano, G. Muscogiuri, L. Fusini, D. Andreini, S. Mushtaq, E. Conte, A. Annoni, A. Formenti, A. G. Gennari, A. I. Guaricci, M. R. Rabbat, G. Pompilio, M. Pepi, and A. Rossi, “Role of computed tomography in COVID-19,” *Journal of Cardiovascular Computed Tomography*, vol. 15, no. 1, pp. 27–36, 2021. Available: <https://www.sciencedirect.com/science/article/pii/S1934592520304366>
- [4] J.-D. Grunwaldt and C. G. Schroer, “Hard and soft X-ray microscopy and tomography in catalysis: bridging the different time and length scales,” *Chem. Soc. Rev.*, vol. 39, pp. 4741–4753, 2010. Available: <http://dx.doi.org/10.1039/C0CS00036A>
- [5] V. Wood, “X-ray tomography for battery research and development,” *Nature Reviews Materials*, vol. 3, no. 9, pp. 293–295, 2018. Available: <https://doi.org/10.1038/s41578-018-0053-4>
- [6] F. Mees, R. Swennen, M. V. Geet, and P. Jacobs, “Applications of X-ray computed tomography in the geosciences,” *Geological Society, London, Special Publications*, vol. 215, no. 1, pp. 1–6, 2003. Available: <https://sp.lyellcollection.org/content/215/1/1>
- [7] D. Harwood-Nash, “Computed tomography of ancient Egyptian mummies,” *Journal of computer assisted tomography*, vol. 3, no. 6, p. 768–773, December 1979. Available: <http://europepmc.org/abstract/MED/389964>
- [8] G. N. Hounsfield, “Computerized transverse axial scanning (tomography): Part 1. description of system,” *The British Journal of Radiology*, vol. 46, no. 552, pp. 1016–1022, 1973, pMID: 4757352. Available: <https://doi.org/10.1259/0007-1285-46-552-1016>
- [9] F. García-Moreno, P. H. Kamm, T. R. Neu, F. Bülk, M. A. Noack, M. Wegener, N. von der Eltz, C. M. Schlepütz, M. Stampanoni, and J. Banhart, “Tomoscopy: Time-resolved tomography for dynamic processes in

- materials,” *Advanced Materials*, vol. 33, no. 45, p. 2104659, 2021. Available: <https://onlinelibrary.wiley.com/doi/abs/10.1002/adma.202104659>
- [10] M. Holler, A. Diaz, M. Guizar-Sicairos, P. Karvinen, E. Färm, E. Härkönen, M. Ritala, A. Menzel, J. Raabe, and O. Bunk, “X-ray ptychographic computed tomography at 16 nm isotropic 3D resolution,” *Scientific Reports*, vol. 4, no. 1, p. 3857, 2014. Available: <https://doi.org/10.1038/srep03857>
- [11] S. Bonnet, A. Koenig, S. Roux, P. Hugonnard, R. Guillemaud, and P. Grangeat, “Dynamic X-ray computed tomography,” *Proceedings of the IEEE*, vol. 91, no. 10, pp. 1574–1587, 2003. Available: <https://doi.org/10.1109/JPROC.2003.817868>
- [12] D. Gilland, B. Mair, J. Bowsher, and R. Jaszczak, “Simultaneous reconstruction and motion estimation for gated cardiac ECT,” *IEEE Transactions on Nuclear Science*, vol. 49, no. 5, pp. 2344–2349, 2002. Available: <https://doi.org/10.1109/TNS.2002.803820>
- [13] A. A. Isola, M. Grass, and W. J. Niessen, “Fully automatic nonrigid registration-based local motion estimation for motion-corrected iterative cardiac CT reconstruction,” *Medical Physics*, vol. 37, no. 3, pp. 1093–1109, 2010. Available: <https://aapm.onlinelibrary.wiley.com/doi/abs/10.1118/1.3301600>
- [14] L. Ritschl, S. Sawall, M. Knaup, A. Hess, and M. Kachelrieß, “Iterative 4D cardiac micro-CT image reconstruction using an adaptive spatio-temporal sparsity prior,” *Physics in Medicine and Biology*, vol. 57, no. 6, pp. 1517–1525, mar 2012. Available: <https://doi.org/10.1088/0031-9155/57/6/1517>
- [15] R. A. Crowther, D. J. DeRosier, and A. Klug, “The reconstruction of a three-dimensional structure from projections and its application to electron microscopy,” *Proceedings of the Royal Society of London. A. Mathematical and Physical Sciences*, vol. 317, no. 1530, pp. 319–340, 1970. Available: <https://royalsocietypublishing.org/doi/abs/10.1098/rspa.1970.0119>
- [16] F. Pfeiffer, “X-ray ptychography,” *Nature Photonics*, vol. 12, no. 1, pp. 9–17, 2018. Available: <https://doi.org/10.1038/s41566-017-0072-5>
- [17] A. Diaz, P. Trtik, M. Guizar-Sicairos, A. Menzel, P. Thibault, and O. Bunk, “Quantitative X-ray phase nanotomography,” *Phys. Rev. B*, vol. 85, p. 020104, Jan 2012. Available: <https://link.aps.org/doi/10.1103/PhysRevB.85.020104>
- [18] The Nobel Prize in Physics 1901. NobelPrize.org. Accessed 6 Jan 2022. Available: <https://www.nobelprize.org/prizes/physics/1901/summary/>
- [19] D. Paganin, *Coherent X-ray optics*. Oxford University Press, 2006, no. 6. Available: <https://doi.org/10.1093/acprof:oso/9780198567288.001.0001>

-
- [20] A. Snigirev, I. Snigireva, V. Kohn, S. Kuznetsov, and I. Schelokov, "On the possibilities of x-ray phase contrast microimaging by coherent high-energy synchrotron radiation," *Review of Scientific Instruments*, vol. 66, no. 12, pp. 5486–5492, 1995. Available: <https://doi.org/10.1063/1.1146073>
- [21] Y. Shechtman, Y. C. Eldar, O. Cohen, H. N. Chapman, J. Miao, and M. Segev, "Phase retrieval with application to optical imaging: A contemporary overview," *IEEE Signal Processing Magazine*, vol. 32, no. 3, pp. 87–109, 2015. Available: <https://doi.org/10.1109/MSP.2014.2352673>
- [22] E. Maire and P. J. Withers, "Quantitative X-ray tomography," *International Materials Reviews*, vol. 59, no. 1, pp. 1–43, 2014. Available: <https://doi.org/10.1179/1743280413Y.0000000023>
- [23] A. Momose, T. Takeda, Y. Itai, and K. Hirano, "Phase-contrast X-ray computed tomography for observing biological soft tissues," *Nature Medicine*, vol. 2, no. 4, pp. 473–475, 1996. Available: <https://doi.org/10.1038/nm0496-473>
- [24] C. David, B. Nohammer, H. H. Solak, and E. Ziegler, "Differential X-ray phase contrast imaging using a shearing interferometer," *Applied Physics Letters*, vol. 81, no. 17, pp. 3287–3289, 2002. Available: <https://doi.org/10.1063/1.1516611>
- [25] J. E. Trebes, S. B. Brown, E. M. Campbell, D. L. Matthews, D. G. Nilson, G. F. Stone, and D. A. Whelan, "Demonstration of X-ray holography with an X-ray laser," *Science*, vol. 238, no. 4826, pp. 517–519, 1987. Available: <https://www.science.org/doi/abs/10.1126/science.238.4826.517>
- [26] G. Faigel and M. Tegze, "X-ray holography," *Reports on Progress in Physics*, vol. 62, no. 3, pp. 355–393, jan 1999. Available: <https://doi.org/10.1088/0034-4885/62/3/002>
- [27] S. W. Wilkins, T. E. Gureyev, D. Gao, A. Pogany, and A. W. Stevenson, "Phase-contrast imaging using polychromatic hard X-rays," *Nature*, vol. 384, no. 6607, pp. 335–338, 1996. Available: <https://doi.org/10.1038/384335a0>
- [28] D. Paganin, T. E. Gureyev, K. M. Pavlov, R. A. Lewis, and M. Kitchen, "Phase retrieval using coherent imaging systems with linear transfer functions," *Optics Communications*, vol. 234, no. 1, pp. 87–105, 2004. Available: <https://www.sciencedirect.com/science/article/pii/S0030401804001312>
- [29] J. Miao, P. Charalambous, J. Kirz, and D. Sayre, "Extending the methodology of X-ray crystallography to allow imaging of micrometre-sized non-crystalline specimens," *Nature*, vol. 400, no. 6742, pp. 342–344, 1999. Available: <https://doi.org/10.1038/22498>
- [30] I. Robinson and R. Harder, "Coherent X-ray diffraction imaging of strain at the nanoscale," *Nature Materials*, vol. 8, no. 4, pp. 291–298, 2009. Available: <https://doi.org/10.1038/nmat2400>

- [31] J. R. Fienup, “Reconstruction of a complex-valued object from the modulus of its Fourier transform using a support constraint,” *J. Opt. Soc. Am. A*, vol. 4, no. 1, pp. 118–123, Jan 1987. Available: <http://www.osapublishing.org/josaa/abstract.cfm?URI=josaa-4-1-118>
- [32] J. Miao, T. Ishikawa, I. K. Robinson, and M. M. Murnane, “Beyond crystallography: Diffractive imaging using coherent X-ray light sources,” *Science*, vol. 348, no. 6234, pp. 530–535, 2015. Available: <https://www.science.org/doi/abs/10.1126/science.aaa1394>
- [33] S. Marchesini, H. N. Chapman, S. P. Hau-Riege, R. A. London, A. Szoke, H. He, M. R. Howells, H. Padmore, R. Rosen, J. C. H. Spence, and U. Weierstall, “Coherent X-ray diffractive imaging: applications and limitations,” *Opt. Express*, vol. 11, no. 19, pp. 2344–2353, Sep 2003. Available: <http://opg.optica.org/oe/abstract.cfm?URI=oe-11-19-2344>
- [34] J. M. Rodenburg and H. M. L. Faulkner, “A phase retrieval algorithm for shifting illumination,” *Applied Physics Letters*, vol. 85, no. 20, pp. 4795–4797, 2004. Available: <https://doi.org/10.1063/1.1823034>
- [35] P. Thibault, M. Dierolf, A. Menzel, O. Bunk, C. David, and F. Pfeiffer, “High-resolution scanning X-ray diffraction microscopy,” *Science*, vol. 321, no. 5887, pp. 379–382, 2008. Available: <https://www.science.org/doi/abs/10.1126/science.1158573>
- [36] Y. Takahashi, A. Suzuki, N. Zettsu, Y. Kohmura, Y. Senba, H. Ohashi, K. Yamauchi, and T. Ishikawa, “Towards high-resolution ptychographic X-ray diffraction microscopy,” *Phys. Rev. B*, vol. 83, p. 214109, Jun 2011. Available: <https://link.aps.org/doi/10.1103/PhysRevB.83.214109>
- [37] M. Guizar-Sicairos and P. Thibault, “Ptychography: A solution to the phase problem,” *Physics Today*, vol. 74, no. 9, pp. 42–48, 2021. Available: <https://doi.org/10.1063/PT.3.4835>
- [38] M. Holler, M. Guizar-Sicairos, E. H. R. Tsai, R. Dinapoli, E. Müller, O. Bunk, J. Raabe, and G. Aeppli, “High-resolution non-destructive three-dimensional imaging of integrated circuits,” *Nature*, vol. 543, no. 7645, pp. 402–406, 2017. Available: <https://doi.org/10.1038/nature21698>
- [39] M. Holler, M. Odstrčil, M. Guizar-Sicairos, M. Lebugle, E. Müller, S. Finizio, G. Tinti, C. David, J. Zusman, W. Unglaub, O. Bunk, J. Raabe, A. F. J. Levi, and G. Aeppli, “Three-dimensional imaging of integrated circuits with macro- to nanoscale zoom,” *Nature Electronics*, vol. 2, no. 10, pp. 464–470, 2019. Available: <https://doi.org/10.1038/s41928-019-0309-z>
- [40] M. Holler, M. Odstrčil, M. Guizar-Sicairos, M. Lebugle, U. Frommherz, T. Lachat, O. Bunk, J. Raabe, and G. Aeppli, “LamNI – an instrument

- for X-ray scanning microscopy in laminography geometry,” *Journal of Synchrotron Radiation*, vol. 27, no. 3, pp. 730–736, May 2020. Available: <https://doi.org/10.1107/S1600577520003586>
- [41] J. W. Goodman, “Introduction to Fourier optics. 3rd,” *Roberts and Company Publishers*, 2005.
- [42] M. Guizar-Sicairos and J. R. Fienup, “Phase retrieval with transverse translation diversity: a nonlinear optimization approach,” *Opt. Express*, vol. 16, no. 10, pp. 7264–7278, May 2008. Available: <http://opg.optica.org/oe/abstract.cfm?URI=oe-16-10-7264>
- [43] A. M. Maiden and J. M. Rodenburg, “An improved ptychographical phase retrieval algorithm for diffractive imaging,” *Ultramicroscopy*, vol. 109, no. 10, pp. 1256–1262, 2009. Available: <https://www.sciencedirect.com/science/article/pii/S0304399109001284>
- [44] P. Thibault, M. Dierolf, O. Bunk, A. Menzel, and F. Pfeiffer, “Probe retrieval in ptychographic coherent diffractive imaging,” *Ultramicroscopy*, vol. 109, no. 4, pp. 338–343, 2009. Available: <https://www.sciencedirect.com/science/article/pii/S0304399108003458>
- [45] P. Thibault and M. Guizar-Sicairos, “Maximum-likelihood refinement for coherent diffractive imaging,” *New Journal of Physics*, vol. 14, no. 6, p. 063004, 2012. Available: <http://dx.doi.org/10.1088/1367-2630/14/6/063004>
- [46] P. Godard, M. Allain, V. Chamard, and J. Rodenburg, “Noise models for low counting rate coherent diffraction imaging,” *Opt. Express*, vol. 20, no. 23, pp. 25 914–25 934, Nov 2012. Available: <http://www.osapublishing.org/oe/abstract.cfm?URI=oe-20-23-25914>
- [47] M. Odstrcil, A. Menzel, and M. Guizar-Sicairos, “Iterative least-squares solver for generalized maximum-likelihood ptychography,” *Opt. Express*, vol. 26, no. 3, pp. 3108–3123, Feb 2018. Available: <http://www.osapublishing.org/oe/abstract.cfm?URI=oe-26-3-3108>
- [48] O. Mandula, M. Elzo Aizarna, J. Eymery, M. Burghammer, and V. Favre-Nicolin, “*PyNX.Ptycho*: a computing library for X-ray coherent diffraction imaging of nanostructures,” *Journal of Applied Crystallography*, vol. 49, no. 5, pp. 1842–1848, Oct 2016. Available: <https://doi.org/10.1107/S1600576716012279>
- [49] B. Enders and P. Thibault, “A computational framework for ptychographic reconstructions,” *Proceedings of the Royal Society A: Mathematical, Physical and Engineering Sciences*, vol. 472, no. 2196, p. 20160640, 2016. Available: <https://royalsocietypublishing.org/doi/abs/10.1098/rspa.2016.0640>

- [50] K. Wakonig, H.-C. Stadler, M. Odstrcil, E. H. R. Tsai, A. Diaz, M. Holler, I. Usov, J. Raabe, A. Menzel, and M. Guizar-Sicairos, “PtychoShelves, a versatile high-level framework for high-performance analysis of ptychographic data,” *Journal of Applied Crystallography*, vol. 53, no. 2, pp. 574–586, 2020. Available: <https://doi.org/10.1107/S1600576720001776>
- [51] J. Ambrose, “Computerized transverse axial scanning (tomography): Part 2. clinical application,” *The British Journal of Radiology*, vol. 46, no. 552, pp. 1023–1047, 1973, pMID: 4757353. Available: <https://doi.org/10.1259/0007-1285-46-552-1023>
- [52] L. De Chiffre, S. Carmignato, J.-P. Kruth, R. Schmitt, and A. Weckenmann, “Industrial applications of computed tomography,” *CIRP Annals*, vol. 63, no. 2, pp. 655–677, 2014. Available: <https://www.sciencedirect.com/science/article/pii/S0007850614001930>
- [53] S. M. Walker, D. A. Schwyn, R. Mokso, M. Wicklein, T. Müller, M. Doube, M. Stampanoni, H. G. Krapp, and G. K. Taylor, “In vivo time-resolved microtomography reveals the mechanics of the blowfly flight motor,” *PLOS Biology*, vol. 12, no. 3, p. e1001823, 2014. Available: <https://doi.org/10.1371/journal.pbio.1001823>
- [54] J. Deng, Y. H. Lo, M. Gallagher-Jones, S. Chen, A. Pryor, Q. Jin, Y. P. Hong, Y. S. G. Nashed, S. Vogt, J. Miao, and C. Jacobsen, “Correlative 3D X-ray fluorescence and ptychographic tomography of frozen-hydrated green algae,” *Science Advances*, vol. 4, no. 11, p. eaau4548, 2018. Available: <https://www.science.org/doi/abs/10.1126/sciadv.aau4548>
- [55] J. Radon, “On the determination of functions from their integral values along certain manifolds,” *IEEE Transactions on Medical Imaging*, vol. 5, no. 4, pp. 170–176, 1986. Available: <https://doi.org/10.1109/TMI.1986.4307775>
- [56] L. A. Shepp and B. F. Logan, “The Fourier reconstruction of a head section,” *IEEE Transactions on Nuclear Science*, vol. 21, no. 3, pp. 21–43, 1974. Available: <https://doi.org/10.1109/TNS.1974.6499235>
- [57] J. Trampert and J.-J. Leveque, “Simultaneous iterative reconstruction technique: Physical interpretation based on the generalized least squares solution,” *Journal of Geophysical Research: Solid Earth*, vol. 95, no. B8, pp. 12 553–12 559, 1990. Available: <https://agupubs.onlinelibrary.wiley.com/doi/abs/10.1029/JB095iB08p12553>
- [58] Y. Censor and T. Elfving, “Block-iterative algorithms with diagonally scaled oblique projections for the linear feasibility problem,” *SIAM Journal on Matrix Analysis and Applications*, vol. 24, no. 1, pp. 40–58, 2002. Available: <https://doi.org/10.1137/S089547980138705X>

-
- [59] J. Ming and W. Ge, “Convergence of the simultaneous algebraic reconstruction technique (SART),” *IEEE Transactions on Image Processing*, vol. 12, no. 8, pp. 957–961, 2003. Available: <https://doi.org/10.1109/TIP.2003.815295>
- [60] J. Wang and Y. Zheng, “On the convergence of generalized simultaneous iterative reconstruction algorithms,” *IEEE Transactions on Image Processing*, vol. 16, no. 1, pp. 1–6, 2007. Available: <https://doi.org/10.1109/TIP.2006.887725>
- [61] M. J. Lipton, C. B. Higgins, D. Farmer, and D. P. Boyd, “Cardiac imaging with a high-speed Cine-CT scanner: preliminary results.” *Radiology*, vol. 152, no. 3, pp. 579–582, 1984, pMID: 6540463. Available: <https://doi.org/10.1148/radiology.152.3.6540463>
- [62] K. A. Miles, “Measurement of tissue perfusion by dynamic computed tomography,” *The British Journal of Radiology*, vol. 64, no. 761, pp. 409–412, 1991, pMID: 2036562. Available: <https://doi.org/10.1259/0007-1285-64-761-409>
- [63] C. R. Brodersen, A. J. McElrone, B. Choat, M. A. Matthews, and K. A. Shackel, “The Dynamics of Embolism Repair in Xylem: In Vivo Visualizations Using High-Resolution Computed Tomography,” *Plant Physiology*, vol. 154, no. 3, pp. 1088–1095, 09 2010. Available: <https://doi.org/10.1104/pp.110.162396>
- [64] R. T. White, A. Wu, M. Najm, F. P. Orfino, M. Dutta, and E. Kjeang, “4D in situ visualization of electrode morphology changes during accelerated degradation in fuel cells by X-ray computed tomography,” *Journal of Power Sources*, vol. 350, pp. 94–102, 2017. Available: <https://www.sciencedirect.com/science/article/pii/S0378775317303567>
- [65] Y. Wu and N. Liu, “Visualizing battery reactions and processes by using in situ and in operando microscopies,” *Chem*, vol. 4, no. 3, pp. 438–465, 2018. Available: <https://www.sciencedirect.com/science/article/pii/S2451929417305247>
- [66] D. Koningsberger and R. Prins, *X-ray absorption: principles, applications, techniques of EXAFS, SEXAFS, and XANES*. New York: John Wiley and Sons, 1988.
- [67] M. Fernandez-Garcia, “XANES analysis of catalytic systems under reaction conditions,” *Catalysis Reviews*, vol. 44, no. 1, pp. 59–121, 2002. Available: <https://doi.org/10.1081/CR-120001459>
- [68] B. Wang, W. Y. Feng, M. Wang, J. W. Shi, F. Zhang, H. Ouyang, Y. L. Zhao, Z. F. Chai, Y. Y. Huang, Y. N. Xie, H. F. Wang, and J. Wang, “Transport of intranasally instilled fine Fe₂O₃ particles into the brain: Micro-distribution, chemical states, and histopathological observation,” *Biological Trace Element Research*, vol. 118, no. 3, pp. 233–243, 2007. Available: <https://doi.org/10.1007/s12011-007-0028-6>

- [69] W.-S. Yoon, C. P. Grey, M. Balasubramanian, X.-Q. Yang, and J. McBreen, "In situ X-ray absorption spectroscopic study on $\text{LiNi}_{0.5}\text{Mn}_{0.5}\text{O}_2$ cathode material during electrochemical cycling," *Chemistry of Materials*, vol. 15, no. 16, pp. 3161–3169, 2003. Available: <https://doi.org/10.1021/cm030220m>
- [70] A. Ito, Y. Sato, T. Sanada, M. Hatano, H. Horie, and Y. Ohsawa, "In situ X-ray absorption spectroscopic study of Li-rich layered cathode material $\text{Li}[\text{Ni}_{0.17}\text{Li}_{0.2}\text{Co}_{0.07}\text{Mn}_{0.56}]\text{O}_2$," *Journal of Power Sources*, vol. 196, no. 16, pp. 6828–6834, 2011, 15th International Meeting on Lithium Batteries (IMLB). Available: <https://www.sciencedirect.com/science/article/pii/S037877531001712X>
- [71] F. Meirer, J. Cabana, Y. Liu, A. Mehta, J. C. Andrews, and P. Pianetta, "Three-dimensional imaging of chemical phase transformations at the nanoscale with full-field transmission X-ray microscopy," *Journal of Synchrotron Radiation*, vol. 18, no. Pt 5, pp. 773–781, 2011. Available: <http://www.ncbi.nlm.nih.gov/pmc/articles/PMC3161818/>
- [72] G. Schmid, M. Obst, J. Wu, and A. Hitchcock, *3D Chemical Imaging of Nanoscale Biological, Environmental, and Synthetic Materials by Soft X-Ray STXM Spectrotomography*. Berlin, Heidelberg: Springer Berlin Heidelberg, 2016, pp. 43–94. Available: https://doi.org/10.1007/978-3-662-48606-1_2
- [73] S. W. T. Price, K. Ignatyev, K. Geraki, M. Basham, J. Filik, N. T. Vo, P. T. Witte, A. M. Beale, and J. F. W. Mosselmans, "Chemical imaging of single catalyst particles with scanning μ -XANES-CT and μ -XRF-CT," *Physical Chemistry Chemical Physics*, vol. 17, no. 1, pp. 521–529, 2015. Available: <http://dx.doi.org/10.1039/C4CP04488F>
- [74] J. Wang, Y.-c. Karen Chen-Wiegart, C. Eng, Q. Shen, and J. Wang, "Visualization of anisotropic-isotropic phase transformation dynamics in battery electrode particles," *Nature Communications*, vol. 7, no. 1, p. 12372, 2016. Available: <https://doi.org/10.1038/ncomms12372>
- [75] J. Ihli, D. Ferreira Sanchez, R. R. Jacob, V. Cuartero, O. Mathon, F. Krumeich, C. Borca, T. Huthwelker, W.-C. Cheng, Y. Shu, S. Pascarelli, D. Grolimund, A. Menzel, and J. A. van Bokhoven, "Localization and speciation of iron impurities within a fluid catalytic cracking catalyst," *Angewandte Chemie International Edition*, vol. 56, no. 45, pp. 14 031–14 035, 2017. Available: <https://onlinelibrary.wiley.com/doi/abs/10.1002/anie.201707154>
- [76] M. Hirose, N. Ishiguro, K. Shimomura, D.-N. Nguyen, H. Matsui, H. C. Dam, M. Tada, and Y. Takahashi, "Oxygen-diffusion-driven oxidation behavior and tracking areas visualized by X-ray spectro-ptychography with unsupervised learning," *CommChem*, vol. 2, no. 1, p. 50, 2019. Available: <https://doi.org/10.1038/s42004-019-0147-y>

-
- [77] J. Becher, D. F. Sanchez, D. E. Doronkin, D. Zengel, D. M. Meira, S. Pascarelli, J.-D. Grunwaldt, and T. L. Sheppard, “Chemical gradients in automotive cu-ssz-13 catalysts for nox removal revealed by operando X-ray spectrotomography,” *Nature Catalysis*, vol. 4, no. 1, pp. 46–53, 2021. Available: <https://doi.org/10.1038/s41929-020-00552-3>
- [78] A. Malecki, G. Potdevin, T. Biernath, E. Eggl, K. Willer, T. Lasser, J. Maisenbacher, J. Gibmeier, A. Wanner, and F. Pfeiffer, “X-ray tensor tomography,” *EPL (Europhysics Letters)*, vol. 105, no. 3, p. 38002, feb 2014. Available: <https://doi.org/10.1209/0295-5075/105/38002>
- [79] C. Donnelly, M. Guizar-Sicairos, V. Scagnoli, S. Gliga, M. Holler, J. Raabe, and L. J. Heyderman, “Three-dimensional magnetization structures revealed with X-ray vector nanotomography,” *Nature*, vol. 547, p. 328, 2017. Available: <https://doi.org/10.1038/nature23006>
- [80] M. Liebi, M. Georgiadis, A. Menzel, P. Schneider, J. Kohlbrecher, O. Bunk, and M. Guizar-Sicairos, “Nanostructure surveys of macroscopic specimens by small-angle scattering tensor tomography,” *Nature*, vol. 527, no. 7578, pp. 349–352, 2015. Available: <https://doi.org/10.1038/nature16056>
- [81] F. Schaff, M. Bech, P. Zaslansky, C. Jud, M. Liebi, M. Guizar-Sicairos, and F. Pfeiffer, “Six-dimensional real and reciprocal space small-angle X-ray scattering tomography,” *Nature*, vol. 527, no. 7578, pp. 353–356, 2015. Available: <https://doi.org/10.1038/nature16060>
- [82] Z. Gao, M. Guizar-Sicairos, V. Lutz-Bueno, A. Schröter, M. Liebi, M. Rudin, and M. Georgiadis, “High-speed tensor tomography: iterative reconstruction tensor tomography (IRTT) algorithm,” *Acta Crystallographica Section A*, vol. 75, no. 2, pp. 223–238, Mar 2019. Available: <https://doi.org/10.1107/S2053273318017394>
- [83] T. A. Grünewald, M. Liebi, N. K. Wittig, A. Johannes, T. Sikjaer, L. Rejmark, Z. Gao, M. Rosenthal, M. Guizar-Sicairos, H. Birkedal, and M. Burghammer, “Mapping the 3D orientation of nanocrystals and nanostructures in human bone: Indications of novel structural features,” *Science Advances*, vol. 6, no. 24, p. eaba4171, 2020. Available: <https://www.science.org/doi/abs/10.1126/sciadv.aba4171>
- [84] M. Georgiadis, A. Schroeter, Z. Gao, M. Guizar-Sicairos, M. Liebi, C. Leuze, J. A. McNab, A. Balolia, J. Veraart, B. Ades-Aron, S. Kim, T. Shepherd, C. H. Lee, P. Walczak, S. Chodankar, P. DiGiacomo, G. David, M. Augath, V. Zerbi, S. Sommer, I. Rajkovic, T. Weiss, O. Bunk, L. Yang, J. Zhang, D. S. Novikov, M. Zeineh, E. Fieremans, and M. Rudin, “Nanostructure-specific X-ray tomography reveals myelin levels, integrity and axon orientations in mouse and human nervous tissue,” *Nature Communications*, vol. 12, no. 1, p. 2941, 2021. Available: <https://doi.org/10.1038/s41467-021-22719-7>

- [85] J. Nelson Weker and M. F. Toney, “Emerging in situ and operando nanoscale X-ray imaging techniques for energy storage materials,” *Advanced Functional Materials*, vol. 25, no. 11, pp. 1622–1637, 2015. Available: <https://onlinelibrary.wiley.com/doi/abs/10.1002/adfm.201403409>
- [86] Y. Sharma, M. Wiecek, F. Schaff, S. Seyyedi, F. Prade, F. Pfeiffer, and T. Lasser, “Six dimensional X-ray tensor tomography with a compact laboratory setup,” *Applied Physics Letters*, vol. 109, no. 13, p. 134102, 2016. Available: <https://doi.org/10.1063/1.4963649>
- [87] I. Gorodnitsky and B. Rao, “Sparse signal reconstruction from limited data using FOCUSS: a re-weighted minimum norm algorithm,” *IEEE Transactions on Signal Processing*, vol. 45, no. 3, pp. 600–616, 1997. Available: <https://doi.org/10.1109/78.558475>
- [88] E. J. Candes, J. K. Romberg, and T. Tao, “Stable signal recovery from incomplete and inaccurate measurements,” *Communications on Pure and Applied Mathematics*, vol. 59, no. 8, pp. 1207–1223, 2006. Available: <https://onlinelibrary.wiley.com/doi/abs/10.1002/cpa.20124>
- [89] G. R. Myers, A. M. Kingston, T. K. Varslot, M. L. Turner, and A. P. Sheppard, “Dynamic tomography with a priori information,” *Applied Optics*, vol. 50, no. 20, pp. 3685–3690, 2011. Available: <http://www.osapublishing.org/ao/abstract.cfm?URI=ao-50-20-3685>
- [90] G. V. Eyndhoven, K. J. Batenburg, D. Kazantsev, V. V. Nieuwenhove, P. D. Lee, K. J. Dobson, and J. Sijbers, “An iterative CT reconstruction algorithm for fast fluid flow imaging,” *IEEE Transactions on Image Processing*, vol. 24, no. 11, pp. 4446–4458, 2015. Available: <https://doi.org/10.1109/TIP.2015.2466113>
- [91] Z. Gao, M. Holler, M. Odstrcil, A. Menzel, M. Guizar-Sicairos, and J. Ihli, “Nanoscale crystal grain characterization via linear polarization X-ray ptychography,” *Chem. Commun.*, vol. 56, pp. 13 373–13 376, 2020. Available: <http://dx.doi.org/10.1039/D0CC06101H>
- [92] H. Ade and B. Hsiao, “X-ray linear dichroism microscopy,” *Science*, vol. 262, no. 5138, pp. 1427–1429, 1993. Available: <http://science.sciencemag.org/content/sci/262/5138/1427.full.pdf>
- [93] K. Sato, K. Okitsu, Y. Ueji, T. Matsushita, and Y. Amemiya, “Demonstration of X-ray linear dichroism imaging with hard X-rays,” *Journal of Synchrotron Radiation*, vol. 7, no. 6, pp. 368–373, 2000. Available: <https://doi.org/10.1107/S0909049500009985>
- [94] R. T. DeVol, C.-Y. Sun, M. A. Marcus, S. N. Coppersmith, S. C. B. Myneni, and P. U. P. A. Gilbert, “Nanoscale transforming mineral phases in fresh nacre,”

- Journal of the American Chemical Society*, vol. 137, no. 41, pp. 13 325–13 333, 2015. Available: <https://doi.org/10.1021/jacs.5b07931>
- [95] P. U. P. A. Gilbert, “Polarization-dependent imaging contrast (PIC) mapping in 2018,” *Microscopy and Microanalysis*, vol. 24, no. S2, p. 454–457, 2018. Available: <https://doi.org/10.1017/S1431927618014514>
- [96] C. A. Stifler, N. K. Wittig, M. Sassi, C.-Y. Sun, M. A. Marcus, H. Birkedal, E. Beniash, K. M. Rosso, and P. U. P. A. Gilbert, “X-ray linear dichroism in apatite,” *Journal of the American Chemical Society*, vol. 140, no. 37, pp. 11 698–11 704, 2018. Available: <https://doi.org/10.1021/jacs.8b05547>
- [97] B. A. Palmer, G. R. Edwards-Gau, B. M. Kariuki, K. D. M. Harris, I. P. Dolbnya, and S. P. Collins, “X-ray birefringence imaging,” *Science*, vol. 344, no. 6187, pp. 1013–1016, 2014. Available: <http://science.sciencemag.org/content/sci/344/6187/1013.full.pdf>
- [98] B. A. Palmer, S. P. Collins, J. Hulliger, C. E. Hughes, and K. D. M. Harris, “Determining molecular orientations in disordered materials from X-ray linear dichroism at the iodine L1-edge,” *Journal of the American Chemical Society*, vol. 138, no. 50, pp. 16 188–16 191, 2016. Available: <http://dx.doi.org/10.1021/jacs.6b09054>
- [99] Y. Zhou, R. Patterson, B. A. Palmer, G. R. Edwards-Gau, B. Kariuki, N. S. S. Kumar, D. W. Bruce, I. P. Dolbnya, S. P. Collins, A. Malandain, and K. D. M. Harris, “Spatially resolved mapping of phase transitions in liquid-crystalline materials by X-ray birefringence imaging,” *Chemical Science*, vol. 10, no. 10, pp. 3005–3011, 2019. Available: <http://dx.doi.org/10.1039/C8SC05285A>
- [100] M. Odstrčil, “Coherent diffractive imaging using table-top sources,” Doctoral Thesis, Chapter 2&3, University of Southampton, 2017. Available: <https://eprints.soton.ac.uk/415955/>
- [101] H. Chang, M. A. Marcus, and S. Marchesini, “Analyzer-free linear dichroic ptychography,” *Journal of Applied Crystallography*, vol. 53, no. 5, pp. 1283–1292, Oct 2020. Available: <https://doi.org/10.1107/S160057672001002X>
- [102] J. Vila-Comamala, A. Diaz, M. Guizar-Sicairos, A. Manton, C. M. Kewish, A. Menzel, O. Bunk, and C. David, “Characterization of high-resolution diffractive X-ray optics by ptychographic coherent diffractive imaging,” *Optics Express*, vol. 19, no. 22, pp. 21 333–21 344, 2011. Available: <https://www.ncbi.nlm.nih.gov/pubmed/22108984>
- [103] K. Momma and F. Izumi, “VESTA 3 for three-dimensional visualization of crystal, volumetric and morphology data,” *Journal of Applied Crystallography*, vol. 44, no. 6, pp. 1272–1276, 2011. Available: <https://doi.org/10.1107/S0021889811038970>

- [104] J. Liu, H. Xia, D. Xue, and L. Lu, “Double-shelled nanocapsules of V₂O₅-based composites as high-performance anode and cathode materials for Li ion batteries,” *Journal of the American Chemical Society*, vol. 131, no. 34, pp. 12 086–12 087, 2009. Available: <https://doi.org/10.1021/ja9053256>
- [105] S. Wang, Z. Lu, D. Wang, C. Li, C. Chen, and Y. Yin, “Porous monodisperse V₂O₅ microspheres as cathode materials for lithium-ion batteries,” *Journal of Materials Chemistry*, vol. 21, no. 17, pp. 6365–6369, 2011. Available: <http://dx.doi.org/10.1039/C0JM04398B>
- [106] I. E. Wachs, “Catalysis science of supported vanadium oxide catalysts,” *Dalton Transactions*, vol. 42, no. 33, pp. 11 762–11 769, 2013. Available: <http://dx.doi.org/10.1039/C3DT50692D>
- [107] G. A. Horrocks, E. J. Braham, Y. Liang, L. R. De Jesus, J. Jude, J. M. Velázquez, D. Prendergast, and S. Banerjee, “Vanadium K-edge X-ray absorption spectroscopy as a probe of the heterogeneous lithiation of V₂O₅: First-principles modeling and principal component analysis,” *The Journal of Physical Chemistry C*, vol. 120, no. 42, pp. 23 922–23 932, 2016. Available: <https://doi.org/10.1021/acs.jpcc.6b06499>
- [108] P. Ferrand, A. Baroni, M. Allain, and V. Chamard, “Quantitative imaging of anisotropic material properties with vectorial ptychography,” *Optics Letters*, vol. 43, no. 4, pp. 763–766, 2018. Available: <http://ol.osa.org/abstract.cfm?URI=ol-43-4-763>
- [109] X. Zhang, B. Cheng, C. Liu, W. Shen, and J. Zhu, “Quantitative birefringence distribution measurement using mixed-state ptychography,” *Optics Express*, vol. 25, no. 25, pp. 30 851–30 861, 2017. Available: <http://www.opticsexpress.org/abstract.cfm?URI=oe-25-25-30851>
- [110] A. Van der Ven, J. Bhattacharya, and A. A. Belak, “Understanding Li diffusion in Li-intercalation compounds,” *Accounts of Chemical Research*, vol. 46, no. 5, pp. 1216–1225, 2013. Available: <https://doi.org/10.1021/ar200329r>
- [111] C. Wei, Y. Hong, Y. Tian, X. Yu, Y. Liu, and P. Pianetta, “Quantifying redox heterogeneity in single-crystalline LiCoO₂ cathode particles,” *Journal of Synchrotron Radiation*, vol. 27, no. 3, pp. 713–719, 2020. Available: <https://doi.org/10.1107/S1600577520002076>
- [112] J. Ihli, R. R. Jacob, M. Holler, M. Guizar-Sicairos, A. Diaz, J. C. da Silva, D. Ferreira Sanchez, F. Krumeich, D. Grolimund, M. Taddei, W. C. Cheng, Y. Shu, A. Menzel, and J. A. van Bokhoven, “A three-dimensional view of structural changes caused by deactivation of fluid catalytic cracking catalysts,” *Nature Communications*, vol. 8, no. 1, p. 809, 2017. Available: <https://doi.org/10.1038/s41467-017-00789-w>

-
- [113] E. H. R. Tsai, J. Billaud, D. F. Sanchez, J. Ihli, M. Odstrčil, M. Holler, D. Grolimund, C. Villevieille, and M. Guizar-Sicairos, “Correlated X-ray 3D ptychography and diffraction microscopy visualize links between morphology and crystal structure of lithium-rich cathode materials,” *iScience*, vol. 11, pp. 356–365, 2019. Available: <http://www.sciencedirect.com/science/article/pii/S258900421830258X>
- [114] F. Zheng, M. Kotobuki, S. Song, M. O. Lai, and L. Lu, “Review on solid electrolytes for all-solid-state lithium-ion batteries,” *Journal of Power Sources*, vol. 389, pp. 198–213, 2018. Available: <http://www.sciencedirect.com/science/article/pii/S0378775318303653>
- [115] N. Mizuno and M. Misono, “Heterogeneous catalysis,” *Chemical Reviews*, vol. 98, no. 1, pp. 199–218, 1998. Available: <https://doi.org/10.1021/cr960401q>
- [116] W. E. Frazier, “Metal additive manufacturing: A review,” *Journal of Materials Engineering and Performance*, vol. 23, no. 6, pp. 1917–1928, 2014. Available: <https://doi.org/10.1007/s11665-014-0958-z>
- [117] M. Holler, J. Raabe, R. Wepf, S. H. Shahmoradian, A. Diaz, B. Sarafimov, T. Lachat, H. Walther, and M. Vitins, “OMNY PIN—A versatile sample holder for tomographic measurements at room and cryogenic temperatures,” *Review of Scientific Instruments*, vol. 88, no. 11, p. 113701, 2017. Available: <https://doi.org/10.1063/1.4996092>
- [118] M. Odstrčil, M. Lebugle, M. Guizar-Sicairos, C. David, and M. Holler, “Towards optimized illumination for high-resolution ptychography,” *Optics Express*, vol. 27, no. 10, pp. 14 981–14 997, 2019. Available: <http://www.opticsexpress.org/abstract.cfm?URI=oe-27-10-14981>
- [119] X. Huang, H. Yan, R. Harder, Y. Hwu, I. K. Robinson, and Y. S. Chu, “Optimization of overlap uniformness for ptychography,” *Optics Express*, vol. 22, no. 10, pp. 12 634–12 644, 2014. Available: <http://www.osapublishing.org/oe/abstract.cfm?URI=oe-22-10-12634>
- [120] I. Johnson, A. Bergamaschi, H. Billich, S. Cartier, R. Dinapoli, D. Greiffenberg, M. Guizar-Sicairos, B. Henrich, J. Jungmann, D. Mezza, A. Mozzanica, B. Schmitt, X. Shi, and G. Tinti, “Eiger: a single-photon counting X-ray detector,” *Journal of Instrumentation*, vol. 9, no. 05, pp. C05 032–C05 032, may 2014. Available: <https://doi.org/10.1088/1748-0221/9/05/c05032>
- [121] M. Guizar-Sicairos, I. Johnson, A. Diaz, M. Holler, P. Karvinen, H.-C. Stadler, R. Dinapoli, O. Bunk, and A. Menzel, “High-throughput ptychography using Eiger: scanning X-ray nano-imaging of extended regions,” *Optics Express*, vol. 22, no. 12, pp. 14 859–14 870, 2014. Available: <http://www.osapublishing.org/oe/abstract.cfm?URI=oe-22-12-14859>

- [122] M. Holler, J. Raabe, A. Diaz, M. Guizar-Sicairos, C. Quitmann, A. Menzel, and O. Bunk, “An instrument for 3D X-ray nano-imaging,” *Review of Scientific Instruments*, vol. 83, no. 7, p. 073703, 2012. Available: <https://doi.org/10.1063/1.4737624>
- [123] H. Mirko and R. Jörg, “Error motion compensating tracking interferometer for the position measurement of objects with rotational degree of freedom,” *Optical Engineering*, vol. 54, no. 5, pp. 1–7, 2015. Available: <https://doi.org/10.1117/1.OE.54.5.054101>
- [124] M. van Heel and M. Schatz, “Fourier shell correlation threshold criteria,” *Journal of Structural Biology*, vol. 151, no. 3, pp. 250–262, 2005. Available: <http://www.sciencedirect.com/science/article/pii/S1047847705001292>
- [125] M. R. Howells, T. Beetz, H. N. Chapman, C. Cui, J. M. Holton, C. J. Jacobsen, J. Kirz, E. Lima, S. Marchesini, H. Miao, D. Sayre, D. A. Shapiro, J. C. H. Spence, and D. Starodub, “An assessment of the resolution limitation due to radiation-damage in X-ray diffraction microscopy,” *Journal of Electron Spectroscopy and Related Phenomena*, vol. 170, no. 1–3, pp. 4–12, 2009. Available: <http://www.sciencedirect.com/science/article/pii/S0368204808001424>
- [126] M. Guizar-Sicairos, A. Diaz, M. Holler, M. S. Lucas, A. Menzel, R. A. Wepf, and O. Bunk, “Phase tomography from X-ray coherent diffractive imaging projections,” *Optics Express*, vol. 19, no. 22, pp. 21 345–21 357, 2011. Available: <http://www.osapublishing.org/oe/abstract.cfm?URI=oe-19-22-21345>
- [127] M. Guizar-Sicairos, S. T. Thurman, and J. R. Fienup, “Efficient subpixel image registration algorithms,” *Opt. Lett.*, vol. 33, no. 2, pp. 156–158, Jan 2008. Available: <http://opg.optica.org/ol/abstract.cfm?URI=ol-33-2-156>
- [128] C. Studholme, D. Hill, and D. Hawkes, “An overlap invariant entropy measure of 3D medical image alignment,” *Pattern Recognition*, vol. 32, no. 1, pp. 71–86, 1999. Available: <https://www.sciencedirect.com/science/article/pii/S0031320398000910>
- [129] Z. Gao, M. Odstreil, S. Böcklein, D. Palagin, M. Holler, D. F. Sanchez, F. Krumeich, A. Menzel, M. Stampanoni, G. Mestl, J. A. v. Bokhoven, M. Guizar-Sicairos, and J. Ihli, “Sparse ab initio X-ray transmission spectrotomography for nanoscopic compositional analysis of functional materials,” *Science Advances*, vol. 7, no. 24, p. eabf6971, 2021. Available: <https://www.science.org/doi/abs/10.1126/sciadv.abf6971>
- [130] J. R. Ebner and M. R. Thompson, “Key structure-activity relationships in the vanadium phosphorus oxide catalyst system,” in *Structure-Activity and Selectivity Relationships in Heterogeneous Catalysis*, ser. Studies in Surface Science and Catalysis, R. Grasselli and A. Sleight, Eds. Elsevier, 1991, vol. 67, pp. 31–42. Available: <https://www.sciencedirect.com/science/article/pii/S0167299108619242>

-
- [131] D. D. Chung, *Composite materials: science and applications*. Springer Science & Business Media, 2010.
- [132] F. Meirer and B. M. Weckhuysen, “Spatial and temporal exploration of heterogeneous catalysts with synchrotron radiation,” *Nature Reviews Materials*, vol. 3, no. 9, pp. 324–340, 2018. Available: <https://doi.org/10.1038/s41578-018-0044-5>
- [133] D. Kim, M. Chung, J. Carnis, S. Kim, K. Yun, J. Kang, W. Cha, M. J. Cherukara, E. Maxey, R. Harder, K. Sasikumar, S. K R S Sankaranarayanan, A. Zozulya, M. Sprung, D. Riu, and H. Kim, “Active site localization of methane oxidation on Pt nanocrystals,” *Nature Communications*, vol. 9, no. 1, p. 3422, 2018. Available: <https://www.ncbi.nlm.nih.gov/pubmed/30143615><https://www.ncbi.nlm.nih.gov/pmc/articles/PMC6109038/>
- [134] T. Famprakis, P. Canepa, J. A. Dawson, M. S. Islam, and C. Masquelier, “Fundamentals of inorganic solid-state electrolytes for batteries,” *Nature Materials*, vol. 18, no. 12, pp. 1278–1291, 2019. Available: <https://doi.org/10.1038/s41563-019-0431-3>
- [135] F. de Groot, “High-resolution X-ray emission and X-ray absorption spectroscopy,” *Chem. Rev.*, vol. 101, no. 6, pp. 1779–1808, 2001. Available: <https://doi.org/10.1021/cr9900681>
- [136] J. A. van Bokhoven and C. Lamberti, *State-of-the-Art X-Ray Spectroscopy in Catalysis*. Wiley-VCH Verlag GmbH & Co. KGaA, 2017, pp. 1029–1054. Available: <http://dx.doi.org/10.1002/9783527699827.ch39>
- [137] S. C. Garcea, Y. Wang, and P. J. Withers, “X-ray computed tomography of polymer composites,” *Compos. Sci. Technol.*, vol. 156, pp. 305–319, 2018. Available: <http://www.sciencedirect.com/science/article/pii/S0266353817312460>
- [138] C. Y. J. Hémonnot and S. Köster, “Imaging of biological materials and cells by X-ray scattering and diffraction,” *ACS Nano*, vol. 11, no. 9, pp. 8542–8559, 2017. Available: <https://doi.org/10.1021/acsnano.7b03447>
- [139] P. J. Withers and M. Preuss, “Fatigue and damage in structural materials studied by X-ray tomography,” *Annual Review of Materials Research*, vol. 42, no. 1, pp. 81–103, 2012. Available: <https://doi.org/10.1146/annurev-matsci-070511-155111>
- [140] A. H. Andersen and A. C. Kak, “Simultaneous algebraic reconstruction technique (SART): A superior implementation of the ART algorithm,” *Ultrasonic Imaging*, vol. 6, no. 1, pp. 81–94, 1984. Available: <http://www.sciencedirect.com/science/article/pii/0161734684900087>
- [141] M. Dierolf, A. Menzel, P. Thibault, P. Schneider, C. M. Kewish, R. Wepf, O. Bunk, and F. Pfeiffer, “Ptychographic X-ray computed tomography at

- the nanoscale,” *Nature*, vol. 467, no. 7314, pp. 436–439, 2010. Available: <http://dx.doi.org/10.1038/nature09419>
- [142] M. Ruitenbeek, R. A. Overbeek, D. C. Koningsberger, and J. W. Geus, *The Selective Oxidation of N-Butane to Maleic Anhydride; Development of Silica-and Titania Supported V-P-O Catalysts*. Dordrecht: Springer Netherlands, 1998, pp. 423–427. Available: https://doi.org/10.1007/978-94-017-0982-8_20
- [143] B. K. Hodnett, “Vanadium-phosphorus oxide catalysts for the selective oxidation of C4 hydrocarbons to maleic anhydride,” *Catalysis Reviews*, vol. 27, no. 3, pp. 373–424, 1985. Available: <http://dx.doi.org/10.1080/01614948508064740>
- [144] M. Ruitenbeek, A. Barbon, E. v. Faassen, and J. Geus, “Evidence for a new type of vanadyl pairs in (VO)2P2O7: an ESR and magnetisation study,” *Catalysis Letters*, vol. 54, no. 3, pp. 101–104, 1998. Available: <https://doi.org/10.1023/A:1019096409678>
- [145] M. Ruitenbeek, “Characterisation of vanadium-based oxidation catalysts,” Thesis, Utrecht University, 1999. Available: <https://dspace.library.uu.nl/handle/1874/731>
- [146] F. Benzi, G. Giuli, S. Della Longa, and E. Paris, “Vanadium K-edge XANES in vanadium-bearing model compounds: a full multiple scattering study,” *Journal of Synchrotron Radiation*, vol. 23, no. 4, pp. 947–952, 2016. Available: <https://doi.org/10.1107/S1600577516008134>
- [147] G. J. Hutchings, “Vanadium phosphate: a new look at the active components of catalysts for the oxidation of butane to maleic anhydride,” *Journal of Materials Chemistry*, vol. 14, no. 23, pp. 3385–3395, 2004. Available: <http://dx.doi.org/10.1039/B404610M>
- [148] J. Wong, F. W. Lytle, R. P. Messmer, and D. H. Maylotte, “K-edge absorption spectra of selected vanadium compounds,” *Physical Review B*, vol. 30, no. 10, pp. 5596–5610, 1984. Available: <https://link.aps.org/doi/10.1103/PhysRevB.30.5596>
- [149] S. Böcklein, G. Mestl, S. V. Auras, and J. Wintterlin, “On the correlation of structure and catalytic performance of VPO catalysts,” *Topics in Catalysis*, vol. 60, no. 19, pp. 1682–1697, 2017. Available: <https://doi.org/10.1007/s11244-017-0847-4>
- [150] N. F. Dummer, J. K. Bartley, and G. J. Hutchings, *Chapter 4 - Vanadium Phosphate Materials as Selective Oxidation Catalysts*. Academic Press, 2011, vol. 54, pp. 189–247. Available: <http://www.sciencedirect.com/science/article/pii/B9780123877727000046>
- [151] D. J. Thompson, M. O. Fanning, and B. K. Hodnett, “Modelling the active sites in vanadyl pyrophosphate,” *Journal of Molecular Catalysis A: Chemical*, vol. 198, no. 1, pp. 125–137, 2003. Available: <http://www.sciencedirect.com/science/article/pii/S138116902005940>

- [152] M.-J. Cheng, W. A. Goddard, and R. Fu, “The reduction-coupled oxo activation (ROA) mechanism responsible for the catalytic selective activation and functionalization of n-butane to maleic anhydride by vanadium phosphate oxide,” *Topics in Catalysis*, vol. 57, no. 14, pp. 1171–1187, 2014. Available: <https://doi.org/10.1007/s11244-014-0284-6>
- [153] P. L. Gai and K. Kourtakis, “Solid-state defect mechanism in vanadyl pyrophosphate catalysts: Implications for selective oxidation,” *Science*, vol. 267, no. 5198, pp. 661–663, 1995. Available: <https://science.sciencemag.org/content/sci/267/5198/661.full.pdf>
- [154] G. Bergeret, M. David, J. P. Broyer, J. C. Volta, and G. Hecquet, “A contribution to the knowledge of the active sites of VPO catalysts for butane oxidation to maleic anhydride,” *Catalysis Today*, vol. 1, no. 1, pp. 37–47, 1987. Available: <http://www.sciencedirect.com/science/article/pii/0920586187800251>
- [155] A. Bortinger, G. Mazzoni, and T. Monti, “Phosphorus/vanadium catalyst preparation,” Feb. 22 2005, US Patent 6,858,561.
- [156] A. Kaestner, B. Münch, P. Trtik, and L. Butler, “Spatiotemporal computed tomography of dynamic processes,” *Opt. Eng.*, vol. 50, no. 12, pp. 123 201–9, 2011. Available: <http://dx.doi.org/10.1117/1.3660298>
- [157] J. W. Gibbs, K. A. Mohan, E. B. Gulsoy, A. J. Shahani, X. Xiao, C. A. Bouman, M. De Graef, and P. W. Voorhees, “The three-dimensional morphology of growing dendrites,” *Scientific Reports*, vol. 5, no. 1, p. 11824, 2015. Available: <https://doi.org/10.1038/srep11824>
- [158] K. Pearson, “LIII. on lines and planes of closest fit to systems of points in space,” *The London, Edinburgh, and Dublin Philosophical Magazine and Journal of Science*, vol. 2, no. 11, pp. 559–572, 1901. Available: <https://doi.org/10.1080/14786440109462720>
- [159] B. Watts, “Calculation of the Kramers-Kronig transform of X-ray spectra by a piecewise laurent polynomial method,” *Opt. Express*, vol. 22, no. 19, pp. 23 628–23 639, Sep 2014. Available: <http://opg.optica.org/oe/abstract.cfm?URI=oe-22-19-23628>
- [160] K. Ohta and H. Ishida, “Comparison among several numerical integration methods for Kramers-Kronig transformation,” *Applied Spectroscopy*, vol. 42, no. 6, pp. 952–957, 1988. Available: <http://as.osa.org/abstract.cfm?URI=as-42-6-952>
- [161] B. Ravel and M. Newville, “ATHENA, ARTEMIS, HEPHAESTUS: data analysis for X-ray absorption spectroscopy using IFEFFIT,” *Journal of Synchrotron Radiation*, vol. 12, no. 4, pp. 537–541, 2005. Available: <https://doi.org/10.1107/S0909049505012719>

- [162] P. T. Nguyen, R. D. Hoffman, and A. W. Sleight, "Structure of (VO)₂P₂O₇," *Materials Research Bulletin*, vol. 30, no. 9, pp. 1055–1063, 1995. Available: <http://www.sciencedirect.com/science/article/pii/0025540895001166>
- [163] "The circles of light," *Nature Reviews Materials*, vol. 3, no. 9, pp. 281–282, 2018. Available: <https://doi.org/10.1038/s41578-018-0052-5>
- [164] G. Vlaic, D. Andreatta, and P. E. Colavita, "Characterisation of heterogeneous catalysts by EXAFS," *Catalysis Today*, vol. 41, no. 1, pp. 261–275, 1998. Available: <http://www.sciencedirect.com/science/article/pii/S0920586198000558>
- [165] M. Holler, J. Ihli, E. H. R. Tsai, F. Nudelman, M. Verezhak, W. D. J. van de Berg, and S. H. Shahmoradian, "A lathe system for micrometre-sized cylindrical sample preparation at room and cryogenic temperatures," *Journal of Synchrotron Radiation*, vol. 27, no. 2, pp. 472–476, Mar 2020. Available: <https://doi.org/10.1107/S1600577519017028>
- [166] S. Gorelick, J. Vila-Comamala, V. A. Guzenko, R. Barrett, M. Salomé, and C. David, "High-efficiency fresnel zone plates for hard X-rays by 100keV e-beam lithography and electroplating," *J. Synchrotron Radiat.*, vol. 18, no. Pt 3, pp. 442–446, 2011. Available: <http://www.ncbi.nlm.nih.gov/pmc/articles/PMC3133522/>
- [167] T. Kohler, "A projection access scheme for iterative reconstruction based on the golden section," in *IEEE Symposium Conference Record Nuclear Science*, vol. 6, 2004, Conference Proceedings, pp. 3961–3965. Available: <https://doi.org/10.1109/NSSMIC.2004.1466745>
- [168] J. Ihli, A. Diaz, Y. Shu, M. Guizar-Sicairos, M. Holler, K. Wakonig, M. Odstrcil, T. Li, F. Krumeich, E. Müller, W.-C. Cheng, J. Anton van Bokhoven, and A. Menzel, "Resonant ptychographic tomography facilitates three-dimensional quantitative colocalization of catalyst components and chemical elements," *The Journal of Physical Chemistry C*, vol. 122, no. 40, pp. 22 920–22 929, 2018. Available: <https://doi.org/10.1021/acs.jpcc.8b05624>
- [169] A. Averbuch, R. R. Coifman, D. L. Donoho, M. Elad, and M. Israeli, "Fast and accurate polar Fourier transform," *Applied and Computational Harmonic Analysis*, vol. 21, no. 2, pp. 145–167, 2006. Available: <https://www.sciencedirect.com/science/article/pii/S1063520305001065>
- [170] M. Odstrčil, M. Holler, J. Raabe, and M. Guizar-Sicairos, "Alignment methods for nanotomography with deep subpixel accuracy," *Optics Express*, vol. 27, no. 25, pp. 36 637–36 652, 2019. Available: <http://www.opticsexpress.org/abstract.cfm?URI=oe-27-25-36637>
- [171] G. T. Herman, *Fundamentals of Computerized Tomography: Image Reconstruction from Projections*. Springer Publishing Company, Incorporated, 2009.

- [172] T. Hildebrand and P. Rügsegger, “A new method for the model-independent assessment of thickness in three-dimensional images,” *Journal of Microscopy*, vol. 185, no. 1, pp. 67–75, 1997. Available: <http://dx.doi.org/10.1046/j.1365-2818.1997.1340694.x>
- [173] J. Kieffer and D. Karkoulis, “PyFAI, a versatile library for azimuthal regrouping,” *Journal of Physics: Conference Series*, vol. 425, no. 20, p. 202012, 2013. Available: <http://dx.doi.org/10.1088/1742-6596/425/20/202012>
- [174] P. Bleuet, E. Welcomme, E. Dooryhee, J. Susini, J.-L. Hodeau, and P. Walter, “Probing the structure of heterogeneous diluted materials by diffraction tomography,” *Nature Materials*, vol. 7, no. 6, pp. 468–472, 2008. Available: <http://dx.doi.org/10.1038/nmat2168>
- [175] W. De Nolf, F. Vanmeert, and K. Janssens, “XRDUA: crystalline phase distribution maps by two-dimensional scanning and tomographic (micro) X-ray powder diffraction,” *Journal of Applied Crystallography*, vol. 47, no. 3, pp. 1107–1117, 2014. Available: <http://dx.doi.org/10.1107/S1600576714008218>
- [176] Y.-S. Yu, M. Farmand, C. Kim, Y. Liu, C. P. Grey, F. C. Strobridge, T. Tylistczak, R. Celestre, P. Denes, J. Joseph, H. Krishnan, F. R. N. C. Maia, A. L. D. Kilcoyne, S. Marchesini, T. P. C. Leite, T. Warwick, H. Padmore, J. Cabana, and D. A. Shapiro, “Three-dimensional localization of nanoscale battery reactions using soft X-ray tomography,” *Nature Communications*, vol. 9, no. 1, p. 921, 2018. Available: <https://doi.org/10.1038/s41467-018-03401-x>
- [177] V. Blum, R. Gehrke, F. Hanke, P. Havu, V. Havu, X. Ren, K. Reuter, and M. Scheffler, “Ab initio molecular simulations with numeric atom-centered orbitals,” *Computer Physics Communications*, vol. 180, no. 11, pp. 2175–2196, 2009. Available: <http://www.sciencedirect.com/science/article/pii/S0010465509002033>
- [178] X. Ren, P. Rinke, V. Blum, J. Wieferink, A. Tkatchenko, A. Sanfilippo, K. Reuter, and M. Scheffler, “Resolution-of-identity approach to Hartree–Fock, hybrid density functionals, RPA, MP2 and GW with numeric atom-centered orbital basis functions,” *New Journal of Physics*, vol. 14, no. 5, p. 053020, 2012. Available: <http://dx.doi.org/10.1088/1367-2630/14/5/053020>
- [179] J. P. Perdew, K. Burke, and M. Ernzerhof, “Generalized gradient approximation made simple,” *Physical Review Letters*, vol. 77, no. 18, pp. 3865–3868, 1996. Available: <https://link.aps.org/doi/10.1103/PhysRevLett.77.3865>
- [180] M. Peña Fernández, A. P. Kao, R. Bonithon, D. Howells, A. J. Bodey, K. Wanelik, F. Witte, R. Johnston, H. Arora, and G. Tozzi, “Time-resolved in situ synchrotron-microCT: 4D deformation of bone and bone analogues using digital volume correlation,” *Acta Biomaterialia*, vol. 131, pp. 424–439, 2021. Available: <https://www.sciencedirect.com/science/article/pii/S1742706121003883>

- [181] Z. Ning, D. S. Jolly, G. Li, R. De Meyere, S. D. Pu, Y. Chen, J. Kasemchainan, J. Ihli, C. Gong, B. Liu, D. L. R. Melvin, A. Bonnin, O. Magdysyuk, P. Adamson, G. O. Hartley, C. W. Monroe, T. J. Marrow, and P. G. Bruce, “Visualizing plating-induced cracking in lithium-anode solid-electrolyte cells,” *Nature Materials*, vol. 20, no. 8, pp. 1121–1129, 2021. Available: <https://doi.org/10.1038/s41563-021-00967-8>
- [182] C. J. Ritchie, C. R. Crawford, J. D. Godwin, K. F. King, and K. Yongmin, “Correction of computed tomography motion artifacts using pixel-specific back-projection,” *IEEE Transactions on Medical Imaging*, vol. 15, no. 3, pp. 333–342, 1996. Available: <https://doi.org/10.1109/42.500142>
- [183] L. ROIBAN, S. LI, M. AOUINE, A. TUEL, D. FARRUSSENG, and T. EPICIER, “Fast ‘Operando’ electron nanotomography,” *Journal of Microscopy*, vol. 269, no. 2, pp. 117–126, 2018. Available: <https://onlinelibrary.wiley.com/doi/abs/10.1111/jmi.12557>
- [184] M. Esmaeili, J. B. Fløystad, A. Diaz, K. Høydalsvik, M. Guizar-Sicairos, J. W. Andreasen, and D. W. Breiby, “Ptychographic X-ray tomography of silk fiber hydration,” *Macromolecules*, vol. 46, no. 2, pp. 434–439, 2013. Available: <https://doi.org/10.1021/ma3021163>
- [185] Z. Yu, J. Wang, and Y. Liu, “High-dimensional and high-resolution X-ray tomography for energy materials science,” *MRS Bulletin*, vol. 45, no. 4, pp. 283–289, 2020. Available: <https://www.cambridge.org/core/article/highdimensional-and-highresolution-xray-tomography-for-energy-materials-science/EB6F4C58D3858FD941317291C13426F1>
- [186] J.-W. Buurlage, F. Marone, D. M. Pelt, W. J. Palenstijn, M. Stampanoni, K. J. Batenburg, and C. M. Schlepütz, “Real-time reconstruction and visualisation towards dynamic feedback control during time-resolved tomography experiments at TOMCAT,” *Scientific Reports*, vol. 9, no. 1, p. 18379, 2019. Available: <https://doi.org/10.1038/s41598-019-54647-4>
- [187] P. K. Anders, M. Beat, and T. Pavel, “Spatiotemporal computed tomography of dynamic processes,” *Optical Engineering*, vol. 50, no. 12, pp. 1–10, 2011. Available: <https://doi.org/10.1117/1.3660298>
- [188] K. A. Mohan, S. V. Venkatakrishnan, J. W. Gibbs, E. B. Gulsoy, X. Xiao, M. D. Graef, P. W. Voorhees, and C. A. Bouman, “TIMBIR: A method for time-space reconstruction from interlaced views,” *IEEE Transactions on Computational Imaging*, vol. 1, no. 2, pp. 96–111, 2015. Available: <https://doi.org/10.1109/TCI.2015.2431913>
- [189] W. Ziling, Y. Ting, L. Ling, and Z. Yunhui, “Feature-based sparse angle tomography reconstruction for dynamic characterization of bio-cellular

- materials,” in *Proc.SPIE*, vol. 10669, 2018, Conference Proceedings. Available: <https://doi.org/10.1117/12.2304935>
- [190] M. Odstreil, M. Holler, J. Raabe, A. Sepe, X. Sheng, S. Vignolini, C. G. Schroer, and M. Guizar-Sicairos, “Ab initio nonrigid X-ray nanotomography,” *Nature communications*, vol. 10, no. 1, p. 2600, 2019. Available: <https://doi.org/10.1038/s41467-019-10670-7>
- [191] D. Banham, J. Zou, S. Mukerjee, Z. Liu, D. Yang, Y. Zhang, Y. Peng, and A. Dong, “Ultralow platinum loading proton exchange membrane fuel cells: Performance losses and solutions,” *Journal of Power Sources*, vol. 490, p. 229515, 2021. Available: <https://www.sciencedirect.com/science/article/pii/S0378775321000641>
- [192] L. Pan, S. Ott, F. Dionigi, and P. Strasser, “Current challenges related to the deployment of shape-controlled Pt alloy oxygen reduction reaction nanocatalysts into low Pt-loaded cathode layers of proton exchange membrane fuel cells,” *Current Opinion in Electrochemistry*, vol. 18, pp. 61–71, 2019. Available: <https://www.sciencedirect.com/science/article/pii/S2451910319301607>
- [193] J. Lee, S. Escribano, F. Micoud, G. Gebel, S. Lyonnard, L. Porcar, N. Martinez, and A. Morin, “In situ measurement of ionomer water content and liquid water saturation in fuel cell catalyst layers by high-resolution small-angle neutron scattering,” *ACS Applied Energy Materials*, vol. 3, no. 9, pp. 8393–8401, 2020. Available: <https://doi.org/10.1021/acsaem.0c00853>
- [194] Y. Nagai, J. Eller, T. Hatanaka, S. Yamaguchi, S. Kato, A. Kato, F. Marone, H. Xu, and F. N. Büchi, “Improving water management in fuel cells through microporous layer modifications: Fast operando tomographic imaging of liquid water,” *Journal of Power Sources*, vol. 435, p. 226809, 2019. Available: <https://www.sciencedirect.com/science/article/pii/S0378775319307943>
- [195] N. Ishiguro, T. Higashino, M. Hirose, and Y. Takahashi, “Nanoscale visualization of phase transition in melting of Sn–Bi particles by in situ hard X-ray ptychographic coherent diffraction imaging,” *Microscopy and Microanalysis*, vol. 26, no. 5, pp. 878–885, 2020. Available: <https://doi.org/10.1017/S1431927620024332>
- [196] H. Quan, D. Kisailus, and M. A. Meyers, “Hydration-induced reversible deformation of biological materials,” *Nature Reviews Materials*, vol. 6, no. 3, pp. 264–283, 2021. Available: <https://doi.org/10.1038/s41578-020-00251-2>
- [197] J. C. da Silva, P. Trtik, A. Diaz, M. Holler, M. Guizar-Sicairos, J. Raabe, O. Bunk, and A. Menzel, “Mass density and water content of saturated never-dried calcium silicate hydrates,” *Langmuir*, vol. 31, no. 13, pp. 3779–3783, 2015. Available: <https://doi.org/10.1021/la504478j>
- [198] A. Kusoglu and A. Z. Weber, “New insights into perfluorinated sulfonic-acid ionomers,” *Chemical Reviews*, vol. 117, no. 3, pp. 987–1104, 2017. Available: <https://doi.org/10.1021/acs.chemrev.6b00159>

- [199] Y. V. Yakovlev, Y. V. Lobko, M. Vorokhta, J. Nováková, M. Mazur, I. Matolínová, and V. Matolín, “Ionomer content effect on charge and gas transport in the cathode catalyst layer of proton-exchange membrane fuel cells,” *Journal of Power Sources*, vol. 490, p. 229531, 2021. Available: <https://www.sciencedirect.com/science/article/pii/S0378775321000793>
- [200] T. Soboleva, K. Malek, Z. Xie, T. Navessin, and S. Holdcroft, “PEMFC catalyst layers: The role of micropores and mesopores on water sorption and fuel cell activity,” *ACS Applied Materials & Interfaces*, vol. 3, no. 6, pp. 1827–1837, 2011. Available: <https://doi.org/10.1021/am200590w>
- [201] D. C. Ghiglia and M. D. Pritt, *Two-Dimensional Phase Unwrapping: Theory, Algorithms And Software*. Wiley, 1998.
- [202] M. Bühner, H. Xu, J. Eller, J. Sijbers, M. Stampanoni, and F. Marone, “Unveiling water dynamics in fuel cells from time-resolved tomographic microscopy data,” *Scientific Reports*, vol. 10, no. 1, p. 16388, 2020. Available: <https://doi.org/10.1038/s41598-020-73036-w>
- [203] X.-B. Cheng, R. Zhang, C.-Z. Zhao, and Q. Zhang, “Toward safe lithium metal anode in rechargeable batteries: A review,” *Chemical Reviews*, vol. 117, no. 15, pp. 10403–10473, 2017, PMID: 28753298. Available: <https://doi.org/10.1021/acs.chemrev.7b00115>
- [204] J. Liu, Z. Bao, Y. Cui, E. J. Dufek, J. B. Goodenough, P. Khalifah, Q. Li, B. Y. Liaw, P. Liu, A. Manthiram, Y. S. Meng, V. R. Subramanian, M. F. Toney, V. V. Viswanathan, M. S. Whittingham, J. Xiao, W. Xu, J. Yang, X.-Q. Yang, and J.-G. Zhang, “Pathways for practical high-energy long-cycling lithium metal batteries,” *Nature Energy*, vol. 4, no. 3, pp. 180–186, 2019. Available: <https://doi.org/10.1038/s41560-019-0338-x>
- [205] A. Manthiram, “A reflection on lithium-ion battery cathode chemistry,” *Nature Communications*, vol. 11, no. 1, p. 1550, 2020. Available: <https://doi.org/10.1038/s41467-020-15355-0>
- [206] P. P. Paul, E. J. McShane, A. M. Colclasure, N. Balsara, D. E. Brown, C. Cao, B.-R. Chen, P. R. Chinnam, Y. Cui, E. J. Dufek, D. P. Finegan, S. Gillard, W. Huang, Z. M. Konz, R. Kostecki, F. Liu, S. Lubner, R. Prasher, M. B. Preefer, J. Qian, M.-T. F. Rodrigues, M. Schnabel, S.-B. Son, V. Srinivasan, H.-G. Steinrück, T. R. Tanim, M. F. Toney, W. Tong, F. Usseglio-Viretta, J. Wan, M. Yusuf, B. D. McCloskey, and J. Nelson Weker, “A review of existing and emerging methods for lithium detection and characterization in Li-ion and Li-metal batteries,” *Advanced Energy Materials*, vol. 11, no. 17, p. 2100372, 2021. Available: <https://onlinelibrary.wiley.com/doi/abs/10.1002/aenm.202100372>
- [207] Z. Deng, X. Lin, Z. Huang, J. Meng, Y. Zhong, G. Ma, Y. Zhou, Y. Shen, H. Ding, and Y. Huang, “Recent progress on advanced imaging techniques for lithium-ion

- batteries,” *Advanced Energy Materials*, vol. 11, no. 2, p. 2000806, 2021. Available: <https://onlinelibrary.wiley.com/doi/abs/10.1002/aenm.202000806>
- [208] V. Etacheri, R. Marom, R. Elazari, G. Salitra, and D. Aurbach, “Challenges in the development of advanced Li-ion batteries: a review,” *Energy Environ. Sci.*, vol. 4, pp. 3243–3262, 2011. Available: <http://dx.doi.org/10.1039/C1EE01598B>
- [209] L. de Biasi, A. O. Kondrakov, H. Geßwein, T. Brezesinski, P. Hartmann, and J. Janek, “Between scylla and charybdis: Balancing among structural stability and energy density of layered NCM cathode materials for advanced lithium-ion batteries,” *The Journal of Physical Chemistry C*, vol. 121, no. 47, pp. 26 163–26 171, 2017. Available: <https://doi.org/10.1021/acs.jpcc.7b06363>
- [210] S.-M. Bak, Z. Shadike, R. Lin, X. Yu, and X.-Q. Yang, “In situ/operando synchrotron-based X-ray techniques for lithium-ion battery research,” *NPG Asia Materials*, vol. 10, no. 7, pp. 563–580, 2018. Available: <https://doi.org/10.1038/s41427-018-0056-z>
- [211] Y. Yang, R. Xu, K. Zhang, S.-J. Lee, L. Mu, P. Liu, C. K. Waters, S. Spence, Z. Xu, C. Wei, D. J. Kautz, Q. Yuan, Y. Dong, Y.-S. Yu, X. Xiao, H.-K. Lee, P. Pianetta, P. Cloetens, J.-S. Lee, K. Zhao, F. Lin, and Y. Liu, “Quantification of heterogeneous degradation in Li-ion batteries,” *Advanced Energy Materials*, vol. 9, no. 25, p. 1900674, 2019. Available: <https://onlinelibrary.wiley.com/doi/abs/10.1002/aenm.201900674>
- [212] A. K. C. Estandarte, J. Diao, A. V. Llewellyn, A. Jnawali, T. M. M. Heenan, S. R. Daemi, J. J. Bailey, S. Cipiccia, D. Batey, X. Shi, C. Rau, D. J. L. Brett, R. Jarvis, I. K. Robinson, and P. R. Shearing, “Operando Bragg coherent diffraction imaging of LiNi_{0.8}Mn_{0.1}Co_{0.1}O₂ primary particles within commercially printed NMC811 electrode sheets,” *ACS Nano*, vol. 15, no. 1, pp. 1321–1330, 2021, pMID: 33355443. Available: <https://doi.org/10.1021/acsnano.0c08575>
- [213] S. S. Zhang, “The effect of the charging protocol on the cycle life of a Li-ion battery,” *Journal of Power Sources*, vol. 161, no. 2, pp. 1385–1391, 2006. Available: <https://www.sciencedirect.com/science/article/pii/S0378775306011839>
- [214] R. Xu, L. S. de Vasconcelos, J. Shi, J. Li, and K. Zhao, “Disintegration of meatball electrodes for LiNi_xMn_yCo_zO₂ cathode materials,” *Experimental Mechanics*, vol. 58, no. 4, pp. 549–559, 2018. Available: <https://doi.org/10.1007/s11340-017-0292-0>
- [215] A. Manthiram, X. Yu, and S. Wang, “Lithium battery chemistries enabled by solid-state electrolytes,” *Nature Reviews Materials*, vol. 2, no. 4, p. 16103, 2017. Available: <https://doi.org/10.1038/natrevmats.2016.103>
- [216] R. Chen, Q. Li, X. Yu, L. Chen, and H. Li, “Approaching practically accessible solid-state batteries: Stability issues related to solid electrolytes and interfaces,”

- Chemical Reviews*, vol. 120, no. 14, pp. 6820–6877, 2020, pMID: 31763824. Available: <https://doi.org/10.1021/acs.chemrev.9b00268>
- [217] S. Gondrom, J. Zhou, M. Maisl, H. Reiter, M. Kröning, and W. Arnold, “X-ray computed laminography: an approach of computed tomography for applications with limited access,” *Nuclear Engineering and Design*, vol. 190, no. 1, pp. 141–147, 1999. Available: <https://www.sciencedirect.com/science/article/pii/S0029549398003197>
- [218] S. H. Jung, U.-H. Kim, J.-H. Kim, S. Jun, C. S. Yoon, Y. S. Jung, and Y.-K. Sun, “Ni-rich layered cathode materials with electrochemo-mechanically compliant microstructures for all-solid-state Li batteries,” *Advanced Energy Materials*, vol. 10, no. 6, p. 1903360, 2020. Available: <https://doi.org/10.1002/aenm.201903360>
- [219] L. Zhou, C. Y. Kwok, A. Shyamsunder, Q. Zhang, X. Wu, and L. F. Nazar, “A new halospinel superionic conductor for high-voltage all solid state lithium batteries,” *Energy Environ. Sci.*, vol. 13, pp. 2056–2063, 2020. Available: <http://dx.doi.org/10.1039/D0EE01017K>
- [220] T. M. M. Heenan, A. Wade, C. Tan, J. E. Parker, D. Matras, A. S. Leach, J. B. Robinson, A. Llewellyn, A. Dimitrijevic, R. Jervis, P. D. Quinn, D. J. L. Brett, and P. R. Shearing, “Identifying the origins of microstructural defects such as cracking within Ni-rich NMC811 cathode particles for lithium-ion batteries,” *Advanced Energy Materials*, vol. 10, no. 47, p. 2002655, 2020. Available: <https://onlinelibrary.wiley.com/doi/abs/10.1002/aenm.202002655>
- [221] R. Koerver, W. Zhang, L. de Biasi, S. Schweidler, A. O. Kondrakov, S. Kolling, T. Brezesinski, P. Hartmann, W. G. Zeier, and J. Janek, “Chemo-mechanical expansion of lithium electrode materials – on the route to mechanically optimized all-solid-state batteries,” *Energy Environ. Sci.*, vol. 11, pp. 2142–2158, 2018. Available: <http://dx.doi.org/10.1039/C8EE00907D>
- [222] M. Georgiadis, A. Schroeter, Z. Gao, M. Guizar-Sicairos, D. S. Novikov, E. Fieremans, and M. Rudin, “Retrieving neuronal orientations using 3D scanning SAXS and comparison with diffusion MRI,” *NeuroImage*, vol. 204, p. 116214, 2020. Available: <https://www.sciencedirect.com/science/article/pii/S1053811919308055>